RECOMMENDATION FOR EXPERIMENTAL STUDIES ON THE SEISMIC BEHAVIOR OF STEEL COMPONENTS AND MATERIALS

by

Helmut Krawinkler
Mahmud Zohrei
Bahman Lashkari-Irvani
Nathaniel G. Cofie
Hassan Hadidi-Tamjed

The John A. Blume Earthquake Engineer Center
Department of Civil Engineering
Stanford University
Stanford, California 94305

A Report on a Research Project Sponsored by the
NATIONAL SCIENCE FOUNDATION
Grant CEE-7902616

September 1983

The John A. Blume Earthquake Engineering Center was established to promote research and education in earthquake engineering. Through its activities our understanding of earthquakes and their effects on mankind's facilities and structures is improving. The Center conducts research, provides instruction, publishes reports and articles, conducts seminars and conferences, and provides financial support for students. The Center is named for Dr. John A. Blume, a well-known consulting engineer and Stanford alumnus.

Address

The John A. Blume Earthquake Engineering Center
Department of Civil Engineering
Stanford University
Stanford, California 94305

50272-101

REPORT DOCUMENTATION PAGE	1. REPORT NO. NSF/CEE-83220	2.	3. Recipient's Accession No. PB84 152743

4. Title and Subtitle
Recommendations for Experimental Studies on the Seismic Behavior of Steel Components and Materials

5. Report Date
September 1983

6.

7. Author(s)
H. Krawinkler, M. Zohrei, B. Lashkari-Irvani, N.G. Cofie, et al.

8. Performing Organization Rept. No.
61

9. Performing Organization Name and Address
Stanford University
J.A. Blume Earthquake Engineering Center
Stanford, CA 94305

10. Project/Task/Work Unit No.

11. Contract(C) or Grant(G) No.
(C)
(G) CEE7902616

12. Sponsoring Organization Name and Address
Directorate for Engineering (ENG)
National Science Foundation
1800 G Street, N.W.
Washington, DC 20550

13. Type of Report & Period Covered

14.

15. Supplementary Notes

16. Abstract (Limit: 200 words)

Results are presented of a study undertaken to identify parameters and testing programs that will permit an evaluation of deterioration and closeness to failure of a component which is part of a structure that may be subjected to severe earthquakes of random character. Testing standards and experimental procedures employed by the research community are reviewed and the purpose of component experimentation is explained from the viewpoint of performance assessment. Low-cycle fatigue properties of structural steel are discussed and the cyclic stress-strain properties of A36 structural steel are analyzed. The seismic response parameters needed for damage evaluation and performance assessment of structural components and for development of representative cyclic loading histories are studied. It is concluded that simple cumulative damage models can be utilized to assess deterioration and failure in structural components. It is recommended that experimentation be directed toward a determination of the structural performance parameters needed for cumulative damage modeling.

17. Document Analysis a. Descriptors

Strains
Earthquakes
Damage
Steel structures
Fatigue (materials)
Mathematical models
Structural steels
Cyclic loads
Components
Earthquake resistant structures
Dynamic structural analysis
Deterioration
Failure
Stresses

b. Identifiers/Open-Ended Terms

H. Krawinkler, /PI

c. COSATI Field/Group

18. Availability Statement	19. Security Class (This Report)	21. No. of Pages
NTIS	20. Security Class (This Page)	22. Price

(See ANSI-Z39.18) See Instructions on Reverse OPTIONAL FORM 272 (4-7) (Formerly NTIS-35) Department of Commerce

ABSTRACT

The study discussed in this report is concerned with experimental procedures for a seismic performance assessment of steel components and materials. The main objective of this study is to identify parameters and testing programs that will permit an evaluation of deterioration and closeness to failure of a component which is part of a structure that may be subjected to one or several severe earthquakes of random character.

In order to achieve this objective, the following aspects are considered in this study and are discussed in this report: (1) An identification of the purpose of component experimentation from the viewpoint of performance assessment; (2) A review of testing standards and of experimental procedures employed by the research community; (3) A review of low-cycle fatigue properties of structural steel, recommendations for testing procedures for materials, and a study of the cyclic stress-strain properties of A36 structural steel; (4) A review of low-cycle fatigue damage models and an assessment of their applicability to the problem of performance evaluation of structural components; (5) An experimental study of component performance, considering the deterioration and failure modes of local buckling in beam flanges and of crack propagation at weldments; (6) An analytical study on those seismic response parameters that are needed for damage evaluation and performance assessment of structural components, and for a development of representative cyclic loading histories.

The conclusion drawn from this study is that simple cumulative damage models can be utilized to assess deterioration and failure in structural components. Thus, experimentation should be directed towards a determination of the structural performance parameters needed for cumulative damage modeling. The basic tests for this purpose are constant amplitude tests in which the deformation parameter used in the damage model is kept constant throughout each test. Several identical specimens need to be tested because at least two performance parameters must be determined and because these parameters may exhibit considerable

scatter. The results of a single test with a preselected loading history cannot be used for a general performance assessment. If a single test is used to check component performance, the applied loading history should be statistically representative of the deformation demands imposed by earthquakes. Recommendations on the selection of such histories and on other aspects of component testing are provided in the last chapter of this report.

ACKNOWLEDGEMENTS

This report summarizes the results of a research project conducted under the sponsorship of the National Science Foundation (Grant CEE-7902616). The authors acknowledge the financial support provided by NSF and the continued encouragement of the Program Manager in charge, Dr. J.B. Scalzi.

The research was conducted at the John A. Blume Earthquake Engineering Center at Stanford University, Professors H.C. Shah and J.M. Gere, Directors. The technical staff of the Center, in particular Mr. J.H. Hessler, provided skillful support throughout this study.

Many thanks are expressed to Professor G.I. Schueller for the many stimulating discussions during the senior author's two months research visit at the Technical University Munich, Germany. The financial support provided for this visit through a project sponsored by the Deutschen Forschungsgemeinschaft (Sonderforschungsbereich 96) is gratefully acknowledged.

TABLE OF CONTENTS

CHAPTER 1

INTRODUCTION

1.1 STATEMENT OF THE PROBLEM

Much experimental work has been done in recent years in laboratories of universities, government and industry directed towards achieving a better understanding of the response of structures to seismic excitations. Whether such experimentation is concerned with materials, structural elements, subassemblies, or complete structures, the objective is usually an evaluation of the resistance-deformation characteristics under "earthquake-like loading." This evaluation may be done for specific purposes such as the development or verification of analytical models, the investigation of low cycle fatigue behavior, or the verification of the integrity of a specific structural system under a specific history of loading.

Irrespective of specific objectives, the final outcome of past and anticipated future experimental research in earthquake engineering should be the development of a reliable set of information for the seismic design of structures, consistent with the risk of damage the user and other segments of society are willing to accept.

In order to arrive at reliable criteria for the design of serviceable and safe structures in seismic environments, it is necessary to draw general conclusions from specific sets of experiments. However, experiments usually are based on a great number of simplifying assumptions and subjective decisions which make an interpretation and generalization of specific test results a very difficult task.

The work discussed in this report is concerned with one specific type of experimentation, that is, testing of subsystems of structural configurations in which the seismic effects are simulated by means of quasi-static cyclic load application. In this type of experimentation the following three fundamental questions must be addressed:

1. For a specific or generic structural system, which subsystems (e.g., materials, elements, connections, subassemblies) need to be investigated experimentally in order that reliable conclusions can be drawn on the performance of the system under severe earthquakes?

2. For a selected subsystem, what type (or types) of loading history will best provide the information needed for an evaluation of the performance of the subsystem?

3. How can the results of individual experiments on a subsystem be utilized to predict the behavior of the subsystem as part of a structural system subjected to various types of ground motions? In other words, what are the strength and deformation parameters that need to be determined experimentally to fully describe the response characteristics of the subsystem under, in the most general term, random cyclic loading?

The emphasis in this report is directed towards an answer to questions 2 and 3 with some effort devoted to the first question. The importance of the latter two questions can be illustrated on a simple example. Let us consider the seismic behavior of moment resisting connections in steel frames. Many types of connectios have been studied experimentally under cyclic load application. The result of past studies is that certain types of connections, whose superior performance was evident from cyclic load studies, are widely and almost exclusively used in highly seismic regions. The design profession and the building officials have confidence in these connections because tests have shown that they "exhibit very ductile behavior and are capable of resisting deformation reversals in excess of those anticipated in severe earthquakes." This qualitative statement suffices for a few types of very ductile connections but may discriminate against other types of connections which cannot obtain this unconditional stamp of approval. Considering that very ductile connections may be rather expensive and may not be needed in regions of lower seismicity, it appears necessary to develop a more quantitative procedure for evaluating connection behavior which permits a correlation between anticipated deformation demand and low cycle fatigue life. It is the subject of this research to develop such quantitative procedures.

Similar arguments can be applied to experimental studies on other structural elements such as beam-column joints, flexural elements that may be susceptible to local or lateral torsional buckling, bracing elements, steel diaphragms, etc. In every case the questions of representative loading history and generalization to other types of anticipated load or deformation reversals need to be addressed.

The need for the development of systematic seismic testing procedures exists also in those segments of the industry which are involved in the fabrication of modular structural units, such as steel storage racks. Here again, the question of adequate seismic performance needs to be addressed. In this industry, proof tests are often prescribed (e.g., Ref. 1) to assess component performance. Except for a few nuclear standards, none of the industrial standards address explicitely the issue of seismic performance. Even if a seismic proof test is to be prescribed, it remains to be answered what form such a proof test should take and how the results of such a proof test can be generalized.

At this time there appear to be very few guidelines in national standards and in the available literature that address the question of systematic testing procedures and evaluation of experimental data. This holds true particularly when it comes to an evaluation of strength and stiffness deterioration of components and their likelihood of failure under cyclic inelastic loadings of the type experienced in earthquakes. In fact, only little information is available on the phenomena involved in deterioration and failure, which makes the development of systematic testing procedures a difficult task.

This report addresses specifically the issues of deterioration and failure, keeping in view the uncertainties in the seismic input and in the structural performance characteristics. In the testing procedures recommended here, consideration is given to these uncertainties which make it necessary that general conclusions be drawn from tests performed under specific and preselected loading histories.

1.2 OBJECTIVES AND SCOPE

The main objective of this study is to develop a set of recommendations for laboratory experimentation on components of steel structures that may be subjected to severe earthquake ground motions. These recommendations are directed towards experimental work intended to produce reliable information which can serve as a basis for the development of rational design criteria or which will demonstrate the integrity and safety of specific structural configurations under various levels of ground motions.

The research is directed towards developing a decision path for experimental investigations which can be followed by all affected user communities such as researchers, the engineering profession, and industry. In particular, the problems of selecting representative cyclic loading histories and interpreting and generalizing test results are addressed in detail.

Emphasis is placed on experimentation for performance assessment of components, where performance refers to deterioration and failure under cyclic inelastic loading. The testing procedures are to result in the determination of low-cycle fatigue parameters which permit, independent of the selected loading histories, a description of the performance characteristics of the component.

In order to achieve these objectives, the following aspects are considered in this research and are discussed in this report:

1. An identification of the purpose of component experimentation from the viewpoint of performance assessment.

2. A review of testing standards and of experimental procedures employed by the research community.

3. A review of low-cycle fatigue damage models and an assessment of their applicability to the problem of performance evaluation of structural components.

4. A review of low-cycle fatigue properties of structural steel, recommendations for testing procedures for materials, and a study of the cyclic stress-strain properties of A36 structural steel.

5. An experimental study of component performance, considering the deterioration and failure modes of local buckling in beam flanges and of crack propagation at weldments. The objectives of this study are to identify performance parameters, assess the applicability of low-cycle fatigure models to the problem of performance evaluation of components, and examine appropriate testing procedures.

6. An analytical study of those seismic response parameters that are needed for a damage evaluation and performance assessment of structural components, and for a development of representative cyclic loading histories.

7. A summary of recommendations for component testing.

CHAPTER 2

PURPOSE AND REVIEW OF COMPONENT EXPERIMENTATION

2.1 PURPOSE OF EXPERIMENTATION

The work discussed in this report is based on the premise that the purpose of experimentation is to obtain information needed for a seismic performance assessment of structures. The issue of performance assessment of components is part of the general problem illustrated in Fig. 2.1.

The figure shows a specific or generic type of structure which has to be designed to resist earthquake ground motions of different severities. Depending on the severity of the ground motion, different criteria may be postulated for the performance of the structure. In order to design for postulated performance criteria, information must be available on all relevant parameters of input and response. The response of structures is governed by component behavior which in turn depends on material characteristics as well as design and fabrication details. Components very often interact with each other, making it difficult to identify suitable boundary conditions for component testing. Component behavior may depend strongly on the applied load or deformation history, which is random, and on structural characteristics which are random as well.

This report tries to address experimentation within the framework set in the previous paragraph. As is illustrated in Fig. 2.1, experimentation may be performed at four levels, ranging from complete structures to subassemblies to components to materials. Only the latter two levels are discussed in this report because they lend themselves to a systematic approach without regard to a specific structural configuration.

There may be a large number of reasons for conducting experiments on structural components. The following enumeration is certainly incomplete but covers the general fields of interest.

1. Development or verification of analytical models

2. Examination of load--deformation characteristics

3. Development of design and detailing requirements

4. Examination of localized failure modes

5. Verification of performance under different levels of seismic demands

6. Proof testing (verification of performance under a specific level of seismic demand).

The parameters of interest in component testing will depend on the purpose of the test and may include several or all of the following:

1. Strength and stiffness properties (load--deflection, moment--rotation, shear force--shear deformation, etc.)

2. Localized stress-strain fields

3. Parameters that permit an assessment of deterioration in strength and stiffness, and of the causes and likelihood of failure in a component.

The emphasis of the work discussed in this report is on the parameters listed last. The parameters listed under 1 and 2 usually will be obtained as well from experimentation for this purpose. Considering the six reasons for experimentation listed before, it can be seen that most of them are concerned with the issue of performance assessment. Although performance may relate to elastic strength and stiffness, for structures subjected to severe earthquakes it relates more likely to deterioration and possible failure under inelastic cyclic deformation demands.

Within the scope of performance assessment, which is the purpose of the experimentation discussed in this report, there are several aspects and definitions that need to be identified as is done in the following paragraphs.

Performance Parameters. Experimentation is usually performed for the purpose of assessing performance parameters. The parameters of interest are associated usually with performance levels of which one could distinguish the following three:

1. Serviceability. In this case elastic stiffness and strength may be the important parameters since the objective is to avoid nonstructural and structural damage (avoidance of permanent deformations).

2. Deformation Demand. This level may be associated with inelastic strength and stiffness, quantities which are needed to predict (usually analytically) the maximum deformations and story drifts in structures subjected to severe earthquakes. Maximum story drifts (for nonstructural elements) and residual deformations (for structural elements) may control the cost of repair of a structure.

3. Deterioration and Safety Against Failure. For this level, performance parameters must be found that permit an assessment of safety against failure, considering the number and magnitudes of inelastic excursions to which a component may be subjected in a severe earthquake.

The work discussed in this report is concerned specifically with the third performance level. There appears to be little need to develop testing techniques for the first two performance levels since these can be assessed adequately through testing with monotonic load application, provided the boundary conditions for the component are simulated adequately. Thus, from here on performance assessment refers to the third level of performance mentioned here.

Failure. In general, failure may be defined as the inability of a component to perform its intended function. In the context of this report, the definition of failure is narrowed down to that of an unacceptable loss of resistance of a component. Thus, failure presumes severe deterioration in strength which renders a component incapable of providing its intended resistance function as part of a structure.

Deterioration. This term refers to a gradual loss of strength or stiffness under cyclic inelastic load (or deformation) reversals. Since deterioration occurs often at a slow rate, it may be acceptable until a limit value of acceptable deterioration is reached. This limit value, which identifies failure, could be defined as a certain percentage of the undeteriorated strength (or stiffness) of a component.

Damage. Within the context of this report, damage is defined as a cumulative parameter which identifies the closeness to failure. Every inelastic excursion is presumed to cause damage in a component, since it accentuates a local failure mechanism (e.g., crack propagation, local instability) and decreases the safety against failure. Failure is presumed to take place when the cumulative damage caused by a series of inelastic excursions reaches a value of one.

Randomness of Seismic Input and Response. Component experimentation is treated in this report from the viewpoint that the seismic input to a structure is not deterministic. The ground excitations a structure may experience will depend on the magnitude and source mechanism of the earthquake, as well as on source-site distance and travel path and site geology. The structural response will also depend on mass, strength and stiffness distribution within the structural system. Consequently, the deformation demand on components, which in the simplest case may be described by the number and magnitudes of inelastic excursions, is random. Therefore, the most important question to be addressed in component experimentation is: How can the information generated from individual tests be generalized to deformation histories which the component may experience as part of a structural system subjected to a random seismic input?

Randomness of Structural Performance. Recognition is given here to the fact that localized phenomena, which lead to deterioration and failure, cannot be described deterministically. They are affected by uncertainties in material properties, localized imperfections (e.g., initial crack size at weldments), and workmanship.

Quasi-Static Cyclic Loading Histories. Throughout this work it is assumed that all relevant information on component performance can be obtained by subjecting isolated components (with appropriate boundary conditions) to quasi-static cyclic loading histories. The term quasi-static implies that loads or deformations may be applied at very low rates, without regard to dynamic effects. The term cyclic refers to the reversible nature of the applied loading, and the term loading history

is used here generically, implying that loads or deformations may be imposed to a specimen in a predetermined manner.

Using the terminology and arguments presented in the preceding paragraphs, the purpose of experimentation can be summarized with the following statement:

> Objective of Experimental Studies on the Seismic Behavior of Components of Steel Structures:
>
> To obtain, through quasi-static cyclic load testing, the information needed for an assessment of the performance of a component which is part of a structure that may be subjected to severe earthquakes. Because of the randomness of the deformation histories the component may experience (due to uncertainties in the seismic input and due to differences in the structural systems of which the component may be a part), parameters must be found that permit a performance assessment under arbitrary load or deformation histories. Emphasis should be on experimentation that permits an evaluation of deterioration and failure, with due consideration given to the effects of the number of inelastic cycles and to the magnitudes of the plastic deformation in each cycle. The uncertainties inherent in structural performance should be considered as well. Since performance is concerned also with serviceability and deformation demands, basic undeteriorated strength and stiffness quantities should also be determined.

This statement addresses experimentation for the purpose of performance assessment and not research experimentation which may have quite different objectives. This report discusses the important aspect that are needed for an implementation of this statement and presents specific recommendations for experimental studies at the end. The aspects addressed are material studies (in order to relate localized failure modes to material parameters), damage modeling (in order to relate deterioration and failure to cyclic deformation parameters), and seismic response predictions (in order to assess the deformation demands for structures and components).

Subsequent discussions will show that a consistent implementation of the stated objective will require much more research work. Performance assessment in this report is based on damage hypotheses which, although shown to be adequate for specific failure modes in Chapter 5, need further verification. Implementation will also be a matter of cost since

a multi-specimen testing program is required to obtain information on the performance parameter. Only further research in this area will show whether this investment is justified in all cases.

The advantages of a multi-specimen testing program in accordance with the previously stated objective can be demonstrated on a specific example. Shown in Fig. 2.2 is the load-deflection response of two cantilever beam specimens subjected to stepwise increasing deflection cycles (2). The two specimens are identical except that the specimen shown in Fig. 2.2b has seven 1 in. bolts in the web connection whereas the specimen shown in Fig. 2.2a has seven 7/8 in. bolts. Although one expects at least as good a behavior of the specimen shown in Fig. 2.2b, it failed considerably earlier than the specimen shown in Fig. 2.2a. The failure was a sudden fracture of the beam flange weld which led to an immediate and severe loss of strength. This unexpected result was obtained although both specimens were most carefully prepared and fabricated and the welds were found to be sound through ultrasonic inspection. One can only guess, but the weld fracture likely occurred because of a large imperfection in the through-direction of the column flange material.

These two tests demonstrate a large uncertainty in the structural performance characteristics since all other parameters are equal. There are several questions that arise from these two tests. What would have been the response of a third specimen of this type? Is the response of the specimen shown in Fig. 2.2b adequate? How would this specimen have performed if it would have been subjected to a different loading history? What general conclusion can be drawn from the response of these two specimens? These are the type of questions that are addressed in the research reported here.

2.2 REVIEW OF COMPONENT EXPERIMENTATION

2.2.1 Review of National Standards

A review of National Standards (ATSM, ANSI, IEEE, NRC) has disclosed a lack of guidelines on seismic performance testing. No standards could be found that address fully the objective of experimentation as defined in the previous section. There are several standards that use the terminology "performance testing", but usually applied generically, and if applied to seismic loading then without specific recommendations.

The one industry that is more specifically concerned with seismic performance testing is the nuclear industry. In this industry the term "fragility" is used extensively. This term denotes the probability of failure of a system, component, or piece of equipment as a function of levels of earthquake excitations. In essence, this covers the objective of experimentation as discussed in this report. However, no specific guidelines could be found on the performance of fragility tests for structural components. It appears that the customary approach is to rely on material fatigue and fracture data and to utilize analytical means to predict component fragility from these data.

Specific requirements for fragility testing are presented in Ref. 3 for equipment of nuclear power generating stations. This standard states that "Fragility testing is used to qualify equipment by determining its ultimate capability. Fragility testing should be performed in a manner which yields equipment capability data which can be translated into any and all of the various requirements from various installations and agencies." This statement addresses the previously mentioned need for generalization of experimental data. However, the quoted standard is not concerned with quasi-static cyclic testing but with dynamic testing utilizing sine beat, or continuous sine, or random-type waveforms.

An interesting piece of information was found in a draft report (4) prepared for the NRC (not a standard). This information has to do with the reliability implications of proof testing. Based on a Bayesian confidence limit on the reliability assuming uniform prior distribution, and assuming a binomial distribution of the number of samples not failing in a proof test, the results shown in Table 2.1 were obtained. The table illustrates that a single proof test is an unreliable measure of performance and that a considerable number of proof tests is needed to assess reliability with a high confidence level.

Outside the nuclear industry no comprehensive guidelines were found on seismic performance testing of structural components. Reference 5 is probably the only building oriented standard that defines a specific but optional cyclic load test. This test consists of stepwise increasing load or displacement cycles, with five cycles performed at each step. The steps are to be increased "until failure of the wall occurs". No

definition is given for failure and no guidelines are presented for an interpretation of test results other than for evaluation of strength and for stiffness at one-third of the maximum load. Specific guidelines are presented for specimen configurations and boundary conditions, and for load application. This standard acknowledges also the uncertainties in structural performance by specifying a minimum of two tests, and a third test if the results of two tests differ by more than 15 percent.

A few other ASTM standards that are concerned with testing of building components are listed in Refs. 6 to 9. References 6 to 8 are concerned primarily with specimen identification and load application for monotonic loading. Reference 6 mentions a racking test for wind loads (incremental loading and unloading) but none refer to a cyclic load test for seismic performance evaluation. The response parameters of interest in these standards are usually strength and elastic stiffness. Reference 9 itemizes the reporting requirements for structural tests. These reporting requirements would apply to seismic performance testing, but should be supplemented in this case with additional requirements concerned with an evaluation of deterioration and failure.

Useful information on testing methods in national standards and in engineering practice can be found in Refs. 10 and 11. Both publications discuss testing methodologies, but with little or no emphasis on steel structures and the problem of seismic performance assessment. In fact, in none of the reviewed building oriented standards any reference was found to seismic performance testing of components of steel structures.

However, at the material level there are several standards that address problems of relevance to the seismic performance of steel components. These are the standards concerned with low-cycle fatigue and fracture testing. Example are the ASTM standards listed as Refs. 12 to 16. These standards define testing procedures and terminology for material tests that form a basis for the understanding of the seismic performance of steel components. These tests are discussed in more detail in Chapters 3 and 4. Information on tests of weldments, which are closer to material tests than component tests, can be found in Chapter 5 of the Structural Welding Code (17).

2.2.2 Review of Experimental Studies

Over the last twenty years, a great number of experimental studies have been performed on the inelastic cyclic load--deformation behavior of components of steel structures. In most cases the objectives were (1) to identify the undeteriorated cyclic load--deformation response and (2) to identify deterioration in strength and stiffness as a function of the number and amplitudes of the applied cycles.

Many studies have shown that the undeteriorated global load--deformation response can be obtained rather accurately from the cyclic stress-strain characteristics of the material, provided that the boundary conditions, specimen geometry, and loading mechanism can be simulated analytically. The undeteriorated global response shows the same patterns as the stress-strain response, characterized by cyclic hardening (for mild steel) and a hysteresis loop that can be represented closely by a Ramberg-Osgood function. Test results show some sensitivity of the undeteriorated response to the applied loading history, but this sensitivity can be related to the cyclic material characteristics. Thus, testing for the purpose of determination of global undeteriorated response appears not to be a sensitive issue, provided that boundary conditions and loading mechanisms are simulated adequately.

The second objective, which has to do with an evaluation of deterioration, is much more difficult to fulfill. In many studies it was found that deterioration is sensitive to the applied loading histories and that an evaluation or prediction of deterioration is a difficult task. Depending on the failure mode and the applied loading history, deterioration may occur at a high or low rate, or may occur early or late in the loading history.

Discounting the problem of global buckling of a member, deterioration and/or failure in all the studies reviewed was a consequence of localized phenomena, such as local buckling, lateral torsional buckling, weld fracture, crack propagation at reduced cross sections (e.g., net section at a bolt line), or slip between bolted plates. Considering strength deterioration, it appears that there are two common modes of deterioration and failure. In one mode, no noticeable deterioration is observed for several cycles and then deterioration occurs at a very fast

rate, in some cases leading to sudden failure (e.g., Fig. 2.2b). In the other mode, there is a threshold against deterioration for a few cycles and then deterioration occurs gradually with either a increasing or decreasing rate (e.g., Fig. 2.3).

These two modes of deterioration and failure are illustrated conceptually in Fig. 2.4. Different models are called for in order to describe the two modes. In the first mode (Fig. 2.4a), the deterioration range covers only a very small portion of the useful life of the component and should be negligible. Thus, only the deterioration threshold range needs to be modeled. In the second mode (Fig. 2.4b), both the deterioration threshold range and the deterioration range should be modeled since much of the life of the component may be spent in the deterioration range. Based on observed data, the first mode is usually associated with crack propagation and fracture, while the second mode is usually associated with local instabilities (local and lateral torsional buckling, or shear buckling).

It has been observed in many tests that deterioration is sensitive to the applied loading history. An example is illustrated in Fig. 2.5, taken from Ref. 19. Figures 2.5c and d show the horizontal load--deflection response of two identical beam-column subassemblies of the type shown in Fig. 2.5a. The only difference between the two tests is in the applied deflection histories which are shown in Fig. 2.5b. In both specimens deterioration is caused by local and lateral torsional buckling in the two beams, but to different degrees. In specimen B1, where the deflection cycles are close to symmetric and stepwise increasing, cyclic hardening without deterioration is observed for several cycles, but after a considerable deflection amplitude is reached, severe deterioration in strength is observed (excursion 27 to 32). In specimen B2 the first excursion is performed monotonically to a large deflection, leading to a much higher strength (compare point 17 of B2 with point 32 of B1). Subsequent small unsymmetric cycles (e.g., 17-19-21) are rather stable, but the following large deflection cycles cause considerable deterioration. It remains to be answered how the behavior of specimen B2 could have been predicted from the information obtained from specimen B1.

Although deterioration is sensitive to loading histories, very little information can be found in the literature on the reasons for the choice of specific histories used by different investigators. The types of histories used range from randomly generated, to arbitrarily selected, to stepwise increasing or decreasing symmetric or unsymmetric load or deflection cycles. In some cases the applied histories were obtained from an inelastic dynamic analysis of the structure of which the component is a part.

The diversity of the loading histories employed in the past makes it difficult to draw general conclusions on deterioration and closeness to failure. Attempts have been made in the past to define "standardized" cyclic loading histories that can be applied to all kinds of elements and subassemblies (e.g., Ref. 20), but the variability in seismic input and in component configurations makes such an approach questionable. Therefore, rather than searching for a unique loading history, several investigators have taken a different approach which is based on classical low-cycle fatigue concepts. Since this approach is pursued further in this study, a brief review is made here of relevant past research.

In the low-cycle fatigue approach, a reference state is identified which for a material or component constitutes a state of failure. From constant amplitude test data, a relationship is established between the number of cycles to failure, N_f, and a relevant deformation parameter δ. In the simplest form, this relationship may be of the type

$$N_f = C^{-1} \delta^{-c} \tag{2.1}$$

where C and c are often referred to as damage parameters. Accepting the linear damage hypothesis, the damage for variable amplitude cycling may be expressed as

$$D = C \sum_{i=1}^{N} \delta_i^c \tag{2.2}$$

where N is the number of cycles and δ_i is the value of the deformation parameter δ in cycle i. The accumulated damage identifies the closeness to failure and a value of D equal to one is supposed to constitute

failure. There is much more that needs to be said about this cumulative damage concept, but this topic is discussed in more detail in Chapter 3. This concept, expressed by Eqs. (2.1) and (2.2) or by more complex equations, has been used by several investigators for an experimental or analytical performance assessment of structures of structural components.

Bertero and Popov (21) were one of the first to report an experimental study on low cycle fatigue behavior of steel beams. A series of strain controlled tests with constant strain amplitudes was performed on M 4x13 beam sections. Under cyclic straining, deterioration was in most cases initiated by local buckling in the flanges which led to the formation of cracks followed by fracture at the wrinkled flanges. However, fracture did occur only after the specimens were subjected to several times the number of cycles causing flange buckling. Under small strain amplitudes (1%) cracking did not occur at the buckles but at the clamped end of the beam, hence, a change in failure mode was evident in this test series. Nevertheless, when plastic strain amplitude vs. number of cycles for all tests is plotted on a log-log scale (see Fig. 2.6) one can detect a reasonably linear relationship. Thus, with the use of plastic strain amplitude as deformation parameter, Eq. (2.1) can be employed to predict approximately the number of cycles leading to flange buckling and to failure. The corresponding equations are shown in Fig. 2.6.

Popov, et al. (22 to 24) reported on experimental studies on various types of beam-to-column connections. Different loading histories were used in these tests, but in most cases cycles with stepwise increasing displacement amplitudes were applied. This set of experiments represents up to this date the most extensive set of information on connections, but it cannot be used directly to develop low cycle fatigue models since for each type of connection only one test was performed. In this research it was also suggested (22,25) to use cumulative energy dissipation as a measure of performance rather than cumulative deformation parameters.

Of particular interest is a study reported in Ref. 26 which is specifically concerned with low cycle fatigue modeling of a single story

portal frame. Monotonic loading tests and constant amplitude fatigue tests as well as random fatigue tests were carried out. It was found that for constant amplitude tests the relationship between story drift δ and number N_f of cycles causing cracks in the welds of the beam-to-column connections can be accurately modeled by an equation of the type shown in Eq. (2.1). When random displacement histories were applied and the root-mean-square value of the amplitudes in a test were plotted on the previously established N_f-δ curve, it was found that these points fell considerably above the N_f-δ curve for constant amplitude testing. This is due to the large damage caused by a few large amplitude cycles but also indicates that random cycling may be a more critical loading history than constant amplitude cycling. This observation was also noted in several low cycle fatigue studies on materials (27).

When various cumulative fatigue damage models were applied in this study to the test results of the random fatigue tests, it was noted that the predicted damage was very sensitive to the cycle counting method and in general was less than unity. When the experimentally determined damage model was used in time history analyses of multistory frames, it was found that significant variations in damage factors were obtained for similar maximum ductility factors in different stories. This observation demonstrates that maximum ductility factors alone are not an adequate measure of performance.

Several studies are reported in the literature that utilize cumulative damage models for materials to predict the damage in structural elements or frames. These studies are primarily of theoretical nature since a prediction of damage based on material fatigue characteristics alone, without regard to stress concentrations, local imperfections, and local buckling phenomena, will not be realistic for most structural elements. However, much can be learned from these studies regarding procedures for damage prediction and relationships between damage, ductility and hysteretic energy dissipation.

Srinivasan and Munse (28) carried out shake table experiments on a single degree of freedom system consisting of a S 5x7.7 element fixed at the base and with weights attached at the top. From the recorded critical strain history and from a computed restoring force history, damages

were predicted based on cumulative damage models for critical strains and hysteretic energy. Although the damages were small for the input motions used in the experiments, the important conclusion drawn from the study was that the damage predicted from the hysteretic energy model was in good agreement with that predicted from the strain history model.

This conclusion was also confirmed in a study reported in Refs. 29 and 30. In this analytical study of single degree of freedom portal frames, damage was predicted from the material fatigue theory presented in Ref. 31. The damage model was modified for sequence effects and variable amplitudes. When the cumulative damage obtained from this model was plotted on a log-log scale against the cumulative hysteretic energy dissipation per unit volume of flange material, a linear relationship with little scatter was observed. Thus, it appears to be quite feasible to develop damage models in terms of hysteretic energy rather than deformation parameters.

An analytical study on low cycle fatigue damage in multistory frames is discussed in Ref. 32. Damage was predicted for a series of frames of different natural frequencies from the cumulative damage model for steel developed by Yao and Munse (33). It is interesting to note that in this study a good correlation was observed between maximum ductility factors and cumulative damage. This observation contradicts the conclusion reported in Ref. 26, which indicates that the relationship between damage and ductility factors depends strongly on the structural configurations that are investigated.

The conclusions that can be drawn from the review of past studies on low cycle fatigue of structural components and complete structures are as follows:

1. A reliable rating of the performance of a component cannot be deduced from a single test, regardless of the loading history used in the test.

2. The use of cumulative damage as an index for rating components is more appropriate than the use of ductility factors.

3. The low cycle fatigue life of components under constant amplitude cycling can in many cases be predicted by an equation of the type shown in Eq. (2.1).

4. It appears feasible to predict the low cycle fatigue life of components under random cyclic loading by means of a cumulative damage model of the type shown in Eq. (2.2). However, based on the scarce information available on this subject, it may be necessary to account for sequence and mean deformation effects, and to pay much attention to a suitable cycle counting method.

5. Damage models can be expressed in terms of deformation parameters but also in terms of hysteretic energy dissipation.

CHAPTER 3

MODELS FOR PERFORMANCE ASSESSMENT

3.1 IDENTIFICATION OF THE PROBLEM

Whatever the specific objective of experimentation may be, the general purpose is usually to provide information that can be used for a design of "safe" structures. The term "safe" may refer to different performance levels, as was discussed in Section 2.1, but is used here in reference to an unacceptable loss of resistance which constitutes failure. Thus, the problem of seismic safety can be viewed as a reliability problem in which the capacity of a structure (or component) should exceed the demand imposed by a random event (earthquake) with an acceptable probability or an acceptable margin of safety. Both capacity and demand are random variables due to uncertainties in seismic input and structural performance.

Freudenthal (34) in 1945 was the first to formulate reliability concepts for structural problems. Since then, these concepts have been applied to many practical problems. For instance, for a single load application, and assuming statistical independence of applied load S and structural resistance R, the probability of structural safety can be expressed by the convolution integral (35)

$$P(R > S) = \int_0^\infty F_S(y)\, f_R(y)\, dy \qquad (3.1)$$

where $F_S(y)$ is the cumulative distribution function of the load intensity and $f_R(y)$ is the probability density function of the structural resistance. This formulation assumes a knowledge of the probabilistic distributions of load and resistance (see Fig. 3.1). If a structure is subjected to a random sequence of n independent loading events of equal distribution $F_S(y)$, and the probability of occurrence of n events in a time period (0,t) is given by $p_n(t)$, then the reliability $L_T(t)$ (probability of survival) can be obtained as (35)

$$L_T(t) = \int_0^\infty \sum_{n=0}^{\infty} p_n(t) \left[F_S(y)\right]^n f_R(y)\, dy \qquad (3.2)$$

For a rare event, such as an earthquake, the probability of occurrence is usually modeled as a Poisson process.

This formulation can be applied directly to seismic safety evaluation, but only under very restrictive conditions. First of all, the formulation assumes that suitable load (demand) and resistance (capacity) parameters can be identified and described probabilistically. This appears to be possible only for the case of linear (elastic) structures, where a loading function can be obtained from a random vibration approach (power spectrum and transfer functions), and where the resistance parameter is an elastic force level. Secondly, the formulation assumes that load and resistance are independent and that the resistance function does not change within the time interval (0,t).

All these assumptions are not valid for structures of interest in this study, that is, structures which will undergo severe inelastic deformations in a major earthquake. In this case, loading and resistance are not independent and inelastic deformations appear to be suitable demand and capacity parameters rather than loads and force resistance. Also, in many cases the resistance will deteriorate before failure takes place (see Fig. 2.4b) and hence the resistance function will depend on the applied loading history.

An approach which circumvents these problems is discussed in the next section. This approach, based on cumulative damage concepts, is being used extensively in material studies and also in structural applications. But in the latter case it is based usually on information obtained from material tests rather than component tests as is advocated in this study. The objective of the next section is not to solve the reliability problem, but to identify relevant parameters which need to be determined analytically and experimentally in order to permit a performance assessment that accounts for the uncertainties in seismic input and structural performance.

3.2 CUMULATIVE DAMAGE MODELS

When a structural material or component is subjected to cyclic loading, it can be assumed that every cycle, whose amplitude exceeds a certain threshold amplitude, will cause microstructural changes that bring the material or component closer to a state of failure. Although these microstructural changes may not alter visibly the overall response, they constitute damage that accumulates from cycle to cycle. Once the accumulated damage, D, exceed a specific limit value, γ, failure will take place. Thus, the probability of failure can be expressed as

$$P_f = P[D > \gamma] \tag{3.3}$$

where D is a function of many parameters as for instance,

- the number of cycles,
- the amplitude or range of each cycle,
- the sequence of cycles (sequence effect),
- the symmetry or lack of symmetry of each cycle (mean effect), and
- the geometry and properties of the material or component.

Damage, as defined in Eq. (3.3), does not have to be a measurable quantity but, if properly defined, it can be used for an assessment of performance and closeness to failure of materials and components. Since this cumulative damage concept has been developed originally for metal fatigue problems, a brief review of this topic is presented next.

3.2.1 Cumulative Damage Models in Metal Fatigue

Baseline data for fatigue evaluation of metals are usually obtained by cycling test specimens at constant stress or strain amplitudes until failure occurs. Such tests are performed for different levels of stress or strain amplitude in order to arrive at curves that relate the number of cycles to failure, N_f, to the stress or strain amplitude.

If the stress amplitude σ is safely below the yield stress (high-cycle fatigue), Basquin (36) has found that N_f can be related to σ rather accurately by the equation

$$\sigma = B\ N_f^b \tag{3.4}$$

where B and b are material parameters. In the low-cycle fatigue regime ($\varepsilon >> \varepsilon_y$), where strain amplitude is used usually to control the experiments, Coffin (37) and Manson (38) have found independently that N_f can be related to the plastic strain amplitude ε_p rather accurately by the equation

$$\varepsilon_p = C\ N_f^c \tag{3.5}$$

Where C and c are material parameters. Morrow (38) proposed the following equation which expresses the strain ampitude in terms of its elastic and plastic components and is valid for both the high and low cycle fatigue regimes:

$$\varepsilon = \varepsilon_e + \varepsilon_p = \frac{B}{E} N_f^b + C\ N_f^c \tag{3.6}$$

Figure 3.2 illustrates graphically this equation and shows the relative importance of elastic and plastic strain components. In the regime of interest to most seismic response studies ($\varepsilon >> \varepsilon_p$), it can be justified to ignore the elastic strain component and to accept the Coffin-Manson relationship (Eq. 3.5) for an estimate of the number of cycles to failure under constant amplitude cycling.

In order to utilize the information from constant amplitude tests for irregular cyclic loading histories, cumulative damage theories are employed in metal fatigue. The simplest and most commonly employed theory is the one propounded by Miner (40) and proposed earlier by Palmgren (41). This theory is based on an assumption of linear damage accumulation throughout the fatigue life, i.e., if it takes N_{fj} cycles of constant amplitude ε_j to cause failure, than the damage per cycle is $1/N_{fj}$, and the accumulated damage after N cycles of different amplitudes ε_i is given as

$$D = \sum_{i=1}^{N} \frac{1}{N_{fi}} \tag{3.7}$$

If the hypothesis of linear damage accumulation (Miner's rule) were to hold true, then a value of accumulated damage of unity would constitute failure. However, the results of many experiments with variable amplitude cycling (e.g., Refs. 42,43) have shown considerable deviations from the value of unity at failure, often resulting in unconservative life predictions.

The two most commonly quoted shortcomings of Miner's rule are that mean stress (or strain) effects and sequence effects are neglected. Mean stress effects in high-cycle fatigue problems are discussed in many papers and several modifications for mean stress effects are suggested (e.g., Refs. 44 and 45). Mean strain effects in low-cycle fatigue problems are usually considered to be of lesser importance. Similarly, sequence effects in high-cycle fatigue problems have been found to be very important in specific cases. Hardrath (46), Corten (47) and Topper, et al., (48) found that for a high-low sequence failure occurred after fewer cycles than predicted, whereas for a reversed low-high sequence failure occurred after more cycles than predicted. But, when there is significant inelastic action at all strain amplitudes, sequence effects appear to be of lesser importance (49 to 51).

There are many modifications to Miner's rule, such as nonlinear models (52) and probabilistic models (53). None of these models are generally applicable and Miner's rule remain the most widely used hypothesis. It is simple to apply and, despite its shortcomings, gives usually adequate predictions for fatigue lives. However, since the life predictions from Miner's rule are uncertain, the limit value of damage that constitutes failure should be taken as a random variable.

One important aspect needs to be considered in damage accumulation, whether Miner's rule or more complex theories are employed. In order to utilize cumulative damage models for an irregular loading history, the time history of stress or strain has to be converted into as many closed cycles as possible since the baseline data are obtained from constant amplitude tests and damage is counted per cycle and not per reversal.

A summary of cycle counting methods has been provided by Dowling (49) and more recently by Fuchs and Stephens (54). These methods include peak, level crossing, range, range-mean, range-pair, rain-flow, and racetrack. Of these various methods, the rain-flow method, proposed originally by Matsuishi and Endo (55), appears to provide consistently reasonable results, especially in LFC studies (e.g., Ref. 54). The basic idea behind this method is to treat small excursions as interruptions of larger excursions and to match the highest peak and the deepest valley, then the next highest and deepest, etc., until peaks and valleys have been paired.

The rain-flow cycle counting method is described schematically in Fig. 3.3. The time history of stress or strain is arranged vertically to form a series of pagoda roofs. Rain-flow initiates at the beginning of the history and at each point of reversal. Every rain flow proceeds downwards until it either meets a rain-flow from a higher roof or reaches a peak which is the starting point of an excursion leading to a peak that exceeds the point from which the rain flow initiated. The horizontal distance between the beginning and end point of each rain flow is counted as a half cycle. For the example in Fig. 3.3 the ranges are shown, in order of their occurrence, in the line diagram below the time history. Note that every part of the history is counted only once. These ranges are quite different from those in the time history and contain four closed cycles.

The use of a proper cycle counting method is important for damage evaluation. In most cases, the largest deformation ranges are not contained directly in the time history and the direct use of time history excursions may lead to a severe underestimation of cumulative damage.

3.2.2 Cumulative Damage Models for Structural Components

Provided that deterioration and failure in a component is caused by material fatigue problems, an extension of material damage models to structural components can be justified. For other deterioration modes, such as local buckling, the validity of such an extension can only be hypothesized and needs experimental verification (see Chapter 5).

Accepting this hypothesis, the following approach could be used for damage and performance assessment of components.

Since earthquakes cause only a small number of cycles, but several of these cycles are usually associated with large inelastic deformations, a low-cycle fatigue approach is called for. Thus, a deformation quantity, rather than a force quantity, is used here to identify the damage potential of a cycle. This deformation quantity, denoted as $\Delta\delta_p$, may be a localized (e.g., strain) or global (e.g., plastic hinge rotation) parameter, depending on the failure mode of the component. Because of the predominance of inelastic deformations, the contribution of elastic deformation to damage is considered negligible. Since deformation cycles usually are not symmetric with respect to the undeformed configuration, the deformation range rather than the amplitude is used as a reference value.

Baseline data for damage modeling can be obtained from constant deformation amplitude tests. Assuming the validity of a Coffin-Manson model (Eq. 3.5), the number of cycles to failure, N_f, can be related to $\Delta\delta_p$ by an equation of the type

$$N_f = C^{-1}(\Delta\delta_p)^{-c} \tag{3.8}$$

Employing Miner's rule of linear damage accumulation, the damage after N cycles with different plastic deformation ranges $\Delta\delta_{pi}$ can be expressed as

$$D = \sum_{i=1}^{N} \frac{1}{N_{fi}} = C \sum_{i=1}^{N} (\Delta\delta_{pi})^c \tag{3.9}$$

This equation is the simplest damage model that can be proposed for structural components. The use of Miner's rule in this model has again the shortcomings that mean effects and sequence effects are not considered. An assessment of these effects is not within the scope of this study but mean effects are appraised peripherally in Chapter 5. Sequence effects are not addressed here because it was found that seismic response histories do not follow an established sequence pattern.

The damage model expressed by Eq. (3.9) indicates that damage in a structural component depends on the magnitudes of the plastic deformation ranges of the individual cycles, $\Delta\delta_{pi}$, the number of inelastic cycles, N, and on the two structural performance parameters C and c. Information on the seismic response parameters $\Delta\delta_{pi}$ and N can be obtained analytically from response studies considering the ground motion characteristics and structural strength and stiffness properties. This is the subject of a study discussed in Chapter 6.

The structural performance parameters C and c need to be determined from component experiments. Unless a better damage model can be developed, these two parameters form the basis for damage accumulation and performance assessment, and their determination should be a primary objective of component experimentation. Chapter 5 discusses an experimental study which is concerned with the determination of C and c and which address the following questions:

- Can the baseline constant-amplitude data for various failure modes be represented by Coffin-Manson type models?
- Does the hypothesis of linear damage accumulation result in realistic life predictions for variable-amplitude loading?
- What kind of experiments are needed to obtain values for the structural damage parameters C and c?
- How large are the uncertainties inherent in the structural damage parameters C and c?

Component performance can be assessed by comparing the accumulated damage given by Eq. (3.9) with the limit value of damage that constitutes failure. As was discussed previously, this limit value would be unity if Miner's rule would hold true in all cases. Because of the shortcomings of Miner's rule, this limit value is more realistically represented by a random variable γ.

The more there is known about the variables contained in Eq. (3.9), the more reliable a performance assessment will be. In the simplest case, mean values of γ (e.g., γ=1.0), C and c could be used together

with predictions of N and $\Delta\delta_{pi}$ obtained from time history analyses. In the most general case, Eq. (3.9) could be combined with Eq. (3.3) to arrive at a probabilistic assessment of component failure, i.e.,

$$P_f = P[D > \gamma] = P[C \sum_{i=1}^{N} (\Delta\delta_{pi})^c > \gamma] \tag{3.10}$$

This formulation presumes that the uncertainties in all the variables contained in Eq. (3.10) can be evaluated and a probabilistic distribution of D can be formulated (see Fig. 3.4). There is much more research needed to arrive at this goal.

CHAPTER 4

EXPERIMENTAL STUDIES ON MATERIALS

4.1 CYCLIC STRESS-STRAIN BEHAVIOR OF A36 STRUCTURAL STEEL

In order to evaluate deterioration in structural components, an accurate prediction of the undeteriorated response under cyclic loading is needed. Such a prediction necessitates a knowledge of all the cyclic phenomena that occur in the component material. Also, in many cases the low-cycle fatigue life of components can be predicted from material fatigue properties and an accurate assessment of the state of strain at critical points. Localized strains must be predictable also in cases where they are used as the plastic deformation ranges in the damage model discussed in Section 3.2.2.

The basis for these predictions is an accurate knowledge of the unaxial stress-strain response of the component material under inelastic cyclic loading. For the most commonly used structural steel, i.e., A36 steel, a thorough study was performed on its cyclic stress-strain characteristics, resulting in quantitative information on cyclic phenomena and in the development of an empirical model that permits an accurate prediction of the cyclic stress-strain response under arbitrary loading histories. This study, which is presented in detail in Ref. 57, is summarized in this section.

4.1.1 Characteristics of Cyclic Stress-Strain Behavior

The cyclic behavior of A36 steel, which is a high stacking fault energy material, is governed by two reference curves, one being the monotonic stress-strain curve and the other being the cyclic stress-strain curve (see Fig. 4.1). The cyclic stress-strain curve is the locus of peak stresses obtained by cycling the material at various strain amplitudes until a saturation stress is obtained. As is evident from Fig. 4.1, A36 steel softens if the strain amplitudes are small and hardens if the strain amplitudes are large.

The importance of the cyclic stress-strain curve for high stacking fault energy materials is that it is a stable reference curve to which the material tries to return regardless of the previously applied loading history. In other words, regardless of the previous history and regardless of the mean strain of cycling, if the material is subjected to a sufficiently large number of constant strain amplitude cycles, the peak stresses will stabilize at a value corresponding to that on the cyclic stress-strain curve for this amplitude. This is illustrated in Fig. 4.2. Figure 4.2a shows a case in which monotonic loading is followed by a series of constant amplitude cycles with a mean strain equal to the strain amplitude. Despite this mean strain, hardening takes place until the stress amplitude coincides with the point on the cyclic stress-strain curve shown in dashed lines. Figure 4.2b shows two cases of the opposite nature, where initially the peak stresses exceed the saturation stresses on the cyclic stress-strain curve, but these saturation stresses are approached in subsequent cycles through softening and mean stress relaxation.

The phenomena that are involved in approaching the saturation stress are either cyclic hardening or cyclic softening in combination with mean stress relaxation. Experimental studies have shown that cyclic hardening is a relatively fast process, whereas cyclic softening and mean stress relaxation are slow processes, i.e., many more cycles are needed to reach saturation. This was confirmed in the study discussed here through the determination of hardening, softening, and mean stress relaxation factors.

The hardening factor is a parameter that identifies the rate at which the available hardening is used up in each excursion. Available hardening, H_a, is defined as the difference in the stress amplitude σ_a of an excursion and the saturation stress σ_s corresponding to the strain amplitude of this excursion, i.e., $H_a = \sigma_s - \sigma_a$. The hardening factor F_H can be obtained from the available hardening through the equation

$$(F_H)_N = \frac{(H_a)_{N-1} - (H_a)_N}{(H_a)_{N-1}} = 1 - \frac{(H_a)_N}{(H_a)_{N-1}} \qquad (4.1)$$

where

$(F_H)_N$ is the hardening factor for the Nth excursion

$(H_a)_{N-1}$ is the available hardening after N-1 excursions

$(H_a)_N$ is the available hardening after N excursions

Hardening factors can be obtained from tests with constant strain amplitude cycling. Typical results from three tests with different strain ampitudes are shown in Fig. 4.3. The data shown in this and the subsequent figures are normalized with respect to yield stress and yield strain. Figure 4.3 shows that the available hardening is used up at a high rate but that this rate decreases during the first few reversals. A slight dependence of the hardening factor on the strain amplitude can be detected also from the data.

The softening factor F_S identifies the rate at which the material softens back to the saturation stress if previous cycling has caused a stress amplitude that exceeds the saturation stress corresponding to the last excursion. The softening factor is defined in the same manner as the hardening factor but using available softening rather than available hardening. Figure 4.4 shows results obtained for the softening factor from three different constant strain amplitude histories. The figure shows that that available softening is used up at a slow rate that decreases also with number of excursions. An amplitude dependence is also indicated, with larger strain amplitudes leading to a larger softening factor.

Unless the mean stress of an excursion $[(\sigma_1 + \sigma_2)/2]$ is zero, cyclic hardening or softening are accompanied by mean stress relaxation. Similar to the hardening and softening factor, a mean stress relaxation factor F_R can be defined to describe the rate at which the mean stress relaxes to zero. Results obtained for the mean stress relaxation factor are shown in Fig. 4.5. The data show that the factor depends on the mean strain as well as on the strain amplitude of the constant amplitude cycles.

These three factors, together with observations on the cyclic stress-strain curves, can be utilized to describe the stress-strain

response of structural steel subjected to arbitrary loading histories. Except for the monotonic stress-strain curve, a typical inelastic excursion is characterized by an elastic range, followed by a gradual decrease in stiffness as shown in Fig. 4.6. At large inelastic strains the rate of decrease in stiffness approaches zero and the stress-strain curve approaches a straight-line bound. Using this bound as a reference line, the following concept can be postulated to describe the cyclic stress-strain behavior of structural steel.

The shape of the stress-strain curve of an excursion depends on the position of positive and negative bounds (lines 1 and 2 in Fig. 4.6) of which one is updated after each excursion. The movement of the bounds depends on the mean stress σ_m and the stress amplitude σ_a of the last excursion. Taking the example shown in Fig. 4.6, the presence of a positive mean stress in the last excursion will cause mean stress relaxation in the next excursion and consequently a downward movement of the negative bound. The amount of movement is governed by the magnitude of σ_m and the previously discussed mean stress relaxation factor.

Further movement of the negative bound is governed by the expected hardening or softening. Since in every excursion the material tries to approach the stabilization stress σ_s corresponding to the strain amplitude of the last excursion, movement of the bound will depend on the difference between σ_s and σ_a. If σ_s is greater than σ_a, cyclic hardening will take place in the next excursion as in the example shown in Fig. 4.6. To account for this hardening, the negative bound is moved further downward by an amount governed by the available hardening H_a and the previously discussed hardening factor. If σ_s is smaller than σ_a, cyclic softening will take place and the negative bound would be moved upwards. The combined movement of the bound due to mean stress relaxation and cyclic hardening or softening determines the final position of the bound (line 3 in Fig. 4.6). This is now the bound that will be approached by the next excursion.

The concept proposed here is simple to apply and accounts for all important cyclic phenomena. The continuous updating of the bounds after each reversal accounts also for the well established phenomenon that the material has a fading memory which pays more attention to recent

excursions. The concept lends itself to mathematical modeling, as is discussed in the next section, and results in an accurate prediction of the cyclic stress-strain behavior in almost all cases relevant to seismic response studies. Minor shortcomings of the concept and more detailed information on cyclic material behavior are presented in Ref. 57.

4.1.2 Mathematical Model for Cyclic Stress-Strain Behavior

In order to utilize the concept discussed in the previous section for mathematical modeling, a number of curves and parameters need to be identified and numerically described. Table 4.1 summarizes these parameters and presents numerical values for the steel used in this study.

There are three curves that form the basis for mathematical modeling. Each one is briefly described next.

Monotonic Stress-Strain Curve. This curve consists of the three branches evident from Fig. 4.1. Using stresses and strains normalized with respect to yield stress and yield strain, the three branches can be described by the following equations:

$$\bar{\sigma} = \bar{\varepsilon} \qquad 0 < |\bar{\varepsilon}| < 1 \qquad (4.2a)$$

$$\bar{\sigma} = 1 \qquad 0 \leq |\bar{\varepsilon}| \leq \bar{\varepsilon}_{sh} \qquad (4.2b)$$

$$\bar{\sigma} = \bar{K} (\bar{\varepsilon}_p)^{\bar{n}} \qquad |\bar{\varepsilon}| > \bar{\varepsilon}_{sh} \qquad (4.2c)$$

In terms of strains ($\bar{\varepsilon} = \bar{\varepsilon}_e + \bar{\varepsilon}_p$), Eq. (4.2c) can be written as

$$\bar{\varepsilon} = \bar{\sigma} + \left(\frac{\bar{\sigma}}{\bar{K}}\right)^{1/\bar{n}} \qquad (4.3)$$

The parameters $\bar{n}$ and $\bar{K}$ are usually obtained from curve fitting. For the steel used in this study, the values for $\bar{n}$ and $\bar{K}$ listed in Table 4.1 provided a good fit to the monotonic stress-strain curve for the strain range of interest ($\varepsilon \leq 0.04$ in./in.).

Cyclic Stress-Strain Curve. This curve, also shown in Fig. 4.1, was obtained from multiple step tests. It is customary to describe this curve by an expression similar to that for the third branch of the monotonic stress-strain curve, i.e.,

$$\bar{\sigma} = \bar{K}' \left(\bar{\varepsilon}_p\right)^{\bar{n}'} \tag{4.4a}$$

or

$$\bar{\varepsilon} = \bar{\sigma} + \left(\frac{\bar{\sigma}}{\bar{K}'}\right)^{1/\bar{n}'} \tag{4.4b}$$

Fitted values for $\bar{n}'$ and $\bar{K}'$ are shown in Table 4.1. These parameters adequately describe the experimentally obtained cyclic stress-strain curve for strain values up to 0.025 in./in.

Hysteresis Curve. This curve, which describes the stress-strain response for an excursion, consists of an elastic range with a stiffness equal to the monotonic elastic stiffness and a nonlinear portion which approaches the stress bounds asymptotically. In the proposed model, the elastic range is assumed to remain constant for each excursion and is assumed to cover a stress range of $1.2\sigma_y$. This assumption is an approximation which does not have much effect on the description of the hysteresis curve.

A model proposed by Dafalias and Popov (58,59) is used to describe the nonlinear portion of the hysteresis curve. The previously discussed straight-line bound is used in this model as an asymptote which is approached by the hysteresis curve. In the nonlinear range a plastic modulus is defined by the following equation:

$$E_p = \frac{\partial \sigma}{\partial \varepsilon_p} = E_p^o \left[1 + h \left(\frac{\delta}{\delta_{in} - \delta}\right)\right] \tag{4.5}$$

where E_p = plastic modulus

ε_p = plastic strain

E_p^o = plastic modulus associated with the bound

δ_{in} = distance from the point of yield to the bound, measured along the stress axis

δ = distance between the instantaneous stress and the bound, measured along the stress axis

h = shape factor chosen to fit the experimental data.

Thus, the plastic modulus decreases continuously and in a manner shown in Fig. 4.7.

The relationship between the tangent modulus E_t and the plastic modulus is given by the equation

$$\frac{1}{E_t} = \frac{1}{E_e} + \frac{1}{E_p} \tag{4.6}$$

where E_e is the elastic modulus. Hence, by combining Eqs. (4.5) and (4.6), the tangent modulus along the curve can be determined. If the strain increment is sufficiently small, this value of tangent modulus can be used to obtain the value of stress at the next station point. Equation (4.5) must be solved incrementally and the obtained accuracy depends on the size of the strain increments used.

When Eq. (4.5) is matched to experimentally obtained hysteresis curves, it is observed that the shape factor h depends on the value of δ_{in}. For larger values of δ_{in}, smaller shape factors should be used for an accurate fit. In the interest of simplicity of the model, a constant shape factor, with emphasis on matching the larger hysteresis loops, is used here. This shape factor and the plastic modulus associated with the bound (slope of the bound) are identified in Table 4.1.

The three curves just discussed, together with the cyclic hardening, softening and mean stress relaxation factors and the rules for movement of the bounds discussed in the previous section, suffice to describe the cyclic stress-strain behavior under variable amplitude cycling. Again for simplicity, constant values can be used for the hardening, softening and mean stress relaxation factors without much effect on prediction accuracy. These constant values, which are averages with emphasis on the first three excursions, are also listed in Table 4.1.

A macro flowchart of the proposed cyclic-stress strain model is shown in Fig. 4.8. The modeling rules, which are discussed in more detail in Ref. 57, can be summarized as follows:

1. Define the monotonic and cyclic stress-strain curves with parameters ($\bar{K}$, $\bar{n}$) and ($\bar{K}'$, $\bar{n}'$), respectively, and define the hysteresis curve shapes with parameters h and E_p^o.

2. Define initial bounds (slope = 0, intercepts $\pm \sigma_y$) for monotonic loading.

3. If monotonic deformation is in tension, assume deformation started from compression yield and vice versa. This is done in order to generate a first excursion to which the modeling rules of step 5 can be applied without modification.

4. After the monotonic excursion rotate both stress bounds about their intercept with the stress axis so that their slopes have a value E_R^o. For all subsequent excursions this slope is maintained.

5. At the end of each excursion, update the subsequent bound in the following fashion:

   a. Calculate the strain ad stress amplitudes (ε_a, σ_a) of the most recent excursion.

   b. Compare the stress amplitude of this excursion with the stress σ_s on the cyclic stress-strain curve corresponding to the strain amplitude ε_a and calculate the stress difference

$$\Delta\sigma = \sigma_s - \sigma_a$$

   c. If $\Delta\sigma$ is greater than zero, hardening is predicted to take place in the next excursion. In this case, update the subsequent bound by moving it outward by an amount equal to $2\ \Delta\sigma\ F_H$.

   d. Is $\Delta\sigma$ is less than zero, softening is predicted to take place in the next excursion. The subsequent bound is then updated by moving it inward by an amount equal to $2\ \Delta\sigma\ F_S$.

   e. Calculate the mean stress σ_m and further move the subsequent bound by an amount equal to $\sigma_m\ F_R$.

6. After every reversal, unload or reload elastically for a stress range of $1.2\ \sigma_y$. One of two situations can arise while in this elastic range.

   a. A reversal could take place. In this case, the stress-strain behavior is elastic till the previous stress-strain curve is reached and deformation is assumed to continue along this curve as if no interruption has taken place.

   b. If a reversal does not occur while in the elastic range, this range is followed by the nonlinear portion of the hysteresis curve whose description is given by the Dafalias-Popov relationship. The

position of the bound corresponding to this excursion has already been determined in step 5 at the end of the previous excursion.

The model was tested on a number of histories for which experimental results were available. In general, the agreement is excellent as can be seen from the four examples shown in Fig. 4.9. The only exceptions are the first one or two excursions following the monotonic loading (see Fig. 4.9a) and excursions with small strain amplitudes. For the latter case the predictions result usually in too small stress amplitudes (see Fig. 4.9c and d). This prediction error comes primarily from the compromise made in chosing a constant shape factor h in the Dafalias-Popov model.

The model presented here is one of several that can be used to describe the cyclic stress-strain behavior of structural steel. Many other models have been proposed in the literature, most of them simpler than the model proposed here but associated with larger inaccuracies in predictions. Examples of widely used models are those described in Refs. 58 to 69.

The use of different models does not change the cyclic characteristics of the material. Returning to the subject of experimentation, specific tests must be performed in order to obtain information on the parameters and curves that control the cyclic inelastic response. The reference curves are the monotonic and cyclic stress-strain curves and the controlling parameters are those that permit an evaluation of cyclic hardening, softening and mean stress relaxation. The next section presents recommendations for pertinent testing procedures.

4.1.3 Recommendations for Experimentation

Monotonic Stress-Strain Curve. The testing procedures and specimen geometries presented in ASTM Standard E8 (70) describe fully the test needed for the determination of this curve. The test should be carried to fracture of the specimen in order to provide a data point for low-cycle fatigue evaluation.

Cyclic Stress-Strain Curve. This curve identifies the steady state response of a material and is defined as the curve through the locus of saturation stresses at various strain amplitudes. In fatigue analysis it is customary to use the stress at half-life as the saturation stress. In earthquake engineering, where the material is subjected only to a small number of cycles, it should be acceptable to assume that saturation is reached after about 10 to 20 cycles.

The specimens used for a determination of this curve should conform to the geometric requirements set forth in ASTM Standard E606 (12). If uniform-gage specimens are used and large strain amplitude cycling is to be performed, the lower limit of the range of ratios of gage length ℓ over diameter d permitted in this standard ($\ell/d = 3 \pm 1$) should be used in order to prevent premature buckling. A self-aligning grip (e.g., Fig. 4.10) should be used since alignment of the test specimen in the testing apparatus poses a major problem.

Different test methods are proposed in the literature for a determination of the cyclic stress-strain curve. Conceptually most suitable is the Companion Specimen Method. In this method several specimens are used and each specimen is cycled to saturation at a preselected strain amplitude. However, this method is costly, because a considerable number of specimens and tests is required, and may give ambiguous results because one curve must be constructed from data obtained on different specimens which may have microstructural variations.

For earthquake engineering studies, a better suited test appears to be the Multiple Step Test. In this test a single specimen is used and the specimen is subjected to step-wise increasing strain amplitude cycles with several (10 to 20) cycles performed at each amplitude. A typical result of such a test is shown in Fig. 4.11.

Not recommended are the sometimes used Incremental Step Test and Monotonic Tension after Cyclic Straining Test. In the first of these two tests, the strain amplitude is first increased gradually in each cycle, up to a maximum amplitude, and then decreased in the same fashion. These blocks of increasing and decreasing cycles are applied repeatedly until saturation is reached. A curve through the peaks of the increasing or

decreasing segment of the last block is taken as the cyclic stress-strain curve. In the second of these two tests the material is pulled to fracture after saturating the material through previous cycling and returning to the stress-strain origin. The stress-strain diagram from this last monotonic excursion is taken as the cyclic stress-strain curve. Based on the observations made on cyclic hardening and softening in Section 4.1.1, the results obtained from these two tests may deviate considerably from the true cyclic stress-strain curve.

Hardening Parameter. The previously discussed hardening factor appears to be a proper measure of cyclic hardening. It can be obtained most suitably from a constant strain amplitude test. Several tests with different strain amplitudes are needed if the amplitude dependence of the hardening factor is deemed to be of importance.

Softening and Mean Stress Relaxation Parameters. In order for softening to occur in a measurable amount, the specimen must first be hardened through cycling with large strain amplitude and then be subjected to constant amplitude cycles with smaller amplitudes. Since the preloading at large amplitudes will cause usually a considerable mean stress upon return to the smaller amplitude, softening and mean stress relaxation will occur together. Thus, both the softening factor and the mean stress relaxation factor have to be determined simultaneously. A procedure for separating softening and mean stress relaxation is discussed in Ref. 57.

4.2 LOW-CYCLE FATIGUE AND FRACTURE TESTING

Deterioration and failure of components is often caused by localized crack initiation and propagation. Testing techniques are needed, therefore, to assess material quality from a viewpoint of low-cycle fatigue and fracture. No attempts are made here to review these two important topics. Recent reviews are presented in Refs. 71 and 72 and detailed information can be obtained from many ASTM Special Technical Publications (e.g., Refs. 73-88) and other reference sources. Applicable testing procedures are presented in several ASTM Standards (Refs. 12 to 16 and 89 to 93).

The purpose of the following discussion is to identify testing needs and relevant testing procedures for structural steel as material for structural components. In effect, there are at least four material zones in which fatigue failure may take place. This is illustrated in the simple T-joint shown in Fig. 4.12. Failure may occur in the base material through cyclic loading in either the longitudinal direction ((1)) or the through-thickness direction ((2)), or in the heat affected zone, HAZ, ((3)) or in the weld material itself ((4)). Failure may also occur in the interface between the weld material and the HAZ.

Basic low-cycle fatigue data for all four material zones can be obtained through standard constant-amplitude low-cycle fatigue testing with machined specimens (12). Such tests are reported in the literature, with the common conclusion that the number of cycles to failure and strain or stress amplitude are related by equations of the type presented in Eqs. (3.4) to (3.6).

However, quite different life predictions were obtained for the different zones. For instance, Miller and Amin (94), who tested specimens of the type shown in Fig. 4.13, concluded that for the same strain range the base material has a life approximately six times longer than that for the welded material.

Adams and Popov (95) tested standard test specimens machined from a welded assembly as shown in Fig. 4.14. Thus, they tested for fatigue strength in the weld material and in the through-thickness direction of a 1-1/2 in. thick plate. They made the following observations from their low-cycle fatigue tests which were performed under stress control. The low cycle fatigue strength in the through direction is poor compared to that in the longitudinal direction. The longitudinal specimens had as much as 12 times the life of the through-thickness specimens. The weld metal behaved better in fatigue than the through direction of the plate provided no visible cracks or inclusions were present.

Based on these studies and others reported in the literature one can arrive at the following conclusions. Base material in the longitudinal direction is very ductile. Fatigue failure under earthquake induced cycling is unlikely except at points of severe stress concentrations (e.g., net sections at bolt holes) and at local buckles which may be

subjected to severe strain reversals. The fatigue properties of base material in the through-direction may be from adequate to poor, depending on the content, distribution, size and shape of inclusions. The fatigue properties of weld metal depend strongly on weld imperfections but may be comparable to or better than those in the through-direction of materials. Because the LCF properties in the through-direction of materials and of weld metals depend severely on imperfections, and on the thickness of plates and size of welds, quantitative conclusions cannot be drawn from a small sample set of tests. There is a need for a comprehensive testing program and a statistical evaluation of data. Test specimens of the types shown in Figs. 4.13 and 4.14 should be suitable for this purpose.

Since the predominant problem at welded (and also bolted) connections is that of crack propagation and fracture, there is much interest in obtaining information on fracture toughness and crack growth rates. A relative quality assessment can be obtained from simple tests such as those described in Refs. 90 and 93. Quantitative assessment of crack growth rates can be achieved from cyclic load tests that relate the crack growth per cycle (da/dN) to a relevant crack propagation parameter such as ΔK, $\Delta\varepsilon$, or ΔJ. The stress intensity range ΔK (96) is used widely for problems of elastic, or, when modified, for elastic-plastic fracture mechanics (which may apply to the through-thickness direction of plates and in many cases to weld metals) but is not suitable if gross yielding occurs around the crack.

In seismic problems such gross yielding may be the rule rather than the exception for plate element loaded in the longitudinal (rolling) direction. For this case no universally applicable crack propagation parameter has been found, but the strain range $\Delta\varepsilon$ (or the plastic strain range $\Delta\varepsilon_p$) close to the crack tip and the ΔJ integral (97) have been used with some success (98 to 101).

Various types of specimens can be used to develop crack growth rate models. Most commonly used are the standard LCF specimen (12), the compact specimen (91) and various bend specimens (17, 91, 98). For cyclic testing with gross yielding of the cross section, the standard LCF specimen appears to be the only choice. The preferred method of

loading is the application of symmetric cycles with strain usually being used as the control parameter.

It is widely accepted that crack propagation testing will result in crack growth rates of the type

$$\frac{da}{dN} = \alpha \, (\Delta x)^{\beta} \tag{4.7}$$

whether x is equal to K, ε, or J. When this relationship, which is usually obtained from symnmetric cycling (except for the compact specimen), is applied to random cycling it is found that the crack closure phenomenon and crack retardation or arrest have an effect and may result in considerable prediction errors. Various procedures have been suggested to account for these phenomena (102 to 104) but are applicable only to problems with localized plasticity.

As useful as crack propagation testing is for material assessment, a direct utilization of the results for a quantitative assessment of component performance is most difficult. Firstly, crack growth rate depends very much on the geometry of the specimens and the crack shape. This difficulty can be overcome, in part, by using geometry dependent crack propagation parameters such as ΔK and ΔJ. Unfortunately, ΔJ is very difficult to evaluate as a function of geometry. Secondly, crack initiation and propagation in components depend strongly on the content, distribution, size, and shape of imperfections. This latter problem leads to the conclusion that material data on crack propagation, and also LCF, are useful baseline data but that much more component experimentation is needed in order to correlate component performance with material performance.

CHAPTER 5

EXPERIMENTAL STUDY OF COMPONENT PERFORMANCE

5.1 INTRODUCTION

The experimental study discussed here is based on the premise that deterioration in resistance is the most relevant parameter for seismic performance assessment of components of steel structures. Stiffness deterioration is also considered and is represented by models similar to those for strength deterioration.

Considering that structural steel is a strain hardening material, it is necessary to separate cyclic hardening phenomena from cyclic deterioration phenomena. In this study, deterioration is based on an undamaged state that includes the effect of cyclic hardening. Thus, deterioration may be present even when the resistance is increasing from one cycle to the next. In order to evaluate deterioration from experimental data it is necessary, therefore, to predict the undamaged resistance considering the effects of cyclic hardening. This is accomplished here with the aid of simplified material hardening rules which are based on the information presented in Chapter 4.

In order to study the feasibility of performance assessment by means of the cumulative damage models discussed in Chapter 3, two series of tests were performed on structural components. The objective was to measure experimentally and to model analytically the deterioration threshold as well the progress of deterioration for two common failure modes in steel structures.

The two failure modes under study are local buckling in beam flanges and crack propagation at weldments. These two failure modes are characteristic for the two distinctly different deterioration patterns identified in Fig. 2.4. Crack propagation of weldments causes little or no component deterioration for a relatively large number of cycles, followed by rapid deterioration once a crack approaches a critical size. Thus, the deterioration threshold is large but the subsequent rate of deterioration is very high (Fig. 2.4a). Local flange buckling, on the

other hand, leads to early strength deterioration of a component (small deterioration threshold) but the deterioration rate is relatively low (Fig. 2.4b).

Simple cantilever beams of small wide-flange sections were selected in this study to permit testing of a large number of specimens at a minimal cost. Two series of specimens were tested, using ten identical specimens for each series. The specimens were subjected to monotonic loading, cyclic loading with constant deflection amplitudes and cyclic loading with variable deflection amplitudes. The constant amplitude tests were used to develop cumulative damage models which were then employed to predict deterioration and failure for the test specimens subjected to variable amplitude loading.

A more detailed discussion of the experimental study described in this chapter is presented in Ref. 72.

5.2 TEST SPECIMENS AND EXPERIMENTAL SETUP

A sketch of the two types of test specimens is presented in Fig. 5.1. All specimens of each type were cut from a single piece of hot rolled A36 structural wide flange shape. Connection details of the specimens are shown in Fig. 5.2. The beam specimens were welded to a column stub (B1 specimens) or to a base plate (B2 specimens). Full penetration butt welds were used for the flange connections and fillet welds for the web connections.

The B1 specimens (Fig. 5.2a) were designed so that crack propagation at the weldments was the predominant mode of deterioration. A W4x13 section with a small b/t ratio (b/t = 11.5) was selected to prevent, as much as possible, the formation of local buckles. A relatively heavy column stub (W8x48) was chosen and continuity plates were provided to prevent column flange distortion and to assure uniform stress transfer from the beam flange to the column.

The B2 specimens (Fig. 5.2b) were designed so that local buckling in the beam flanges was the predominant mode of deterioration. A W6x9 section with a b/t ratio of 18.9 was selected for this purpose.

Tension tests were performed from coupon specimens cut from the beam flanges. Typical stress-strain diagrams obtained from these tests are shown in Fig. 5.3. Based on the material yield strength and the measured section properties listed in Table 5.1, values were computed for the yield strength and elastic stiffness for each specimen. These predicted values are listed also in Table 5.1.

The cantilever beam specimens were connected rigidly to a test frame. A lateral bracing system was provided to prevent lateral torsional buckling of the beams. Horizontal loads were applied in a predetermined pattern to the tip of the cantilever. The test setup for each type of specimen, with the lateral bracing system in place, is shown in Fig. 5.4.

The instrumentation system was dictated by the objective of the study, that is, the detection and measurement of localized failure modes and of deterioration in the overall load-deformation response. Overall response was recorded through the measurement of applied load, tip deflection and plastic hinge rotation at the beam end. The latter quantity was deduced from pairs of extensometers attached to the specimens as shown in Fig. 5.2b. Tip deflection was used as the control parameter for the input loading history.

Localized parameters of interest were strains, sizes and shapes of local buckles, and sizes and geometry of cracks. In the B1 specimens, nominal strains across the flange were measured close to the crack plane in order to serve as basic deformation parameter for damage models. In the B2 specimens, strain gages were applied to the flanges at locations where local buckling was anticipated. In these specimens the objective was to detect the onset of buckling from the strain measurements monitored at both sides of the flange. The location of strain gages for both test series is shown in Fig. 5.2. In order to measure large post-yield strains, special annealed constantan foil strain gages with tough high elongation polyimide backing were used. Sand blasting of the steel surface proved to increase substantially the working life of the gages and is highly recommended for similar applications.

Sizes and shapes of local buckles were measured from photos taken at peak deflection points. This method proved to be sufficiently accurate

at a stage at which local buckling led to noticeable deterioration in resistance.

Much effort was invested in the measurement of crack size and geometry. The emphasis in this study was on the measurement of crack depth which is the parameter used in the crack growth modeling discussed later in this chapter.

Various methods are available for measuring crack depth and crack surface dimensions. A summary of widely used techniques is presented in Table 5.2 which is based on a recent survey of available methods (105). The strain gage filament method cannot be used for crack depth measurement. The compliance sensing method requires the availability of a calibration curve prior to the testing of the specimens. Considering the limited number of our specimens and the high fabrication costs, this method was not employed. Acoustic and electrical methods are involved with high equipment costs and are difficult to employ in conjunction with the complex geometry of welded connections. The notch region extension method has been developed for creep tests only. Thus, only optical methods and fractographic methods together with some other recently developed techniques were utilized in this study.

Surface crack dimensions could be measured up to 0.1 mm accuracy using a fluorescent spray dye and a magnifying glass. A more precise way of obtaining surface dimensions (i.e., crack length and crack mouth opening) and shallow cracks depths (up to about 0.5 mm deep) was to employ a silicone-base precision impression material as suggested by Cheng, et al. (106). The depth of deep cracks was measured approximately by inserting a 0.001" thick copper plate into the cracks. The most reliable and accurate measurements of crack geometry, for deep cracks, were obtained from a fractographic study of the striation markings on the fracture surface.

5.3 LOADING PROGRAM

Each of the two test series consisted of experiments on ten identical specimens. The experiments in each series can be classified as monotonic, cyclic with constant amplitudes, and cyclic with variable amplitudes. Presented here is a general description of each category and

of the characteristics of the input command signal used in the experiments.

Monotonic Tests: The objective of monotonic tests was to identify the monotonic load-deformation characteristics and to obtain reference parameters for the cyclic tests. The input command signal used for the tip deflection history had a ramp (linear) shape. Such a signal maintains a constant deflection rate throughout the history and is most suitable for monotonic tests in the inelastic range. A slow rate of 0.02 in/sec was used in the monotonic tests.

Cyclic Tests with Constant Amplitude: Tests were conducted under constant amplitude cycling to determine the parameters of the damage models. A sinusoidal wave form was used to control the input deflection histories. Sine wave signals not only provide an optimum control over the input signal but, by maintaining a continuous change in the displacement rate, replicate more realistically the loading character experienced by a structural member. The average displacement rate in a quarter cycle was selected to define a sine wave and was assigned a value between 0.02 and 0.05 in/sec for all cyclic tests. For an input tip deflection history in the form of $\dot{\delta} = \delta_a \sin(2\pi/T)t$, the average deflection rate was computed as

$$\dot{\delta}_{ave} = \frac{\int_0^{T/4} \dot{\delta}\, dt}{T/4} = \frac{\int_0^{T/4} \delta_a \frac{2\pi}{T} \cos \frac{2\pi}{T} t\, dt}{T/4} = \frac{4\delta_a}{T} = 4\delta_a f$$

where δ_a is the amplitude of the sine wave and T and f are the period and frequency of the wave, respectively.

Cyclic Tests with Variable Amplitudes: One specimen in each test series was subjected to a tip deflection history with variable amplitudes. The objective of these experiments was to assess the accuracy of the developed damage models. Several blocks of history were applied repeatedly to the specimens until failure occurred. The input signal consisted of haver sine and invert haver sine waves and the average deflection rate was kept constant at a value of 0.05 in/sec.

The deflection amplitudes of the individual tests were selected so that damage parameters could be evaluated for the range of interest in

seismic response studies. Because of the highly inelastic nature of seismic response histories, damage modeling was based on plastic deformation ranges and no regard was given to the elastic deformation components. Plastic deflection ranges $\Delta\delta_p$ (as defined in Fig. 5.5), plastic hinge rotation ranges $\Delta\theta_p$ (equal to $\Delta\delta_p/\ell$) and plastic strain ranges $\Delta\varepsilon_p$ are used in this chapter as deformation parameters for damage models.

5.4 TEST SERIES B1--CRACK PROPAGATION STUDY

The objective of this test series is to implement a testing program for the performance assessment of a component whose useful life is governed by crack propagation at weldments. Damage modeling and performance assessment are done using low-cycle fatigue and fracture mechanics approaches. As will be discussed, the two approaches are equivalent and give acceptable life predictions for the test specimen subjected to arbitrary cyclic loading.

Section properties of the ten specimens tested in this series are given in Table 5.1a. Table 5.3 presents a summary of the testing program for each specimen.

5.4.1 Test Results and Observations

5.4.1.1 Behavior under Monotonic Loading

Although all test specimens were cut from the same piece of steel section, differences exist in the monotonic load-deflection behavior of the individual specimens. This is evident from Fig. 5.6 which shows P-δ diagrams for six specimens. The curves start to deviate at loads corresponding to approximately $0.6P_y$. The differences at supposingly elastic stress values must be attributed to variations in the microgeometry at the supports which result in stress raisers of different geometry and intensity. In the strain hardening region, the P-δ diagrams are essentially parallel but show a scatter band of about 5% of the strength values.

Also shown in Fig. 5.6 is the predicted P-δ response. The prediction is based on the measured stress-strain response of tension specimens and accurate modeling of moment-curvature along the beam. Despite this accurate modeling, which includes also modified stress-strain properties in the heat affected zone (107), the resistance of the specimens is underestimated considerably.

The underestimation of the load response in the inelastic range indicates shortcomings in the method of predicting the load-deflection (or moment-curvature) response from stress-strain diagrams based on a standard tension test. Since the yield strengths reported in the mill tests match closely with those obtained from coupon tests performed in our laboratory, it is very unlikely that differences in yield strength can account for the severe underestimation in load response. More likely, the sources of discrepancies are larger than expected material strength properties in the heat affected zone and strain gradient effects along the beam and through the cross sections. Although the differences in load response are a matter of concern, the issue was not pursued further because the absolute load values are not of primary importance in the context of this study.

Typical moment-strain responses for three specimens are shown in Fig. 5.7. The strains were measured at identical location, that is, at the centerline of the flange and 5/8 in. away from the weld toe. The figure shows large variations of the moment-strain behavior in the elastic and early inelastic range, while the differences due to variations in the yield stress are much smaller as the curves converge at high strain levels. The variations must be attributed to residual stress effects due to welding and to effects of connection microgeometry in the vicinity of the welds. These effects are caused primarily by differences in workmanship. Since strain is the most relevant parameter for modeling of crack propagation, this scatter will be one source of uncertainty in damage and life predictions.

Figure 5.8 shows moment-strain relationships measured in specimen B1-4 at different points on the flange at a distance of 5/8 in. from the weld toe. There are again major differences between the curves in the high stiffness region which are due to the connection microgeometry. At the end of the excursion, the strain at the centerline of the tension flange is less than the strain close to the edge of the tension flange and is higher than the strain at the centerline of the compression flange. This behavior, which was consistent for all specimens, may be attributed to the presence of residual stresses due to welding and possibly to an eccentricity between the flange load and weld reaction at

the support. The moments due to these eccentric forces tend to decrease the compressive strains and increase the tensile strains.

5.4.1.2 Behavior under Constant Amplitude Cycling

The cyclic load-deflection response of several B1 specimens is shown in Fig. 5.9. Only a few cycles of the complete histories are shown since many of the cycles are of almost identical shape. The response is characterized by cyclic hardening in the first few cycles, a relatively long period of stabilization in the load response, and a final stage of rapid deterioration and subsequent flange fracture.

In all constant amplitude tests the load response is slightly unsymmetric even in the stabilization stage where the peak loads are consistently smaller at even numbered reversals (negative loads). The main causes of this unsymmetric behavior are cyclic plasticity effects and redistribution of strains.

The deterioration phase for all specimens is short and occupies less than 10% of the life of the specimens. Deterioration resulted from advanced stages of crack propagation at the weld toe. Some minor flange buckling was noticed at later stages in life, especially in large deflection amplitude tests, but is not believed to contribute substantially to deterioration. Final fracture occurred as a result of unstable crack growth at flange welds.

Figures 5.9c and d compare the behavior of two specimens with the same deflection amplitude but with significantly different lives (N_f = 90 cycles for specimen B1-7 versus N_f = 45 cycles for specimen B1-8), and Fig. 5.9e presents the behavior of a specimen with the same amplitude but with a mean deflection equal to the deflection amplitude. The load-deflection behavior and hysteresis loop shapes of all three specimens are almost identical, except that the specimen with mean deflection exhibits a somewhat higher strength in the positive loading direction. The life of the mean deflection specimen (N_f = 83 cycles) is between the lives of the two specimens without mean deflection.

Typical moment-strain relationships for B1 specimens are presented in Fig. 5.10. Strain gages were located at about 5/8 in. from the weld

toe as shown in Fig. 5.2. The nominal strains measured at these locations show the following trends. Even when the displacement cycles are symmetric with respect to the undeformed configuration, the measured strain cycles consistently exhibit a considerable drift in the direction of the first plastic excursion. Also, the strain range for successive cycles increases, although at a decreasing rate until stabilization is almost reached. In part, the drifting phenomenon can be attributed to cyclic plasticity and a redistribution of strains. In part, the drifting may have been caused by inadequate bond of the strain gages.

Since these two phenomena could not be separated, the stabilized loops were taken as the plastic strain ranges for damage modeling. This compromise should be acceptable since the plastic strain ranges did not increase by much from the second to the stabilized cycle. Even if the exact plastic strain range could be identified for each cycle, the utilization of a varying plastic strain range would complicate damage modeling considerably and unduly.

A comparison of Figs. 5.10a and b shows that the presence of a mean deflection in specimen B1-10 did not have much effect on the plastic strain range compared to specimen B1-8 which had the same deflection amplitude without mean deflection. In fact, all three specimens cycled with a deflection amplitude of approximately 1.5 in. had almost identical plastic strain ranges. However, specimens cycled with larger deflection amplitudes show a considerable scatter in plastic strain ranges. This is illustrated in Fig. 5.11 which shows a plot of plastic deflection range versus plastic strain range for the eight specimens subjected to constant amplitude cycling. The plot indicates that the relationship between a global (deflection range) and local (strain range) deformation quantity is random and is another source of uncertainty in performance assessment.

5.4.1.3 Observations on Crack Propagation at Weldments

Crack propagation at the beam flange welds, as shown in Fig. 5.12, was the cause of damage and fracture in the B1 specimens. The behavior of the specimens was consistent in some respects and inconsistent in others. Differences in workmanship were responsible for large variations

in notch geometries at the weld toe and, therefore, for large variations in initial crack sizes.

In most of the specimens, the predominat crack propagation occurred at the centerline of the flange (below strain gage 3 in Fig. 5.2) with a single crack growing through the flange thickness. In a few specimens, however, edge cracks which propagated along the flange were equally or more important. But also in these specimens the centerline cracks grew to considerable sizes so that the specimens would have fractured at the centerline soon after the actual fracture initiated by edge cracks. Thus the effects of the edge cracks were ignored in crack propagation analysis.

Consistently, cracks propagated from surface imperfections (notches) at the weld toe or at the coping and in none of the specimens internal imperfections in the welds were of importance. Small surface cracks were observed very early in the history at the weld toe, in some cases already during the first excursion. After a few reversals small surface cracks joined, forming a relatively long but shallow crack. This crack propagated through the heat affected zone at an increasing rate. During this stage usually a smaller crack appeared on the opposite side of the flange at the coping and propagated through the thickness (Fig. 5.13). In smaller deflection amplitude tests, the two cracks joined and the resulting through crack propagated across the flange during several cycles until fracture occurred. Figure 5.12 illustrates such a case. At load point 161 the crack at the weld toe was still growing through the thickness. The through crack was formed at load point 165 and propagated for 3 more cycles until fracture occurred at load point 171. In larger amplitude tests, however, the through crack developed only during the last excursion. Figure 5.14 illustrates such a case. At load point 33 (Fig. 5.14a), there were deep cracks at the weld toe and at the coping but a through crack had not yet formed. The through crack and flange fracture occurred during the next cycle (Fig. 5.14b).

Figure 5.15 presents fracture surfaces for 3 specimens. Regions of crack propagation on the fracture surface are marked by a series of striations which are traces of the crack tip at each load reversal point. Joining of cracks that originated at the weld toe and the coping

created an inclination in the crack plane. In specimens B1-5 and B1-6 (Figs. 5.15a and b), two sets of striations at opposite sides of the flange can be distinguished and none of the striations extend across the flange thickness. This indicates that the through crack occurred in the last excursion. In specimen B1-7 (Fig. 5.15c), there are striations that extend across the flange thickness. This indicates that a through crack was formed earlier and then propagated across the flange in the last few cycles.

Magnified pictures of striations on the fracture surface are presented in Fig. 5.16. The striations are easily distinguishable at the later stages of life when there is a considerable increase in crack size after each load cycle and the striations are farther apart. The striations have a semi-elliptical shape. Crack contour shapes for two specimens are shown in Fig. 5.17. The aspect ratio of the ellipse increases with the depth of the crack. There are clear signs of crack joining for specimen B1-8 (Fig. 5.17b).

Much futile effort was invested in attempts to identify initial crack sizes and early crack growth through measurements using a silicone-base impression material. The main problem with using this material is lack of penetration. Measurements of the impressions under an optic microscope revealed that for crack openings less than 0.002 in. the penetration was poor. Thus, reliable measurements could not be obtained for shallow cracks for which also the striation markings were not clearly distinguishable. As it turns out, more exact measurement of shallow cracks would not have helped much in crack propagation modeling because in the initial stage of cracking the crack shapes were irregular, more than one surface imperfection was often involved in crack formation and joining of cracks occurred before a consistent crack front was developed.

Attempts to deduce an initial crack size from measurements of imperfections at the weld toe were equally fruitless. No correlation was found between geometric parameters of the imperfections and an initial crack size which could have been used for crack propagation modeling. A typical surface imperfection, as measured from an imprint of the impression material, is shown in Fig. 5.18. No sharp notches are evident which would permit the deduction of an initial crack size.

In view of these observations it was concluded that a reliable measurement of initial crack sizes is impossible and that initial crack growth cannot be modeled analytically with confidence. Thus, it was decided to deduce an equivalent initial crack size from crack measurements at a more advanced stage of cracking. This approach is discussed in Section 5.4.2.2.

5.4.1.4 Behavior under Variable Amplitude Cycling

Specimen B1-9 was subjected to an irregular tip deflection history. This history was intended to represent a realistic seismic response history. To obtain this history, the strength and stiffness properties of the beam were assumed to be representative for a single degree of freedom system with a period of 0.5 seconds whose response to the N21E component of the Taft record of the 1952 Kern County earthquake was predicted analytically. A bilinear load-deflection model was used in this analysis with a stiffness ratio of 0.085. The resulting deflection response history, with the elastic excursions eliminated for convenience, is shown in Fig. 5.19. According to this history, the maximum deflection range (points 11 to 20) is 6.4 in. which corresponds to a maximum nominal strain range at the gage location of approximately 0.050.

The history shown in Fig. 5.19 was applied repeatedly to the specimen. At the end of block 5 the crack depth was approximately equal to 0.01 in. and major crack propagation started in block 6. In block 7, only the larger rising excursions in the history (up to point 21) caused much of the crack propagation and the rest of the history did not have a noticeable effect on the growth of cracks. Major strength and stiffness deteriorations also occurred in this block. At load point 11 of the 7th block, a through crack was formed at the flange centerline due to the joining of a deep crack originating from the weld toe and a shallow crack originating from the cope. Thereafter, the crack grew longitudinally and unstable growth occurred at load point 21. Figure 5.20 compares the load-deflection behavior in blocks 1 and 7.

The results of this single test are used in Section 5.4.2.3 to check the adequacy of the life prediction methods proposed next.

5.4.2 Damage Modeling for Crack Propagation at Weldments

The results of test series B1 are used to develop empirical models for damage accumulation and life prediction in welded beam-to-column connections subjected to severe inelastic cycling. The main objectives of this exercise are, first, to find out which types of models are suitable for this purpose and, second, to assess the uncertainties in life predictions and to identify the sources of uncertainties. A comprehensive statistical evaluation is not possible because of the small number of test specimens. No attempts are made here to generalize the models to connections of different geometry. This would require a much more comprehensive parameter study. The utilization of a geometry dependent fracture mechanics parameter, such as ΔJ integral, should make it possible to generalize the results through future research work.

The empirical modeling is based on the following assumptions:

1. Crack growth initiates from surface imperfections at the weld toe at the flange centerline.

2. The surface crack propagates through the thickness of the flange until unstable crack growth occurs leading to a through crack.

3. The crack propagation through the flange thickness is not associated with noticeable deterioration in strength and stiffness of the specimen, whereas subsequent crack growth across the flange width occurs at a high rate and is accompanied by rapid deterioration in strength and stiffness.

4. Since the life associated with crack growth across the flange width is small, the deterioration stage can be neglected in damage modeling and life prediction. Thus, failure is defined as the occurrence of a through crack.

These assumptions appear to be justified based on the results obtained from test series B1. Even in those specimens in which edge cracks occurred prior to or simultaneous with centerline cracks, the latter either were the source of failure or grew close to unstable crack size when failure was caused by edge cracks.

The premise of the proposed damage modeling is that it is possible to relate the accumulated damage to a relevant deformation parameter. The use of a global deformation parameter, such as plastic hinge rotation, would be desirable from the viewpoint of seismic response analysis, but is a poor choice in this case because of the predominated effect of localized strains on crack propagation. Thus, localized strain histories are used as measures of the severity of inelastic cycles. Since this study is concerned with the effects of cycles with large plastic deformations, the effects of the elastic strain components on damage accumulation are ignored and only the plastic strain range, $\Delta\varepsilon_p$, is considered.

The location of strain measurement is expected to have a considerable influence on damage modeling. Localized measurements close to the crack tip would be most desirable but are impossible to record in a specimen of the type used in this study. Thus, rather arbitrarily, strain measurements were taken at a distance of 5/8 in. from the weld toe. As reported in Section 5.4.1.2, the recorded measurements are reasonably consistent and a constant deflection amplitude test corresponds closely to a constant strain amplitude test. However, the strain gages had a limited life and at the stage of large crack growth no reliable measurements were obtained. It was not possible, therefore, to evaluate the effect of large crack sizes on nominal strain measurements. In evaluating the damage models developed in this section, it can only be hypothesized that the models will be of similar form if the strain measurements are taken closer to the crack tip.

Two approaches are used here to develop damage models. One is based on the conventional low cycle fatigue approach in which the number of cycles to failure is correlated with the plastic strain range. The other is a plastic fracture mechanics approach in which a crack propagation model is used to trace crack growth from an initial crack size to a critical crack size.

The data presented in Table 5.3 point out the problems in damage modeling for crack propagation at weldments. As can be seen, the number of cycles to failure for specimens with identical deflection amplitudes vary by a factor which is as high as two. Most of the differences in

life must be attributed to workmanship which causes large variations in initial imperfections at the weld toe. As a consequence, damage modeling will have to be based on widely scattered data and should include statistical parameters where possible.

5.4.2.1 Low-Cycle Fatigue Approach

Using the results of the constant amplitude tests, the number of cycles to failure, N_f, is related to the plastic strain range, $\Delta\varepsilon_p$, as shown in Fig. 5.21. With some generosity one can draw a straight regression line through the points plotted on a log-log scale. This line gives credence to the hypothesis that N_f and $\Delta\varepsilon_p$ for constant amplitude tests can be related by a Coffin-Manson relationship of the form $N_f = C^{-1}(\Delta\varepsilon_p)^{-c}$. A statistical evaluation of the scatter around the regression line was not attempted because of the small number of data points. One can speculate from the data points that the scatter band is of uniform width along the regression line, indicating that the uncertainty in life prediction can be expressed by the randomness of the parameter C alone.

Adopting a Coffin-Manson relationship for constant amplitude cycling, it becomes a matter of philosophy whether the hypothesis of linear damage accumulation can be accepted for variable amplitude cycling. If damage is related directly to crack size, linear damage accumulation breaks down because the rate of crack growth increases rapidly with crack size. However, there is no evident reason why this relationship should be made. As long as the purpose of a cumulative damage model is to predict likelihood of failure, a crack size below the critical crack size is not at all related linearly to damage. Thus, there appears to be no evident argument why linear damage accumulation should be less acceptable for crack propagation problems than for other low-cycle fatigue problems.

Using linear damage accumulation (Miner's rule), the damage per cycle of strain range $\Delta\varepsilon_i$ is equal to $1/N_{fi}$ and the accumulated damage is given by

$$D = \sum_{i=1}^{N} \frac{1}{N_{fi}} = C \sum_{i=1}^{N} (\Delta\varepsilon_{pi})^c \qquad (5.1)$$

Ideally, a limit value of D equal to one should constitute failure. There are many flaws in this relationship but its simplicity makes it attractive for seismic response studies in which more refined models would add an unwarranted complexity because of the many other uncertainties involved (seismic input motion, response evaluation, identification of localized strain histories, human factors affecting fabrication, etc.). The most evident flaws are the acceptance of Miner's rule for any low-cycle fatigue problem and the disregard of mean deformations and sequence effects. Many studies have shown that even in tightly controlled laboratory experiments on machined low-cycle fatigue specimens, and using deformation histories without mean stresses or mean strains, failure may occur at damage values significantly different from one. This problem can only be amplified through the use of structural component specimens and random deformation histories which may include large mean deformations. It appears to be necessary, therefore, to assign a probabilistic distribution to the limit value of D associated with failure, rather than using a deterministic value of one.

It may be of some interest to correlate the number of cycles to failure directly with a global deformation parameter in order to avoid the need for calculating localized strains. Clearly, this correlation is only for convenience and has no phenomenological justification because of the nonlinear relationship between local and global deformation parameters. Because of this nonlinear relationship, the scatter from a regression line should be larger when a global response parameter is used. This is illustrated in Fig. 5.22 which shows a log-log plot of N_f versus the plastic rotation range $\Delta\theta_p$ ($\Delta\theta_p = \Delta\delta_p/\ell$). It is interesting to note that a regression line fits very well to the three auxiliary data points (marked by a + sign) which represent the mean lives of the specimens with identical rotation ranges. Thus, it appears to be possible to correlate, at least in specific cases, the number of cycles to failure with a global deformation parameter. Whenever this is possible, the utilization of a low-cycle fatigue model in seismic response studies is greatly simplified.

5.4.2.2 Fracture Mechanics Approach

The observations made in this testing program justify the assumption that the specimens, when subjected to highly inelastic deformation cycles, spend almost all of their useful life in the crack propagation stage. Thus, life predictions can be based on the trace of crack growth from an initial crack size, a_o, to a critical crack size a_c, provided that a_o and a_c can be determined and a reliable propagation model can be developed. Various approaches are used in the literature to relate crack growth rate da/dN to localized deformation parameters. In plastic fracture mechanics, the most widely used parameters appear to be the crack openings displacement (COD), the ΔJ integral, and the nominal plastic strain range $\Delta\varepsilon_p$.

The use of a geometry dependent parameter such as ΔJ would permit a generalization of crack propagation models to structural elements of different geometry. However, the J integral is not well defined at this time except for simple crack shapes, and ambiguities are involved in the evaluation of ΔJ because of the crack closure phenomenon.

Thus, it was decided to use the plastic strain range $\Delta\varepsilon_p$ as basic deformation parameter. Ideally, strain measurements should be taken as close as possible to the crack plane. In this study, strains are measured at a distance of 5/8 in. from the weld toe at which cracks originated. The resulting strains are nominal strains which do not account for stress concentrations at the imperfections and for localized changes in strain distribution as cracks propagate. The reason for using these nominal strains is not only that it is extremely difficult to measure strains very close to the crack plane in welded connections, but it is equally difficult to predict the localized strains by analytical means. An analytical prediction would necessitate, amongst others, a detailed knowledge of the cyclic stress-strain behavior of the material in the heat affected zone through which the cracks propagate.

Solomon (99) has shown that the logarithm of the crack depth, a, is related linearly to the number of cycles provided that all cycles are of equal strain amplitude close to the crack. His tests indicate that this linear relationship holds true for the full range of crack propagation, from very small cracks to cracks approaching unstable crack growth (Fig. 5.23). In the component tests performed in our study, deflections and

not strains were controlled in the constant amplitude tests. However, the nominal strains recorded close to the crack plane (Fig. 5.10) did stabilize to an almost constant amplitude after several reversals. Thus, it can be justified to consider the constant deflection amplitude tests as constant strain amplitude tests.

For all constant amplitude tests the crack depth, a, was plotted versus the number of cycles, N, on a semi-log paper using primarily the data for large crack sizes which could be measured more accurately. The most reliable data were obtained from photos of the magnified fracture surface which showed clean striation lines for large cracks. Typical fracture surfaces are shown in Fig. 5.16.

The plots of crack depth, a, versus number of cycles, N, shown in Fig. 5.24 lend credence to the hypothesis that the logarithm of a and N are linearly related, at least in the range of large crack sizes. Straight lines (shown solid in the graphs) can be placed with reasonable to very good accuracy through the data points. When the slopes of these lines are plotted on a log-log paper against the plastic strain ranges, $\Delta\varepsilon_p$, the results shown in Fig. 5.25 are obtained. This figure indicates that, for constant amplitude tests, crack growth rate and plastic strain amplitude can be related by an equation of the form

$$\frac{da}{dN} = \alpha a(\Delta\varepsilon_p)^{\beta} \tag{5.2}$$

In this crack growth rate model, the parameters α and β depend on the material properties, the geometry of the specimen, the shape of the crack, and on the location at which strains are measured. If the strains would have been measured closer to the crack plane, larger strains would have been obtained and smaller crack growth rates (as a function of $\Delta\varepsilon_p$) would have been predicted.

It must be said that considerable judgment had to be exercised in placing straight lines through the crack size data of a few of the tests, especially for specimen B1-7 (Fig. 5.24e). In several tests, the range of "reliable" crack size measurement is very small and the accuracy of the measurements depends on judgment in identifying striation markings. Thus, the accuracy of some of the data points in Fig. 5.25 may be questionable but it is noted that none of the points deviate much from the regression line.

It is of interest to compare the values of α and β obtained from this study (α = 124, β = 1.90) with the values reported by Solomon (99) (α = 19.2, β = 1.86). The small difference in β indicates that the exponent in Eq. (5.2) is insensitive to the location of strain measurement and is not affected much by the fact that in our study the crack propagates through the heat affected zone. The large discrepancy in the coefficient α is attributed to differences in reference strain measurements (Solomon measured at the crack plane) and the effects of the heat affected zone. The crack growth rate model obtained in this study would be almost identical to that obtained by Solomon if the plastic strain ranges are multiplied by a factor of approximately 2.70.

In order to use a crack growth rate model for life predictions, it is necessary to trace crack growth from an initial crack size, a_o, to a critical crack size, a_c. Provided that Eq. (5.2) is valid for the full range of crack growth, the number of cycles to failure for constant strain amplitude cycling can be obtained as

$$N_f = \alpha^{-1} \ln \frac{a_c}{a_o} (\Delta\varepsilon_p)^{-\beta} \tag{5.3}$$

The validity of a single crack growth rate model for the full range of crack sizes, from a_o to a_c, has not been verified in this study because of the difficulties encountered in measuring small crack depths. Solomon's study (99) presents some evidence that, for a constant plastic strain range, d(ln a)/dN is constant for a range from very small cracks to cracks approaching the critical crack size. Thus, the assumption of a single da/dN relationship, as given by Eq. (5.2), appears to be acceptable. Moreover, the acceptance of a single da/dN relationship becomes inconsequential for life predictions, because of the manner in which the initial crack size is defined later in this study.

Equation (5.3) contains four parameters (α,β,a_o,a_c) which are random variables. The data of this study and of Solomon's work indicate that the uncertainty in the exponent β of the crack growth rate model is relatively small and may be neglected. The uncertainty in the coefficient α should then account for the variability in the fracture properties of the material and in crack geometry, as well as for the scatter

in strain range measurements. Short of a comprehensive research program there is no way how this uncertainty can be evaluated statistically. It is assumed, therefore, in the following discussion that α has a deterministic value and that all uncertainties can be lumped in the evaluation of the intial crack size a_o.

Compared to α and β, the uncertainty in a_o is believed to be large because the initial crack size is greatly affected by workmanship and the resulting imperfections at the weld toe where cracks initiate. As was discussed previously, it is impossible to obtain reliable measurements of a_o because of irregular crack growth and joining of small cracks in the early stage of loading. Thus, it was decided to predict an equivalent initial crack size analytically and in a manner which incorporates all uncertainties in life predictions. For this purpose, the regressed values of α and β as shown in Fig. 5.25 are used to solve Eq. (5.3) for a_o, using the crack size at N_f-2 cycles for a_c. This was done to eliminate the effect of unstable crack growth during the last two cycles. The data for this calculation process and the resulting statistics on a_o are shown in Table 5.4. The corresponding extrapolation lines to a_o are shown in Fig. 5.24, illustrating the fit of the data points to the regressed da/dN relationship given in Fig. 5.25.

The mean of the equivalent initial crack size is 0.00163 and the standard deviation is 0.00123, indicating a considerable scatter in initial crack size. Using a critical crack size of half the flange thickness, the ratio of predicted life based on mean-σ of a_o to that based on mean + σ of a_o is equal to 1.48. This ratio gives some indication of the uncertainty to be expected in life predictions.

An exact evaluation of the critical crack size a_c is difficult and may not be needed because small variations in a_c have little effect on life predictions. In the specimens tested in this study, the crack size that caused unstable crack growth through the flange thickness was somewhat larger than half the flange thickness when a crack propagated only from the weld toe, and somewhat smaller than half the flange thickness when cracks propagated from the weld toe as well as from the inside of the flange at the coping.

It is important to note that the life prediction model for constant amplitude cycling, given by Eq. (5.3), is identical in form to the Coffin-Manson relationship for the low-cycle fatigue approach, given as $N_f = C^{-1}(\Delta\varepsilon_p)^{-c}$. The equivalence of parameters is given by

$$C = \alpha \left(\ln \frac{a_c}{a_o}\right)^{-1}$$
$$c = \beta \qquad (5.4)$$

Provided that a deterministic crack growth rate model can be accepted, this equivalence indicates that the uncertainty in the Coffin-Manson relationship can be assigned to the parameter C and is caused primarily by variations in initial crack size. A comparison of the low-cycle fatigue model and the fracture mechanics model shows that they are in good agreement. The exponent c is 1.99 whereas β is 1.90, and the coefficient C is 32.9 whereas $\alpha(\ln a_c/a_o)^{-1}$ is 26.5, using half the flange thickness for a_c and the calculated mean value of a_o.

As it is evident from Fig. 5.25, the data points for specimens B1-4 and B1-5 have the largest distance from the regression line. Specimen B1-4 is the only specimen for which the crack growth data at later stages of the crack propagation through the flange thickness could not be obtained (Fig. 5.24b) since fracture initiated at a corner crack on the opposite flange. If we eliminate the data point for this specimen from Fig. 5.25 and use the least square method to get a new crack growth rate model, the new values for parameters α,β and $\alpha(\ln a_c/a_c)$ will be 156, 1.96, and 33.3 respectively. These revised fracture mechanics model parameters are in excellent agreement with the low-cycle fatigue model parameters based on the nominal strain measurements.

Crack Propagation and Life Prediction for Variable Amplitude Cycling: Under variable amplitude cycling, the crack closure phenomenon is expected to have an influence on crack propagation. Crack growth rate is believed to be proportional to the strain range in which the crack is opened. At some point in the rising load excursion the crack opens and it may or may not close during the subsequent falling load excursion, depending on the strain range of the excursion. For large cracks, crack closure is sometimes noticeable on a load-deformation curve by an inflection point in the falling load excursion. This is due to the

sudden increase in stiffness as the surfaces of the crack come in contact with each other and provide additional area for carrying the load.

In the experimental results obtained in this study, a crack closure point could not be distinguished on the load-deformation plots as the surface of cracks is small compared to the cross-sectional area, except for the last few cycles before fracture. Identification of the instance of closing of the crack mouth may give some indication of crack closure, but for the specimens tested this procedure was believed to be unreliable.

Even if it would have been possible to identify the point of crack closure, the data obtained from this study would have been insufficient to incorporate the crack closure phenomenon in crack propagation modeling. For instance, sequence effects would have to be considered since crack closure affects a sequence of small to large cycles in a different manner than a sequence of large to small cycles. A pilot study on the seismic response of inelastic system has also shown that seismic response cycles do not follow an recognizable sequence pattern.

In view of these considerations, it was decided to ignore the crack closure phenomenon in crack propagation modeling for cycles with variable amplitudes. There is some indication from the test results that the crack closure phenomenon may not be of critical importance provided that the falling load excursion has a sufficient strain range to permit full crack closure. This is indicated by the consistent crack growth rates which were obtained from all tests with constant strain amplitudes, and by the behavior of specimen B1-10 which was subjected to cycles with considerable mean deformations but whose crack growth rate was similar to that of a specimen with cycles without mean deformation.

Ignoring the crack closure phenomenon, it appears to be justified to use the simple crack growth rate model given by Eq. (5.2) in order to trace crack growth for cycles with variable strain amplitudes. Assuming an initial crack size a_o, the crack size a_N after N cycles with different plastic strain ranges, $\Delta\varepsilon_i$, is then given by

$$\ln \frac{a_N}{a_o} = \alpha \sum_{i=1}^{N} (\Delta\varepsilon_{pi})^{\beta} \qquad (5.5)$$

Using the critical crack size a_c for a_N, failure is expected to occur under the condition

$$\alpha \left(\ln \frac{a_c}{a_o}\right)^{-1} \sum_{i=1}^{N} (\Delta\varepsilon_{pi})^{\beta} = 1 \qquad (5.6)$$

A comparison of this equation with the cumulative damage model presented in the low-cycle fatigue approach [Eq. (5.1)] shows that both approaches result in identical failure definitions provided that the equivalence in parameters [see Eq. (5.4)] is established. The identical form of failure definitions indicates that the acceptance of linear damage accumulation (Miner's rule) in the low-cycle fatigue approach is equivalent to the acceptance of a single da/dN relationship in the fracture mechanics approach.

The equivalence of the two approaches reveals that a cumulative damage model can be based also on the fracture mechanics approach, i.e.,

$$D = \sum_{i=1}^{N} \frac{1}{N_{fi}} = \alpha\left(\ln \frac{a_c}{a_o}\right)^{-1} \sum_{i=1}^{N} (\Delta\varepsilon_{pi})^{\beta} \qquad (5.7)$$

This formulation may be preferable to that based on the Coffin-Manson relationship because it provides the possibility for generalization to welded connections of different geometry. What is needed for this purpose is a more comprehensive statistics on a_o and the utilization of a geometry dependent crack propagation parameter (e.g., ΔJ) in lieu of $\Delta\varepsilon_p$.

5.4.2.3 Damage Accumulation and Life Prediction for Variable Amplitude Test

The variable amplitude test discussed in Section 5.4.1.4 is used to examine the adequacy of the life prediction models presented in the previous section. In this test, a through crack at the center of the flange and subsequent rapid deterioration were observed during the seventh application of the tip deflection history shown in Fig. 5.19. The instance of unstable crack growth through the flange thickness (a/a_c = 1.0) in the seventh block and the measured crack sizes at the end of the fifth and sixth block are marked on the diagram shown in Fig. 5.26.

Equation (5.1) is used to predict damage accumulation and Eq. (5.2) is used to predict crack growth throughout the loading history. It was shown in the previous section that both equations will result in identical life predictions, provided the parameters of the models are identical and provided the same plastic strain ranges are used. The issue of appropriate strain ranges is as yet unresolved in crack propagation problems because it is closely tied in with the crack closure phenomenon. Most conveniently, strain ranges could be identified as they appear in the loading history. There are physical arguments that this should not be done in certain instances. For instance, considering the two rising excursions AB and CD shown in Fig. 5.27a, it is likely that the small reversal BC will not lead to crack closure and therefore crack propagation may be governed by the strain range AD rather than by the individual ranges AB and CD. In this case it may be appropriate to use the strain ranges AD and CB (Fig. 5.27c), rather than the strain ranges AB and CD (Fig. 5.27b), for crack propagation modeling. In this manner, the small excursion CB is considered to be an interruption of the large excursion AD. There is no evident reason, however, to apply the same argument if the reversal BC is of sufficient strain range to cause crack closure.

In order to obtain an indication of the range of life predictions, two methods are employed to identify the plastic strain ranges. In the low-cycle fatigue approach [Eq. (5.1)], the rain-flow cycle counting method is employed to order excursions in the manner shown in Fig. 5.27c. The corresponding plastic strain ranges are tabulated in Table 5.5. Ideally, the rain-flow cycle counting method should rearrange the excursions into a series of closed cycles (same positive and negative strain range). An inspection of Table 5.5 shows that this holds true except for the beginning and the end of the history (small strain ranges) and except for the largest strain range (range 20-27). This largest strain range will have a considerable effect on damage accumulation since only very few large strain ranges are contained in the history. In order to account for this largest strain range, damage accumulation is based on cycles whose strain ranges are given by the positive $\Delta\varepsilon_p$, i.e., the strain ranges which cause opening of the crack.

The damage accumulation during the first application of the history is tabulated in Table 5.5. At the end of the first block the accumulated damage is equal to 0.30. The strain ranges measured during the second block differed by up to 10% from those measured in the first block and strain measurements became unreliable soon thereafter. Thus, equal strain ranges (as measured in the second block) and therefore equal damage were assumed for each subsequent block. Assuming that failure occurs when the accumulated damage is equal to one, failure was predicted to occur after 3.33 blocks (see Fig. 5.26).

In the fracture mechanics approach (Eq. (5.2)), the individual excursions were not reordered and crack growth was predicted directly from the strain ranges of the rising excursions of the history ($\bar{\Delta}\varepsilon_p$). Thus, the crack size a_j at the end of block j can be predicted from the equation

$$\ln \frac{a_j}{a_{j-1}} = \alpha \sum_{i=1}^{N} \left(\bar{\Delta}\varepsilon_{pi}\right)^{\beta} \qquad (5.8)$$

The right hand side of this equation amounts to 1.309, if the values α and β from Fig. 5.25 are employed and the $\bar{\Delta}\varepsilon_{pi}$ of all rising excursions of block 2 are used. With this formulation crack growth and fracture (crack size equal to a_c) depend primarily on the initial crack size a_o. Using the mean value of the calculated a_o values, fracture is predicted after 3.74 blocks. The corresponding crack growth curve is shown in Fig. 5.26. The difference in the lives predicted from this curve and from the low-cycle fatigue model (3.74 blocks versus 3.33 block) comes from the following sources. The effect of rain-flow cycle counting is to decrease the predicted life by a factor of 0.855, whereas the effect of using the low-cycle fatigue model [Eq. (5.1)] rather than the fracture mechanics model [Eq. (5.2)] is to increase the life by a factor of 1.04 (because of differences in the empirical model parameters). Thus, the ratio of life predictions from the two approaches chosen here is 0.855 x 1.04 = 0.89 which corresponds to the ratio of 3.33/3.74.

Both approaches underestimate considerably the life of the specimen when the mean value of the initial crack size a_o is used. When the mean minus standard deviation of the initial crack size a_o is employed in the

fracture mechanics approach, the predicted crack growth (solid line in Fig. 5.26) approaches but is still less than that observed in the test specimen. Definite conclusions cannot be drawn from these observations because the initial crack size for specimen B1-9 is not known. However, presuming that a_o for specimen B1-9 is within the range of a_o for the other specimens, it can be said that the low-cycle fatigue and crack propagation models discussed in this section give conservative estimates of life to failure. This conservatism comes from the use of Miner's rule in the low-cycle fatigue model or the neglect of crack closure phenomena in the crack propagation model. The results also suggest that it may not be necessary to use cycle counting methods to reorder the plastic deformation ranges in crack propagation problems.

5.4.3 Conclusions

The cyclic load-deformation behavior of the B1 specimens shows a long deterioration threshold and a relatively short range of rapid deterioration. Ignoring the deterioration range, failure can be defined as the onset of noticeable deterioration which is associated with the occurrence of a through crack in the flange.

Low-cycle fatigue and plastic fracture mechanics approaches can be used to predict the lives under cyclic deformations. Realistic predictions are obtained using the two approaches, however, large uncertainties are involved due to differences in initial imperfections. Thus, the most critical parameter in life prediction is the equivalent initial crack size a_o, which is a random variable with large scatter. Much more work needs to be done to obtain statistically acceptable data for a_o for different weld sizes and geometries. The approach used in this study, that is, the extension of the a-N line to N=0, appears to be appropriate for this purpose.

A tensile mean deformation appears to have no detrimental effect on crack growth as long as the strain range is sufficiently large to cause crack closure.

A damage accumulation model can be formulated from fracture mechanics data, utilizing a crack growth rate model and information on initial and critical crack sizes.

Realistic but conservative life predictions are obtained for a specimen subjected to excursions with different amplitudes, if linear damage accumulation is assumed in the low-cycle fatigue approach and a single da/dN relationship is assumed in the fracture mechanics approach.

The plastic fracture mechanics approach is considered to have a higher potential than the low-cycle fatigue approach for life predictions for crack propagation and fracture modes of failure. The advantage of this approach is that the use of a statistically acceptable initial crack size together with the use of the ΔJ integral could lead to a general mathematical formulation which can be applied to components with different geometries and crack shapes. This will require, however, much more research on the evaluation of the initial crack size and the ΔJ integral.

The parameters needed for damage modeling and performance assessment can be obtained from a series of constant amplitude tests. Because of the randomness of the model parameters, in particular of the initial crack size a_o, as large a number of specimens as possible should be tested in order to evaluate the uncertainty in the model parameters.

5.5 TEST SERIES B2 — LOCAL BUCKLING STUDY

The objectives of test series B2 are (a) to identify the characteristics of a local buckling mode of failure in plastic hinge regions of beams, and (b) to implement a testing program for the performance assessment of a component whose useful life is governed by strength and stiffness deterioration due to local buckling.

The specimens for this test series were designed so that local buckling of beam flanges occurred at relatively small hinge rotations. This was accomplished by selecting flanges with a large width to thickness ratio (b/t = 18.9). The intent of the design was that flange buckling should cause considerable deterioration in strength and stiffness before other localized failure modes, such as crack propagation, will start to affect the load-deformation response.

Section properties of the ten specimens tested in this series are given in Table 5.1b. Table 5.6 presents a summary of the testing program for each specimen. In all cyclically loaded test specimens deterioration due to local buckling was followed by crack propagation and fracture either at the flange weld or at the local buckles. The last column in

Table 5.6 identifies the number of load reversals applied to each specimen before a through-crack was formed at the weldment and started to propagate across the flange. This information is supplemented by the total number of load reversals to final flange fracture.

5.5.1 Test Results and Observations

5.5.1.1 Behavior under Monotonic Loading

Applied load versus tip deflection diagrams for three B2 specimens are shown in Fig. 5.28. Although all test specimens were cut from the same piece of steel section, considerable differences are evident in the post elastic response. Also shown in the figure is the predicted P-δ response. As in the B1 specimens, and for the reasons discussed in Section 5.4.1.1, the post-elastic strength is underestimated considerably. The predicted strain hardening stiffness, however, is similar to the measured ones until local buckling leads to strength deterioration. This instance can be identified from the experimental load-deflection curve as the instance when the experimentally obtained stiffness starts to deviate from the predicted one. Figure 5.28 shows how the actual undeteriorated curve can be constructed by continuing the experimental load-deflection curve parallel to the predicted curve.

It can be noted from Fig. 5.28 that nonlinear behavior starts considerably below the theoretical yield load P_y. The reasons for this phenomenon are more evident from an inspection of load-rotation and moment-strain curves discussed next.

Section rotations at 6 in. from the base plate were calculated from the extension (in the tension flange) and contraction (in the compression flange) of extensometers (shown in Fig. 5.2) according to the following formula:

$$\theta = \tan^{-1} \frac{|\Delta \ell_g|}{\frac{d}{2} + s}$$

in which $\Delta \ell_g$ is the change in gage length and s is the distance from the gage to the flange surface. An average value of measurements on the tension and compression flanges was assumed to represent the section rotation. Figure 5.29 shows typical load-rotation curves based on

measurements on the tension flange (θ_t) and the compression flange (θ_c) and the average of these two (θ_a).

Nonlinearity in the P - θ_c curves starts at load levels around 5 kips, which is considerably below the theoretical yield load P_y. The P - θ_t curves are linear for a longer range but become nonlinear at load levels which are also smaller than P_y. Whereas the early nonlinearity in P - θ_t may be attributed to residual stresses, the very early nonlinearity in P - θ_c indicates that localized inelastic deformations in the compression flange close to the welded connection occur very early in the loading history. These localized deformations, however, did not have a definite effect on the load carrying capacity of the member whereas the local flange buckling, once it was noticed from visual observations, led to a noticeable drop in the slope of the P - δ or P - θ curves and to subsequent strength deterioration. Thus, the effect of early localized inelastic deformations is neglected in the damage formulation discussed later in this chapter.

Similar to the load-rotation behavior, a difference exists in moment-strain plots for tension and compression flanges, i.e., for the tension flange the initial linearity in the curves persists longer than for the compression flange. Figure 5.30 presents strain readings from pairs of strain gages (one on the inside and one on the outside) of compression flanges. Figure 5.30a shows that for compression strain gages which are very close to the support, nonlinearity may start at very small loads. This confirms the observation made from the load-rotation curves about the early occurrence of localized inelastic deformations in the compression flange close to the weldment.

Provided that strain gages are located at appropriate points of the compression flange, the onset of local buckling can be identified from the moment-strain plots as the instance when the strain measurements at opposite sides of the flange deviate significantly from one another (Fig. 5.30b). However, much judgment and guess work is involved in interpreting the strain gage results because the state of strain in a pair of "buckling" gages depends so much on the location of the gages with respect to the buckle shape and on localized deformation fields. Thus, it was decided to identify the occurrence of local buckling not

from strain gage results but from visual observations of flange shapes and from the onset of noticeable deviations of the load-deflection response from the expected undeteriorated response.

There is only one consistent conclusion that can be drawn from a detailed study of the strain gage results. This conclusion is that the data show trends but numerical values of strains depend strongly on residual stresses, localized deformation, proximity to discontinuities (weld toe, coping) and shapes of local buckles. Thus, an analytical prediction of strain in the critical region of beams similar to the B2 specimens will be a most difficult if not impossible task. For this reason, a global deformation parameter (plastic hinge rotation) rather than a localized deformation (strain) is used in the damage models discussed later.

5.5.1.2 Behavior under Constant Amplitude Cycling

The cyclic load-deflection response of several B2 specimens is shown in Fig. 5.31. Disregarding the occurrence of local buckling, the behavior is expected to be similar to that of the B1 specimens, characterized by cyclic hardening in the first few cycles, a relatively long period of stabilization in the load response, and a final stage of rapid deterioration and subsequent flange fracture. However, in the B2 specimens, buckling occurred either during the first excursion or, for small deflection amplitudes, after a small number of reversals. During several cycles following the onset of flange buckling, the buckles grew considerably in size and significant deterioration in the load carrying capacity of the specimens can be notices. To identify the amount of deterioration from Fig. 5.31, it must be considered that the deteriorated response includes a noticeable amount of strain hardening during the first few cycles. After several cycles, the rate of growth in buckle size decreased continuously and the rate of deterioration in strength, stiffness and hystersis energy decreased accordingly. Similar to the B1 specimens, final rapid deterioration and subsequent flange fracture occurred as a result of crack propagation at weld toes.

Figure 5.31d presents the behavior of a specimen (B2-10) with the same deflection amplitude as the one presented in Fig. 5.31c (B2-5) but

with a mean deflection approximately equal to the deflection amplitude. The hysteresis loop shapes of both specimens are almost identical and the rate of deterioration is very similar in both specimens. This indicates that the mean deflection did not have a significant effect on the load-deflection response.

Table 5.7 summarizes basic response parameters of the B2 specimens subjected to constant amplitude cycling. In this table, P is the peak load at the load reversal point, K is the elastic stiffness at the start of loading for the first monotonic excursion and the unloading stiffness for all other excursions, and E is the hysteresis energy which is defined as the area inside the hysteresis loops. The plastic deflection amplitude ($\Delta\delta_p/2$) shown in the table is the one corresponding to the first excursion. Due to the deterioration in strength and stiffness this parameter will vary slightly during the subsequent excursions. As can be seen from Table 5.7, different responses were obtained in the two opposite directions. This is due mainly to the slightly unsymmetric geometry of the specimens at the connection. However, the trends in the two directions are generally the same.

Cyclic load-rotation curves for two B2 specimens are presented in Fig. 5.32. The average rotation θ_a, as defined in Section 5.5.1.1, has been used to obtain these curves. The shapes of the loops are similar to those of the corresponding load-deflection diagrams. Minor irregularities in the load-rotation loops may be attributed to the localized nature of rotation measurements and the somewhat irregular change in buckle shapes during the cyclic loading. A progressive increase in rotation in the positive direction, as a consequence of the progressive increase in buckle size, is noticeable. The rotations at peak points in the negative direction remain almost constant except for the very large amplitude test (specimen B2-6).

The measured plastic rotation ranges are in all cases close to $\Delta\delta_p/\ell$, indicating that the computed quantity $\Delta\delta_p/\ell$ is a good approximation of the plastic rotation range $\Delta\theta_p$.

Typical moment-strain relationships for B2 specimens subjected to constant amplitude cycling are presented in Fig. 5.33. As discussed in Section 5.5.1.1, the output of pairs of strain gages located on both

faces of a flange was only marginally useful in detecting the onset of local buckling. The recorded strains are the result of axial deformations due to overall bending and localized bending deformations due to flange buckling. The magnitude and sign of the local bending strains depend strongly on the location of the strain gage with respect to the buckle shape. Since the buckle shape varied from specimen to specimen, no general conclusions can be drawn from the strain measurement. Figure 5.33a shows an example where the strain range decreases continuously with cycling whereas in the example of Fig. 5.33b the strain range decreases severely from the first to the second cycle and then continuously increases with cycling.

5.5.1.3 Observations on Flange Buckling and Crack Propagation

Photos of the specimen flanges were taken at the peak deflection points. Two of these photos taken at two consecutive load reversal points for specimen B2-3 are presented in Fig. 5.34. At reversal point 19 (Fig. 5.34a) the right flange is buckled and the left flange is partially straightened, while in the next reversal (Fig. 5.34b) the left flange is buckled and the right flange is partially straightened.

Figure 5.35 shows different buckle shapes for different specimens during the course of the experiments. Some specimens have single buckles in their flanges (specimen B2-4, Fig. 5.35a) while others have double buckles (specimens B2-6 and B2-8, Figs. 5.35b and c). Some buckles occur inwards while others occur outwards. Figure 5.36 compares the stable shapes (based on photos taken after the rate of growth in buckle size decreased considerably) for different specimens. Although there exist major differences in buckle shapes even for specimens with the same load history (specimens B2-4 and B2-8, Figs. 5.35a and c), these differences appear to have little effect on the overall response of the specimens as will be discussed later in this chapter.

Measurements of buckle sizes (maximum deflection of the flange due to buckling) were taken from the photos of flange buckles. The results of these measurements are plotted against the number of cycles in Figs. 5.37 and 5.38. The data points shown in these figures indicate three stages in life. During the first stage no buckling occurs and the buckle

size remains zero. This may be called a deterioration threshold stage. For the flange configuration tested in this study, this stage occupies only a portion of the first monotonic excursion if the deflection amplitude is large. The second stage starts with the onset of buckling and is characterized by a high rate of growth in buckle size. The third stage is characterized by a decreasing growth rate in buckle size which is an indication of stabilization in buckle shapes.

Considering the data points of Fig. 5.37 it appears that, for a given deflection amplitude, the buckle growth rates in the second stage are similar for both flanges (positive and negative loading directions) and are nearly constant for several cycles. Thus, one can place, with some generosity, a straight line through the data points of each test. The slopes of these lines increase consistently with the deflection amplitude. When the slopes of these lines (db/dN) are plotted in a log-log scale against the plastic rotation range $\Delta\theta_p$, the results shown in Fig. 5.39 are obtained. A buckle growth rate model of the exponential type, as shown on the figure, appears to be indicated by the data.

For specimen B2-10, which has a mean deflection approximately equal to the deflection amplitude, the data points of buckle size versus number of cycles in the second stage show initially a high slope for loading in the positive direction (Fig. 5.38). However, after two cycles the slope of the b-N diagram approaches the slope of the b-N diagram for specimen B2-5 (Fig. 5.37b). The latter specimen had the same deflection history as B2-10 but with zero mean. This pilot test indicates that a mean deflection increases the rate of growth of buckles for one or two cycles but that thereafter the effect of mean deformation appears to diminish.

Final failure of all but one cyclically loaded specimens was caused by fracture at the flange welds. Although no refined crack growth measurements were taken in this test series, several consistent observations could be made from simple measurements at the crack surfaces and from an inspection of the load-deformation response.

Surface cracks were observed very early in the load history, in most cases already during the first excursion. The most common initial crack locations were at the flange centerline at the toe of the weld and under

the coping. In a few cases small cracks at the weld toes at the edges of the flange were notices but these cracks did not grow significantly. In all cases crack propagation occurred first through the thickness of the flange resulting in a single through-crack symmetrically located with respect to the flange centerline. The through-thickness growth took place from both sides of the flange, i.e., from the side of the weld toe and the side of the coping. Once the two cracks joined, the single through-crack propagated across the width of the flange until fracture occurred.

The initial surface crack at the weld toe was usually in the order of 0.8 in. long but very shallow in depth. Only the center portion (approximately 1/2 in.) of the surface crack propagated through the flange depth until it joined with the crack initiating from the coping. The through-thickness crack growth did not cause a measurable deterioration in resistance which indicates that the reduction in area was small and was compensated by a redistribution of strains. However, once a through-crack was formed and the crack propagated across the width of the flange, deterioration of resistance was evident from the load--deformation diagrams (see load deterioration curves presented in Section 5.5.2.1). Nevertheless, for this relatively thin flange (b/t = 18.9), crack growth across the width of the flange was stable for several cycles and fracture occurred only when the crack propagated across approximately half the flange width. The significance of this observation cannot be evaluated since the resistance at the stage of fracture had deteriorated to 60 to 70 percent of the undamaged resistance and a large portion of this deterioration was caused by the local buckling phenomenon. In fact, the strength deterioration caused by local buckling made it impossible to draw quantitative conclusions from the crack growth information.

In all but two cyclically loaded specimens major crack propagation and fracture occurred at the weld in the "top" flange (in horizontal beam configuration). In specimen B2-8, fracture occurred at the "bottom" flange, probably because the weld in the top flange had a small reinforcement angle and the weld toe was smoother than in the other specimens. Figure 5.40 shows the crack growth for the last three cycles for

this specimen. In specimen B2-6, fracture did not take place at the weld but at the buckle in the top flange.

5.5.1.4 Behavior under Variable Amplitude Cycling

As was discussed in Section 5.4.1.4, the deflection history for the variable amplitude tests represents the response of a single degree of freedom system to a realistic earthquake ground motion. For specimen B2-9, the response was scaled so that the maximum deflection range (points 11 to 20 in Fig. 5.19) is 2.08 in. which corresponds to a plastic rotation range of 0.038 rad. This history was applied six times to the test specimen.

Flange buckling was noticed at the "bottom" flange in excursion 10-11 of the first block. Buckle sizes increased at a moderate rate from one block to the next until the end of block 3. From block 4 on, the rate of buckle growth decreased due to the stabilization in buckle shape. Figure 5.41 shows the buckle shape at load point 20 in the first block and at the corresponding load points in the next three blocks.

At the end of the third block, cracks with opening of about 0.05 in. and length of about 1 in. existed at the weld toes in both flanges. At the end of the sixth block, both cracks were about 3 in. long, but there was no unstable crack growth or sudden fracture at this point where the test was stopped.

The strength response of specimen B2-9 for the first three blocks is presented in Table 5.8. It was during these blocks that major deterioration in strength occurred due to flange buckling. In subsequent blocks the rate of deterioration decreased until the 5th block when a through-crack was formed and propagated across the flange and caused substantial deterioration in load carrying capacity of the specimen.

Figure 5.42 compares the load-deflection response of the first and third blocks. Although the hysteresis loops in the third block are quite similar to those of the first block, a careful comparison reveals that strength and stiffness have deteriorated by about ten percent or more.

5.5.2 Interpretation of Test Results

5.5.2.1 Strength Deterioration

As a measure of strength deterioration, the ratio P/P_u was evaluated for each reversal where

P = measured peak load

P_u = "undeteriorated" peak load, i.e., the load which the specimen could have sustained, at a given displacement amplitude, if no deterioration would have taken place.

As was discussed previously, P_u depends on the displacement amplitude and on the amount of hardening that has taken place during the previous reversals. Thus, P_u will increase from reversal to reversal until stabilization of the cyclic response is attained. Hardening rules of the type discussed in Chapter 4 were used to obtain realistic values for P_u. In order to account for inaccuracies in the mathematical model and for variations in the stress-strain response, the predicted monotonic P_u-δ relationship was matched with the measured behavior in the region in which the test specimens did not suffer damage (see Section 5.5.1.1).

This procedure can be applied directly to the tests with constant and symmetric displacement amplitudes. In specimen B2-10 the displacement history had a constant mean value and correspondingly a mean load. To account for mean stress relaxation, this mean load was relaxed at a rate of 5% per reversal.

Figure 5.43 presents plots of P/P_u versus the number of reversals, 2N, (N = number of cycles) for different specimens. As can be seen from these plots, the rate of strength deterioration in two consecutive reversals differs for the first one or two cycles, especially in specimens with higher deflection amplitudes. In these cycles, the deterioration during an even-numbered reversal is generally much higher than the deterioration during the preceding odd-numbered reversal. This phenomenon, which is in agreement with the differences in buckle sizes at odd and even-numbered reversals (Fig. 5.37), is attributed to cyclic plasticity effects. In the first excursion, the tension flange is strained in the plastic range, and under load reversal this flange undergoes large plastic straining and Bauschinger effect which will accentuate the local buckling process.

Except for these differences in the first few deterioration causing reversals, the deterioration rates for even and odd numbered reversals are very similar and follow a consistent pattern. In sequence, the following four ranges can be identified: a short range of deterioration threshold in which flange buckling has not occurred or is insignificant, and three deterioration ranges. In the first deterioration range, deterioration proceeds at a high rate which is associated with the continuous growth of the flange buckles (Fig. 5.37). In the second range, deterioration proceeds at a slow and almost constant rate due to the stabilization in buckle size. These two ranges are followed by a range of rapid deterioration which is caused solely by crack propagation at the welds or buckles. Although small cracks formed early in the history, these cracks had no noticeable effect on strength until they grew through the thickness of the flange and propagated across the flange. Table 5.6 lists the number of reversals to through-crack and to fracture for each specimen.

With a reasonable degree of accuracy the first and second deterioration range for each specimen can be represented by two straight lines as shown in Fig. 5.43. The observed start of crack propagation across the flange coincides with the reversal in which the data points for one or both flanges deviate from the second line.

In the constant amplitude test with a mean deflection (specimen B2-10), a high rate of strength deterioration is noticed at the beginning due to the large first excursion, but after the first three reversals the data points show approximately the same slope as the fitted line in the first deterioration range of specimen B2-5 (Fig. 5.43b). The latter specimen has the same deflection amplitude as B2-10 but with zero mean. The slope of the second deterioration line (in the stabilization stage) for B2-5 is slightly higher than the corresponding line for B2-10. The pilot test performed on specimen B2-10 indicates that mean deformations do have an effect on deterioration but that this effect diminishes under repeated cycling. Under random cycling, this effect is not believed to be substantial unless the deformation histories are very unsymmetrical and are dominated by a few large inelastic excursions with large mean values. In the deterioration models

discussed in Section 5.5.3 the mean deformation effects are not considered.

5.5.2.2 Stiffness Deterioration

Figure 5.44 shows plots of K/K_u, where K_u is the initial elastic loading stiffness (undeteriorated stiffness) and K is the measured unloading stiffness at odd-numbered reversals. Similar trends are exhibited by the data points recorded at the even-numbered reversals. Like in the strength deterioration plots, four ranges can be distinguished here, a short range of deterioration threshold, and three deterioration ranges. Again, two lines (stiffness deterioration lines) can be fitted to the data points of all specimens in the first and second deterioration range as shown in Fig. 5.44a to d. The first line, which has a higher slope, is valid for the rapid deterioration stage and the second line with a smaller slope approximates the data points in the range of stabilization. The points deviate from this second line after the start of crack propagation across the flange.

For specimen B2-10 (Fig. 5.44c), similar to the strength deterioration plot, there is initially a large drop in stiffness due to the first large excursion, but after the first three reversals the data points have the slope of the stiffness deterioration lines for specimen B2-5 (Fig. 5.44b).

5.5.2.3 Hysteresis Energy Deterioration

In order to evaluate the cyclic energy deterioration, the undeteriorated values of the hysteresis energy for each excursion (area enclosed by the load-deflection curve and the deflection axis) had to be calculated. The mathematical description of the undeteriorated load-deflection curve was based on a Ramberg-Osgood type expression in the form of

$$\delta = \frac{P}{K} + \frac{\alpha}{K(2P_y)^{r'-1}} P^{r'} \qquad (5.9)$$

where

δ = deflection

P = load

K = elastic stiffness

P_y, α, r' = model parameters

The model parameters α and r' were obtained from curve fitting. The cyclic exponent r' changes from excursion to excursion to reflect the effect of cyclic hardening. The undeteriorated values of hysteresis energy were obtained by integrating the expression for the hysteresis curve given by Eq. (5.9). Reference 72 presents details of this procedure.

Hysteresis energy deterioration plots are presented in Fig. 5.45. The plots exhibit the same general pattern as the strength and stiffness deterioration plots (Figs. 5.43 and 5.44). However, the third deterioration range (high rate of deterioration due to crack propagation) is shorter for the energy deterioration since a deviation of the data points from the second detrioration line does not happen until the last one or two cycles when substantial drops in strength and stiffness lead to an increased reduction in the hysteresis loop areas.

For specimen B2-10 the effect of mean deflection is limited to the first two excursions, i.e., deterioration starts earlier than for specimen B2-5 which has a history with the same deflection amplitude but with zero mean. The slope of the first deterioration line is the same for both specimens (see Fig. 5.45a and e) but the slope of the second line is somewhat less for B2-5 than for B2-10.

5.5.3 Damage Modeling for Local Buckling

The nonlinear deterioration pattern of the constant amplitude tests discussed in the previous sections indicates that a single cumulative damage model cannot be developed for the full range of interest. It appears to be feasible, however, to use a series of damage models which describe individually the different ranges, i.e., the deterioration threshold range and the deterioration ranges.

Based on the experimental data it can be justified to represent the deterioration behavior for constant amplitude cycling by a piecewise linear diagram as shown in Fig. 5.46. Thus, no deterioration will occur for the first N_o cycles, then deterioration takes place at a constant rate Δd^I for N_1 cycles, followed by deterioration at a constant but smaller rate Δd^{II} for N_2 cycles, and followed by rapid deterioration due to crack propagation across the flange (range III).

In this section, empirical models for the deterioration in ranges I and II are discussed. No attempts are made to model deterioration in range III because this range is associated with rapid deterioration and is not considered to be part of the useful life of the specimens.

The length of the deterioration threshold range for the local buckling mode is a function of the b/t ratio of the beam flange and the yield strength of the material. For the specimens tested in this study, the threshold range was too small to permit the development of a damage model from the experimental data. It is conceivable, but not verified in this study, that for constant amplitude cycling the number of reversals to deterioration initiation, $2N_o$, can be obtained from a Coffin-Manson relationship, i.e.,

$$2N_o = C_o^{-1}((\Delta\theta_p)^{-c_o} \qquad (5.10)$$

This simple model was used to identify the reversal at which deterioration commences. For the test specimens the exponent c_o was taken as 1.0 and the coefficient C_o was taken as 25.6 which corresponds to the observed start of deterioration under monotonic loading (N_o = 0.5) at a plastic hinge rotation of 0.039 rad. This choice is judgmental but of little effect on life predictions because of the very short deterioration threshold life of the test specimens.

In order to formulate damage models, a definition of failure must be associated with the models. In this study, failure is defined as the attainment of an acceptable limit deterioration. Figure 5.46 shows that a multilinear damage pattern exists already for constant amplitude cycling. In order to simplify the mathematical modeling, it is assumed that only the deterioration threshold and the first deterioration range need to be considered in damage modeling. This assumption will result in

conservative life predictions and may be realistic in many cases because for large plastic hinge rotations the limit of acceptable deterioration will likely be less than the crossover deterioration x_1.

5.5.3.1 Deterioration Rate Models

The slopes of the first and second deterioration lines in Figs. 5.43, 5.44 and 5.45 are a measure of the rate of decrease in strength, stiffness and hysteresis energy per reversal in the first and second deterioration range. If these slopes are plotted versus the plastic rotation ranges $\Delta\theta_p$ on logarithmic scales, using all specimens with constant deflection amplitudes, both of the two sets of data points show a linear trend (Fig. 5.47). The lines fitted to these sets of data have the general mathematical form of

$$\Delta d = A(\Delta\theta_p)^a \qquad (5.11)$$

where A and a are parameters that depend on the properties of the structural component, and Δd is the deterioration in strength, stiffness or hysteresis energy per reversal. The linear correlation for the data points in the first deterioration range is quite good whereas a large scatter is evident in the second deterioration range.

The small sample set of data did not permit a statistical evaluation of uncertainties in the model parameters A and a, but it can be seen from Fig. 5.47 that in the first deterioration range the data points are scattered in a narrow band around the regression lines (solid lines), whether strength, stiffness or hysteresis energy deterioration is considered. It should be acceptable to lump all modeling uncertainties in the coefficient A which would simplify the probabilistic modeling of the deterioration behavior.

In order to convert the deterioration rate model into a damage model, let us denote with "x" the limit of acceptable deterioration that constitutes failure. If only the first deterioration range is considered, then the deterioration for constant amplitude cycling occurs at a constant rate from zero to x. The number of reversals spent in the deterioration range is then given by

$$2N_1 = \frac{x}{\Delta d} = xA^{-1} \left(\Delta\theta_p\right)^{-a} \tag{5.12}$$

which is again a relationship of the Coffin-Manson type. The number of reversals to failure (i.e., to deterioration x) is the sum of the reversals spent in the deterioration threshold range [given by Eq. (5.10)] and in the deterioration range, i.e.,

$$2N_f = 2N_o + 2N_1 = C_o^{-1}\left(\Delta\theta_p\right)^{-c_o} + xA^{-1} \left(\Delta\theta_p\right)^{-a} \tag{5.13}$$

This equation describes the useful life of the test specimens subjected to constant amplitude cycling, using a linear combination of the two Coffin-Manson models.

5.5.3.2 Deterioration and Damage Models for Variable Amplitude Cycling

The existence of a deterioration threshold range in addition to a deterioration range complicates considerably the damage modeling for variable amplitude cycling. In essence, every loading history must be resolved into two components in the time domain, a first component that exhausts the deterioration threshold range followed by a second component that causes deterioration. Assuming that this resolution can be accomplished, the number of reversals, $2N_o$, spent in the deterioration threshold range can be obtained by setting the cumulative damage of the deterioration threshold model equal to one, i.e.,

$$D_o = C_o \sum_{i=1}^{2N_o} \left(\Delta\theta_{pi}\right)^{c_o} = 1 \tag{5.14}$$

This formulation presumes linear damage accumulation for the model given by Eq. (5.10).

Every reversal following the first $2N_o$ reversals will then cause deterioration. If we assume that the deterioration rate model given by Eq. (5.11) is valid for variable amplitude cycling, the deterioration after a total of 2N reversals can be obtained as

$$d = \sum_{i=2N_o+1}^{2N} \Delta d_i = A \sum_{i=2N_o+1}^{2N} \left(\Delta\theta_{pi}\right)^{a} \tag{5.15}$$

This deterioration model can be converted into a standard low-cycle fatigue damage model by using Eq. (5.12) and assuming linear damage accumulation, i.e.,

$$D = x^{-1} A \sum_{i=2N_o+1}^{2N} (\Delta\theta_{pi})^a \qquad (5.16)$$

where a damage value of one corresponds to attainment of the limit value of acceptable damage, x.

In the formulation presented here, sequence effects and mean deformation effects are neglected.

Considering the physical phenomenon of buckle formation and incomplete recovery under load reversal, it appears to be appropriate to consider small excursions as interruptions of larger excursions. Thus, it is recommended to apply a cycle counting method (e.g., rain-flow method) to identify the individual excursions, rather than to use the excursions as they appear in the time history response.

In order to examine the adequacy of the proposed models, the results of the variable amplitude test (sepcimen B2-9) are used to compare actual deterioration with predictions. The deflection history of specimen B2-9 was reduced to a set of deflection ranges using the rain-flow cycle counting method. These deflection ranges were converted into plastic rotation ranges needed for mathematical modeling. Equation (5.14) was used to determine the start of deterioration and Eq. (5.15) was used to predict the deterioration in strength (peak loads). Table 5.9 lists the predicted deterioration for the first 3 blocks of the deflection history. Deterioration starts in excursion 8-9 and continues as shown in the table. The corresponding excursions in the three blocks do not have the same plastic rotation ranges due to the deterioration in resistance as loading continues. This causes some nonlinearity in total deterioration from one block to another.

Figure 5.48 compares the actual peak load deterioration from the variable amplitude test with the predicted deterioration. The experimental data points show a deterioration threshold and a range of almost linear deterioration extending over more than two blocks. This gives some credence to the hypothesis of linear damage accumulation for range

I. Close to the end of block three the rate of deterioration decreases, indicating that a portion of this block is spent in deterioration range II. The predicted deterioration is somewhat larger than the experimental one when only deterioration in range I is considered (solid line). The differences between experimental and predicted deterioration become small when the crossover into range II is considered (dashed line). For practical purposes, the prediction based on range I deterioration should be adequate.

Returning to Eqs. (5.14) and (5.16), it must be pointed out that the proposed separation into a deterioration threshold model and a deterioration model is difficult to apply in practical problems. The employment of the two models necessitates a separation of the time history response in order to isolate $2N_o$ and makes it impossible to apply consistently a cycle counting method which is independent of the time sequence of excursions.

To circumvent this problem, one could combine the two low-cycle fatigue models as was done in Eq. (5.13) in which the number of reversals to failure for constant ampitude cycling was identified. Applying Miner's rule to Eq. (5.13) the total damage for variable amplitude cycling could be expressed as

$$D = \sum_{i=1}^{2N} \frac{1}{2N_{fi}} = \sum_{i=1}^{2N} \frac{1}{C_o^{-1}(\Delta\theta_{pi})^{-c_o} + xA^{-1}(\Delta\theta_{pi})^{-a}} \qquad (5.17)$$

Clearly, this damage formulation is conceptually not correct because it is impossible to assign a single damage rate to the deterioration threshold range and the deterioration range. In this formulation the deterioration threshold is ignored and deterioration is assumed to commence at the first excursion but occurs at a rate $\Delta d'$ which is smaller than Δd^I, see Fig. 5.49.

Despite these evident inconsistencies, the formulation proposed in Eq. (5.17) may be useful because it permits an approximate damage assessment without consideration of the time sequence of excursions. The

damage assessment may even be rather accurate if one of the two ranges is small compared to the other.

5.5.4 Conclusions

In the local buckling mode of failure under cyclic loading, deterioration in strength, stiffness, and hysteresis energy occurs after a period of deterioration threshold. Three different ranges with almost constant deterioration rates can be distinguished in the deterioration stage. In the first range deterioration occurs at a relatively high rate which is associated with a rapid increase in flange buckle size. In the second range, there is a decrease in deterioration rate which is due to the stabilization in buckle shape. In the third range, the strength, stiffness, and hysteresis energy deteriorate rapidly as a result of advanced stages of crack propagation at weldments or buckles.

The rate of deterioration in the first deterioration range can be described rather accurately by a power function. For constant amplitude cycling, a Coffin-Manson model can be used to relate the number of excursions spent in the first deterioration range to an acceptable limit of deterioration. As far as the beneficial life of the member is concerned, it should be sufficiently accurate to consider only the deterioration threshold range and the first deterioration range and to express the period spent in each range by a Coffin-Manson model.

For variable ampitude cycling a series of linear models can be used to predict deterioration threshold and deterioration. The amount of deterioration can be predicted by first exhausting the damage model used for deterioration threshold and then using a linear cumulative deterioration model for the deterioration range. Life prediction can be based on two independent damage functions which individually describe the deterioration threshold range and the deterioration range. Alternatively, an approximate damage assessment may be achieved by means of a single damage function which linearizes the damage per reversal in the combined threshold and deterioration rane.

Although sequence effects and mean deformation effects have been neglected in the damage models, the deterioration observed in a variable amplitude test could be predicted with adequate accuracy. A pilot test

has shown that a large mean deformation accelerates deterioration for one or two reversals but that the effect of mean deformation diminishes thereafter.

As in the B1 specimens, the parameters needed for damage modeling and performance assessment can be obtained from a series of constant amplitude tests. Because of the nonlinearity in the deterioration behavior of local buckling, four parameters need to be determined, two for the deterioration threshold range and two for the deterioration range. These parameters depend primarily on the b/t ratio of the flanges and the yield strength of the material. This dependence on only two variables should make it possible to obtain comprehensive information on the local buckling mode of deterioration from a limited and affordable testing program.

CHAPTER 6

SEISMIC RESPONSE PARAMETERS FOR BILINEAR SINGLE DEGREE OF FREEDOM SYSTEMS

6.1 INTRODUCTION

The experimental study discussed in Chapter 5 has demonstrated that for specific failure modes simple cumulative damage models can be used to describe component performance. The damage models contain structural performance parameters (C and c, or A and a) as well as seismic response parameters (N and $\Delta\delta_p$ or $\Delta\theta_p$ or $\Delta\varepsilon_p$). For a performance assessment under seismic excitations, N will be the number of damaging cycles and $\Delta\delta_p$ (or $\Delta\theta_p$ or $\Delta\varepsilon_p$) will be the plastic deformation range of the individual cycles.

The purpose of this chapter is to discuss a methodology that can be used for an evaluation of the seismic response parameters N and $\Delta\delta_p$. The information derived from this study can be used for damage evaluation and provides a first step towards the solution of the general reliability problem expressed by Eq. (3.10) in Chapter 3 and repeated here:

$$P_f = P[D > \gamma] = P\left[C \sum_{i=1}^{N} (\Delta\delta_{pi})^c > \gamma\right] \tag{6.1}$$

It is by no means a simple task to obtain statistically acceptable data on all the random variables contained in Eq. (6.1) and to provide a solution process for this equation. The latter is not even attempted here since the objective of this study is directed towards experimentation. From this viewpoint, the following questions are addressed in this chapter.

1. How can one develop statistically representative information on the seismic response parameters of interest for damage modeling and performance assessment.

2. Does the information generated here justify the adoption of the testing procedures recommended in this report? In other words, is there a need to determine the structural damage parameters through the multi-specimen

testing program discussed in Chapter 5 and summarized in Chapter 7.

3. How can one develop loading histories for component testing that are statistically representative of the effects of severe earthquakes (see Chapter 7).

The study discussed in this chapter is only exploratory because it is based on the assumptions that structural systems can be represented by bilinear single degree of freedom systems and that the plastic deformation ranges of structural components can be deduced from the seismic response of the single degree of freedom systems.

Clearly, these assumptions must be justified and methods must be developed that permit a correlation between the plastic deformation ranges of individual components and the response parameters of single degree of freedom systems. A study on this topic is in progress and will be reported at a later date.

Even with the aforementioned assumptions, the determination of statistical seismic response parameters is a formidable task. There are three types of variables that need to be considered, the elastic natural period of the SDOF systems, the structural characteristics of the SDOF systems, and the characteristics of the seismic ground motions. Thus, a complete study should provide response parameters for the three-dimensional matrix shown in Fig. 6.1, utilizing a statistically acceptable subset of ground motions for each row of ground motion characteristics.

The individual rows of ground motion characteristics could be magnitude, source-site distance, and site soil condition, with due consideration given in each case to the effect of strong motion duration. The individual rows of structural systems characteristics could be yield level, strain hardening ratio (ratio of strain hardening stiffness to elastic stiffness), and viscous damping, with due consideration given to stiffness degradation (e.g., Clough's model) and P-δ effect.

In the exploratory study discussed here, only systems with an elastic natural period of 0.5 sec. and 5% viscous damping are considered. Yield level and strain hardening ratio of the bilinear SDOF systems are varied as discussed in Section 6.3. An ensemble of six

recorded ground motions is used to represent the seismic input, covering a wide range of ground motion characteristics and strong motion durations. The selection of the ground motions and the scaling to a common severity level are discussed in Section 6.2

Each structural system is subjected to each earthquake record and the time history response is evaluated. The data from the time history responses are used to develop information on the following aspects:

1. Probabilistic distribution of plastic deformation range $\Delta\delta_p$.
2. Number of inelastic excursions or half cycles, N'.
3. Statistics of the maximum plastic deformation range $(\Delta\delta_p)_{max}$.
4. Statistics of the mean value of plastic deformations with respect to the original configuration, $\delta_{p,mean}$.
5. Statistics of the maximum ductility ratio $\mu = \delta_{max}/\delta_y$.
6. Accumulated hysteretic energy and total dissipated energy (hysteretic energy plus viscous damping energy).

The term δ is used here generically to identify a deformation quantity. For a bilinear SDOF system it refers to the deflection of the system. For the plastic deformation (deflection) range of bilinear systems, two definitions ($\Delta\delta_p'$ and $\Delta\delta_p''$) are used in this chapter. These two definitions, designated as engineering and material science definitions, are illustrated in Fig. 6.2. The two definitions are related by $\Delta\delta_p'' = \Delta\delta_p' (1-\alpha)$ where α is the strain hardening ratio.

It is important to note that the plastic deformation ranges in this study are not taken directly from the time history response but are obtained by applying the rain-flow cycle counting method to the time history response. This decision is based on available information on low-cycle fatigue damage studies and on the experience gained from the study discussed in Chapter 5. It is generally acknowledged (although not proven in many cases) that more realistic damage assessments are obtained for low-cycle fatigue problems if smaller excursions are treated as interruptions of larger excursions rather than taking each

excursion as it occurs in the time domain (see Section 3.2.1). The rain-flow method orders excursions in an appropriate manner and results also in the largest possible number of closed cycles.

Nevertheless, since also the rain-flow methods results not only in closed cycles but also individual excursions without a counterpart, a counting of cycles becomes somewhat ambiguous. Thus, in this chapter the number of excursions, N', is counted rather than the number of cycles, N. For damage evaluation the relationship N=N'/2 should be sufficiently accurate. It should be noted also that only inelastic excursions are counted since elastic excursions are not believed to contribute much to damage accumulation.

The following sections discuss the systems and ground motions used in this exploratory study and present a summary of the results. A more detailed discussion of this study is presented in Ref. 108.

6.2 DESCRIPTION OF GROUND MOTIONS

6.2.1 Selection of Ground Motions

Six horizontal components of California strong motion records from five different events are selected in this study to cover a realistic range of duration, site conditions, distance and magnitude. No attempt is made to group records according to similar characteristics. Only such records are selected whose acceleration spectrum resembles that of the ACT-3 (109) ground motion spectrum for the proper site condition, because the ATC-3 base shear equation is used to define the yield levels of the selected systems (see Section 6.3). This choice makes it possible to use the ACT-3 spectra for scaling of the ground motions to a common severity level. This scaling is discussed in detail in Section 6.2.2.

Table 6.1 gives summary informtion on the selected records. The corrected values for ground accelerations published by the California Institute of Technology Earthquake Engineering Research Laboratory (110) are used to describe the records. Pertinent characteristics of the records, with regard to structural behavior, are listed in Table 6.2.

The near-field/far-field categorization is based on the tabulation presented by Krinitzsky and Chang (111). The soil profile types are in

accordance with the ATC-3 soil profile classifications and are obtained either from the study done by Seed, Ugas and Lysmer (112) or from a consideration of similarity between the acceleration spectrum of the record and the ATC-3 ground motion spectrum for a specific soil profile. The parameter I_o represents the intensity of a record in a quantitative way and is defined as:

$$I_o = \int_o^{T_o} a^2(t)dt \tag{6.2}$$

where T_o is the total duration of the record and a(t) is the ground acceleration at time t.

The strong motion durations D_{sm} are those suggested by McCann-Shah (113) except in two cases. For records A001 component S00E and V315 component West the Vanmarcke-Lai (114) values of duration are used because McCann-Shah list no duration for the latter record and recommend a surprisingly large duration for the former record. The Vanmarcke-Lai definition is used for these records because of the close similarity it offers in concept to McCann-Shah definition. A short time span is added to both ends of the strong motion duration in order to initiate vibrations at the beginning and account for possible inelastic excursions at the end of the strong motion segment.

The parameter I_{sm} is defined in the same manner as I_o except that I_{sm} is calculated for only the strong motion portion of the record. This parameter is an indicator for the total energy imparted to the system by the strong ground shaking. The root mean square acceleration, RMSA, in Table 6.2 is calculated from the following expression:

$$RMSA = \left[\frac{1}{D_{sm}} \int_o^{D_{sm}} a^2(t)dt\right]^{1/2} \tag{6.3}$$

I_{sm} is related to RMSA through the following equation:

$$I_{sm} = (RMSA)^2 D_{sm} \tag{6.4}$$

The values of I_{sm} in Table 6.2 are calculated from this equation.

Also listed in Table 6.2 are the values of the aforementioned parameters for the scaled records. Notice that the values of scaled RMSA are

very similar for all the records. This implies that the scaled records contain comparable amplitudes (on the average).

6.2.2 Scaling of Ground Motions

In this study, it is decided to use the statistically obtained and smoothened ATC-3 ground motion spectra as the basis for scaling of the ground motion records to a common severity level. The spectra used for this purpose are the ATC-3 ground motion spectra for highly seismic regions (effective peak ground acceleration of 0.4g, $A_v = A_a = 0.4$) and proper site conditions. These spectra for the two types of soil profiles of interest in this study are shown in Fig. 6.3.

The acceleration values of each ground motion record are scaled by a factor that permits close matching of the elastic acceleration spectrum of the record with the proper ATC-3 ground motion spectrum over the period range of interest. The reason for not using peak ground acceleration, PGA, as the basis for scaling is because recent studies, such as Vanmarcke (115), have indicated that scaling of accelerograms based on peak acceleration alone introduces systematic errors that are due to indirect correlation between the PGA and other ground motion parameters such as duration and predominant frequency. Because the ATC-3 ground motion spectrum provides a link between the ground motion and the structural system, it is felt that the procedure employed in this work is well suited for scaling the ground motion records to a common severity level.

Figure 6.4 shows two examples of scaled response spectra for two records based on the procedure used in this study (solid lines), as well as the scaled spectra based on a scaled PGA of 0.4g (dashed lines). Although the individual matched spectra show significant deviations from the ATC-3 spectra in several period ranges, in average the matching was adequate. Figure 6.5 shows spectra obtained by averaging the spectral accelerations for all four scaled records with soil profile type 1 (Fig. 6.5a) and for the two scaled records with soil profile type 2 (Fig. 6.5b). Also displayed are the corresponding ATC-3 ground motion spectra. From the figures it can be concluded that on the average the scaled response spectra of the selected records match the ATC-3 spectra rather well especially for records having type 1 soil profile.

In order to examine how well all six selected records on the average resemble the ground motion represented by the ATC-3 spectra, for each record the scaled spectral accelerations for discrete periods are divided by the corresponding ATC-3 spectral values, $(S_{a,scaled}/S_{a,ATC-3})$, and the average values (for all six records) of this ratio are computed. A plot of this ratio for the period range of interest (0.2 to 2.0 seconds) is presented in Fig. 6.6. The largest value of this ratio is 1.173 (at 0.7 seconds) while the smallest value is 0.817 (at 1.8 seconds). At the period of 0.5 seconds, which is the period of the systems used in this study, the ratio is 1.11.

6.3 DESCRIPTION OF STRUCTURAL SYSTEMS

In this research, structures are represented as single degree of freedom, SDOF, viscously damped oscillators with bilinear (hardening) restoring force characteristics. A typical bilinear SDOF system is shown in Fig. 6.7. Such a system is defined by an elastic stiffness K, a strain hardening ratio α, a yield resistance F_y, a viscous damping constant C_d and a mass M.

The elastic stiffness K and mass M of each system are selected so that the elastic natural period $T = 2\pi(M/K)^{1/2}$ takes on the desired value of 0.5 seconds. The strain hardening ratio α is defined as the ratio of post-elastic to elastic stiffness. The selected values for α are 0.0 (elastic-plastic), 0.1, 0.3, 0.5 and 1.0 (elastic).

The selection of the yield level F_y is tied in with the elastic response of the system and the ATC-3 design philosophy. In the ATC-3 approach, described in more detail in Ref. 109, the smoothened and soil profile dependent ground motion spectra are modified somewhat and the modified spectral values are divided by a factor R to arrive at a seismic design coefficient C_s. Multiplication of the coefficient C_s with the seismically effective weight W gives the design base shear requirement which for single degree of freedom systems is equal to the required yield resistance F_y, i.e.:

$$F_y = C_s W \tag{6.5a}$$

For the soil types of interest in this study, C_s is defined as

$$C_s = \frac{1.2\ A_v S}{RT^{2/3}} \leq \frac{2.5\ A_a}{R} \qquad (6.5b)$$

where

S = coefficient for soil profile characteristics of the site

A_v = coefficient representing effective peak velocity related acceleration

A_a = coefficient representing the effective peak acceleration

R = response modification factor

T = fundamental period of the structural system.

For an effective peak ground acceleration of 0.4g ($A_a = 0.4$), which is used here to scale all records to the same severity level (see Section 6.2.2), the coefficient C_s is given by (A_v is normally equal to A_a for regions of high seismicity):

$$C_s = \frac{0.48\ S}{RT^{2/3}} \leq \frac{1}{R} \qquad (6.6)$$

The value of S for soil profile types 1 and 2, which are encountered in this work, is 1.0 and 1.2, respectively. Soil profile type 1 is a profile with rock of any characteristic, either shale-like or crystalline in nature. Such material may be characterized by a shear wave velocity greater than 2500 feet per second. Also included in type 1 are sites with stiff soil conditions where the soil depth is less than 200 feet and the soil types overlying rock are stable deposits of sands, gravels, or stiff clays. Soil profile type 2 is a profile with deep cohesionless or stiff clay conditions, including sites where the soil depth exceeds 200 feet and the soil types overlying rock are stable deposits of sands, gravels, or stiff clays.

If R is taken equal to unity in Eq. (6.6), the value C_sW can be viewed as a judgmental estimate of the strength demand for an elastic system. Thus, the factor R is employed to reduce the elastic strength

demand for systems which can undergo inelastic deformations. Values of R equal to 4 and 8 are selected here to incorporate a wide range of framing systems as well as to determine the effect of different yield levels on response parameters. For a period of 0.5 seconds, the normalized yield levels, $C_s = F_y/W$, for R equal to 4 and 8 are 0.19 and 0.095 for soil type 1, and 0.228 and 0.114 for soil type 2, respectively. These yield levels are used throughout this study and are identified in the subsequent sections by the appropriate R value.

The employment of the ATC-3 formulation [Eq. (6.6)] and of ATC-3 type R values for the purpose of defining yield levels provides a link with an existing design methodology. However, the R values are not consistent indicators of the reduction in the elastic force demands for the selected set of ground motions. Multiplication of the normalized yield levels C_s with Rg will not necessarily result in the acceleration values of the ATC-3 ground motion spectra and will rarely ever result in the proper values of the acceleration response spectra of the selected and scaled ground motions. There are two reasons for these discrepancies. Firstly, in the ATC-3 approach there are differences between the lateral design acceleration (C_s for R = 1 multiplied by gravity acceleration g) and the acceleration values of the ground motion spectra. These differences, as illustrated in Fig. 6.8 for soil profile types 1 and 2, are based on judgmental considerations which provide for a more conservative force demand for long period structures. Secondly, there are differences between the ATC-3 ground motion spectra and the response spectra of the selected and scaled ground motions (see Fig. 6.4).

In order to relate the selected yield levels to the ATC-3 ground motion spectra and to the elastic response spectra of the scaled ground motions, two additional parameters, R' and R", are employed. The parameter R' identifies the ratio of the ATC-3 ground motion spectral acceleration to the normalized yield level times g. The parameter R" identifies the ratio of the acceleration response spectral value of a scaled ground motion to the normalized yield level times g. Values of R' and R" are listed in Table 6.3 for the six records used in this study and a period of 0.5 seconds.

In the interpretation of the results presented in Section 6.6, the discrepancies between R, R' and R" should be considered. In effect, R" is the true ratio of elastic force demand to yield resistance for the systems and ground motions utilized in this study. However, because of the period shifts in the inelastic response and the highly irregular shapes of the elastic response spectra (particularly in the vicinity of T = 0.5 seconds), there is no reason to emphasize the importance of an exact strength reduction factor.

For all systems investigated in this study, a damping of 5 percent of critical damping is assumed. This choice is made because the ATC-3 ground motion spectra are based on 5 percent damping. No attempts are made here to investigate the effects of different damping ratios on the structural response parameters.

6.4 RESPONSE COMPUTATION AND DATA ACQUISITION

Since the inelastic force--deformation response of structures or their components is history dependent, implementation of a classical random vibration approach becomes quite difficult. Although equivalent linearization techniques, ELTs, make a random vibration approach possible (116,117) the validity of these techniques for highly nonlinear systems is still in question. Also, the equivalent linearization technique does not provide information on mean deformations (drifting of the response), evaluates deformation amplitudes rather than deformation ranges and does not permit the utilization of the rain-flow cycle counting method for reordering the plastic deformation ranges. Thus, conventional step-by-step time history analysis is employed in this study since this method provides information on all parameters of interest for damage evaluation and performance assessment.

The linear acceleration method is applied to solve the equation of motion for the SDOF viscously damped system. In addition to the force-deformation response, energy terms are evaluated from the following equations:

Damping Energy: $DE_i = DE_{i-1} + \frac{1}{2} C_d (\dot{\delta}_{i-1}^2 + \dot{\delta}_i^2) \Delta t$

Kinetic Energy: $KE = \frac{1}{2} M \dot{\delta}_a^2$

Input Energy: $IE_i = IE_{i-1} + \frac{1}{2} [\dot{\delta}_{g,i-1}(F_{i-1} + C_d \dot{\delta}_{i-1}) + \dot{\delta}_{g,i}(F_i + C_d \dot{\delta}_i)] \Delta t$

where

$\dot{\delta}$ = relative velocity

$\dot{\delta}_g$ = ground velocity

$\dot{\delta}_a$ = absolute velocity = $\dot{\delta} + \dot{\delta}_g$

The hysteretic energy, HE, is calculated from direct step-by-step integration of the area under the force-deformation curve and the recoverable strain energy, RSE, is calculated as $F\delta/2$. These calculations are carried out with the deformation axis as the reference line. The input energy is related to the other energy terms by the equation

$$IE = DE + KE + HE + RSE.$$

For each system, the time history data of deformation and energy terms are stored on tape and reduced in a form suitable for interpretation. In the first reduction process, data are presented graphically in the form of time history plots and cumulative frequency plots of deformation parameters. The purpose of these graphical representations is a visual inspection of patterns and trends in response behavior. These trends are discussed in the next section. In the second reduction process, the data are evaluated numerically and also statistically whenever possible. The results of the second reduction process are discussed in Section 6.6.

In the first reduction process the inelastic excursions (half cycles) are divided into two categories. Those with increasing deformations from beginning to end are designated as "increasing" half cycles, and those with decreasing deformations are designated as "decreasing" half cycles. The following plots are prepared and inspected for each system and each seismic event:

1. Time history of response deformation normalized with respect to yield deformation, δ/δ_y.

2. Time history of energy terms normalized with respect to elastic strain energy $0.5F_y\delta_y$.

3. Cumulative frequency polygon of normalized response deformations, δ/δ_y. This polygon is developed by applying the so called probability analyzer (118) to the time history of δ/δ_y.

4. Ordered and normalized plastic deformation ranges, $\Delta\delta_p/\delta_y$, for increasing and decreasing excursions (half cycles) for each event. The data are presented in form of the one minus cumulative frequency polygon of $\Delta\delta_p/\delta_y$, with the observed values ordered in magnitude, starting with the largest value, and the corresponding cumulative frequency for each value estimated from i/N, where i is the order of the value and N is the total number of observations. Note that the estimation i/N is a biased estimator.

6.5 OBSERVATIONS ON RESPONSE OF DIFFERENT SYSTEMS

The time history results show consistently a distinct drifting of the deformation response of the elastic-plastic systems (α = 0.0) whereas strain hardening systems exhibit a response which is essentially symmetric with respect to the undeformed configuration. To explore this behavior more thoroughly, additional time history analyses are performed for systems with very small strain hardening (α=0.01, 0.03 and 0.05).

Figure 6.9 shows examples of typical response histories. These examples present an ensemble of response histories for different structural systems subjected to the record A004. The heavy lines in the figures identify the time spent in the inelastic regime. It is apparent from the figures that the deformations occur predominantly in one direction for the elastic-plastic systems while even a very small strain hardening ratio (α = 0.03) alters this behavior considerably. Yet, the amount of time spent in the elastic and inelastic regimes remains essentially unchanged. This observation holds true for systems with

different yield levels as well as for different input records. The same observation is also reported by Riddle and Newmark (119). The drifting characteristic of elastic-plastic systems leads to larger values of ductility than for hardening systems. Thus, it must be concluded that ductility demands derived from elastic-plastic systems are not representative for the demands on hardening systems even if the hardening ratio is small.

Figure 6.10 shows examples of cumulative frequency polygons of δ/δ_y for different systems and records. It can be seen that, except for the elastic-plastic systems, the deformation histories have a close to zero median and are essentially symmetric. This observation is important in the evaluation of cumulative fatigue damage because of the mean effect. The drifting of the elastic-plastic systems is clearly evident from the cumulative frequency polygons.

The ordered plastic deformation ranges $\Delta\delta_p'/\delta_y$ (one minus cumulative frequency polygon) for the same systems are shown in Fig. 6.11. The figure includes the plots for both increasing and decreasing half cycles. It can be observed that for most systems and records the curves for increasing and decreasing half cycles are very similar, except for a few elastic-plastic systems. This similarity is due to the almost identical number of increasing and decreasing half cycles (which at most differ by two) and the fact that, because of the employment of the rainflow cycle counting method, a large percentage of these half cycles are pairs which form full cycles, i.e., have the same plastic deformation range.

Figure 6.11 shows also that even for elastic-plastic systems the curves for increasing and decreasing half cycles usually do not differ by a great amount. This indicates that, despite the significant drifting of the deformation response of elastic-plastic systems in the time history domain, the plastic deformation ranges are of similar magnitude and frequency for increasing and decreasing half cycles.

These observations made from the plots of ordered plastic deformation ranges are used as a justification for combining increasing and decreasing half cycles in the statistical evaluation discussed in Section 6.6. In fact, a separate statistics for increasing and

decreasing half cycles would be meaningless because of the arbitrary choice of a positive direction of acceleration for each input record.

Figure 6.12 presents the time histories of energy terms (normalized to elastic strain energy) for systems with a period of 0.5 seconds, R equal to 4 and various α values, subjected to the same input record. The figure indicates that the time variation of dissipative energy terms (DE and HE) is similar, regardless of the strain hardening ratio α. In fact, the variation is also similar for both yield levels (R = 4 and 8). Considering the energy terms at the end of the strong motion, it can be notices that the energy dissipated by viscous damping, DE, increases with α whereas the hysteretic energy, HE, is almost the same for all inelastic systems (α = 0.0 to 0.5). These trends are observed for both R equal to 4 and 8 and all records used in this study. The effect of yield level on HE (not normalized) is generally insignificant, with somewhat larger values of HE obtained for R equal to 4 than for R equal to 8 in most cases. More specific conclusions on dissipative energy terms are discussed in Section 6.6.4.

6.6 STATISTICAL ANALYSIS OF RESPONSE PARAMETERS FOR SYSTEMS WITH A PERIOD OF 0.5 SECONDS

In this section a statistical approach is used to quantify seismic response parameters and to evaluate the uncertainties inherent in seismic response. Only SDOF systems with an undamped elastic period of 0.5 seconds and 5% damping are used. The system parameters varied in the study are the yield level F_y (using R = 4 and 8) and the strain hardening ratio α. A generalization of the results to systems of different restoring force characteristics and periods is not attempted but can be achieved by applying the proposed approach in a more comprehensive parameter study.

All deformation parameters are normalized with respect to yield deformation δ_y while energy terms are normalized with respect to elastic strain energy, $0.5F_y\delta_y$. Emphasis in the evaluation of results is placed on the engineering definition of plastic deformation ranges, $\Delta\delta_p'$, since the material science definition values $\Delta\delta_p''$ can be obtained directly by multiplying the former by the factor $(1 - \alpha)$.

6.6.1 Probabilistic Analysis of Plastic Deformation Ranges

6.6.1.1 Model Fitting and Verification

For a utilization of the damage model discussed in Chapters 3 and 5 it is necessary to know the magnitudes of all plastic deformation ranges $\Delta\delta_{pi}$. By knowing the distribution of $\Delta\delta_p$ and the number of inelastic half cycles it is possible to determine $\Delta\delta_{pi}$ values and eventually estimate the anticipated damage. In order to obtain a mathematical formulation for the plastic deformation ranges, fitting of the analytically obtained $\Delta\delta_{pi}/\delta_y$ values to a probabilistic distribution function is attempted. The justification for choosing a proper theoretical distribution for a variable describing a physical phenomenon could be based either on a conceptual understanding of the phenomenon, or on matching the observed data to a standard distribution, or on a combination of both. The consideration of physical inclinations of plastic deformation ranges is not feasible at this time because the physical phenomenon is not fully understood. Thus, the primary concern herein is to look for a tractable, smooth mathematical function to summarize the distribution of the observed data. The choice of mathematical functions is limited to commonly used probabilistic models.

A graphical presentation in the form of a cumulative frequency polygon is used to recognize the most likely probabilistic model to describe the observed data. The choice of the cumulative frequency polygon, CFP, over the histogram is based on the consideration that the latter requires grouping both data and mathematical models into selected intervals, ignoring some of the information in the sample by losing exact values of the observations. The cumulative shapes can be evaluated directly by plotting each observation as a specific point side by side with the complete and continuous cumulative distribution function, CDF, of the model.

The plotting and comparison of the cumulative curves can be simplified by using probability paper on which the cumulative distribution function of a specific probability law plots as a straight line. With such paper, the comparison between the model and data is reduced to a comparison between the cumulative frequency plygon of the data and a straight line.

In plotting the cumulative frequency polygon, the set of observations for each event is ordered in increasing value. Denoting these ordered values (order statistics) $\Delta\delta_{p1}/\delta_y, \ldots, \Delta\delta_{pi}/\delta_y, \ldots, \Delta\delta_{pN}/\delta_y$, the corresponding cumulative frequency for each value is estimated from i/N+1 which is an unbiased estimator. In doing so, each data point corresponding to a specific half cycle is assumed to be independent from others. This assumption is necessary to permit the use of order statistics.

The CFP of the observed $\Delta\delta_{pi}/\delta_y$ values for each event (a given system and input record) are plotted on several different probability papers representing different probabilistic models such as, uniform, Gaussian, lognormal and Type I extreme-value. It is found that a lognormal distribution represented the data reasonably well for each event individually. Figure 6.13 illustrates the individual CFPs of the data points for a system with T = 0.5 second, R = 4 and α = 0.1 subjected to different events, plotted on a lognormal probability paper. The data points usually appear in pairs except at the extremes, with each pair forming a complete cycle. This characteristic arises directly from the use of the rain-flow cycle counting method. If the data points are separated into increasing and decreasing half cycles, it is found that the CFPs for the two cases would look very similar. This allows the combination of increasing and decreasing half cycles into a single data set. In addition, by combining the data points from different events, the concept of increasing and decreasing classification becomes irrelevant due to arbitrariness of the assumed sign conventions.

Making the assumption that the individual half cycles in a single event are independent, it can be justified to combine the values of $\Delta\delta_{pi}/\delta_y$ of all six events and perform order statistics on the complete sample set. This will result in the most likely distribution of $\Delta\delta_p/\delta_y$ for a given system (specific values of T, F_y and α) due to major ground shaking. Because it is found that a lognormal distribution represents the data reasonably well for each event individually, it is expected that the combined data of all six events will also be represented well with a lognormal distribution. The distribution of the combined data will represent an average of the CDFs of the sample tests (law of large

numbers), meaning that it represents the distribution of the plastic deformation ranges for a specific system.

A lognormal probability density function $f_y(y)$ is defined as:

$$f_Y(y) = \frac{1}{y\sqrt{2\pi}\,\sigma_{\ell nY}} \exp\left\{-\frac{1}{2}\left[\frac{1}{\sigma_{\ell nY}}\left(\ell n \frac{y}{\bar{m}_Y}\right)\right]^2\right\} \qquad y > 0 \qquad (6.7)$$

The CDF of y, $F_Y(y)$, is most easily evaluated using a table of the normal distribution $F_U(u)$ in the following manner:

$$F_Y(y) = F_U(u) \qquad (6.8)$$

where

$$u = \frac{1}{\sigma_{\ell nY}} \ell n \frac{y}{\bar{m}_Y} \qquad (6.9)$$

Using the above formulations to represent the combined data, a systematic method is needed to estimate the parameters $\bar{m}_Y$ and $\sigma_{\ell nY}$ so as to fit a straight line to the data points on the probability paper as satisfactorily as possible. The method advocated by Gumbel (120) which is a modification of the classical method of moments, is employed for this purpose. The method is also a special case of the least-square error procedure which makes it attractive for linear representations such as probability papers. In this method the two parameters $\bar{m}_Y$ and $\sigma_{\ell nY}$ of the probabilistic model are estimated from the following equations:

$$\ell n\, \bar{m}_Y = \frac{1}{n} \sum_{i=1}^{n} \ell n \frac{\Delta\delta_{pi}}{\delta_y} \qquad (6.10)$$

$$\sigma_{\ell nY} = S \frac{\left(\ell n \frac{\Delta\delta_p}{\delta_y}\right)}{\sigma_n} \qquad (6.11)$$

where

$$S\left(\ell n \frac{\Delta\delta_p}{\delta_y}\right) = \left[\frac{1}{n} \sum_{i=1}^{n} \left(\ell n \frac{\Delta\delta_{pi}}{\delta_y} - \ell n\, \bar{m}_Y\right)^2\right]^{1/2}$$

and σ_n is the so called normal standard deviation which is only a function of sample size n. Values of σ_n are calculated from

$$\sigma_n^2 = \frac{1}{n} \sum_{i=1}^{n} \left(\frac{i}{n+1}\right)^2 - \left(\frac{1}{n} \sum_{i=1}^{n} \frac{i}{n+1}\right)^2 \qquad (6.12)$$

The parameters $\bar{m}_Y$ and $\sigma_{\ell nY}$ calculated from this procedure are summarized in Table 6.4. Values are presented for all structural systems investigated and for the engineering and material science definitions of plastic deformation ranges [$\Delta\delta_p'' = (1-\alpha)\Delta\delta_p'$].

In order to check whether the data deviate a statistically significant amount from the model prediction, a Kolmogorov-Smirnov goodness of fit (K-S) test was performed. The K-S test (121) is concerned with the degree of agreement between the distribution of a set of sample values and some specified theoretical distribution. It concentrates on the deviations between the hypothesized cumulative distribution function $F_Y(y)$ and the observed cumulative polgyon $F^*(y_i)$ estimated from i/n, where y_i is the i^{th} observed value in a sample size of n observations ordered in an increasing manner.

Figure 6.14 shows the combined observed data of $\Delta\delta_{pi}'/\delta_y$ (engineering definition) for a system with R=4 and α=0.1 plotted on a lognormal probability paper along with the fitted lognormal distribution shown as a straight line. Also displayed are the K-S test curves for two levels of significance (5 and 20 percent) above and below the hypothesized line. None of the points fall outside the limiting K-S test curve lines which implies that the hypothesized model should not be rejected at the twenty percent significance level.

The K-S goodness-of-fit test performed for all systems shows that the fitted lognormal distributions are accepted in every case with at least 5 percent level of significance, and in most cases with 20 percent. This indicates that the fitted distributions are significantly in accordance in all cases with the combined values of $\Delta\delta_p/\delta_y$. Thus, the lognormal distribution is an acceptable representation of the values of $\Delta\delta_p/\delta_y$ for a specific system subjected to an event of the type represented by the ground motions used in this study.

6.6.1.2 Discussion of Results

In order to illustrate how well a lognormal distribution fitted to the combined events fits the data points for individual events, the predicted distribution of $\Delta\delta_p'/\delta_y$ (engineering definition) for a system with R=4 and α=0.1 (shown in Fig. 6.14) is plotted along the data points

in Fig. 6.13. It is observed that the proposed model fits the individual events reasonably well except for the record A001 component S00E. The poor fit to this record comes as no surprise because of the breakdown in CDF when the number of observations is small (large sample size for order statistics).

Figure 6.15 shows, in a linear-linear plot, the fitted CDF for a system with R=4 and α=0.1, together with the observed data points for all events combined, whereas Fig. 6.16 shows the same CDF with data points ordered separately for each individual event. These figures show clearly the high frequency of small plastic deformation ranges and the low frequency of large plastic deformation ranges. The value of $\Delta\delta_p'/\delta_y$ corresponding to the mode (point with the largest probability) is found to be very small (approximately equal to 0.1) for this system as well as for all other systems investigated in this study.

The fitted cumulative distribution functions of $\Delta\delta_p'/\delta_y$ for systems with different α values are exhibited in Fig. 6.17 for R equal to 4 and 8. It can be seen from both graphs that for a given cumulative frequency value the expected value of $\Delta\delta_p'/\delta_y$ increases with the strain hardening ratio α. This demonstrates that systems with small strain hardening contain more half cycles with smaller $\Delta\delta_p'/\delta_y$. It is evident from Fig. 6.17 that in all cases the frequency of large plastic excursions is very low while the frequency of small plastic excursions is very high. Although individual small excursions contribute relatively little to damage, the high frequency of small excursions indicates that their cumulative effect on damage may be considerable. The very low frequency of very large excursions, on the other hand, illustrates the importance of the maximum plastic deformation range on damage accumulation. Thus, an accurate evaluation of $(\Delta\delta_p)_{max}$ is in order and is discussed later in this chapter.

The parameters of the fitted lognormal distribution are listed in Table 6.4. Shown in this table are the parameters $\bar{m}_Y$ and $\sigma_{\ell nY}$, as well as the population mean m_Y and the standard deviation σ_Y. The values of m_Y and σ_Y of each fitted lognormal distribution can be calculated from the following equations:

$$m_Y = \bar{m}_Y \exp(1/2\ \sigma^2_{\ell nY}) \tag{6.13}$$

$$\sigma^2_Y = m^2_Y \left[\exp(\sigma^2_{\ell nY}) - 1\right] \tag{6.14}$$

with the coefficient of variation v_Y defined as

$$v_Y = \frac{\sigma_Y}{m_Y} = \left[\exp(\sigma_{\ell nY}) - 1\right]^{1/2} \tag{6.15}$$

The following trends can be observed from the values listed in Table 6.4.

The values of median $\bar{m}_Y$ (with $F_Y(y) = 0.5$) for the different systems indicate a strong dependence on the strain hardening ratio α when the engineering definition for $\Delta\delta_p$ is used (significant increase in $\bar{m}_Y$ as α increases), however, for the material science definition the values of $\bar{m}_Y$ are essentially independent of α. As R changes from 4 to 8 the median $\bar{m}_Y$ increases by a factor larger than 2.0 (between 2.7 and 2.08 for different α values). The values of $\sigma_{\ell nY}$ tend to decrease somewhat with α. The values of the population mean m_Y increase by a factor considerably larger than two when the yield level is reduced by a factor of two (from R=4 to R=8). The coefficient of variation v_Y tends to be higher for small values of α and decreases as the yield level increases.

6.6.1.3 Truncation of CDF of Plastic Deformation Ranges

Because the method used in the estimation of the lognormal distribution parameters $\bar{m}_Y$ and $\sigma_{\ell nY}$ utilizes the sample mean and standard deviation (see Section 6.6.1.1), more weight is placed on the central region of the distribution than on the tail regions in fitting the observed data points. This leads to rather inaccurate fitting at large $\Delta\delta_p/\delta_y$ values as is evident from Figs. 6.14 and 6.15.

The CDFs of $\Delta\delta_p/\delta_y$ for different systems are developed for the purpose of predicting the values of $\Delta\delta_{pi}/\delta_y$ for different values of inelastic half cycles N'. When using the CDF alone (e.g., by dividing the CDF into equal frequency intervals), the value of maximum normalized plastic deformation range $(\Delta\delta_p)_{max}/\delta_y$ would be dependent on the value of N', i.e., small values of $(\Delta\delta_p)_{max}/\delta_y$ would be predicted for small values of N'. However, as is evident from Fig. 6.13, this dependence does not exist for the observed data.

Because of this shortcoming of the fitted CDFs in the region of large $\Delta\delta_{pi}/\delta_y$ values (inaccurate fitting of data and unacceptable values of $(\Delta\delta_p)_{max}/\delta_y$ for small N' values), it is decided to conduct a separate study on the statistics of $(\Delta\delta_p)_{max}/\delta_y$. The results of this study are discussed in Section 6.6.3.1. The statistical information on $(\Delta\delta_p)_{max}/\delta_y$ can be utilized to modify the CDFs of $\Delta\delta_p/\delta_y$ in a manner that permits a realistic prediction of all $\Delta\delta_{pi}/\delta_y$ values for different N' values.

The modification of the CDF, to account for the information on $(\Delta\delta_p)_{max}/\delta_y$, can be achieved by truncating the original PDF by specifying limitations on the largest value of $\Delta\delta_p/\delta_y$ from the statistics of $(\Delta\delta_p)_{max}/\delta_y$.

When $(\Delta\delta_p)_{max}/\delta_y$ is treated as a random variable whose PDF is expressed by $f_{Y_{max}}(y_{max})$, $(0 \leq y_{max} = (\Delta\delta_p)_{max}/\delta_y \leq \infty)$, then the truncated PDF and CDF of the random variable $y = \Delta\delta_p/\delta_y$, denoted as $f'_Y(y)$ and $F'_Y(y)$, are related to the original $f_Y(y)$ through the following relationships:

$$f'_Y(y) = \int_o^\infty \left[f_{Y/Y_{max}}(y/y_{max})\right]\left[f_{Y_{max}}(y_{max})\right]dy_{max} \tag{6.16}$$

and

$$F'_Y(y) = \int_o^y f'_Y(u)du \tag{6.17}$$

where

$$f_{Y/Y_{max}}(y/y_{max}) = k' f_Y(y)$$

and

$$k' = \frac{1}{\int_o^{y_{max}} f_Y(y)dy}$$

This formulation can be simplified considerably when $(\Delta\delta_p)_{max}/\delta_y$ can be treated deterministically (taken for instance as sample mean or mean plus standard deviation). Then the truncated PDF and CDF can be written as follows (see Fig. 6.18):

$$f'_Y(y) = \begin{cases} kf_Y(y) & \text{for } 0 \leq y \leq (\Delta\delta_p)_{max}/\delta_y \\ 0 & \text{for } y > (\Delta\delta_p)_{max}/\delta_y \end{cases} \tag{6.18}$$

and

$$F'_Y(y) = \begin{cases} kF_Y(y) & \text{for } 0 \leq y \leq (\Delta\delta_p)_{max}/\delta_y \\ 1 & \text{for } y > (\Delta\delta_p)_{max}/\delta_y \end{cases} \tag{6.19}$$

where

$$k = \frac{1}{\int_0^{(\Delta\delta_p)_{max}/\delta_y} f_Y(y)dy} = \frac{1}{F_Y[(\Delta\delta_p)_{max}/\delta_y]}$$

For a given number of inelastic half cycles, N', values of $\Delta\delta_{pi}/\delta_y$ could be determined from $F'_Y(y)$ by setting the largest value equal to $(\Delta\delta_p)_{max}/\delta_y$ (with $F'_Y(y) = 1.0$) and obtaining the other N'-1 values by dividing the $F'_Y(y)$ into N' equal frequency intervals of 1/N' (see Fig. 6.19). The same values for $\Delta\delta_{pi}/\delta_y$ can be obtained from the original $F_Y(y)$ by setting the largest value equal to $(\Delta\delta_p)_{max}/\delta_y$ (with $F_Y(y) = 1/k$) and reading the other N'-1 values at frequency values i/kN', i=1 to N'-1. It should be added that this procedure is simply one way of selecting values of $\Delta\delta_{pi}/\delta_y$ from the CDF, since any value between 0.0 and 1/k can be assigned randomly to the cumulative frequencies (except for $(\Delta\delta_p)_{max}/\delta_y$ which has a cumulative frequency $F_Y(y) = 1/k$).

The truncation of the CDF suggested here may lead to a considerable improvement in the prediction of large plastic deformation ranges. These are the ranges that contribute most to damage accumulation.

6.6.2 Number of Inelastic Half Cycles (Excursions)

The number of inelastic half cycles, N', is an important parameter in assessing the accumulated damage. Table 6.5 lists the values of $\bar{N}'$ for each system and each event individually. It is evident from the table that N' is very much dependent on the strong motion duration of input motion. This parameter is also influenced strongly by the yield level, with smaller yield levels (R=8) associated with larger values of N'. The effect of hardening ratio α on N' is not very strong, but N' tends to increase slightly with α.

The arithmetic mean values of inelastic half cycles for different systems and the combined events, $\bar{N}'$, are listed at the bottom of

Table 6.5. A probabilistic distribution for N' could not be obtained because of the small number of events (six) considered in this study. The same trends as those observed for the individual events are evident for $\bar{N}'$, i.e., $\bar{N}'$ is dependent weakly on hardening ratio and strongly on yield level.

A regression analysis is performed in order to study the dependence of N' on the strong motion duration D_{sm}. The results of this analysis show a rather consistent pattern but must be interpreted with caution because of the small sample set of events used in this study and because of the difference in strong motion durations obtained from different definitions.

A least-square error procedure with N' as the dependent variable is carried out for each system, considering initially the values from all six events. However, the results in every case are biased (more so in cases with R=4) by the values obtained for the S90W component of the record A001. The values of N' for this event, considering its strong motion duration (25.4 seconds), are very small in comparison with other events, as is apparent from Table 6.5. To avoid this bias it is decided to disregard the values for N' for this specific record and to consider only the other five events. Figure 6.20 shows the results of the regression analysis along with the observed points for these five events. The analysis indicates a strong linear dependence of N' on D_{sm} in all cases as is evident from the plots in the figure and even more so from the values of the correlation coefficient ρ.

A comparison of the individual regression lines shows that the dependence of N' on α is weak. Because of this weak dependence, another regression analysis is performed using the average values of N' for the four different α values (α=0.0, 0.1, 0.3, 0.5). Based on this analysis, the predicted number of inelastic half cycles N', independent of α, can be estimated from the strong motion duration D_{sm} through the following equations:

$$N' = -19.7 + 4.2\, D_{sm} \qquad \text{for R=4} \qquad (6.20a)$$

$$N' = -10.9 + 3.9\, D_{sm} \qquad \text{for R=8} \qquad (6.20b)$$

A graphical representation of these equations together with the calculated data points is shown in Fig. 6.21.

These results should not be extrapolated beyond the range of durations used in this study. The small sample set of events used herein shows consistent trends but more data are needed for a thorough evaluation of the random variable N'. Also, no attention is paid in this evaluation to the frequency contents of the ground motions, such as the central frequency, which may have a significant effect on the number of inelastic half cycles.

6.6.3 Statistical Analysis of Other Response Parameters

In this section the maximum plastic deformation range, $(\Delta\delta_p)_{max}$, the mean plastic deformation, $\delta_{p,mean}$, and the ductility ratio, μ, of the system responses to the six ground motions are evaluated statistically. As was pointed out in Section 6.6.1.3, the statistics of $(\Delta\delta_p)_{max}$ is needed to supplement the information contained in the CDF of the plastic deformation ranges. The mean plastic deformation is a measure of the symmetry, or lack thereof, of the seismic response. A considerable mean plastic deformation indicates drifting of the seismic response which may affect damage accumulation. The ductility ratio is an index which is used commonly as a measure of damage. A comparison will be made between $(\Delta\delta_p)_{max}$ and μ in order to assess the damage indices.

Basic statistical measures, i.e., sample mean m and standard deviation s, are calculated for each parameter and the influence of system variables on these parameters is studied. Type I extreme-value distributions are proposed for a probabilistic evaluation of $(\Delta\delta_p)_{max}$ and μ.

6.6.3.1 Maximum Plastic Deformation Range

Values of the normalized maximum plastic deformation range, $(\Delta\delta_p)_{max}/\delta_y$, for different systems and input records are tabulated in Table 6.6. For a given structural system, the $(\Delta\delta_p)_{max}/\delta_y$ values for different input records vary by as much as a factor of 2.38. The values from the table indicate that the record A001 component S90W produced in most cases the largest values of $(\Delta\delta_p)_{max}/\delta_y$. It is also observed that, as R changes from 4 to 8, the values of $(\Delta\delta_p)_{max}/\delta_y$ increase in all cases by a factor greater than 2.0.

Table 6.7 presents the results of the statistical evaluation of the normalized maximum plastic deformation range for different systems. The analysis is based on the values obtained from all of the six events.

The following observations can be made from Table 6.7. The $(\Delta\delta_p)_{max}/\delta_y$ values (using the mean or the mean plus standard deviation) for R equal to 8 are considerably larger than twice those for R equal to 4. The ratio of maximum plastic deformation ranges (mean values) for R=8 and R=4 varies from 2.78 to 3.76, but with the exception of α = 0.0 the ratio does not exceed 3.0. With this one exception, the ratio is only moderately sensitive to strain hardening. Using the engineering definition, the values for mean and mean plus standard deviation of $(\Delta\delta_p)_{max}/\delta_y$ increase moderately with the strain hardening ratio with the exception of α = 0.0 and R=8. Since $(\Delta\delta_p'')_{max} = (1-\alpha)(\Delta\delta_p')_{max}$, a strong reversed trend is observed, revealing the significant dependence of the material science definition values on α which is also evident from Table 6.7.

Since the plastic deformation ranges are described by a lognormal distribution, which is shown by Gumbel (120) to be of an exponential type, it is likely that the random variable $(\Delta\delta_p)_{max}$ will have a Type I extreme-value distribution. A Type I extreme-value distribution (Gumbel distribution) may be written in the following forms:

$$P_Y(y) = \exp\left[-e^{-a(y-b)}\right] \qquad \text{CDF} \qquad (6.21)$$

$$p_Y(y) = a\exp\left[-a(y-b)-e^{-a(y-b)}\right] \qquad \text{PDF} \qquad (6.22)$$

The parameters a and b are related to the population mean m_Y and standard deviation σ_Y through the following equations:

$$m_Y = b + \frac{E}{a} \approx b + \frac{0.577}{a} \qquad (6.23)$$

(E is "Euler's constant")

$$\sigma_Y^2 = \frac{\pi^2}{6a^2} \approx \frac{1.645}{a^2} \qquad (6.24)$$

Having calculated sample mean, m, and standard deviation, s, for different systems, it is possible to calculate the distribution parameters

a and b from Eqs. (6.23) and (6.24) based on the method of moments, i.e., by setting $m_Y = m$ and $\sigma_Y = s$.

The predicted distributions of $(\Delta\delta_p')_{max}/\delta_y$ for systems with different α values and R equal to four and eight are plotted in Fig. 6.22. The figure emphasizes the significance of the yield level on the $(\Delta\delta_p')_{max}/\delta_y$ values and indicates a moderate influence of the strain hardening ratio.

6.6.3.2. Mean Plastic Deformation

A statistical evaluation of $\delta_{p,mean}$ is discussed in this section. To place this discussion into perspective, it should be said that the need for incorporating mean effects in seismic damage studies has not been fully established. In fact, the pilot tests discussed in Chapter 5 have shown that these effects may not be of foremost importance unless the mean plastic deformations are very large. However, the quantity $\delta_{p,mean}$ is of importance in the evaluation of seismic response behavior. A small value of $\delta_{p,mean}$ indicates a seismic response which is essentially symmetric with respect to the undeformed configuration whereas a large $\delta_{p,mean}$ indicates considerable drifting of the deformation response.

For each system and each record the normalized mean plastic deformation $\delta_{p,mean}/\delta_y$ is calculated as the centroid (first moment) of all plastic deformation ranges according to the following expression (see Fig. 6.23 for definition of the parameters):

$$\delta_{p,mean}/\delta_y = \left| \frac{\sum_{i=1}^{N'} \Delta\delta_{pi} \times \bar{\delta}_{pi}/\delta_y^2}{\sum_{i=1}^{N'} \Delta\delta_{pi}/\delta_y} \right| \qquad (6.25)$$

The reason for using absolute values is that the choice of the signs for deformation histories is arbitrary.

Table 6.8 lists the values of $\delta_{p,mean}/\delta_y$ for different systems and records. The sample mean and standard deviation of the values presented in Table 6.8 are shown in Table 6.9. This table shows clearly that the elastic-plastic systems exhibit a significant drifting which increases with a decrease in the yield level, while all strain hardening systems exhibit a response which is essentially symmetric with respect to the origin (small mean plastic deformation). It can be seen also that the

mean effect becomes more negligible as α increases. Thus, the question of mean deformation effect on damage accumulation appears to be relevant only for systems with very small or no strain hardening. The above observations are also evident from Fig. 6.24 which shows the mean values of Table 6.9 (engineering definition).

6.6.3.3. Ductility Ratio

The ductility ratio is generally thought to be a measure of the ability of a structure to sustain plastic deformations before failure. Most commonly, the ductility ratio μ is defined as the ratio of maximum deformation over yield deformation, i.e.,

$$\mu = \left| \frac{\delta_{max}}{\delta_y} \right| \tag{6.26}$$

where the deformation quantity δ may be curvature, rotation, deflection or any other suitable parameter. In this study, δ refers to the relative displacement of a single degree of freedom system.

Table 6.10 shows the values of μ for different systems and for each event separately. A relatively large scatter of the data for each system is apparent from these values. The statistical summary of μ for different systems is presented in Table 6.11. The foremost observation from Table 6.11 is the extremely large mean value of μ for systems with α = 0.0 and R=8 which resulted from the drifting exhibited by the elastic-plastic systems. This demonstrates that for highly inelastic systems the ductility demand of elastic-plastic systems is not representative for the ductility demand of strain hardening systems.

Except for systems with α = 0.0, the mean ductility ratio tends to increase slightly with α and the values for R=8 are somewhat larger than twice those for R=4. Disregarding these minor variations, Table 6.11 shows that for a period of 0.5 seconds the "ductility ratio" for α = 1.0 (elastic systems) is a good indicator for the ductility demand for strain hardening systems, but not so for elastic-plastic systems.

Attempts can be made to relate the ductility ratio μ to $(\Delta\delta_p')_{max}$ (engineering definition). If the half cycle corresponding to the maximum plastic deformation range $(\Delta\delta_p')_{max}$ is fully symmetric with respect to the undeformed configuration, then the following relationship should hold:

$$\mu = \frac{1}{2} \frac{(\Delta\delta_p')_{max}}{\delta_y} + 1 \qquad (6.27)$$

The value of one is added in this equation to account for the elastic deformation range of the half cycle. Figure 6.25 shows that the above relationship is close to the truth for strain hardening systems when using the mean values for μ and $(\Delta\delta_p')_{max}/\delta_y$ from this work. This demonstrates symmetry of the largest excursion, again with the exception of the elastic-plastic systems. For elastic-plastic systems, a conservative estimate of μ can be obtained from:

$$\mu = \frac{1}{2} \frac{(\Delta\delta_p')_{max}}{\delta_y} + \frac{\delta_{p,mean}}{\delta_y} + 1 \qquad (6.28)$$

In a recent statistical evaluation of the seismic response of non-linear systems by Riddle and Newmark (119), the inelastic deamplification factors (used to obtain inelastic response spectra from elastic response spectra) for elastic-plastic systems are expressed as a function of ductility and damping ratio. According to this study, the deamplification factor ϕ_μ for the velocity region of the spectra, in which the period of 0.5 seconds is located, is given as:

$$\phi_\mu = (p\mu - q)^{-r}$$

where

$p = q + 1$

$q = 2.70\ \beta^{-0.40}$

$r = 0.66\ \beta^{-0.04}$

β = damping ratio in percent ($2 \leq \beta \leq 10$)

From this equation, the ductility ratio can be calculated for a given ϕ_μ as follows:

$$Q = \frac{q + \phi_\mu^{-1/r}}{p} \qquad (6.29)$$

The calculated values of p, q and r are 2.418, 1.418 and 0.619, respectively, for 5 percent damping ($\beta = 5$).

Table 6.12 lists the corresponding values of μ based on the Riddle-Newmark formulation (designated as μ_{R-N}), the Newmark and Hall method (designated as μ_{N-H}), together with the mean values obtained in this study for elastic-plastic systems with period of 0.5 seconds and 5 percent damping (see Table 6.11). The strength reduction factor R" is used in this table since R" is indeed the true reduction factor (see Section 6.3).

From the table it is evident that the ductility values obtained from this study are in close agreement with those obtained from the Riddle-Newmark approximation. The Newmark-Hall approximation underestimates the ductility demand for elastic-plastic systems slightly for R"=4.9 but very severely for R"=9.8.

In order to justify the choice of a suitable distribution function for the ductility ratio μ, the cumulative frequency polygon, CFP, for the normalized deformations, δ/δ_y, of each individual deformation history (see Fig. 6.10) is examined. Since most of the CFPs resemble the shape of a Gaussian distribution, several CFPs are plotted on normal probability paper. The results show that for elastic-plastic systems the CFPs deviate considerably from that of a normal distribution while for strain hardening systems an acceptable and at times remarkably close fit is observed. Thus it should be acceptable to assume that for strain hardening systems the deformation time history has the nature of a Gaussian process and its distribution is of a normal type. This assumption has been used extensively in random vibration studies.

Assuming a normal distribution for δ/δ_y, which is of an exponential type, the ductility ratio μ is expected to be of a Type I extreme-value distribution. Knowing the sample mean and standard deviation of μ, the parameters of the distribution, a and b, can be calculated with the procedure discussed in Section 6.6.3.1. Figure 6.26 shows the Type I extreme-value distributions for systems with different α values and R equal to four and eight. Apart from elastic-plastic systems, Fig. 6.26 shows graphically that, in general, the ductility ratio tends to increase with α (not considering elastic systems), however, the dependence of μ on α is not very significant. Again, the exceptional behavior of the elastic-plastic systems (α = 0.0) is clearly evident from this figure.

6.6.4 Hysteretic Energy Dissipation

Since the amount of hysteretic energy dissipated by the structure is proportional to the inelastic deformations, the hysteretic energy may serve as a parameter to indicate the severity of damage. Suiden (56) has investigated the possibility of estimating the cumulative damage by means of the dissipated hysteretic energy at the plastic hinge regions of nonlinear structures.

In fact, an alternative way of evaluating cumulative damage is to use hysteretic energy dissipation per cycle, HE, rather than plastic deformation range $\Delta\delta_p$ in Eqs. (3.8) and (3.9) For bilinear nondeteriorating systems the hysteretic energy dissipation per cycle i and the corresponding plastic deformation range $\Delta\delta_p''$ (material science definition) are related by (see Fig. 6.27):

$$HE_i = 2F_y \left(\Delta\delta''_{pi}\right) \tag{6.30}$$

Thus, there is no difference whether HE or $\Delta\delta_p''$ is used in damage evaluation. Moreover, this relationship provides a simple means of calculating from the previously presented results (the distribution of $\Delta\delta_p''/\delta_y$, number of inelastic half cycles, etc.) the total energy dissipated by inelastic deformations during the strong ground motion. The total hysteretic energy dissipation, HE_t, normalized with respect to elastic strain energy, $0.5F_y\delta_y$, can be calculated as

$$\frac{HE_t}{0.5F_y\delta_y} = \sum_{i=1}^{N} \frac{HE_i}{0.5F_y\delta_y} \approx 2 \sum_{j=1}^{N'} \frac{\Delta\delta''_{pj}}{\delta_y} \tag{6.31}$$

where N is the number of inelastic cycles while N' is the number of inelastic half cycles.

This calculation is in most cases an approximation because not every pair of inelastic excursions (half cycles), as obtained from rain-flow cycle counting, forms necessarily a closed cycle. However, based on a comparison between the observed values of $HE_t/0.5F\delta_y$ (calculated from the force-deformation response) and observed values of $2\Sigma\Delta\delta''_{pj}/\delta_y$, this approximation is quite accurate for bilinear nondeteriorating systems.

Table 6.13 presents the normalized total hysteretic energy dissipated during the strong motion for different systems and records. These values are calculated directly from the force-deformation response of the systems. Also listed in this table are the values for normalized total dissipated energy (hysteretic energy plus damping energy), $TDE/0.5F_y\delta_y$, at the end of the strong motion duration. As can be seen from the table, the total dissipated energy increases generally as α increases from 0.0 to 0.5 whereas the values of $HE_t/0.5F_y\delta_y$ are not very sensitive to the strain hardening ratio, particularly for R equal to four. Based on this observation, the normalized hysteretic energies for all α values (α = 0.0, 0.1, 0.3 and 0.5) and the same R are averaged with the results presented in Table 6.14.

Tables 6.13 and 6.14 show that the normalized values of HE_t increase in general by a factor close to four when R is increased from four to eight. This indicates that the dissipated hysteretic energy is of similar magnitude for R equal to four and eight since the elastic strain energy ($0.5F_y\delta_y$) for R equal to four is four times that for R equal to eight.

Equation (6.31) provides a link between the values of $\Delta\delta_p''/\delta_y$ (material science definition) and $HE_t/0.5F_y\delta_y$, making it possible to examine the procedure developed in this chapter (Section 6.6.1.3) for determining statistically representative values of $\Delta\delta_{pi}/\delta_y$. To carry out this examination, a comparison is made between observed and predicted values of $HE_t/0.5F_y\delta_y$, using the results of a regression analysis on the variation of $HE_t/0.5F_y\delta_y$ with D_{sm}. The predicted values are computed from Eq. (6.31) with the values of $\Delta\delta_{pi}''/\delta_y$ obtained from the aforementioned procedure. This procedure requires the utilization of the previously developed CDFs for the plastic deformation ranges, the statistical information on the maximum plastic deformation ranges, and the regression analysis of N' versus D_{sm}.

To accomplish the comparison, a series of bilinear systems with a period of 0.5 seconds, α values of 0.0, 0.1, 0.3 and 0.5, and yield levels corresponding to R equal to four and eight are selected. For the predicted values of $HE_t/0.5F_y\delta_y$ the input motions are assumed to have a strong motion duration of 7.5, 9.5, 11.2, 13.2 and 15.6 seconds. Three

of these values (7.5, 11.2 and 15.6 seconds) match the durations of the ground motion records used in this research and the other two values (9.5 and 13.2 seconds) are added to cover uniformly the selected range of duration. The duration range is chosen to conform with the duration range of the regression lines relating N' to D_{sm}.

The maximum normalized plastic deformation range, $(\Delta\delta_p'')_{max}/\delta_y$, for each system is treated as a deterministic parameter and its value is set equal to the corresponding mean m in Table 6.7. The number of inelastic half cycles N', independent of α, for different strong motion durations are computed from Eqs. (6.20a) and (6.20b) for R equal to 4 and 8, respectively.

After determining the values of $(\Delta\delta_p'')_{max}/\delta_y$ and N' for each system and input motion duration, the procedure described in Section 6.6.1.3 is applied in order to determine N' values of $\Delta\delta_{pi}''/\delta_y$. Table 6.15 lists the calculated values of $2\Sigma\Delta\delta_{pi}''/\delta_y$ for different systems and strong motion durations. Since the values in Table 6.15 have been obtained from statistical information on $\Delta\delta_p''/\delta_y$ and N', they should represent, according to Eq. (6.31), statistically acceptable predictions of $HE_t/0.5F_y\delta_y$ for different systems and durations.

The results indicate that the influence of α on predicted values of $HE_t/0.5F_y\delta_y$ is not very pronounced. A similar observation was made earlier on the dependence of observed values of normalized HE_t on α. The weak dependence of the predicted HE_t on α, in spite of the strong dependence of $(\Delta\delta_p'')_{max}/\delta_y$ on α (see Table 6.7), can be explained by noticing that for the various α values the difference in magnitudes of $\Delta\delta_{pi}''/\delta_y$ decreases, compared to the difference in $(\Delta\delta_p'')_{max}/\delta_y$, as smaller inelastic half cycles are selected from the CDF. Consequently, the summation of all the $\Delta\delta_{pi}''/\delta_y$ values becomes less sensitive to α. The decrease of the predicted HE_t with α (Table 6.15) would be even smaller if the dependence of the N'-D_{sm} relationship on α would have been considered, since N' consistently increases with α (see Table 6.5). Because of this observation, the predicted values of $HE_t/0.5F_y\delta_y$ (values in Table 6.15) for all α values are averaged with the results shown in Table 6.16. Also listed in this table are the values of the observed

average normalized HE_t (independent of α, see Table 6.14) for those ground motion records with similar strong motion durations.

Figure 6.28 shows the predicted values of $HE_t/0.5F_y\delta_y$ as listed in Table 6.16, along with the regression lines. A linear dependence is evident from the graph and the values of ρ. This linearity is partially attributed to the linear relationship assumed between the number of inelastic half cycles and D_{sm}.

For the purpose of a direct comparison between the results of a regression analysis for the predicted and observed values of normalized HE_t, a regression analysis is performed as well on the dependence of the observed average normalized HE_t values on D_{sm}, using all data points except the one corresponding to D_{sm} = 25.4 seconds. This data point is omitted because it was disregarded in the regression analysis of N' versus D_{sm}. The observed data points and the corresponding regression lines are shown in Fig. 6.29. Also shown in this figure are the regression lines based on predicted data from Fig. 6.28.

There are evident differences between the regression lines from predicted and observed data. These differences come from the assumption of a linear relationship between N' and D_{sm}, but also from simplifying assumptions made in the statistical evaluation of $\Delta\delta_p$ and $(\Delta\delta_p)_{max}$. For instance, it was assumed that the CDF of $\Delta\delta_p$ and the statistical parameters describing $(\Delta\delta_p)_{max}$ are not dependent on the strong motion duration. Such a dependence likely exists, particularly in the CDF of $\Delta\delta_p$, but is not evident from the results of the small sample set of records used in this study. A consideration of the dependence on strong motion duration would complicate considerably an evaluation of response parameters. It is questionable whether this complication is warranted in view of the not so great differences between observed and predicted results noted in Fig. 6.29.

6.6.5 Variation of Cumulative Damage with Strong Motion Duration

Ignoring the mean deformation and sequence effects, the cumulative damage D, based on a Coffin-Manson type relationship and Miner's rule of linear damage accumulation, can be evaluated from Eq. (3.9) which is repeated here:

$$D = C \sum_{i=1}^{N} (\Delta\delta_{pi})^c \tag{6.32}$$

Let us assume a SDOF system in which the deformation parameter of a component can be linearly correlated with the plastic deflection range $\Delta\delta_p'$ (e.g., $\Delta\theta_p \approx \Delta\delta_p'$ for a simple portal frame with plastic hinges at the beam ends). Then the information discussed in this chapter can be applied directly for damage assessment.

In order to illustrate the dependence of accumulated damage on strong motion duration D_{sm}, let us assume further that the exponent c in Eq. (6.32) is deterministic and equal to 2.0. Using the damage caused by the largest cycle [$\bar{D} = C(\Delta\delta_p')^c_{max}$] as a normalizing factor, the normalized cumulative damage, $D/\bar{D}$, can be written in the following form:

$$\frac{D}{\bar{D}} = \frac{C \sum_{i=1}^{N} (\Delta\delta_{pi}')^2}{C[(\Delta\delta_p')_{max}]^2} \tag{6.33}$$

This equation is utilized here to assess cumulative damage, by using either the $\Delta\delta_p'/\delta_y$ values obtained from the responses to the individual records (observed values), or the $\Delta\delta'_p/\delta_y$ values obtained from the fitted CDFs of the plastic deformation ranges (predicted values). In order to permit a comparison between the two methods, the normalizing factor $\bar{D}$ in both cases is computed from the mean values of $(\Delta\delta_p')_{max}/\delta_y$ as listed in Table 6.7.

A system with α = 0.1 and R=4 is used for this example. Since the parameter N in Eq. (6.33) is the number of inelastic cycles and not the number of inelastic half cycles, the largest plastic deformation range and then every other plastic deformation range (N = N'/2) are considered for damage accumulation. Figure 6.30 shows data points for $D/\bar{D}$ as well as regression lines for both observed and predicted data. The observed values of $D/\bar{D}$ are computed from the response of the system to each of the six records whereas the predicted values are computed for the strong motion durations listed in Table 6.16.

In the predictions, the number of inelastic cycles for different values of D_{sm} is taken as half of the value obtained from Eq. (6.20a).

The procedure outlined in Section 6.6.1.3 is employed for the purpose of determining values of $\Delta\delta'_{pi}/\delta_y$, using the mean of $(\Delta\delta'_p)_{max}/\delta_y$ from Table 6.7 to modify the CDF of the plastic deformation ranges. The correlation coefficient for the predicted regression line shown in Fig. 6.30 is very close to one (ρ=0.999), showing that for the range of durations used in this example (7.5 to 15.6 seconds) the predicted damage increases linearly with duration.

Comparing the two regression lines shown in Fig. 6.30, it can be said that, in average, the damage obtained from responses to the input records (observed) is in good agreement with the damage obtained from statistical information on N and $\Delta\delta_p$ (predicted). This simple example demonstrates that the statistical information generated on the number of inelastic excursions, N', and on the individual plastic deformation ranges, $\Delta\delta_{pi}$, can be used indeed to predict the cumulative damage. The example illustrated here is based on a deterministic value of $(\Delta\delta_p)_{max}/\delta_y$ (the mean value). A probabilistic damage evaluation could be achieved by taking advantage of the statistical information on $(\Delta\delta_p)_{max}/\delta_y$ (see Section 6.6.3.1) and by generating a probabilistic distribution for N'. The latter aspect will require an extensive study that utilizes a much large number of sample input records.

The most important observation to be made from the results shown in Fig. 6.30 is the strong dependence of accumulated damage on the strong motion duration. This observation demonstrates the need for a cumulative damage concept in the assessment of seismic performance. The conventionally used ductility factor does not account for duration effects and may be a misleading parameter for performance assessment. For instance, an increase in strong motion duration from eight to sixteen seconds may lead to 100% increase in accumulated damage (using the "predicted" regression line in Fig. 6.30).

6.7 OBSERVATIONS ON RESPONSE CHARACTERISTICS OF SYSTEMS WITH PERIODS OTHER THAN 0.5 SECONDS

A statistical study of response parameters for SDOF system with elastic natural periods other than 0.5 seconds is not within the scope of this study. However, a pilot study is performed, utilizing the

structural systems discussed in Section 6.3 (bilinear and nondegrading), with natural periods of 0.2, 0.5, 1.0 and 2.0 seconds, but employing only the Taft record (A004) as input motion. The purpose of this pilot study is to identify trends of importance from the viewpoint of damage assessment.

The following observations are made from this pilot study which is discussed in more detail in Ref. 108.

It appears that the lognormal distribution is an acceptable representation of the plastic deformation ranges, regardless of the period. Furthermore, the inelastic half cycles usually emerge in pairs, with each pair forming a complete cycle, except for half cycles with very large plastic deformation ranges.

For a given R" value (i.e., a yield level obtained by dividing the elastic force demand by a constant factor) the number of inelastic half cycles, N', increases severely with a decrease in period and increases moderately with a decrease in yield level.

The maximum plastic deformation range and the ductility ratio depend strongly on the yield level. For a given R", very large values for these parameters are obtained at a period of 0.2 seconds.

The drifting of elastic-plastic systems is evident for all periods. It is largest for short period structures and decreases considerably with an increase in natural period.

For systems with equal R", the accumulated damage is inversely proportional to the natural period. This is apparent from the values of normalized hysteretic energy which increase severely with decreasing periods. For T=0.2 seconds the considerably larger values of maximum plastic deformation range and the higher number of inelastic half cycles indicate that for systems with short natural periods the accumulated damage will increase significantly.

6.8 EFFECTS OF STIFFNESS DEGRADATION AND P-δ ON SEISMIC RESPONSE PARAMETERS

The statistical study discussed in Section 6.6 was concerned with bilinear nondegrading structural systems. In this section a summary is

presented of observations made from a study that considers the same systems and records, but accounts for stiffness degradation and P-δ effects. Again only systems with an elastic natural period of 0.5 seconds are considered. This study is discussed in more detail in Ref. 122.

The P-δ (gravity load) effect can be incorporated approximately in the system response by reducing the restoring force $F(\delta)$ by the amount $\frac{mg}{h}\delta$, where mg is the weight of the system and h is the story height. Thus, in order to include the P-δ effect, a straight line of slope -mg/h must be superimposed on the restoring force--deflection diagram of the system without P-δ effect (see Fig. 6.31). One of the results of this superposition is a reduction of the elastic stiffness K and the yield level $K\delta_y$ by factor of $1-\theta$, where $\theta = \frac{mg}{Kh}$ is the P-δ parameter used in this study. The other result is a reduction of the strain hardening stiffness from αK to $(\alpha-\theta)K$.

Failure for this system (without regard to strength deterioration) is defined as the point at which the displacement equals δ_f as shown in Fig. 6.31. At this point the lateral resistance becomes zero and the system becomes unstable. This type of system failure can only occur if $\theta > \alpha$ since δ_f can be related to δ_y by the equation $\delta_f = \delta_y (1-\alpha)/(\theta-\alpha)$.

Stiffness degradation can be incorporated through one of the many models available in the literature. A modified version of Clough's model is used in this study. The modification, suggested in Ref. 123, is illustrated in Fig. 6.32. After unloading to point A, the original Clough model would reload along the path AB, but the modified model reloads along the path ACB provided the line AC has a greater slope than the line AB.

The procedures discussed in Section 6.6 are applied to the modified systems in order to obtain statistical information on the seismic response parameters. A comparison of deteriorating and nondeteriorating systems with and without P-δ effect leads to the following observations.

The response of systems with P-δ effect is very similar to that of systems without P-δ effect and with an equivalent strain hardening ratio of $\alpha-\theta$, provided that $\alpha-\theta$ is not negative. When the parameter $\alpha-\theta$ is

negative (negative post-elastic stiffness), the response drifts rapidly to one side and system failure will occur when the deflection reaches the value δ_f. The average times to failure (average for the six ground motion records) for nondegrading elastic-plastic systems (α=0.0) and different values of θ are shown in Fig. 6.33 for yield levels corresponding to R equal to 4 and 8.

Stiffness degradation does not have a detrimental effect on time to failure for systems with small negative post-elastic stiffness. To the contrary, for R=4 stiffness degradation increases the time to failure in most cases and prevents the failure of systems, which would fail without stiffness degradation, in some cases.

The plastic deformation ranges of nondegrading systems fit a lognormal distribution better than those of stiffness degrading systems. Using the engineering definition for $\Delta\delta_p/\delta_y$, the fitted lognormal distribution for degrading systems pass the K-S test for a level of significance of 10% in all cases for α=0.0 and 0.1, but fail the test for a level of significance of 1% in most cases for α=0.3 and 0.5, The effect of stiffness degradation on the fitted CDF of the plastic deformation ranges is of the type shown in Fig. 6.34.

Stiffness degradation increases considerably the number of plastic deformation ranges, N', but much more so for R=4 than R=8. In fact, the values of N' for R=4 and R=8 are very similar. This is evident from Fig. 6.35 which shows the results of a regression analysis of N' on D_{ms} for degrading and nondegrading systems.

Stiffness degradation does not have a predominant effect on the maximum plastic deformation range. It tends to increase the mean values of $(\Delta\delta_p')_{max}/\delta_y$ for systems with higher yield levels (R=4) but tends to decrease these values for systems with lower yield levels (R=8).

Stiffness degradation reduces considerably the drifting of elastic-plastic systems. This is evident from the mean plastic deformation which in average is much smaller for stiffness degrading systems than for nondegrading systems.

Stiffness degrading systems do not need to dissipate as much energy through inelastic deformations as do nondegrading systems. This is

evident from Fig. 6.36 which shows the results of a regression analysis of $HE_t/0.5\ F_y\delta_y$ on D_{sm} for deteriorating and nondeteriorating systems.

The observations made here are based on a study that considers only systems with a period of 0.5 seconds. General conclusions cannot be drawn unless a wide range of periods is considered through a more comprehensive study.

6.9 SUMMARY AND CONCLUSIONS

The objective of the work discussed in this chapter was to quantify the seismic response parameters that are of interest in damage accumulation and performance assessment. Exploratory studies were performed which showed consistent trends and permitted the development of a methodology that should be applicable to bilinear and stiffness degrading SDOF systems.

The approach taken here was to subject single degree of freedom systems to an ensemble of recorded ground motions. Evaluation of the responses resulted in statistical information on the number and magnitudes of inelastic excursions as well as on other response parameters of interest. This statistical information was then utilized to develop a procedure for predicting the values of plastic deformation ranges imposed on the structural system by a major ground shaking.

In this investigation, structural systems were represented as bilinear single degreee of freedom systems with different yield levels and strain hardening stiffnesses. The assigned values of yield level were tied in with the elastic response of the system and the ATC-3 design philosophy. For systems with a period of 0.5 seconds, a comprehensive study was performed by subjecting these systems to a series of six ground motion records. The selected ground motions reflect different strong motion durations, magnitudes and site conditions. All records were scaled to a common severity level on the basis of the ATC-3 ground motion spectra. For systems with periods other than 0.5 seconds, only a limited investigation was carried out using the Taft record of the 1952 Kern County earthquake.

The damage parameters of interest were the number and magnitudes of all plastic deformation ranges, the maximum plastic deformation range as well as the mean plastic deformation with respect to the origin. The determination of these parameters was based on the rain-flow cycle counting method which is best suited for low-cycle fatigue evaluation. As additional measures, the accumulated hysteretic energy, total dissipated energy and the ductility ratio were also considered.

The novelty of this approach is that emphasis is placed on the evaluation of all inelastic excursions that may contribute to damage, and not on the maximum inelastic deformation alone. Major conclusions drawn from this study are:

- Plastic deformation ranges fit satisfactorily to a lognormal distribution. This fit was tested statistically for systems with a period of 0.5 seconds while for other periods only a graphical examination was performed.

- Although individual small excursions contribute relatively little to no damage, the high frequency of small excursions indicates that their cumulative effect on damage may be considerable. The very low frequency of very large excursions illustrates also the importance of the maximum plastic deformation range on damage accumulation.

- The statistical study for systems with a period of 0.5 seconds reveals a strong dependence of the cumulative damage on the strong motion duration, demonstrating the need for a cumulative damage concept in the assessment of seismic performance. The study also indicates that the number of inelastic excursions tends to increase linearly with the duration of strong motion and is only weakly dependent on the strain hardening stiffness.

- Systems with short natural periods have a larger cumulative damage potential than systems with long periods.

- Elastic-plastic systems display a considerable drifting of the deformation response characterized by a large mean plastic deformation, whereas strain hardening systems respond essentially symmetric with respect to the undeformed configuration.

- The conventionally used ductility ratio does not account for duration effects and may be a misleading measure of the damage potential.

Simple numerical examples indicated that the statistical information generated on the number of inelastic excursions and on the plastic deformation ranges can be used, through the procedure developed in this study, to predict cumulative damage. The examples performed in this study utilized a deterministic value for the maximum plastic deformation range (the mean value). A probabilistic damage evaluation could be achieved by taking advantage of the statistical information provided for the maximum plastic deformation range and by generating a probabilistic distribution for the number of inelastic excursions. The latter aspect will require an extensive study that employs a large number of sample input records.

In order to apply the proposed methodology, a more extensive study should be performed, utilizing a comprehensive set of ground motion records and structural systems, covering a practical range of periods and accounting for the effects of duration, magnitude, source distance and site geology. The results of such a comprehensive study could be used, in conjunction with experimentation and cumulative damage models, for the following purposes:

- Assessment of the damage potential and probability of failure of structures subjected to severe earthquakes.
- Development of fragility curves. Given the strength (yield level) of a structure or structural components, it should be possible to assess the probability of failure for various levels of severity of earthquakes (represented by magnitude and site dependent acceleration spectra).
- Development of representative loading histories for experimental investigations. Such loading histories should be statistically representative samples of the response expected in severe earthquakes. This issue is discussed further in Chapter 7.

CHAPTER 7

RECOMMENDATIONS FOR COMPONENT TESTING

The recommendations made here are for experimentation which has the objectives outlined in Section 2.1. The two main objectives identified in this section are:

1. Determination of undeteriorated load--deformation characteristics.

2. Determination of parameters that permit an assessment of deterioration and closeness to failure.

The determination of undeteriorated load--deformation characteristics can be accomplished through a cyclic load test, or perhaps even through a monotonic load test, that takes advantage of knowledge on the cyclic stress-strain properties of the material, and that accounts for the boundary conditions of the component as part of the structural configuration. Information on boundary conditions can be obtained from analytical response predictions or from quasi-static or dynamic (shake table) tests of prototypes or scale models of complete structures or representative substructures.

No specific recommendations are made here for the determination of undeteriorated response characteristics because these characteristics can be obtained as a by-product of experimentation directed towards the second objective. The second objective has to do with an assessment of deterioration and failure under any type of deformation history the component may undergo when it is part of a structural system which may be subjected to one or several severe earthquakes during its expected life time.

For this purpose, parameters must be determined that permit a generalization of test results to random loading histories. A single test cannot provide the information needed for this purpose. In Chapters 3 to 5 it was attempted to show that a multi-specimen testing program is an appropriate means for the determination of parameters that permit an

assessment of component performance under random loading. Performance assessment may be based on cumulative damage models of which the one given by Eq. (3.9) is the simplest one.

Equation (3.9) assumes the existence of a Coffin-Manson type relationship [Eq. (3.8)] between a relevant deformation parameter ($\Delta\delta_p$) and the number of cycles to failure under constant amplitude cycling. The parameters that determine this relationshp are the coefficient C and the exponent c. If the hypothesis of linear damage accumulation can be accepted, then the damage model is fully defined with only these two parameters [e.g., Eq. (3.9)].

Thus, experimentation for performance assessment (deterioration and failure) should be directed towards the determination of the structural performance (damage) parameters C and c. Testing procedures for this purpose are discussed in the next section. The two major problems in implementing these testing procedures are, firstly, the uncertainties inherent in the parameters C and c, and secondly, a lack of confidence in the accuracy of the damage model. The first problem can be addressed by testing a statistically representative sample set of specimens, whereas the second problem can be addressed only through further research.

7.1 MULTI-SPECIMEN TESTING PROGRAM

This testing program is concerned with the determination of the structural performance parameters C and c needed to describe the deterioration threshold range, or the deterioration range, or both ranges together (see Fig. 2.4). The following aspects need to be considered in such a testing program.

Types of Loading Histories. Baseline data on low-cycle fatigue behavior are always obtained from constant amplitude tests. These tests will provide the information on C and c by plotting, on a log-log scale, the number of cycles to "failure" against the deformation range of each test. "Failure" in this context denotes the onset of noticeable deterioration (for modeling of deterioration threshold) or the attainment of an acceptable limit of deterioration (for modeling of deterioration). The term "constant amplitude test" refers to

symmetrically applied cycles of constant load or deformation amplitude. In low-cycle fatigue studies, deformation amplitude is usually preferred to load amplitude. If the inelastic deformations are large, it can be assumed that damage is caused by plastic deformations alone and the elastic deformation component may be neglected. Thus, the plastic deformation range, $\Delta\delta_p$, appears to be the best suited parameter for a correlation with the number of cycles to failure. Figure 7.1 shows two constant deformation amplitude cycles and the corresponding plastic deformation ranges. Because of cycling hardening or deterioration, a constant deformation amplitude test may result into slightly different plastic deformation ranges. Unless these differences are large, there should be no need to change from a constant deformation amplitude test to a constant plastic deformation range test which is much more difficult to perform.

Tests with variable amplitude cycling cannot be used to obtain information on C and c, but are most useful to examine the accuracy of the cumulative damage model given by Eq. (3.9). Such tests may be used to evaluate the uncertainty in the limit value of damage, γ, that constitutes failure (see Section 3.2.2). The histories selected for variable amplitude tests can be based on subjective decisions, or more appropriately, should be based on expected seismic response behavior. Representative loading histories are discussed in Section 7.2.

Other useful histories include histories with large mean deformations and histories which consider sequence effects (high-low and low-high sequences). If such tests disclose considerable mean deformation or sequence effects, the simple damage model given by Eq. (3.9) is inadequate and should be supplemented by additional parameters.

Number of Tests. Simply, the more tests there are performed, the more reliable the information will be. The pilot studies discussed in Chapter 5 have shown that constant amplitude lives, and therefore the parameters C and c, may exhibit a considerable scatter. This scatter may come from differences in microstructural properties and differences in manufacture, fabrication and workmanship. The scatter appears to be larger and is of more consequence in brittle failure modes (fracture) than in failure modes caused by gradual deterioration.

As an absolute minimum, two constant amplitude tests are required in order to determine the parameters C and c. The confidence to be placed in results obtained from only two tests should be low, unless similar tests have shown that the scatter in lives is very small and that the $N_f - \Delta\delta_p$ relationship can be described accurately by a Coffin-Manson type model [Eq. (3.8)]. The number of tests that should be performed is a function of cost and of the cumulative experience gained in testing of a specific component or failure mode. Without prior experience, a statistically representative sample of specimens should be tested at various amplitudes in order to evaluate the uncertainties in C and c. As more information becomes available on specific failure modes, the number of tests can possibly be reduced considerably. For instance, in the crack propagation study discussed in Section 5.4, it is conceivable that the exponent β in the damage model given by Eq. (5.7) is insensitive to variations in geometry and initial imperfections. If this is shown to be true, the effects of geometry and imperfections (initial crack size) can be assessed from tests at only one representative strain amplitude.

Representative Deformation Parameters. The damage model expressed by Eqs. (3.8) and (3.9) is based on the existence of a deformation parameter $\Delta\delta_p$ that correlates with the number of cycles to failure. The choice of a suitable deformation parameter depends on the source of deterioration and failure. If the source is localized, so should be the deformation parameter. For instance, in a crack propagation and fracture mode of failure, the state of strain or strain energy at the crack tip region defines the crack growth rate and the corresponding deformation parameter ($\Delta\varepsilon_p$, ΔJ). If the failure mode involves a region, the deformation parameter should be regional and not local (e.g., plastic hinge rotation for local buckling mode of deterioration).

Test Control. In order to determine the parameters C and c, tests need to be performed in which the deformation parameter to be used in Eq. (3.8) is kept constant in each test. This is by no means a simple task, particularly if a localized deformation parameter (e.g., strain) is used. Controlling a localized parameter, such as strain, in a test poses two distinct problems. First, strain measurements are always

subject to measurement errors and test control is lost once a strain gage results in unreliable measurements. Secondly, a generalization of test results is most difficult because localized strain histories can hardly ever be predicted analytically with confidence for loading histories different from those used in the tests. It appears to be more suitable to use a global deformation parameter for test control when possible. This can be done if a constant global deformation amplitude test results approximately in a constant plastic deformation range for the localized parameter used for damage modeling. This was done, for instance, in the crack propagation study discussed in Chapter 5 where deflection control was used in the constant amplitude tests which resulted in close to constant plastic strain ranges. Furthermore, if a relationship can be established from the tests between the global and local deformation parameters, a generalization of test results is much facilitated.

Evaluation and Utilization of Test Results. Experimentation of the type discussed here provides information on the performance parameters C and c and their uncertainties. An assessment of the relative performance of different components can be achieved directly from a comparison of the Coffin-Manson relationships. Such a comparison should account for the uncertainties in C and c which may differ considerably from component to component.

An assessment of component performance as part of a structure can be based on the cumulative damage model [Eq. (3.9)] and analytical predictions of the seismic demand. For instance, a time history analysis of a structure, of which the component is a part, could be performed to identify the number and magnitudes of the plastic deformation ranges the component may experience. Substitution of these values into Eq. (3.9) will result in a damage parameter for the component as part of a specific structure subjected to a specific ground motion.

A more general approach is to base performance assessment on statistical information on deformation demands. Such statistical information was derived in Chapter 6 for a limited range of single degree of freedom systems. More research needs to be done to cover a comprehensive range of structural systems and to correlate component

deformation demands with the statistical deformation demands (number and magnitudes of plastic deformation ranges) derived for structural systems.

Applications. The testing procedures recommended here can be applied to most components whose performance is governed by local failure modes. The following examples cover many of the failure modes of importance in the seismic response of steel structures.

1. Beam and Column Bending. In bending, these elements may be subjected to local and lateral torsional buckling. In both modes a deterioration threshold and gradual deterioration of the type shown in Fig. 2.4b are expected. The testing and modeling procedures discussed in Section 5.5 can be utilized in both cases. The plastic hinge rotation appears to be the best suited deformation parameter for damage modeling.

2. Crack Propagation and Fracture at Beam-to-Column Moment Connections. In beam to column flange connections, failure may occur at the weld toe, within the weld, at the weld to column interface or in the column material (see Fig. 4.12). In beam to column web connections, failure is likely to occur at the beam flange to continuity plate connection (Fig. 7.2). Thus, several failure modes have to be investigated, requiring an extensive parameter study. When considerable inelastic deformations are expected, a localized deformation parameter (e.g., $\Delta\varepsilon_p$, ΔJ) should be used for damage modeling. In the through-thickness direction of the column flange, where the state of stress is likely elastic, a local stress parameter ($\Delta\sigma$, ΔK) appears to be a better choice.

3. Shear Behavior of Beam-Column Joints. Failure modes due to shear distortion in joints include shear buckling of the panel zone, weld fracture in doubler plate connections, and beam weld fracture (see Fig. 7.3). For all three modes, the average angle of shear distortion of the panel zone should be an appropriate deformation parameter.

4. Fracture at Net Sections of Bolted Moment Splices. The critical sections are the first bolt line in the beam flange and the last bolt

line in the splice plate (see Fig. 7.4). Fracture is a consequence of necking across the net section or, more likely, of crack propagation initiated at stress concentrations at the bolt holes. Localized strain at the bolt holes would be the most relevant deformation parameter but is difficult to measure and to correlate with a global deformation parameter. Thus, an average strain across the bolt line appears to be a better parameter for damage modeling.

5. Fracture at Net Sections of Bolted Brace Connections. This failure mode is similar to the one discussed in the fourth example. Again, average strain across the net section of the connected leg should be a suitable deformation parameter. Displacement across the connection would be an inappropriate parameter for damage modeling because it includes the slip between the connected plates.

Each one of the failure modes listed in these examples can be evaluated by means of the testing procedures recommended here. However, there are also failure modes for which the testing procedures would have to be modified. The most important example is the member buckling mode which leads to unsymmetic and pinched hysteresis loops. In this case, performance assessment based on constant amplitude testing appears to be inappropriate. Difficulties would also be encountered if two (or more) failure modes occur simultaneously and affect each other (e.g., simultaneous local and lateral torsional buckling). It is conceivable that the proposed damage model still applies, provided that both failure modes can be described by the same deformation parameter. Only further research will show to what extent this is true.

It must be emphasized that the proposed testing procedures are based on two hypotheses. One is the existance of a Coffin-Manson relationship between N_f and $\Delta\delta_p$, the other is the acceptance of Miner's rule. Both hypotheses are based on empirical observations and cannot be derived from theory. Miner's rule has proven shortcomings, i.e., the neglect of mean deformation and sequence effects. Thus, performance assessment based on this type of testing will be only approximate. Nevertheless, it should be feasible and probably quite accurate if an appropriate deformation parameter $\Delta\delta_p$ is chosen for damage modeling. The

selection of this deformation parameter, which depends on the failure mode, is therefore a critical aspect of testing.

It is often advocated (see Section 2.2.2) to use a hysteretic energy term rather than deformation as a damage parameter. This should be feasible if the energy term is as localized as the deformation quantity. For instance, ΔJ is a localized energy term for crack propagation and may be a better parameter than plastic strain range. As an other example, hysteretic energy dissipation in beam bending could be used instead of plastic hinge rotation to model local buckling, since the two quantities are closely related. It would be conceptually wrong, however, to use a global hysteretic energy term to model a localized failure mode such as crack propagation and fracture.

7.2 SINGLE SPECIMEN TESTING PROGRAM

For economic reasons the single specimen testing program needs to be considered although it will not permit a performance assessment of the type discussed in the previous section.

For verification purposes (proof testing) one could decide to predict the largest possible deformation demand on the component for the largest possible earthquake and apply a loading history which exceeds this demand in number of excursions and size of deformation amplitudes. This is not the most useful approach since only very few realistic components would survive this rigorous test. The alternative is to develop a loading history based on a statistical seismic response evaluation, including information on the probabilistic distribution of plastic deformation ranges and statistically acceptable values for the number of damaging excursions, the maximum plastic deformation range, and the mean plastic deformation. This was the purpose of the study summarized in Chapter 6.

For the development of statistically representative cyclic loading histories, the strength and stiffness characteristics of the structure of which the component is a part must be known. Based on these characteristics, an equivalent single degree of freedom system can be developed for which the statistical parameters discussed in Chapter 6 can be determined. These parameters, which apply for the structural

system, must be converted into corresponding component parameters [N', $(\Delta\delta_p)_{max}$, $\delta_{p,mean}$]. Procedures that can be used for this purpose are presently under development (124).

Knowing the component response parameters, the procedure outlined in Section 6.6.1.3 can be utilized to derive N' values of the plastic deformation ranges $\Delta\delta_{pi}$. The magnitudes of $\Delta\delta_{pi}$ depend on the choice of $(\Delta\delta_p)_{max}$, which may be the mean, or the mean plus standard deviation, or a selected percentile value of the probabilistic distribution. The number N' depends on the choice of strong motion duration D_{sm}.

Loading histories can now be generated that result in N' excursions with plastic deformation ranges $\Delta\delta_{pi}$. Because the statistical information on $\Delta\delta_p$ has been obtained by employing the rain-flow cycle counting method to time history results, the N' ranges should not be linked together directly to form a loading history unless the ranges are ordered so that each subsequent excursion is of increasing magnitude. Only in this case will the rain-flow ranges and time history ranges be identical. For a randomly arranged history, a trial and error procedure has to be employed to arrange excursions so that all plastic deformation ranges $\Delta\delta_{pi}$ are recovered once the rain-flow cycle counting method is applied to the history.

An example of loading history generation is shown in Fig. 7.5. In this example, a SDOF system with T=0.5 seconds, R=4 and α=0.0 is assumed to represent the structural system. It is further assumed that the response parameters of the component are the same as those of the SDOF system. The number of inelastic excursions, N', is taken as 27 (arithmetic mean from Table 6.5), the mean plus standard deviation of $(\Delta\delta_p)_{max}$ is $6.06\delta_y$ (see Table 6.7) and the mean plastic deformation $\delta_{p,mean}$ is $1.73\delta_y$ (see Table 6.9). With this information, 27 plastic deformation ranges are obtained from the CDF of $\Delta\delta_p$ (see Section 6.6.1.3). Two examples of loading histories that are generated from these 27 $\Delta\delta_{pi}$ values are shown in Fig. 7.5. Although the two histories appear to be totally different, they have identical plastic deformation ranges (shown in the line diagrams to the right of the histories) and an identical mean plastic deformation of $1.73\delta_y$. Thus, both histories are expected to cause the same damage (if sequence effects can be ignored)

and both histories contain statistically obtained characteristics of the seismic response of the system.

A component test with one of these loading histories will be an indication of component performance within the constraints of the selected seismic response parameter. If integrity is to be demonstrated with less uncertainty, more conservative values should be selected for $(\Delta\delta_p)_{max}$ (e.g., 95 percentile value) and N' (based on a statistics of D_{sm} and regression of N on D_{sm}). Thus, in a single test one can consider the uncertainties in ground motions, but not the uncertainties in structural performance. Only a multi-specimen testing program can provide information on the latter uncertainties.

7.3 ADDITIONAL CONSIDERATIONS

This report has addressed a specific type of component experimentation, that is, quasi-static cyclic load testing. In this type of testing, the issues of strain rate effects and size effects must be addressed.

Strain rate effects will always be present in quasi-static testing in which the rate of straining of the material may be 1/100 to 1/1000 of that in the simulated event, the earthquake. It is widely accepted that these strain rate effects are not very important in the seismic response of steel structures. An increase in strain rates leads to an increase in strength properties (see Fig. 7.6) and to a slight change in the hysteresis loops (125,126). These effects should not change the performance of a component by much. However, insufficient evidence is available in the literature to draw the same conclusion on the effect of strain rates on localized failure modes such as crack propagation. Although tests have disclosed little sensitivity of crack growth rates to the cycling frequency in the elastic regime (127), it is not known whether the same holds true in the regime of plastic fracture mechanics.

Size effects come into play when reduced scale models of components are tested. Here again, a distinction should be made between size effects on basic stress-strain properties and size effects on local failure modes. A reduction in size leads to a small increase in yield stress for tension specimens and to a sizable increase in yield stress

for bending elements (128) because of the increase in strain gradient. These increases should not have much effect on performance.

However, size effects may have a very strong influence on deterioration and failure caused by crack propagation. Not only are crack growth rates size dependent but, more important, initial imperfections which are the source of crack growth cannot be reproduced at reduced scales. This holds true for the fusion zones of all types of welded connections and for base material stressed in the through direction (perpendicular to the direction of rolling). In this direction, the size and distribution of imperfections depends strongly on the thickness of the plate. Thus, it is hardly every possible to draw quantitative conclusions on seismic performance from tests with reduced scale models if the failure mode is governed by crack propagation. This holds true whether the scale is 1:2 or 1:20.

Size effects should be of lesser and often negligible importance when a deterioration and failure mode is of regional nature. For instance, it should be feasible to study local and lateral torsional buckling modes of deterioration on small rolled shapes and draw general conclusions on the seismic performance of large rolled shapes.

Thus, the type of failure mode will determine whether reduced scale models can be used for performance assessment. Small-scale models (e.g., 1:5 and smaller) should not be used for a quantitative assessment of individual failure modes in components. Their value lies in an assessment of overall strength--deformation characteristics of structural configurations which cannot be tested in the prototype domain because of size constraints.

REFERENCES

1. "Specifications for the Design, Testing, and Utilization of Industrial Steel Storage Racks," ANSI MH16.1.

2. Popov, E.P., and Stephen, R.M., "Cyclic Loading of Full-Size Steel Connections," Steel Research for Construction, Bulletin No. 21, American Iron and Steel Institute, New York, N.Y., Feb. 1972.

3. "Recommended Practices for Seismic Qualification of Class 1E Equipment for Nuclear Power Generating Stations," ANSI/IEEE Standard 344.

4. Smith, P.D., and Dong, R.G., "Correlation of Seismic Experience Data in Nonnuclear Facilities with Seismic Equipment Qualification in Nuclear Plants," draft of a report to the NRC, November 1982.

5. "Standard Practice of Load Tests for Shear Resistance of Framed Walls for Buildings," ASTM Standard E564, Draft No. 8, February 1982.

6. "Conducting Strength Tests of Panels for Building Construction," ASTM Standard E72.

7. "Standard Method for Static Load Testing of Framed Floor or Roof Diaphragm Construction for Buildings," ASTM Standard E455.

8. "Flexural Tests of Beams and Girders for Building Construction," ASTM Standard E529.

9. "Standard Practice for Reporting Data from Structural Tests of Building Construction, Elements, Connections, and Assemblies," ASTM Standard E575.

10. "Full-Scale Load Testing of Structures," ASTM STP 702, American Society for Testing and Materials, 1980.

11. "State-of-the-Art of Structural Test Methods for Walls, Floors, Roofs and Complete Buildings," NBS Building Science Series 58, U.S. Department of Commerce, November 1974.

12. "Standard Recommended Practice for Constant-Amplitude Low-Cycle Fatigue Testing," ASTM Standard E606.

13. "Standard Test Method for Constant-Load Amplitude Fatigue Crack Growth Rates Above 10^{-8} m/Cycle," ASTM Standard E647.

14. "Standard Test Method for J_{IC}, A Measure of Fracture Toughness," ASTM Standard E813.

15. "Standard Definitions of Terms Relating to Constant-Amplitude Low-Cycle Fatigue Testing," ASTM Standard E513.

16. "Standard Terminology Relating to Fracture Testing,," ASTM Standard E616.

17. "Structural Welding Code," AWS D1.1, American Welding Society.

18. Popov, E.P., and Malley, J.O., "Eccentrically Braced Frames (EFBs)," Chapter 11 of Monograph on Beam-to-Column Building Connections, ASCE, in preparation.

19. Krawinkler, H., Bertero, V.V., and Popov, E.P., "Inelastic Behavior of Steel Beam-to-Column Subassemblages," Report No. EERC 71-7, College of Engineering, University of California, Berkeley, October 1971.

20. "Code of Practice for General Structural Design and Design Loadings for Buildings," NZS 4203:1976, Standards Association of New Zealand, 1976.

21. Bertero, V.V., and Popov, E.P., "Effects of Large Alternating Strains of Steel Beams," Journal of the Structural Division, ASCE, Vol. 91, No. ST 1, February 1965.

22. Popov, E.P., and Pinkney, R.B., "Cyclic Yield Reversals on Steel Building Connections," Journal of the Structural Division, ASCE, Vol. 95, No. ST 3, March 1969.

23. Popov, E.P., and Pinkney, R.B., "Behavior of Steel Building Connections Subjected to Inelastic Strain Reversals," Steel Research for Construction, Bulletins No. 13 and 14, American Iron and Steel Institute, November 1968.

24. Popov, E.P., and Stephen, R.M., "Cyclic Loading of Full Size Steel Connections," EERC Report No. 70-3, College of Engineering, University of California, Berkeley, 1970.

25. Popov, E.P., and Bertero, V.V., "Cyclic Loading of Steel Beams and Connections," Journal of the Structural Division, ASCE, Vol. 99, No. ST 6, June 1973.

26. Mizuhata, K., Gyoten, Y., and Kitamura, H., "Study on Low Cycle Fatigue of Structural Frames Due to Randomly Varying Load," Preprints, 6th World Conference on Earthquake Engineering, New Delhi, India, January 1977.

27. Dowling, N.E., "Fatigue Failure Predictions for Complicated Stress-Strain Histories," T. & A.M. Report No. 337, Department of Theoretical and Applied Mechanics, University of Illinois, Urbana, Illinois, January 1971.

28. Srinivasan, R., and Munse, W.H., "Fatigue Damage in Seismic Steel Members," Proceedings, International Conference on Planning and Design of Tall Buildings, Vol. 2, ASCE-IABSE, 1972.

29. Suidan, M.T., and Eubanks, R.A., "Cumulative Fatigue Damage in Seismic Structures," Journal of the Structural Division, ASCE, Vol. 99, No. ST 5, May 1973.

30. Suidan, M., and Eubanks, R.A., "Cumulative Fatigue Damage in Seismic Structures," Proceedings, 5th World Conference on Earthquake Engineering, Rome, Italy, June 1973.

31. Morrow, J.D., "Cyclic Plastic Strain Energy and Fatigue of Metals," ASTM, STP No. 378, June 1964.

32. Kasiraj, I., "Fatigue Failure of Nonlinear Multistory Seismic Structures," Journal of the Structural Division,, ASCE, Vol. 98, No. ST 3, March 1972.

33. Yao, J.T.P., and Munse, W.H., "Low-Cycle Axial Fatigue Behavior of Mild Steel," ASTM, STP No. 338, October 1962.

34. Freudenthal, A.M., "The Safety of Structures," Proceedings, ASCE, October 1945.

35. Freudenthal, A.M., Garrelts, J.M., and Shinozuka, M., "The Analysis of Structural Safety," Journal of the Structural Division, ASCE, Vol. 92, No. ST1, February 1966.

36. Basquin, O.H., "The Exponential Law of Endurance Tests," Proceedings, ASTM, Vol. 10, Part II, 1910, p. 625.

37. Coffin, L.F., Jr., "A Study of the Effect of Cyclic Thermal Stresses in Ductile Metals," Transactions of ASME, Vol. 76, pp. 931-950, 1954.

38, Manson, S.S., "Behavior of Materials under Conditions of Thermal Stress," NACA TN 2933, 1954.

39. Morrow, J., "Cyclic Plastic Strain Energy and Fatigue of Metals," Internal Friction, Damping and Cyclic Plasticity, ASTM STP 378, 1965.

40. Miner, M.A., "Cumulative Damage in Fatigue," Journal of Applied Mechanics, September 1945.

41. Palmgren, A., "Die Lebensdauer von Kugellagern," Z. Vereines Deutscher Ingenieure, 68, 1924 (in German).

42. Leve, H.L., "Cumulative Damage Theories," Metal Fatigue: Theory and Design, A.F. Madayag, Coordinating author, John Wiley & Sons, 1969, pp. 170-203.

43. Bussa, S.L., Sheth, N.J., and Swanson, S.R., "Development of a Random Load Life Prediction Model," Materials Research and Standards, ASTM, Vol. 12, No. 3, March 1972, pp. 31-43.

44. Morrow, J., "Fatigue Properties of Metals," Section 3.2 of Fatigue Design Handbook, Society of Automotive Engineers, 1968.

45. Smith, K.N., Watson, P., and Topper, T.H., "A Stress-Strain Function for the Fatigue of Metals," Report No. 21, Solid Mechanics Division, University of Waterloo, Ontario, Canada, October 1969.

46. Hardrath, H.F., "A Review of Cumulative Damage for Fatigue," Committee of the Structure and Materials Panel Advisory Group for Aeronautical Research and Development, NASA Langley Research Center, Hampton, VA., June 1965.

47. Corten, H.T., "Overstressing and Understressing in Fatigue," Metals Engineering Design, ASME Handbook, O.J. Horger, Ed., McGraw-Hill, 1965, pp. 231-241.

48. Topper, T.H., Sandor, B.I., and Morrow, J., "Cumulative Fatigue Damage under Cyclic Strain Control," Journal of Materials, Vol. 4, No. 1 March 1969, pp. 189-199.

49. Dowling, N.E., "Fatigue Failure Predictions for Complicated Stress-Strain Histories," Report No. 337, Department of Theoretical and Applied Mechanics, University of Illinois, January 1971.

50. Topper, T.H. and Sandor, B.I., "Effects of Mean Stress and Prestrain on Fatigue Damage Summation," Effects of Environment and Complex Load History on Fatigue Life, ASTM STP 462, 1970, pp. 93-104.

51. Manson, S.S., "Fatigue: A Complex Subject - Some Simple Approximations," Experimental Mechanics, Vol. 5, No. 7, July 1965.

52. Marco, S.M. and Starkey, W.L., "A Concept of Fatigue Damage," Transactions of ASME, Vol. 76, 1954, pp. 627-632.

53. Sweet, A.L., and Kozin, F., "Investigation of a Random Cumulative Damage Theory," Journal of Meterials, ASTM, Vol. 3, No. 4, December 1968, pp. 802-823.

54. Fuchs, H.O., and Stephens, R.I., Metal Fatigue in Engineering, John Wiley and Sons, 1978.

55. Matsuishi, M., and Endo, T., "Fatigue of Metals Subjected to Varying Stress," presented at Japan Society of Mechanical Engineers, Fukuoka, Japan, 1968.

56. Suidan, M.T., "On Cumulative Fatigue Damage in Seismic Structures," Ph.D. Thesis, Civil Engineering Department, University of Illinois, Urbana, Illinois, 1971.

57. Cofie, N.G., "Cyclic Stress-Strain and Moment-Curvature Relationships for Steel Beams and Columns," Ph.D. Dissertation, Department of Civil Engineering, Stanford University, June 1983.

58. Dafalias, Y.F., and Popov, E.P., "Plastic Internal Variables Formalism of Cyclic Plasticity," Journal of Applied Mechanics, ASME, Vol. 43, Dec., 1976.

59. Dafalias, Y.F., "On Cyclic Anisotropic Plasticity," Ph.D. Thesis, University of California, Berkeley, 1975.

60. Ramberg, W., and Osgood, W.R., "Description of Stress-Strain Curves by Three Parameters," National Advisory Committee for Aeronautics, TN902, 1943.

61. Masing, G., "Eigenspannunger und Verfestigung beim Messing," Proceedings of the Second International Congress for Applied Mechanics, Zurich, September, 1926.

62. Martin, J.F., Topper, T.H., and Sinclair, G.M., "Computer Based Simulation of Cyclic Stress-Strain Behavior with Applications to Fatigue," Materials Research and Standards, MTRSA, Vol. 11, No. 2, pp. 23.

63. Santhanam, T.K., "Model for Mild Steel in Inelastic Frame Analysis," Journal of the Structural Division, ASCE, Vol. 105, No. ST1, Jan. 1979.

64. Jhansale, H.R., "A New Parameter for the Hysteresis Stress-Strain Behavior of Metals," Journal of Eng. Materials and Technology, Trans. ASME, Jan. 1973, pp. 33.

65. Popov, E.P. and Ortiz, M., "Macroscopic and Microscopic Cyclic Metal Plasticity," Keynote Address, Proceedings of the Third Eng. Mech. Specialty Conference, ASCE, Austin, Texas, September 17-19, 1979.

66. Atkan, A.E., Karlson, B.I. and Sozen, M.A., "Stress-Strain Relationships of Reinforcing Bars Subjected to Large Strain Reversals," Civil Eng. Studies, SRS No. 297, University of Illinois, Urbana-Champaign, Illinois, June 1973.

67. Halford, G.E. and Morrow, JoDean, "Low Cycle Fatigue in Torsion," Proceedings, ASTM, Vol. 62, 1962, pp. 695-707.

68. Menegotto, M. and Pinto, P., "Method of Analysis for Cyclically Loaded Reinforced Concrete Plane Frames Including Changes in Geometry and Nonelastic Behavior of Elements Under Combined Normal Force and Bending," IABSE Symposium on the Resistance and Ultimate Deformability of Structures Acted on by Well-Defined Repeated Loads, Lisbon, 1973.

69. Petersson, H. and Popov, E.P., "Constitutive Relatives for Generalized Loadings," Journal of the Engineering Mechanics Division, ASCE, Vol. 103, No. EM4, August 1977.

70. "Standard Methods for Tension Testing of Metallic Materials," ASTM Standard E8.

71. ASCE Committee on Fatigue and Fracture Reliability, "Fatigue and Fracture Reliability: A State-of-the-Art Review," Journal of the Structural Division, ASCE, Vol. 108, No. ST1, Jan. 1982.

72. Zohrei, M., "Cumulative Damage in Components of Steel Structures under Cyclic Inelastic Loading," Ph.D. Dissertation, Department of Civil Engineering, Stanford University, December 1982.

73. Fracture Toughness Testing, ASTM STP 381, 1968.

74. Fatigue Crack Propagation, ASTM STP 415, 1967.

75. Effects of Environment and Complex Load History on Fatigue Life, ASTM STP 462, 1970.

76. Damage Tolerance in Aircraft Structures, ASTM STP 486, 1971.

77. Testing for Prediction of Material Performance in Structures and Components, ASTM STP 515, 1972.

78. Cyclic Stress Strain Behavior--Analysis, Experimentation and Failure Prediction, ASTM STP 519, 1973.

79. Progress in Flaw Growth and Fracture Toughness Testing, ASTM STP 536, 1973.

80. Mechanics of Crack Growth, ASTM STP 590, 1976.

81. Fracture Crack Growth and Spectrum Loads, ASTM STP 595, 1976.

82. Cracks and Fracture, ASTM STP 601, 1976.

83. Flaw Growth and Fracture, ASTM STP 631, 1977.

84. Cyclic Stress-Strain and Plastic Deformation Aspects of Fatigue Crack Growth, ASTM STP 637, 1977.

85. Fatigue Testing of Weldments, ASTM STP 648, 1978.

86. Elastic-Plastic Fracture, ASTM STP 668, 1979.

87. Fatigue Mechanisms, ASTM STP 675, 1949.

88. Proceedings of the 12th National Symposium on Fracture Mechanics, ASTM STP 700, 1982.

89. Standard Recommended Practice for Constant Amplitude Axial Fatigue Tests of Metallic Materials," ASTM Standard E466.

90. "Standard Methods for Notched Bar Impact Testing of Metallic Materials," ASTM Standard E23.

91. "Standard Test Methods for Plane-Strain Fracture Toughness of Metallic Materials," ASTM Standard E399.

92. "Standard Practice for R-Curve Determination," ASTM Standard E561.

93. "Standard Practice for Fracture Testing with Surface-Crack Tension Specimens," ASTM Standard E740.

94. Miller, W.R., and Amin, H.S., "Low-Cycle Fatigue in Welds," Journal of Experimental Mechanics, SESA, Vol. 15, No. 6, June 1975.

95. Adams, C.J., and Popov, E.P., "Through Thickness Fatigue Properties of Steel Plate," Bulletin No. 217, Welding Research Council, July 1976.

96. Paris, P.C., "The Growth of Fatigue Cracks due to Variations in Load," Ph.D. Thesis, Lehigh University, 1962.

97. Rice, J.R., "A Path-Independent Integral and the Approximate Analysis of Strain Concentration by Notches and Cracks," Journal of Applied Mechanics, Vol. 35, 1968, pp. 378-386.

98. Crooker, T.W., and Lange, E.A., "Low Cyclic Fatigue Crack Propagation Resistance of Materials for Large Welded Structures," Fatigue Crack Propagation, ASTM STP 415, 1967, pp. 94-125.

99. Solomon, H.D., "Low-Cycle Fatigue Crack Propagation in 1018 Steel," Journal of Materials, Vol. 7, No. 3, September 1972, pp. 229-306.

100. Mowbray, D.F., "Use of a Compact-Type Strip Specimen for Fatigue Crack Growth Rate Testing in the High-Rate Regime," in Elastic-Plastic Fracture, ASTM STP 668, 1979, pp. 736-752.

101. Dowling, N.E., "Geometry Effects and the J-Integral Approach to Elastic-Plastic Fatigue Crack Growth," Cracks and Fracture, ASTM STP 601, American Society for Testing and Materials, 1976, pp. 19-32.

102. Wheeler, O.E., "Spectrum Loading and Crack Growth," Journal of Basic Engineering, Transactions of ASME, Vol. 94, 1972, pp. 181-186.

103. Willenborg, J., Engle, R.M., and Wood, H.A., "A Crack Growth Retardation Model Using an Effective Stress Concept," WPAFB, TM-71-1-FBR, 1971.

104. Elber, W., "The Significance of Fatigue Crack Closure," Damage Tolerance in Aircraft Structures, ASTM STP 486, 1971, pp. 230-242.

105. Lloyd, G.J., "On the Use of Electrical Analogues in Crack Propagation Experiments," Report No. 2818, Risley Engineering and Materials Laboratory, United Kingdom Atomic Energy Authority, March 1976.

106. Cheng, Y.W., McHenry, I.H., and Read, D.T., "Crack-Opening Displacement of Surface Cracks in Pipeline Steel Plates," ASTM Symposium on Fracture Mechanics, Los Angeles, June 1981.

107. Higashida, Y., "Strain Controlled Fatigue Behavior of Weld Metal and Heat-Affected Base Metal in A36 and A514 Steel Welds," Ph.D. Thesis, Department of Metallurgical Engineering, University of Illinois, Urbana, Illinois, 1976.

108. Lashkari-Irvani, B., "Cumulative Damage Parameters for Bilinear Systems Subjected to Seismic Excitations," Ph.D. Dissertation, Department of Civil Engineering, Stanford University, August 1983.

109. Applied Technology Council, Tentative Provisions for the Development of Seismic Regulations for Buildings, National Bureau of Standards, Special Publication 510, ATC Publication ATC 3-06, June 1978.

110. California Institute of Technology, Earthquake Engineering Research Laboratory, "Strong Motion Earthquake Accelerograms, Digitized and Plotted Data," Vol. 2, Parts A through Y, 1969-1975.

111. Krinitzsky, E.L., and Chang, F.K., "State-of-the-Art for Assessing Earthquake Hazards in the United States; Earthquake Intensity and the Selection of Ground Motions for Seismic Design," Miscellaneous Paper S-73-1, Report 4, September 1975, U.S. Army Engineer Waterways Experiment Station, Vicksburg, Miss.

112. Seed, H.B., Ugas, C., and Lysmer, J., "Site-Dependent Spectra for Earthquake-Resistance Design," Report No. EERC 74-12, Earthquake Engineering Research Center, University of Californi, Berkeley, California, November 1974.

113. McCann, M.W., and Shah, H.C., "Determining Strong-Motion Duration of Earthquakes," Bulletin of the Seismological Society of America, Vol. 69, No. 4, August 1979, pp. 1253-1265.

114. Vanmarcke, E.H., and Lai, S.S., "Strong-Motion Duration of Earthquakes," Publication No. R77-16, Department of Civil Engineering, Massachusetts Institute of Technology, Cambridge, Mass., July 1977.

115. Vanmarcke, E.H., "State-of-the-Art for Assessing Earthquake Hazards in the United States; Representation of Earthquake Ground Motion: Scaled Accelerograms and Equivalent Response Spectra," Miscellaneous Paper S-73-1, Report 14, August 1979, U.S. Army Engineer Waterways Experiment Station, Vicksburg, Miss.

116. Iwan, W.D., and Lutes, L.D., "Response of the Bilinear Hysteretic System for Stationary Random Excitation," Journal of the Acoustical Society of American, Vol. 43, No. 3, 1968.

117. Barber, T., and Wen, Y.K., "Equivalent Linearization of Hysteretic Structures," Proceedings, The ASCE Specialty Conference on Probabilistic Mechanics and Structural Reliability, Tucson, Arizona, January 1979.

118. Newland, D.E., An Introduction to Random Vibrations and Spectral Analysis, Logman, 1975.

119. Riddle, R., and Newmark, N.M., "Statistical Analysis of the Response of Nonlinear Systems Subjected to Earthquakes," Civil Engineering Studies, Structural Research Series No. 468, Department of Civil Engineering, University of Illinois, Urbana, Illinois, August 1979.

120. Gumbel, E.F., Statistics of Extremes, Columbia University Press, 1958.

121. Benjamin, J.R., and Cornell, C.A., Probability, Statistics, and Decision for Civil Engineers, Mc-Graw Hill, 1970.

122. Hadidi-Tamjed, H., "Seismic Response of SDOF Systems Including P-δ Effect and Stiffness Degradation," Engineer's Thesis, Department of Civil Engineering, Stanford University, August 1983.

123. Mahin, S.A. and Bertero, V.V., "An Evaluation of Some Methods for Predicting the Seismic Behavior of Reinforced Concrete Buildings," Report No. EERC 75-5, University of California, Berkeley.

124. Lee, D.G., "Accurate and Simplified Models for Seismic Response Prediction of Steel Frame Structures," Ph.D. Dissertation, Department of Civil Engineering, Stanford University, in preparation.

125. Hanson, R.D., "Post-Elastic Dynamic Response of Mild Steel Structures," Ph.D. Dissertation, California Institute of Technology, May 1965.

126. Almuti, A.M., and Hanson, R.D., "Static and Dynamic Cyclic Yielding of Steel Beams," Journal of the Structural Division, ASCE, Vol. 99, No. ST6, June 1973.

127. Rolfe, S.T. and Barsom, J.M., Fracture and Fatigue Control in Structures, Prentice-Hall, Inc., Englewood Cliffs, New Jersey.

128. Richards, C.W., "Effect of Size on the Yielding of Mild Steel Beams," Proceedings, ASTM, 1958.

129. Moncarz, P.D. and Krawinkler, H., "Theory and Application of Experimental Model Analysis in Earthquake Engineering," John A. Blume Earthquake Engineering Center, Report No. 50, Department of Civil Engineering, Stanford University, June 1981.

TABLES AND FIGURES

Table 2.1 Number of Proof Tests to Achieve a Given Reliability with a Given Confidence (Ref. 4)

	Confidence Level %						
	50%	60%	70%	80%	90%	95%	99%
Reliability, R_L	Number of Proof Tests						
0.6	1	1	2	3	4	5	9
0.7	1	2	3	4	6	8	12
0.8	3	4	5	7	10	13	20
0.9	6	8	11	15	21	28	43
0.95	13	17	23	31	44	58	89
0.99	68	91	119	160	229	298	458

Table 4.1 Summary of Stress-Strain Parameters

Parameter	Symbol	Value
Yield Stress	σ_y	45.6 ksi
Yield Strain	ϵ_y	0.00157
Strain Hardening Strain	ϵ_{sh}	$14\epsilon_y$
Young's Modulus	E_e	29000 ksi
Slope of Stress Bound	E_p^o	$0.0075E^e$
Shape Factor	h	45.0
Elastic Stress Range	$C\sigma_y$	$1.2\sigma_y$
Monotonic Stress-Strain Curve Strength Coefficient	$\overline{K}$	0.51
Monotonic Stress-Strain Curve Hardening Exponent	$\overline{n}$	0.23
Cyclic Stress-Strain Curve Strength Coefficient	$\overline{K}'$	0.90
Cyclic Stress-Strain Curve Hardening Exponent	$\overline{n}'$	0.19
Hardening Factor	F_H	0.45
Softening Factor	F_S	0.07
Mean Stress Relaxation Factor	F_R	0.05

Table 5.1 Section Properties of Test Specimens

(a) B1 Specimens

Specimen	d(in)	b(in)	t_f (in)	t_w (in)	I (in^4)	ℓ (in)	M_y^* (k-in)	P_y^{**} (Kip)	K^{***}(K/in)
B1-1	4.252	4.049	0.350	0.265	11.883	40.19	273.9	6.82	16.47
B1-2	4.247	4.056	0.354	0.264	11.966	40.00	276.1	6.90	16.83
B1-3	4.251	4.055	0.350	0.267	11.924	40.06	274.9	6.86	16.69
B1-4	4.250	4.056	0.355	0.267	12.020	40.13	277.2	6.91	16.75
B1-5	4.253	4.055	0.356	0.269	12.068	40.25	278.1	6.91	16.66
B1-6	4.243	4.052	0.353	0.264	11.926	40.13	275.4	6.86	16.62
B1-7	4.237	4.053	0.355	0.266	11.925	40.06	275.7	6.88	16.69
B1-8	4.230	4.054	0.349	0.268	11.745	40.13	272.2	6.78	16.36
B1-9	4.236	4.048	0.347	0.265	11.708	40.06	270.8	6.67	16.39
B1-10	4.238	4.053	0.348	0.264	11.758	40.06	271.8	6.79	16.46

$^*M_y$ = Theoretical yield moment of section ($M_y = 2\sigma_y I/d$ in which σ_y = 49.0 Ksi is the yield stress)

$^{**}P_y = M_y/\ell$

$^{***}K$ = Theoretical elastic stiffness of section ($K = 3EI/\ell^3$)

(b) B2 Specimens

Specimen	d(in)	b(in)	t_f(in)	t_w(in)	I(in^4)	ℓ (in)	M_y^*(k-in)	P_y^{**}(Kip)	K^{***}(K/in)
B2-1	5.927	3.983	0.211	0.174	16.54	36.00	295.8	8.22	31.91
B2-2	5.917	3.984	0.213	0.174	16.60	36.12	297.4	8.23	31.70
B2-3	5.902	3.985	0.212	0.176	16.47	36.06	295.8	8.20	31.61
B2-4	5.924	3.980	0.210	0.174	16.46	36.00	294.5	8.18	31.75
B2-5	5.918	3.987	0.210	0.175	16.46	36.06	294.8	8.18	31.59
B2-6	5.923	3.988	0.210	0.174	16.48	36.12	294.9	8.17	31.47
B2-7	5.924	3.990	0.211	0.175	16.56	36.06	296.3	8.22	31.78
B2-8	5.924	3.985	0.210	0.174	16.47	36.06	294.7	8.18	31.61
B2-9	5.925	3.985	0.212	0.175	16.61	36.06	297.1	8.24	31.88
B2-10	5.923	3.988	0.213	0.177	16.68	36.12	298.7	8.27	31.87

$^*M_y$ = Theoretical yield moment of section ($My = 2\sigma_y I/d$ where σ_y = 53.0 Ksi is the yield stress)

$^{**}P_y = M_y/\ell$

$^{***}K$ = Theoretical elastic stiffness of section ($K = 3EI/\ell^3$)

Table 5.2 Crack Size Measurement Techniques (Ref. 105)

Technique	Comments
Direct Optical	Scribed lines on side of specimen or travelling vernier microscope. Tedious and subject to observer error although cameras may be used. Accuracy depends on crack front being normal to specimen surface. Can be used through gas box/ cell window etc.
Strain Gauge Filaments	Each filament breaks as crack propagates past it. Accuracy dependent on existence of straight crack front. Difficult to use in environment. Non-continuous.
Compliance Sensing	Measurements made from deflections of loading arm. Useful for stress-corrosion cracking and sodium testing where large chambers are present. Principal disadvantages (which usually preclude it from use) are that measurements include linkage deflections and that compliance is a function of load and therefore will vary in a non-uniform load test. Insensitive at short crack lengths.
Ultrasonic Techniques	High cost of equipment. Difficult to calibrate and interpret in present context. Probes incompatible with high temperature environment. Most accurate technique available but not suitable for single-edge notch or contoured double cantilever bend specimen. Averaging of any crack curvature dependent on probe size.
Acoustic Emission	Not fully developed for reliable use; extensive electronic gating required to discriminate during loading cycles. Theory of observed emissions in fatigue not well understood. Equipment extremely expensive; technique of no use in liquid metals.
AC Electrical Method	Utilizes skin effect and therefore is a surface measurement and subject to crack curvature errors. Finds widespread use in stress-corrosion testing as it avoids any plating-out effects associated with DC methods.
DC Potential Method	Current held constant, voltage rise noted. Flexible, output may be used to semi-automate testing. The most widely used technique in fatigue, creep crack growth, crack initiation in COD tests, hydrogen embrittlement tests. Very accurate calibrations required, equipment modifications needed. Oxide bridging can affect results in high-temperature tests. Cannot be used in electrically conducting fluids.
Measurements of Striation Spacing	Post-test technique, measurements of ductile fatigue striation spacing made in scanning electron microscope. Variation of technique is to program-load specimen and 'beach-mark' specimen surface and subsequently examine. Method susceptible to microstructural influences upon crack propagation rate. Non-continuous.
Notch Region Extension Method	Post-test technique for creep tests only; a micro photomontage of surface of cracked region is prepared and the time dependence of the notch region is obtained from the overall specimen extension measured during the test and the creep rate of an unnotched bar. Useful for in-sodium testing. Material must deform by creep in the presence of a notch for method to be valid.

Table 5.3 Testing Program for B1 Specimens

Specimen	Deflection History	Deflection Amplitude, $\Delta\delta/2$ (in)	Plastic Deflection Amplitude $\Delta\delta_p/2$ (in)	Plastic Rotation Amplitude at Base, $\Delta\theta_p/2 = \Delta\delta_p/2\ell$ (rad)	No. of Cycles to Through Crack/ Complete Flange Fracture	Stabilized End Load Response (Kips)	Stabilized Plastic Strain Amplitude at 5/8" from Weld Toe, $\Delta\varepsilon_p/2$ (in/in)
B1-1	monotonic	12.000	11.170	0.278	---	---	---
B1-2	cyclic with zero mean	3.073	2.358	0.0590	14/14	12.026	0.0215
B1-3	cyclic with zero mean	3.111	2.408	0.0601	8/8	11.733	0.0280
B1-4	cyclic with zero mean	3.084	2.373	0.0591	15/15	11.900	0.0258
B1-5	cyclic with zero mean	2.493	1.809	0.0449	21/21	11.412	0.0184
B1-6	cyclic with zero mean	2.490	1.806	0.0450	18/18	11.360	0.0201
B1-7	cyclic with zero mean	1.422	0.812	0.0203	90/92	10.187	0.0100
B1-8	cyclic with zero mean	1.453	0.830	0.0207	45/46	10.194	0.0113
B1-9	variable amplitude	---	---	---	---	---	---
B1-10	cyclic with mean equal to 0.729"	1.458	0.819	0.0204	83/86	10.514	0.0110

Table 5.4 Prediction of Initial Crack Size a_o

Specimen	$\Delta\varepsilon_p$(in/in)	$\bar{N}_f=N_f-2$	$a_{\bar{N}_f}$(in)	a_o(in)
B1-3	0.0560	6	0.068	0.00302
B1-4	0.0516	13	0.046	0.00014
B1-5	0.0368	19	0.094	0.00111
B1-6	0.0402	16	0.152	0.00183
B1-7	0.0200	88	0.219	0.00034
B1-8	0.0226	43	0.178	0.00333
Mean Value	-	-	--	0.00163
Standard Deviation, σ	--	-	--	0.00123

Table 5.5 Cumulative Damage for a Single Block in Variable Amplitude Test (Specimen B1-9)

Range	$\Delta\varepsilon_p$(%)	D (Cumulative Damage)	Range	$\Delta\varepsilon_p$(%)	D (Cumulative Damage)
S-1	+0.54	0.0010	17-16	-0.80	
1-4	-2.46		18-15	+1.31	0.1276
2-3	+0.66	0.0025	19-12	-2.07	
3-2	-0.66		20-27	+5.10	0.2158
4-11	+5.07	0.0896	21-24	-1.73	
5-8	-1.16		22-23	+1.16	0.2204
6-7	+0.75	0.0915	23-22	-1.16	
7-6	-0.75		24-21	+1.73	0.2307
8-5	+1.16	0.0961	25-26	-1.20	
9-10	-1.47		26-25	+1.20	0.2357
10-9	+1.47	0.1035	27-30	-3.27	
11-20	-5.06		28-29	+2.75	0.2615
12-19	+2.07	0.1182	29-28	-2.75	
13-14	-0.61		30-31	+3.25	0.2975
14-13	+0.61	0.1195	31-32	-2.28	
15-18	-1.31		32-E	+0.75	0.2994
16-17	+0.80	0.1217			

Table 5.6 Testing Program for B2 Specimens

Specimen	Deflection History	Deflection Amplitude, $\Delta\delta/2$ (in)	Plastic Deflection Amplitude, $\Delta\delta_p/2$ (in)	Plastic Rotation Amplitude at Base, $\Delta\theta_p/2=\Delta\delta_p/2\ell$	No. of Reversals to Through Crack/Complete Flange Fracture
B2-1	monotonic	(8.57)	---	---	---
B2-2	monotonic	(6.10)	---	---	---
B2-3	cyclic with zero mean	1.015	0.675	0.0187	27/31
B2-4	cyclic with zero mean	1.042	0.696	0.0193	31/37
B2-5	cyclic with zero mean	0.765	0.431	0.0120	43/55
B2-6	cyclic with zero mean	1.595	1.242	0.0344	(crack in buckle)
B2-7	cyclic with zero mean	0.606	0.284	0.00788	49/65
B2-8	cyclic with zero mean	1.031	0.691	0.0192	22/28
B2-9	variable amplitude	--	--	--	--
B2-10	cyclic with mean equal to 0.973"	0.777	0.438	0.0121	57/71

Table 5.7 Cyclic Response Parameters for Constant Amplitude Tests, B2 Specimens

	B2-4 δ = 1.042" $\Delta\delta_p/2$ = 0.696" $\Delta\theta_p/2$ = 0.0193 rad			B2-5 δ = 0.765" $\Delta\delta_p/2$ = 0.431" $\Delta\theta_p/2$ = 0.0120 rad			B2-6 δ = 1.595" $\Delta\delta_p/2$ = 1.242" $\Delta\theta_p/2$ = 0.0344 rad			B2-7 δ = 0.606" $\Delta\delta_p/2$ = 0.284 $\Delta\theta_p/2$ = 0.00788 rad			B2-8 δ = 1.031" $\Delta\delta_p/2$ = 0.691" $\Delta\theta_p/2$ = 0.0192 rad			B2-10 δ = 0.777" $\Delta\delta_p/2$ = 0.438" $\Delta\theta_p/2$ = 0.0121 rad		
2N	P*	K**		P	K	E***	P	K	E	P	K	E	P	K	E	P	K	E
(Rev)	(kips)	(kip/in)		(kips)	(kip/in)	(kip-in)	(kips)	(kip/in)	(kip-in)	(kips)	(kip/in)	(kip-in)	(kips)	(kip/in)	(kip-in)	(kips)	(kip/in)	(kip-in)
0	0	31.7		0	31.6	0	0	31.5	0	0	31.8	0	0	31.6	0	0	31.9	0
1	10.94	31.5		10.49	31.6	4.15	11.05	29.0	12.72	10.08	31.8	2.56	10.76	31.4	6.95	11.13	30.0	14.39
2	-10.96	29.2		-10.71	27.1	7.50	-10.26	21.0	24.31	-10.43	31.0	4.40	-11.15	27.1	13.29	-10.41	30.5	6.84
3	11.55	28.7		10.97	31.2	7.00	11.48	27.1	22.75	10.68	31.7	4.05	11.39	30.2	12.60	11.15	27.9	7.64
4	-11.12	26.9		-11.00	26.1	6.90	-9.24	19.3	22.63	-10.60	30.8	4.03	-11.42	25.8	12.66	-10.58	26.8	6.49
5	11.55	27.6		11.04	30.8	6.87	10.38	25.2	20.80	10.74	31.2	3.90	11.44	28.4	12.15	11.08	27.1	7.47
26	-9.00	23.3		-10.52	23.7	6.45	-6.34	12.5	13.73	-10.21	29.5	3.80	-7.52	19.0	9.53	-9.94	22.5	6.33
27	9.00	23.8		10.35	27.9	6.42	7.19	16.8	13.30	10.37	29.6	3.71	8.35	20.4	9.02	10.18	24.3	6.51
28	-8.88	22.1		-10.50	23.5	6.50	-6.22	12.4	13.50	-10.20	29.5	3.75	-3.72	-	-	-9.90	22.4	6.20
35	8.10	22.9		10.03	27.1	6.20	6.64	15.5	12.16	10.26	29.6	3.74				9.95	23.5	6.47
36	-8.32	20.7		-10.19	22.8	6.31	-5.80	12.0	12.57	-10.13	29.5	3.70				-9.66	21.9	6.48
37	5.60	16.3		9.96	27.0	6.23	6.17	14.8	11.71	10.21	29.6	3.68				9.90	23.4	6.40
42				-9.98	22.4	6.19	-5.26	11.5	10.49	-10.00	29.4	3.73				-9.54	21.3	6.27
43				9.63	26.5	6.21	3.33	6.5	7.18	10.13	29.5	3.68				9.74	22.8	6.13
44				-9.84	22.3	6.18	-2.86	-	-	-9.98	29.4	3.70				-9.47	21.2	6.12
53				8.88	23.5	6.05				9.59	28.9	3.67				9.50	22.0	6.15
54				-9.53	20.6	5.94				-9.68	28.9	3.62				-9.28	20.2	6.04
55				6.34	-	-				9.46	28.5	3.64				9.41	21.9	6.16
63										8.39	22.3	3.64				8.66	21.3	5.99
64										-9.22	25.6	3.63				-8.82	19.2	5.84
65										6.46	-	-				8.36	20.5	5.67
69																7.00	18.6	5.37
70																-8.13	16.6	5.24
71																5.04	-	-

*P = peak load

**K = elastic stiffness (rev. 0), unloading stiffness (other rev.)

***E = hysteresis energy

Table 5.8 Peak Loads in Variable Amplitude Test (Specimen B2-9)

Block No.	2N (Rev)	P (kips)	Block No.	2N (Rev)	P (kips)	Block No.	2N (Rev)	P (kips)	Block No.	2N (Rev)	P (kips)
1	1	7.16		26	-7.33		51	8.22		76	-8.97
	2	-9.99		27	11.14		52	-8.82		77	8.49
	3	5.35		28	-10.14		53	8.67		78	-8.42
	4	-10.45		29	10.64		54	-10.77		79	10.58
	5	8.57		30	-10.42		55	9.82		80	-10.28
	6	-8.34		31	10.72		56	-8.42		81	8.01
	7	7.09		32	-8.36		57	8.26		82	-5.76
	8	-9.47		33	6.72		58	-8.74		83	7.90
	9	9.77		34	-9.52		59	9.83		84	-6.57
	10	-9.09	2	35	6.62		60	-6.90		85	7.76
	11	11.16		36	-10.68		61	10.65		86	-8.30
	12	-11.13		37	3.10		62	-9.62		87	8.20
	13	8.83		38	-10.98		63	10.16		88	-10.10
	14	-6.28		39	7.58		64	-9.88		89	9.22
	15	8.76		40	-8.50		65	10.24		90	-7.97
	16	-7.30		41	6.11		66	-7.90		91	7.83
	17	8.55		42	-9.34		67	6.35		92	-8.25
	18	-9.17		43	9.04		68	-4.35		93	9.20
	19	9.07		44	-8.91	3	69	2.70		94	-6.59
	20	-11.13		45	11.03		70	-9.93		95	10.24
	21	10.23		46	-10.98		71	4.06		96	-9.04
	22	-8.82		47	8.47		72	-10.26		97	9.72
	23	8.60		48	-5.90		73	7.22		98	-9.30
	24	-9.19		49	8.45		74	-8.05		99	9.84
	25	10.26		50	-6.83		75	5.90		100	-7.56
										101	6.24

Table 5.9 Predicted Deterioration for Specimen B2-9

Range	$\Delta\theta_p$ (rad)	Δd (%/rev.)	d (%)
S_1-1	0.0015	0	
1-4	0.0156	0	
2-3	0.0020	0	
3-2	0.0020	0	
4-11	0.0334	0	
5-8	0.0052	0	
6-7	0.0023	0	
7-6	0.0023	0	
8-9	0.0096	0.115	0.115
9-10	0.0064	0.059	
10-9	0.0064	0.059	0.233
11-20	0.0381	1.215	
12-19	0.0124	0.181	
13-14	0.0029	0.016	
14-13	0.0029	0.016	
15-18	0.0064	0.059	
16-17	0.0032	0.018	
17-16	0.0032	0.018	
18-15	0.0064	0.059	
19-12	0.0124	0.181	1.996
20-27	0.0344	1.019	
21-24	0.0094	0.114	
22-23	0.0058	0.050	
23-22	0.0058	0.050	
24-21	0.0094	0.114	
25-26	0.0055	0.045	
26-25	0.0055	0.045	
27-30	0.0218	0.471	
28-29	0.0167	0.300	
29-28	0.0167	0.300	
30-31	0.0202	0.416	
31-34	0.0137	0.215	
32-33	0.0035	0.022	
33-32	0.0035	0.022	
34-E_1	0.0004	0	5.179
S_2-35	0.0019	0.008	
35-38	0.0156	0.269	
36-37	0.0038	0.025	
37-36	0.0038	0.025	
38-45	0.0328	0.944	
39-42	0.0058	0.051	
40-41	0.0030	0.017	
41-40	0.0030	0.017	
42-39	0.0058	0.051	
43-44	0.0074	0.075	
44-43	0.0074	0.075	6.736
45-54	0.0387	1.246	
46-53	0.0127	0.189	
47-48	0.0028	0.015	
48-47	0.0028	0.015	
49-52	0.0148	0.246	
50-51	0.0039	0.025	
51-50	0.0039	0.025	
52-49	0.0148	0.246	
53-46	0.0127	0.189	8.932
54-61	0.0358	1.091	
55-58	0.0103	0.134	
56-57	0.0010	0.002	
57-56	0.0010	0.002	
58-55	0.0103	0.134	
59-60	0.0059	0.052	
60-59	0.0059	0.052	10.399
61-64	0.0237	0.543	
62-63	0.0182	0.347	
63-62	0.0182	0.347	
64-65	0.0220	0.480	
65-66	0.0103	0.134	
66-67	0.0038	0.024	
67-E_2	0.0024	0.011	12.285
S_3-69	0.0015	0.005	
69-72	0.0218	0.471	
70-71	0.0040	0.027	
71-70	0.0040	0.027	
72-79	0.0351	1.055	
73-76	0.0070	0.068	
74-75	0.0044	0.032	
75-74	0.0044	0.032	
76-73	0.0070	0.068	
77-78	0.0087	0.099	
78-77	0.0087	0.099	14.268
79-88	0.0408	1.365	
80-87	0.0143	0.232	
81-82	0.0036	0.023	
82-81	0.0036	0.023	
83-86	0.0085	0.096	
84-85	0.0047	0.036	
85-84	0.0047	0.036	
86-83	0.0085	0.096	
87-80	0.0143	0.232	16.407
88-95	0.0374	1.177	
89-92	0.0118	0.167	
90-91	0.0078	0.082	
91-90	0.0078	0.082	
92-89	0.0118	0.167	
93-94	0.0075	0.078	
94-93	0.0075	0.078	18.238
95-98	0.0251	0.601	
96-97	0.0197	0.397	
97-96	0.0197	0.397	
98-99	0.0235	0.537	
99-100	0.115	0.160	
100-101	0.0047	0.035	
101-E_3	0.0029	0.016	20.381

Table 6.1 Summary Information on Selected Records

Earthquake Location	Earthquake Date & Time	Magnitude	Station and Components Used in this Study	Location of Instrument	EERL Record Identification
Imperial Valley, California	May 18, 1940 20:37 PST	6.3	El Centro, S00E,S90W	First floor of a two story massive concrete heavily reinforced building	A001
Kern County, California	July 21, 1952 4:35 PST	7.7	Taft Lincoln School Tunnel, N21E	One story school building (Ref. 57)	A004
Lower California	December 30, 1934 5:52 PST	6.5	El Centro, N90E	First floor of a two story massive concrete heavily reinforced building	B024
San Fernando, California	February 9, 1971 6:00 PST	6.6	Castaic Old Ridge Route, N69W	Instrument Shelter (Ref. 57)	D056
Long Beach, California	March 10, 1933 17:54 PST	6.3	Public Utilities Building, West	4 Story building	V315

Table 6.2 Pertinent Characteristics of Selected Records

Record Identification	Distance (km) Epicenter	Distance (km) Fault	Near-Field or Far-Field	Soil Profile Type	Unscaled I_o $10^4 cm^2/sec^3$	Unscaled I_{sm} $10^4 cm^2/sec^3$	Unscaled RMSA cm/sec^2	Unscaled PGA g	Scale Factor	Scaled I_o $10^4 cm^2/sec^3$	Scaled I_{sm} $10^4 cm^2/sec^3$	Scaled RMSA cm/sec^2	Scaled PGA g	Strong Motion Duration D_{sm} Seconds
A001,S00E	10	12	NF	2	11.4595	6.5932	93.76	.348	1.29	19.0698	10.9772	120.95	.449	7.5
A001,S90W	10	12	NF	2	8.0707	7.6695	54.95	.214	1.90	29.1352	27.6152	104.40	.407	25.4
A004,N21E	43	42	NF	1	3.4020	2.4699	46.96	.156	2.50	21.2625	15.4367	117.40	.390	11.20
B024,N90E	64	-	FF	1	3.8876	3.4051	46.72	.183	2.33	21.1054	18.4159	108.85	.426	15.60
D056,N69W	29	26	NF	1	6.1760	5.5745	60.80	.271	1.67	17.2242	15.4848	101.53	.453	15.08
V315,West	27	-	NF	1	2.5643	2.3589	51.54	.159	2.25	12.9818	11.9119	115.96	.358	8.88

Table 6.3 Values of R' and R" for the Selected Records at T=0.5 seconds

Record Identification	Spectral Acceleration (g) ATC-3 Spectrum $A_v = A_a = 0.4$	Spectral Acceleration (g) Scaled Record	R=4 C_s	R=4 R'	R=4 R"	R=8 A_s	R=8 R'	R=8 R"
A001, S00E	1.00	1.078	0.228	4.39	4.73	0.114	8.77	9.46
A001, S90W	1.00	1.212	0.228	4.39	5.32	0.114	8.77	10.63
A004, N21E	0.80	0.952	0.190	4.21	5.01	0.095	8.42	10.02
B024, N90E	0.80	0.909	0.190	4.21	4.78	0.095	8.42	9.57
D056, N69W	0.80	0.913	0.190	4.21	4.81	0.095	8.42	9.61
V315, West	0.80	0.909	0.190	4.21	4.78	0.095	8.42	9.57
Average				4.27	4.90		8.54	9.81

Table 6.4 Statistics of $\Delta\delta_p/\delta_y$ for Different Systems (T=0.5 seconds)

	Engineering Definition								Material Science Definition							
	R=4, R'=4.27, R"=4.90				R=8, R'=8.54, R"=9.81				R=4, R'=4.27, R"=4.90				R=8, R'=8.54, R"=9.81			
	α=0.0	α=0.1	α=0.3	α=0.5	α=0.0	α=0.1	α=0.3	α=0.5	α=0.0	α=0.1	α=0.3	α=0.5	α=0.0	α=0.1	α=0.3	α=0.5
Number of Observations	161	163	180	198	218	220	243	259	161	163	180	198	218	220	243	259
Median, $\bar{m}_Y$	0.458	0.587	0.717	0.968	1.009	1.221	1.706	2.613	0.458	0.528	0.502	0.484	1.009	1.099	1.194	1.306
$\sigma_{\ell nY}$	1.564	1.328	1.382	1.198	1.622	1.702	1.555	1.266	1.564	1.328	1.382	1.198	1.622	1.702	1.555	1.266
Mean, m_Y	1.557	1.417	1.863	1.984	3.760	5.197	5.715	5.823	1.557	1.275	1.304	0.992	3.760	4.678	4.000	2.911
Standard Deviation, σ_Y	5.056	3.115	4.468	3.549	13,50	21.50	18,27	11.60	5,056	2.803	3.128	1.775	13.50	19.35	12.79	5.798
C.O.V., v_Y	3.247	2.198	2.398	1.789	3.59	4.137	3.197	1.992	3.247	2.198	2.398	1.789	3.590	4.137	3.197	1.992

Table 6.5 Values of N' for Different Systems (T = 0.5 seconds) and Records

Record Identification	Strong Motion Duration, D_{sm} (seconds)	R	N' α=0.0	α=0.1	α=0.3	α=0.5
A001, S00E	7.5	4	9	9	11	11
		8	16	14	18	20
A001, S90W	25.4	4	30	27	29	35
		8	49	55	65	73
A004, N21E	11.20	4	26	26	28	36
		8	36	32	38	40
B024, N90E	15.60	4	36	41	47	49
		8	49	51	53	51
D056, N69W	15.08	4	43	43	47	47
		8	47	45	45	47
V315, West	8.88	4	17	17	18	20
		8	21	23	24	28
Mean Vales N'		4	27	27	30	33
		8	36	37	41	43

Table 6.6 Values of $(\Delta\delta_p)_{max}/\delta_y$ for Different Systems (T=0.5 seconds) and Records

Record Identification	Engineering Definition								Material Science Definition							
	R=4, R'=4.27, R"=4.90				R=8, R'=8.54, R"=9.81				R=4, R'=4.27, R"=4.90				R=8, R'=8.54, R"=9.81			
	α=0.0	α=0.1	α=0.3	α=0.5	α=0.0	α=0.1	α=0.3	α=0.5	α=0.0	α=0.1	α=0.3	α=0.5	α=0.0	α=0.1	α=0.3	α=0.5
A001, S00E	3.91	4.93	6.69	7.30	16.02	10.25	17.13	19.57	3.91	4.44	4.68	3.65	16.02	9.22	11.99	9.79
A001, S90W	7.31	7.83	7.28	7.65	18.51	20.10	22.55	19.98	7.31	7.05	5.10	3.82	18.51	18.09	15.78	9.99
A004, N21E	3.74	3.26	4.15	4.81	13.84	14.78	14.95	17.94	3.74	2.93	2.91	2.41	18.84	13.30	10.46	8.97
B024, N90E	5.20	3.40	3.73	4.96	13.76	10.39	12.20	13.49	5.20	3.06	2.61	2.48	13.76	9.35	8.54	6.75
D056, N69W	4.21	5.96	7.24	7.09	29.24	19.26	22.80	19.70	4.21	5.36	5.07	3.54	29.24	17.33	15.96	9.85
V315, West	4.80	4.37	4.40	4.47	13.32	12.98	10.95	10.13	4.80	3.94	3.08	2.24	13.32	11.63	7.66	5.06

Table 6.7 Statistics of $(\Delta\delta_p)_{max}/\delta_y$ for Different Systems (T=0.5 seconds)

	Engineering Definition								Material Science Definition							
	R=4, R'=4.27, R"=4.90				R=8, R'=8.54, R"=9.81				R=4, R'=4.27, R"=4.90				R=8, R'=8.54, R"=9.81			
	α=0.0	α=0.1	α=0.3	α=0.5	α=0.0	α=0.1	α=0.3	α=0.5	α=0.0	α=0.1	α =0.3	α=0.5	α=0.0	α=0.1	α=0.3	α=0.5
Mean, m	4.862	4.960	5.582	6.047	18.28	14.63	16.76	16.80	4.862	4.464	3.908	3.023	18.28	13.16	11.73	8.401
Standard Deviation, s	1.204	1.577	1.511	1.317	5.333	3.900	4.618	3.718	1.204	1.419	1.058	0.659	5.333	3.509	3.232	1.860
C.O.V., v	.248	.318	.271	.218	.292	.267	.275	.221	.248	.318	.271	.218	.292	.267	2.75	.221

Table 6.8 Values of $\delta_{p,mean}/\delta_y$ for Different Systems (T=0.5 seconds) and Records

Record Identification	Engineering Definition								Material Science Definition							
	R=4, R'=4.27, R"=4.90				R=8, R'=8.54, R"=9.81				R=4, R'=4.27, R"=4.90				R=8, R'=8.54, R"=9.81			
	α=0.0	α=0.1	α=0.3	α=0.5	α=0.0	α=0.1	α=0.3	α=0.5	α=0.0	α=0.1	α=0.3	α=0.5	α=0.0	α=0.1	α=0.3	α=0.5
A001, S00E	.0187	.1151	.0978	.1317	1.919	.9551	.3203	.0852	.0187	.1279	.1076	.1313	1.919	.9663	.3149	.0578
A001, S90W	.7779	.2397	.0443	.0315	11.90	.3017	.1005	.0616	.7779	.2535	.0728	.0658	11.99	.2935	.1092	.0738
A004, N21E	1.783	.2985	.1306	.0571	4.505	.3718	.0977	.0793	1.783	.2951	.1217	.0489	4.505	.3866	.0944	.0600
B024, N90E	2.917	.4078	.1441	.0309	4.627	.2161	.0298	.0590	2.917	.4055	.1422	.0202	4.627	.1962	.0289	.0721
D056, N69W	2.210	.2441	.0843	.1606	18.20	1.119	.2486	.2653	2.210	.2295	.1144	.1968	18.20	1.079	.2115	.3117
V315, West	2.663	.4658	.0142	.0091	1.835	.2659	.0772	.0451	2.663	.4537	.0337	.0236	1.835	.2779	.1043	.0140

Table 6.9 Statistics of $\delta_{p,mean}/\delta_y$ for Different Systems (T=0.5 seconds)

	Engineering Definition								Material Science Definition							
	R=4, R'=4.27, R"=4.90				R=8, R'=8.54, R"=9.81				R=4, R'=4.27, R"=4.90				R=8, R'=8.54, R"=9.81			
	α=0.0	α=0.1	α=0.3	α=0.5	α=0.0	α=0.1	α=0.3	α=0.5	α=0.0	α=0.1	α=0.3	α=0.5	α=0.0	α=0.1	α=0.3	α=0.5
Mean, m	1.728	0.295	0.086	0.070	7.179	0.538	0.146	0.099	1.728	0.294	0.099	0.081	7.179	0.533	0.144	0.098
Standard Deviation, s	1.029	0.115	0.045	0.056	5.979	0.359	0.103	0.075	1.029	0.109	0.036	0.063	5.979	0.352	0.093	0.097
C.O.V., v	0.595	0.391	0.529	0.800	0.833	0.667	0.706	0.760	0.595	0.371	0.361	0.783	0.833	0.660	0.649	0.992

Table 6.10 Values of μ for Different Systems (T=0.5 seconds) and Records

Record Identification	R=4, R'=4.27, R"=4.90					R=8, R'=8.54, R"=9.81				
	α=0.0	α=0.1	α=0.3	α=0.5	α=1.0	α=0.0	α=0.1	α=0.3	α=0.5	α=1.0
A001, S00E	3.260	3.612	4.876	5.568	4.685	12.099	7.001	9.774	12.191	9.388
A001, S90W	4.846	6.422	5.356	4.987	5.291	19.508	12.462	12.288	11.143	10.601
A004, N21E	4.319	2.925	3.431	3.546	4.994	13.672	8.912	8.861	10.110	9.988
B024, N90E	6.404	2.986	3.180	3.660	4.743	12.958	7.185	7.405	7.980	9.485
D056, N69W	5.233	4.719	5.174	5.455	4.794	30.241	12.613	12.439	12.422	9.611
V315, West	5.562	3.448	3.785	3.882	4.755	8.518	9.461	7.281	6.627	9.511

Table 6.11 Statistics of μ for Different Systems (T=0.5 seconds)

	R=4, R'=4.27, R"=4.90					R=8, R'=8.54, R"=9.81				
	α=0.0	α=0.1	α=0.3	α=0.5	α=1.0	α=0.0	α=0.1	α=0.3	α=0.5	α=1.0
Mean, m	4.937	4.019	4.300	4.516	4.877	16.17	9.606	9.675	10.08	9.764
Standard Deviation, s	0.986	1.226	0.865	0.845	0.209	7.081	2.249	2.083	2.137	0.420
C.O.V., v	0.200	0.305	0.201	0.187	0.043	0.438	0.234	0.215	0.212	0.043

Table 6.12 Comparison of Ductility Ratios μ for Elastic-Plastic Systems (T=0.5 seconds)

R"	$\phi_\mu = \frac{1}{R"}$	μ_{R-N}	$\mu_{N-H} = \frac{1}{\phi_\mu}$	μ_{mean} This Study
4.90	0.204	5.98	4.90	4.94
9.81	0.102	17.13	9.81	16.17

Table 6.13 Normalized Hysteretic (HE_t) and Total Dissipated (TDE) Energy Terms for Different Systems (T=0.5 seconds) and Records

Record Identification	R=4, R'=4.27, R"=4.90								
	α=0.0		α=0.1		α=0.3		α=0.5		α=1.0
	$\frac{HE_t}{0.5F_y\delta_y}$	$\frac{TDE}{0.5F_y\delta_y}$	$\frac{HE_t}{0.5F_y\delta_y}$	$\frac{TDE}{0.5F_y\delta_y}$	$\frac{HE_t}{0.5F_y\delta_y}$	$\frac{TDE}{0.5F_y\delta_y}$	$\frac{HE_t}{0.5F_y\delta_y}$	$\frac{TDE}{0.5F_y\delta_y}$	$\frac{TDE}{0.5F_y\delta_y}$
A001, S00E	32.0	43.0	33.76	45.76	36.92	53.45	34.67	57.44	40.82
A001, S90W	72.07	106.61	76.44	113.37	76.06	118.90	70.61	124.48	111.3
A004, N21E	52.07	72.32	52.36	73.95	53.55	79.76	50.77	84.03	82.41
B024, N90E	52.44	79.79	53.34	82.19	55.69	89.29	54.99	96.58	92.33
D056, N69W	78.96	110.49	82.44	117.03	85.39	127.70	80.05	134.10	115.0
V315, West	32.19	46.75	32.80	48.32	32.46	50.04	31.33	53.29	60.72

Table 6.13 continued

Record Identification	R=8, R'=8.54, R"=9.81								
	α=0.0		α=0.1		α=0.3		α=0.5		α=1.0
	$\frac{HE_t}{0.5F_y\delta_y}$	$\frac{TDE}{0.5F_y\delta_y}$	$\frac{HE_t}{0.5F_y\delta_y}$	$\frac{TDE}{0.5F_y\delta_y}$	$\frac{HE_t}{0.5F_y\delta_y}$	$\frac{TDE}{0.5F_y\delta_y}$	$\frac{HE_t}{0.5F_y\delta_y}$	$\frac{TDE}{0.5F_y\delta_y}$	$\frac{TDE}{0.5F_y\delta_y}$
A001, S00E	115.9	150.95	126.1	171.38	147.3	231.13	114.9	225.9	163.9
A001, S90W	260.3	354.14	277.3	388.6	287.7	457.2	256.0	480.8	446.8
A004, N21E	211.8	282.99	217.4	302.38	240.7	372.20	242.4	453.30	329.6
B024, N90E	179.3	245.15	188.8	263.51	204.1	306.6	203.6	354.1	369.3
D056, N69W	231.7	310.55	258.7	360.0	294.7	462.2	252.0	461.8	462.1
V315, West	122.2	161.72	123.9	168.61	108.9	158.46	106.7	181.99	242.9

Table 6.14 Average Observed Values of Normalized HE_t

Record Identification	Strong Motion Duration, D_{sm} (sec.)	I_{sm} cm^2/sec^3	$HE_t/0.5F_y\delta_y$	
			R=4, R'=4.27, R"=4.90	R=8, R'=8.54, R"=9.81
A001, S00E	7.5	109772	34.34	126.05
A001, S90W	25.4	276151	73.79	270.32
A004, N21E	11.2	154366	52.19	288.07
B024, N90E	15.6	184159	54.11	193.95
D056, N69W	15.08	154848	81.71	259.27
V315, West	8.88	119119	32.19	115.42

Table 6.15 Predicted Values of Normalized HE_t

Strong Motion Duration, D_{sm} (sec.)	R=4				R=8			
	α=0.0	α=0.1	α=0.3	α=0.5	α=0.0	α=0.1	α=0.3	α=0.5
7.5	24.70	24.82	22.57	19.35	100.67	87.81	85.03	74.50
9.5	37.18	37.75	34.51	29.89	135.15	120.0	116.79	103.43
11.2	48.23	49.16	45.05	39.17	165.62	148.32	144.71	128.81
13.2	62.49	63.89	58.63	51.13	200.61	180.76	176.68	157.86
15.6	78.38	80.29	73.75	64.44	240.08	217.31	212.70	190.56

Table 6.16 Comparison Between Average Predicted and Observed Values of Normalized HE_t

Strong Motion Duration, D_{sm} (sec.)	Predicted		Observed	
	R=4	R=8	R=4	R=8
7.5	22.86	87.00	34.34	126.05
9.5	34.83	118.84	--	--
11.2	45.40	146.87	52.19	228.07
13.2	59.04	178.98	--	--
15.6	74.22	215.16	54.11	193.95

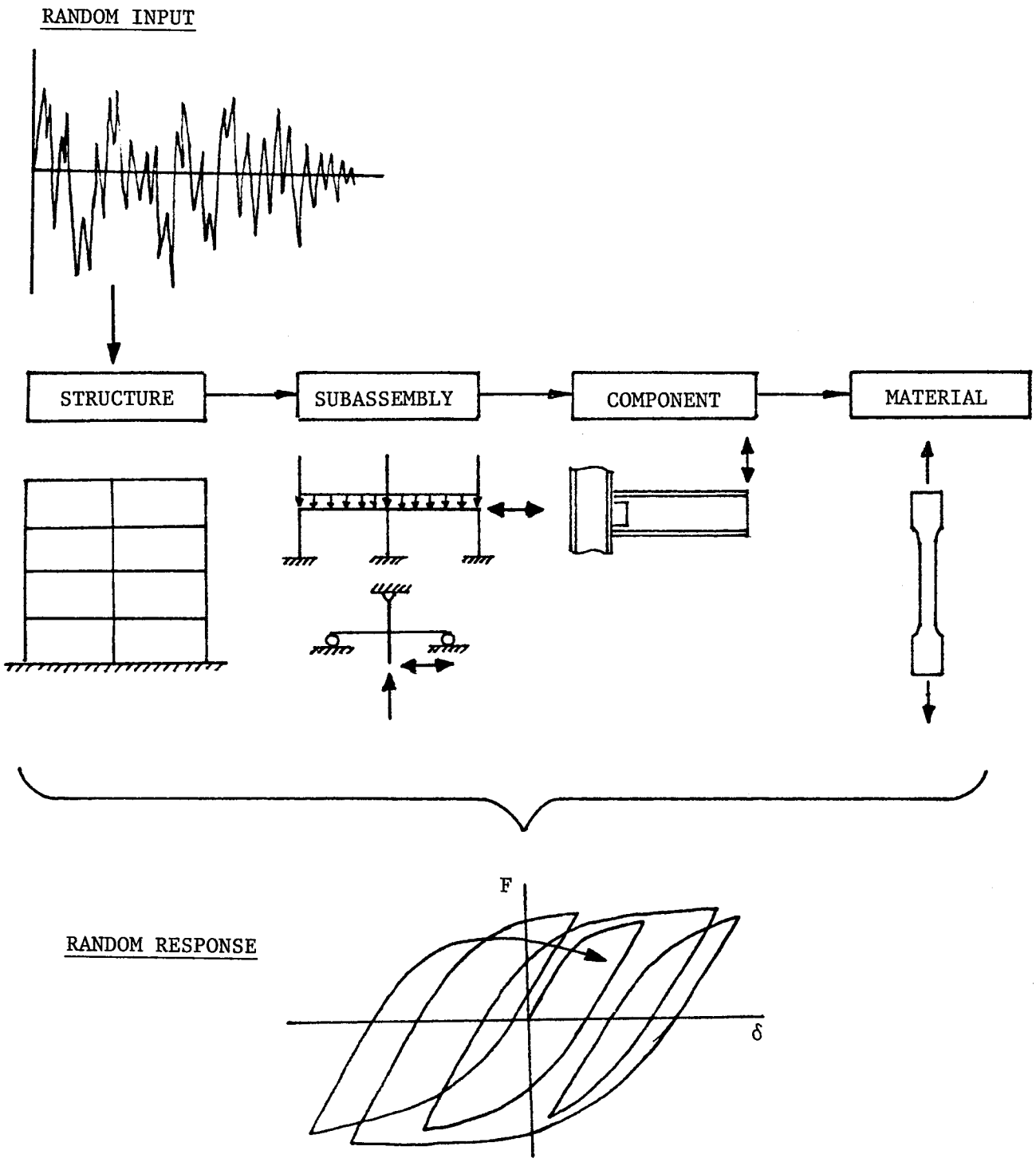

Fig. 2.1 Experimentation for Seismic Performance Assessment

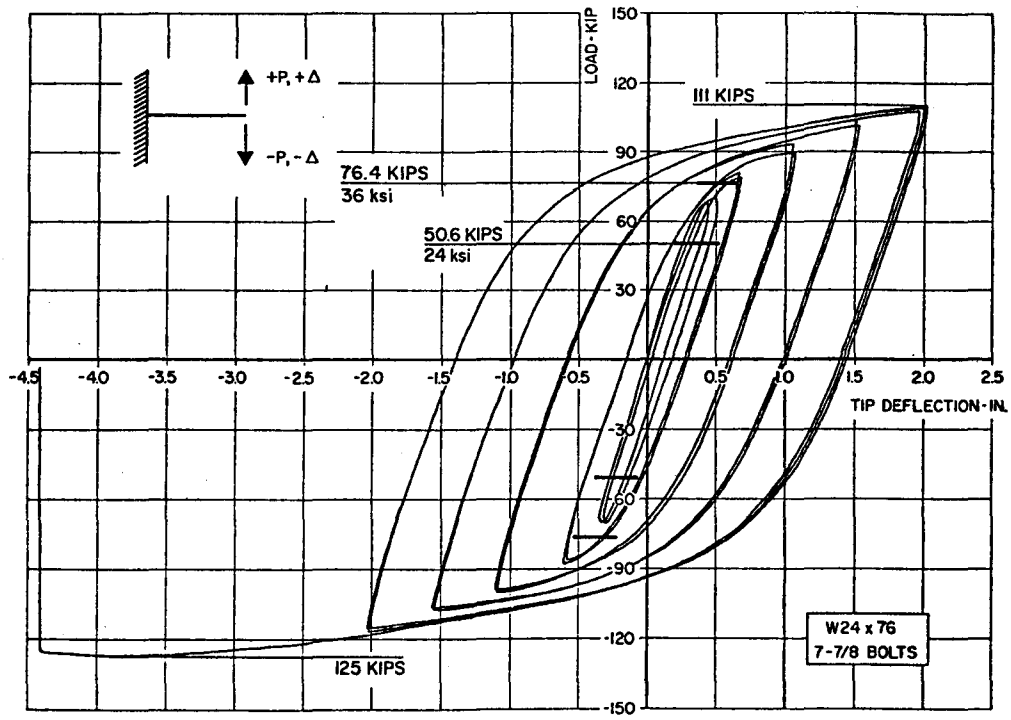

(a)

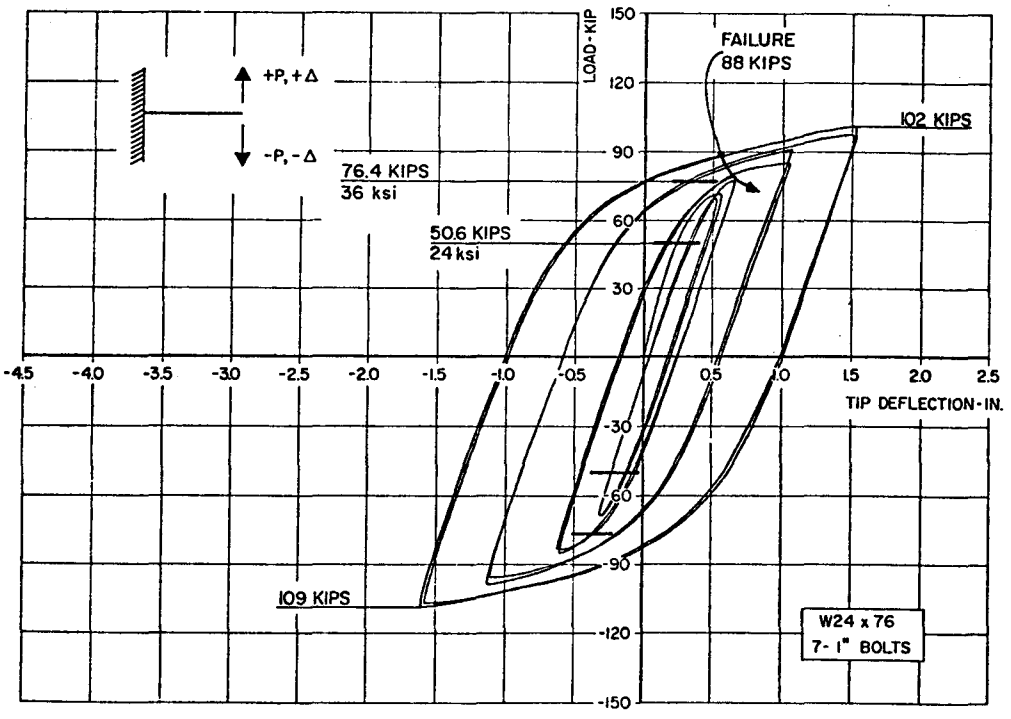

(b)

Fig. 2.2 Load--Deflection Response of Two Beams with Welded Flange and Bolted Web Connection (Ref. 2)

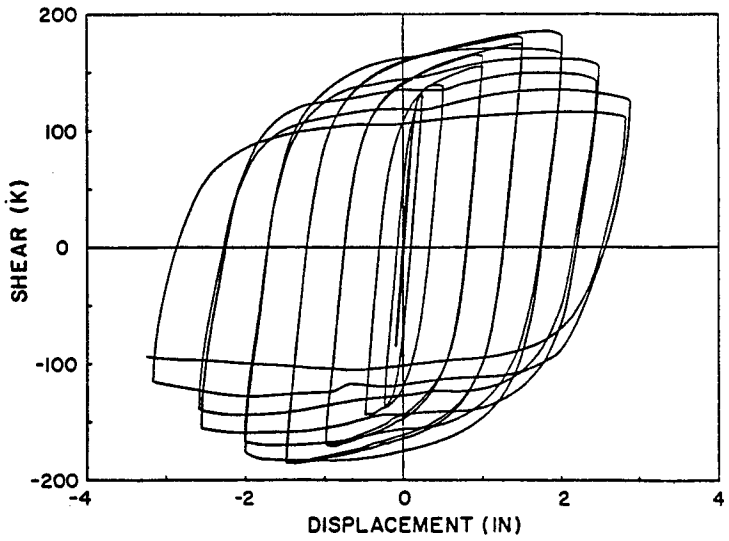

Fig. 2.3 Gradual Deterioration of Strength and Stiffness (Ref. 18)

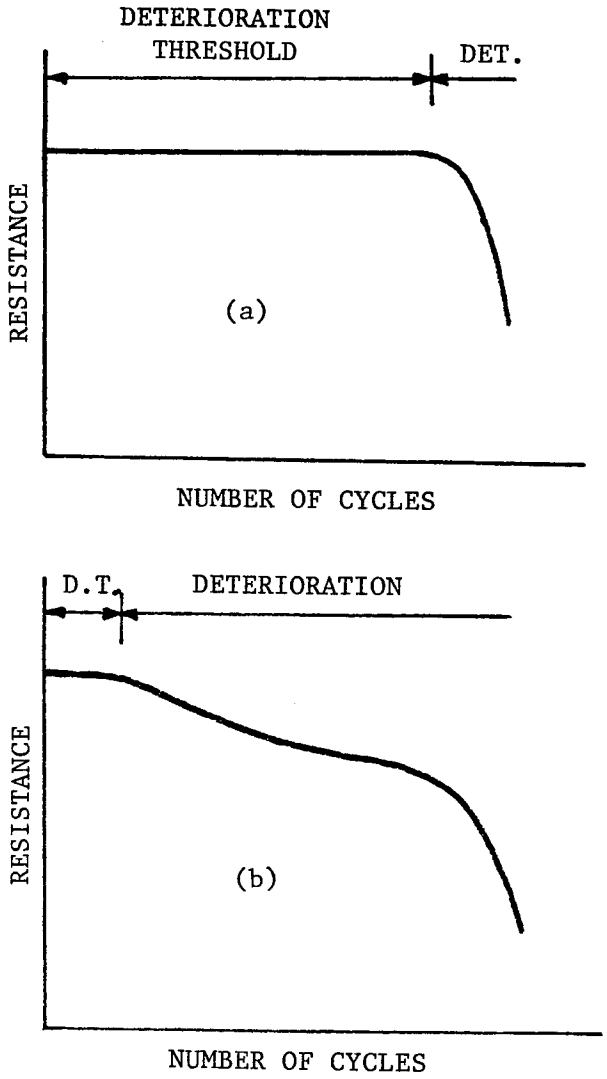

Fig. 2.4 Modes of Deterioration and Failure

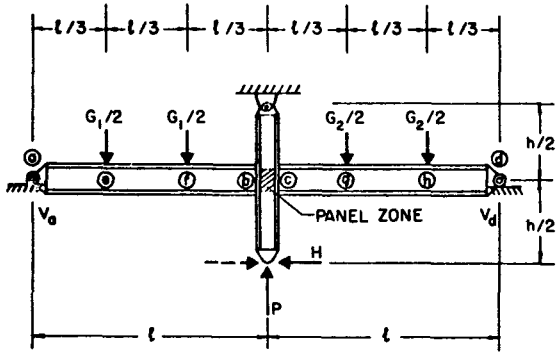

(a)

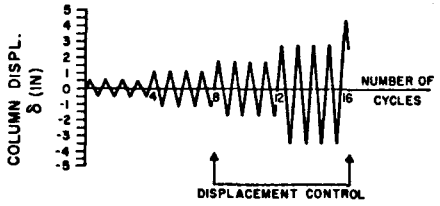

SPECIMEN B-1

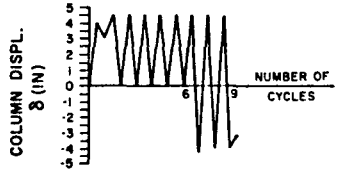

SPECIMEN B-2

(b)

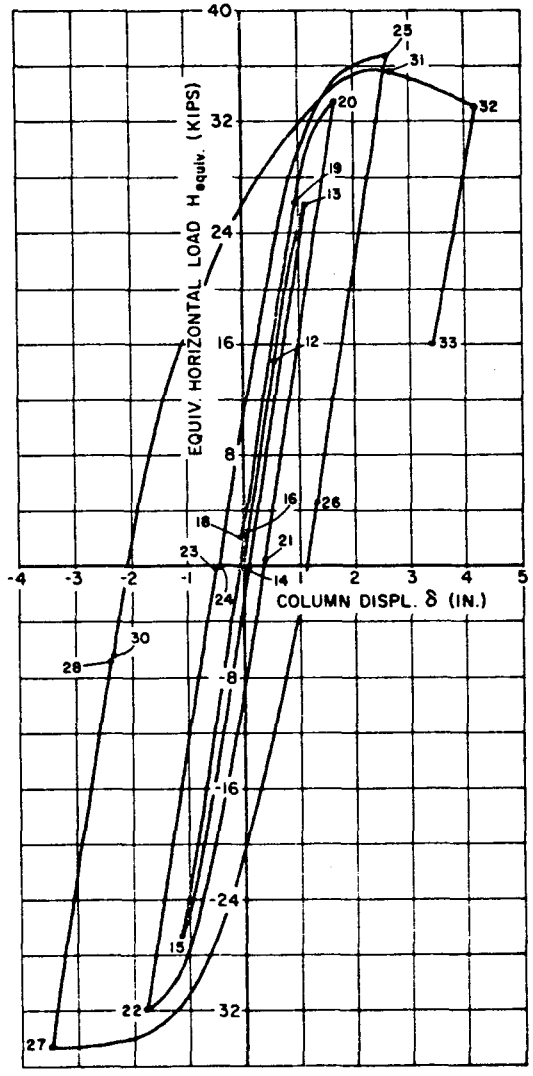

SPECIMEN B-1

(c)

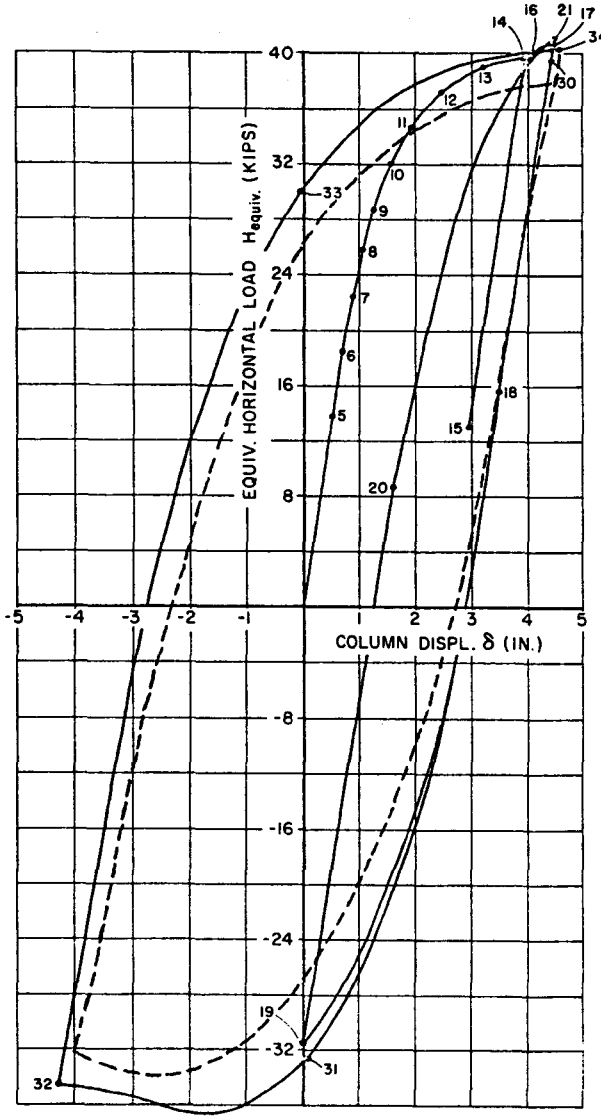

SPECIMEN B-2

(d)

Fig. 2.5 History Dependence of Deterioration (Ref. 19)

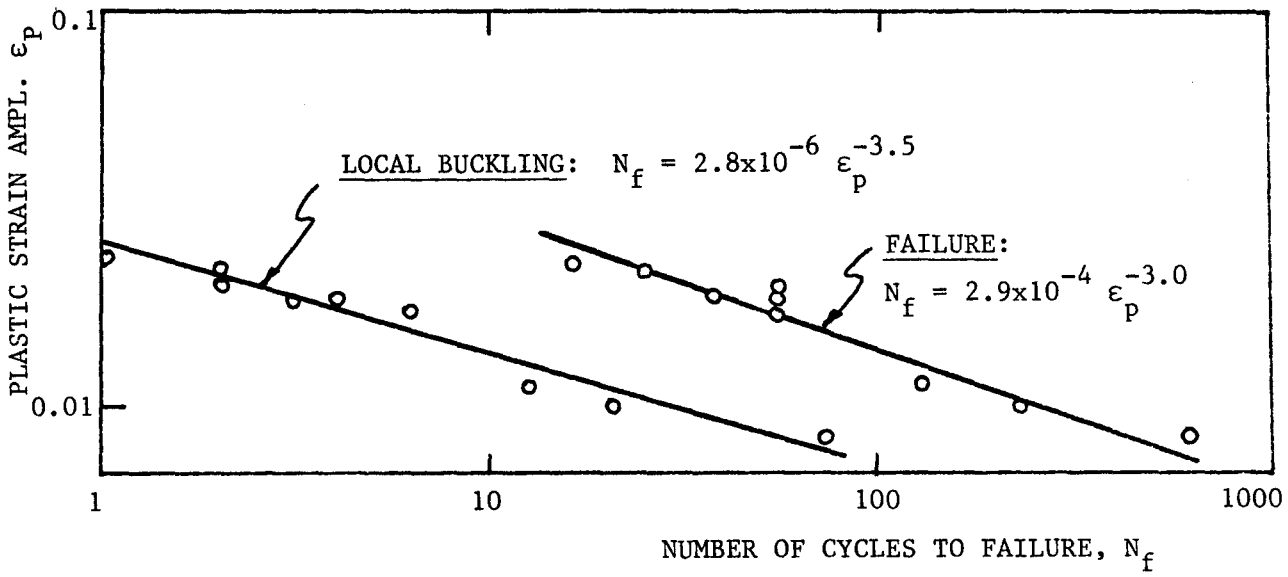

Fig. 2.6 Low-Cycle Fatigue Lives for Specimens of Ref.21

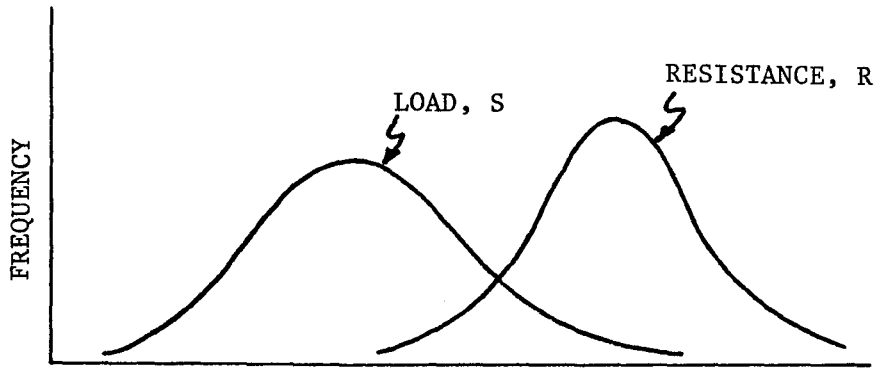

Fig. 3.1 Probabilistic Description of Load and Resistance

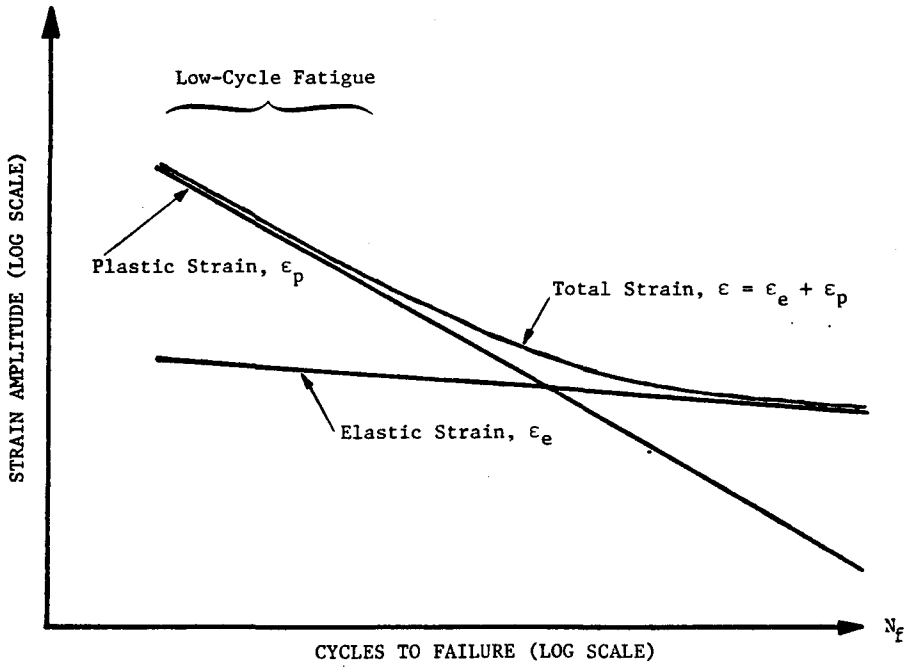

Fig. 3.2 Strain-Life Curves for Metal Fatigue

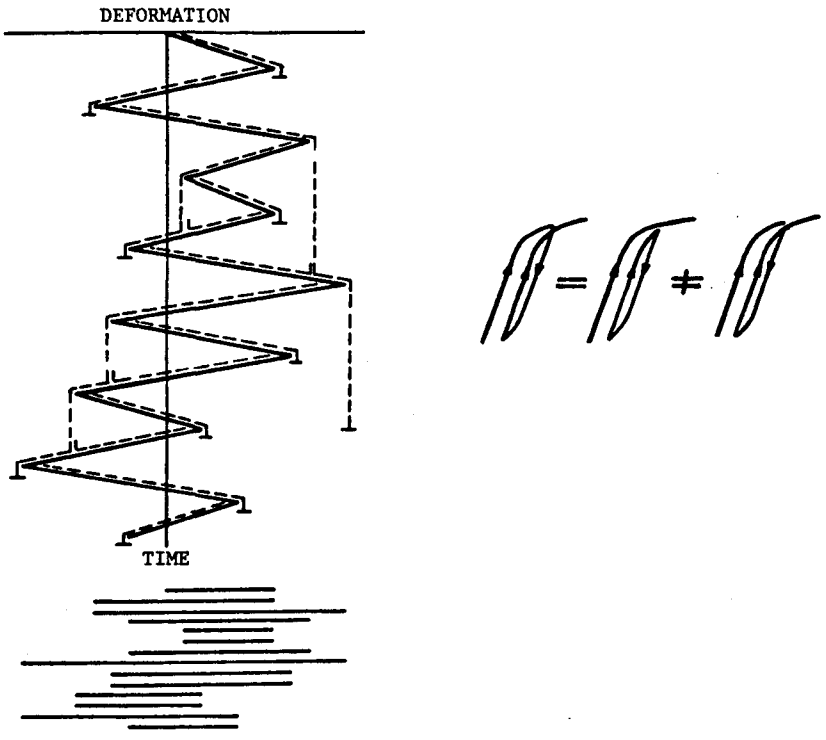

Fig. 3.3 Example of Rain-Flow Cycle Counting Method

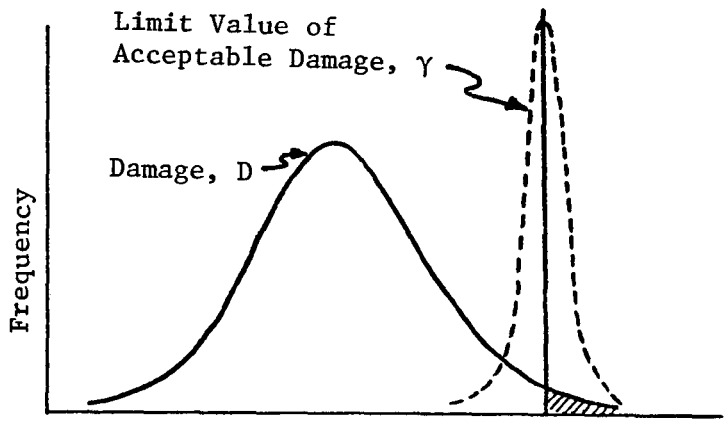

Fig. 3.4 Probabilistic Description of Damage D and its Limit Value γ

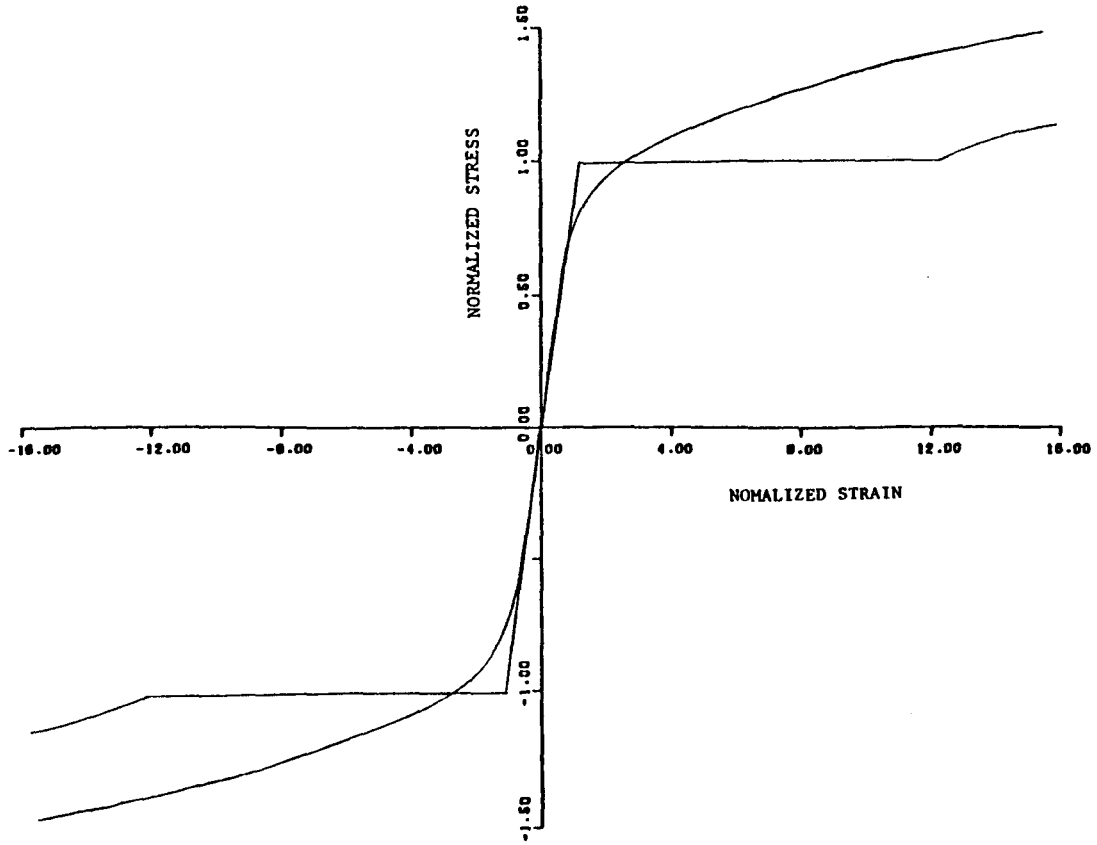

Fig. 4.1 Monotonic and Cyclic Stress-Strain Curves

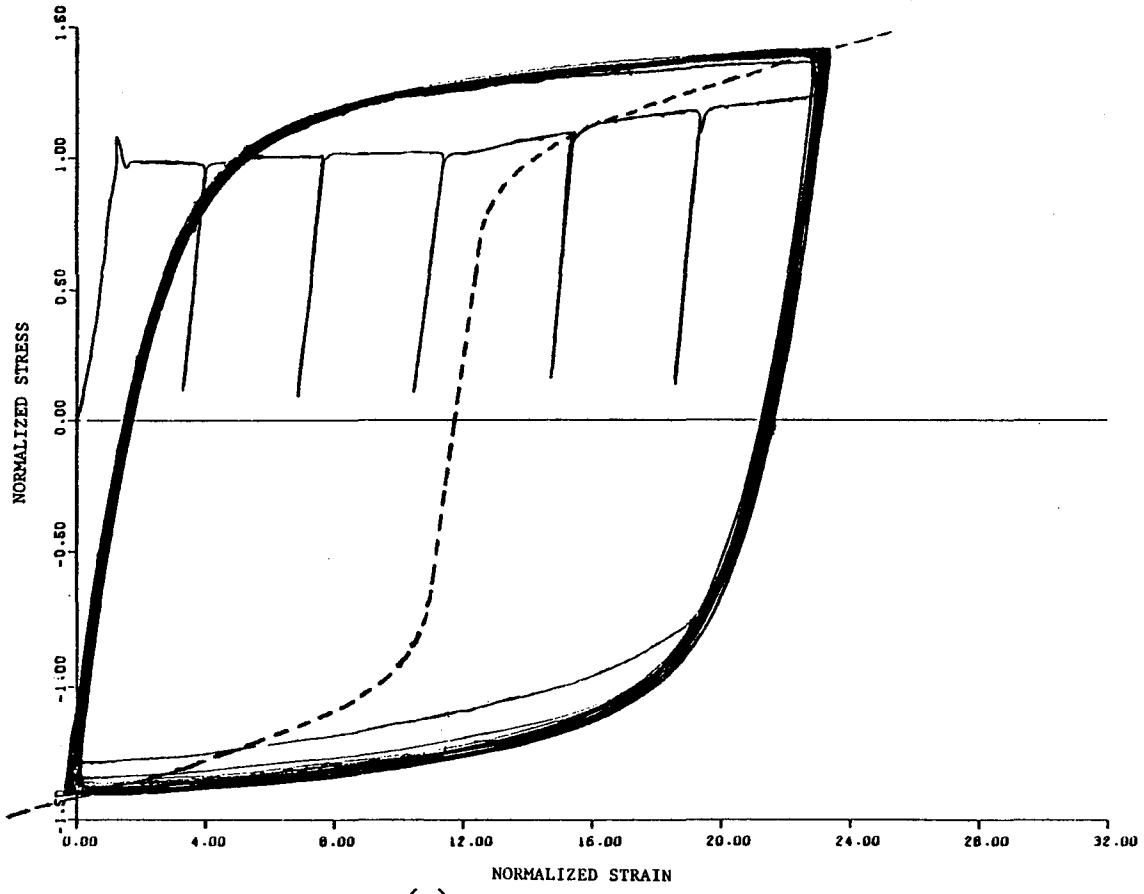

(a)

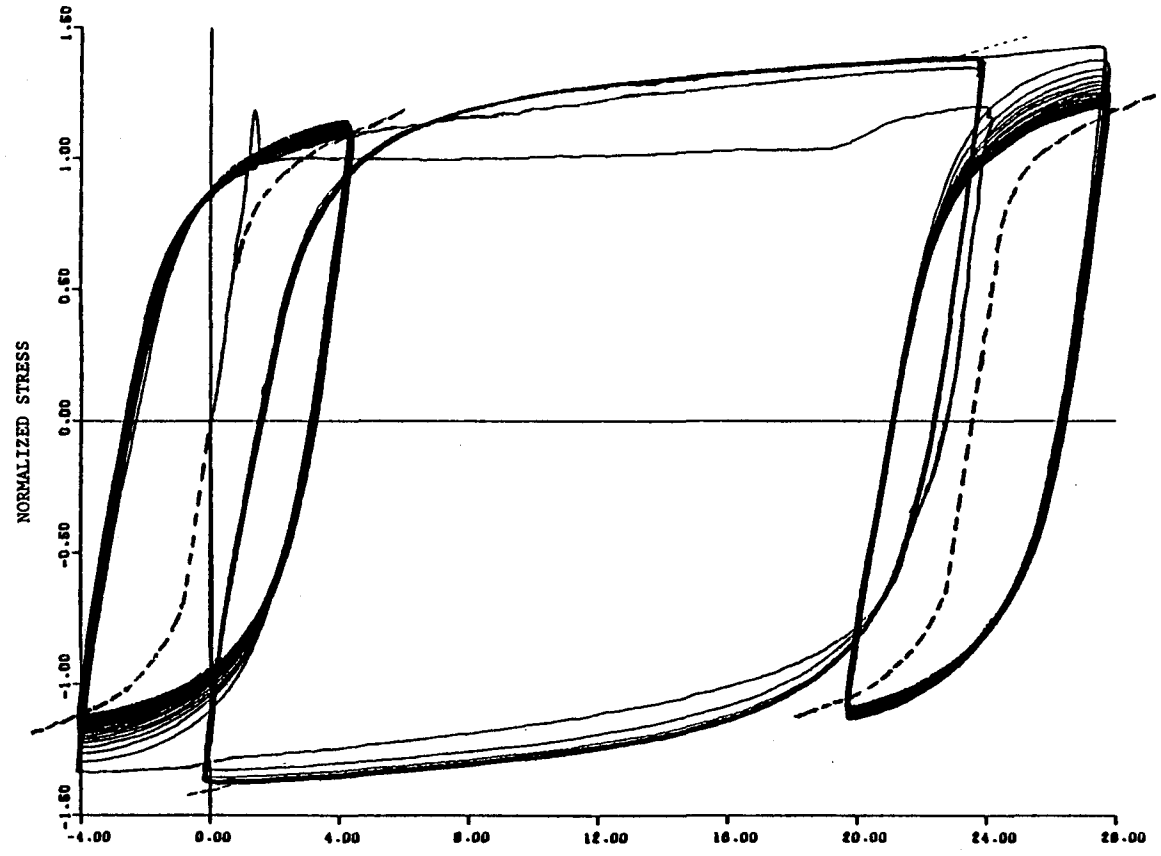

(b) NORMALIZED STRAIN

Fig. 4.2 Stabilization of Cyclic Stress-Strain Response

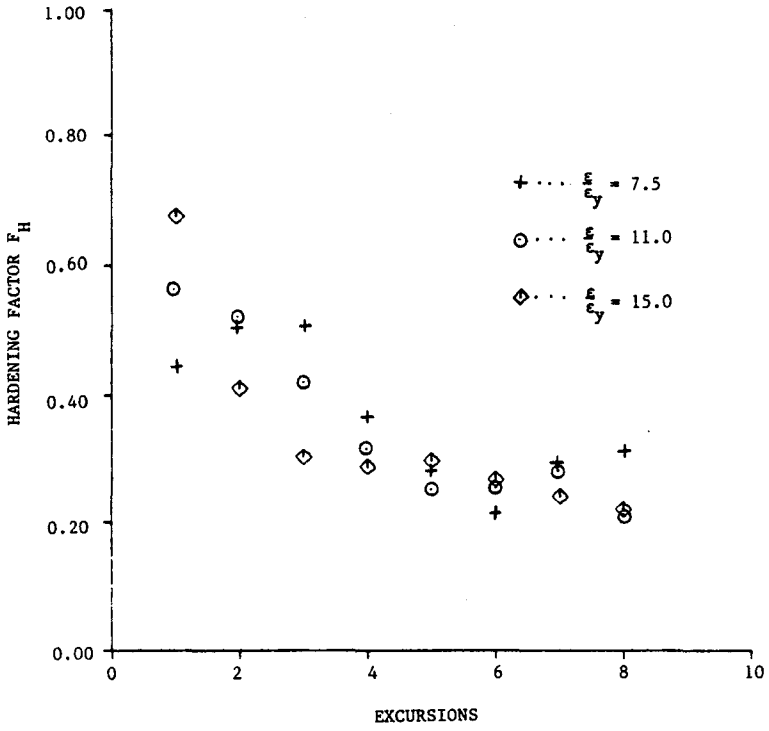

Fig. 4.3 Hardening Factor versus Number of Excursions

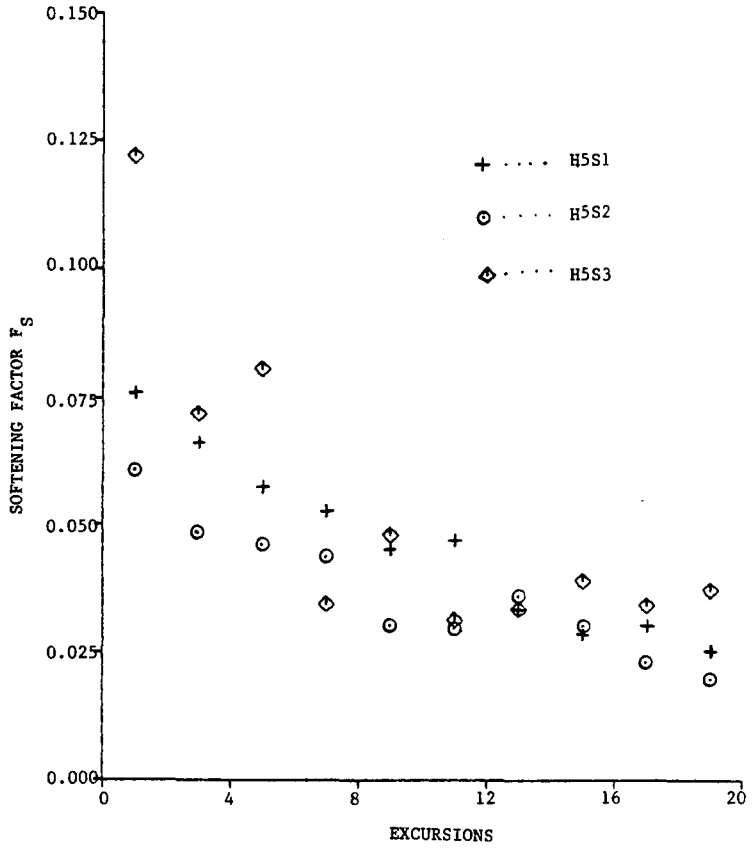

Fig. 4.4 Softening Factor versus Number of Excursions

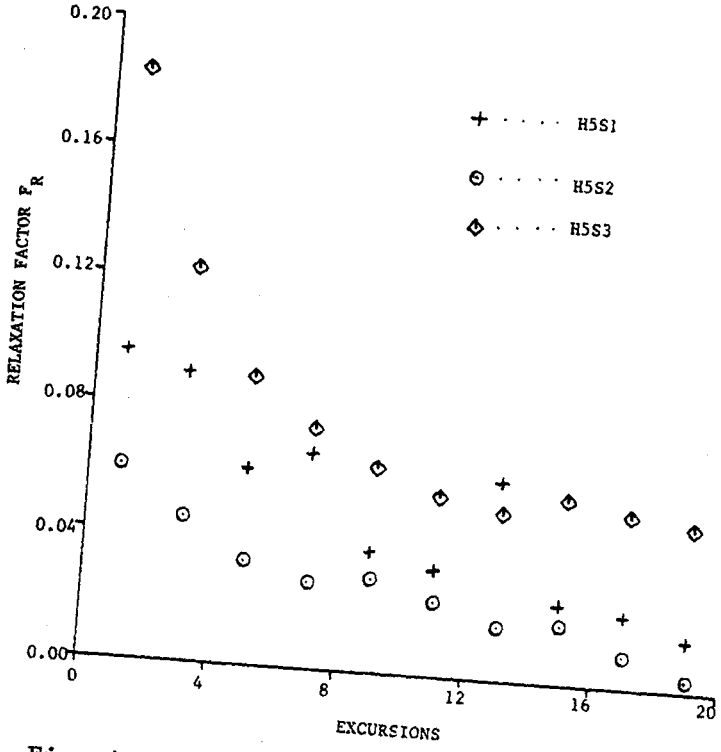

Fig. 4.5 Mean Stress Relaxation Factor versus Number of Excursions

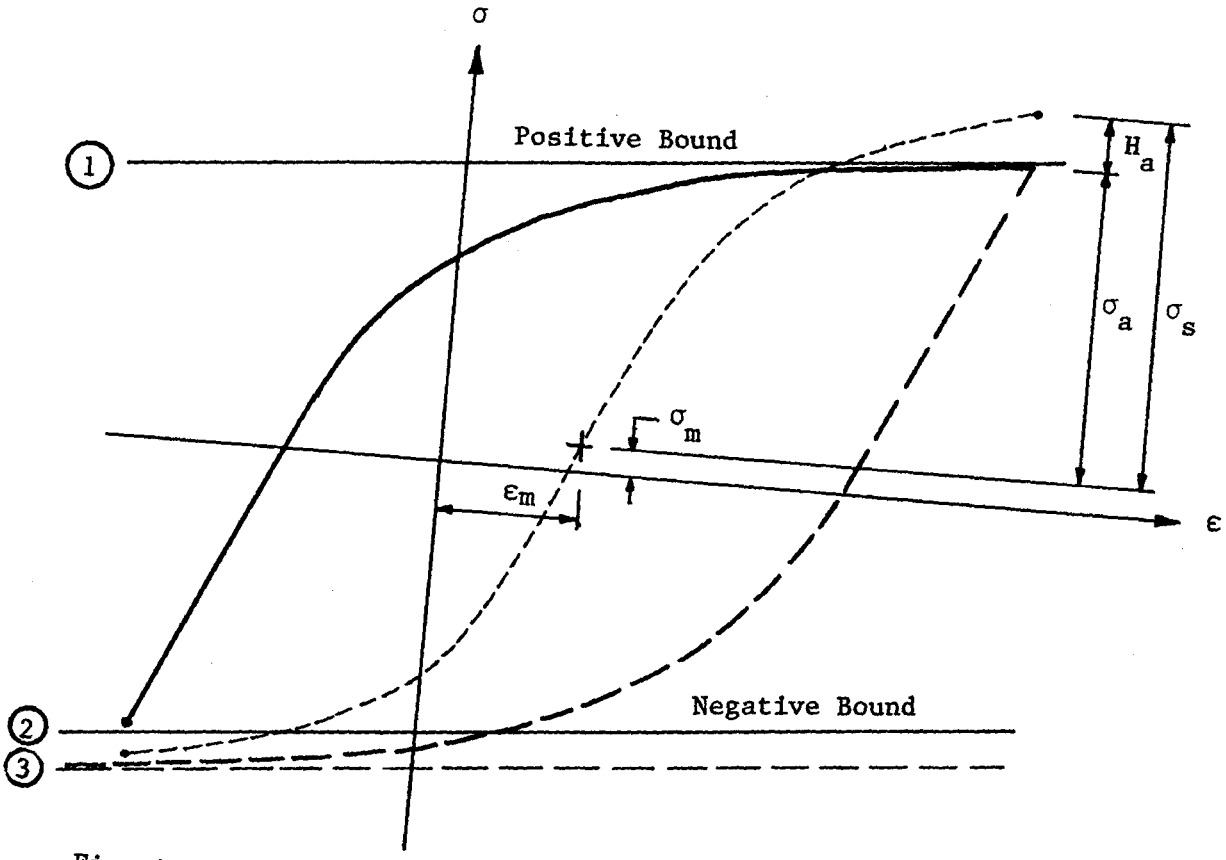

Fig. 4.6 Shape of Hysteresis Curves and Movement of Bounds

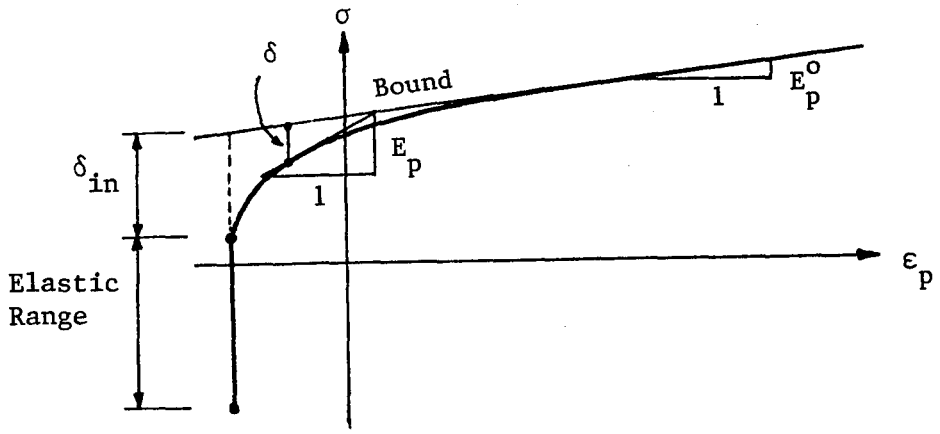

Fig. 4.7 Dafalias-Popov Model for Hysteresis Curve

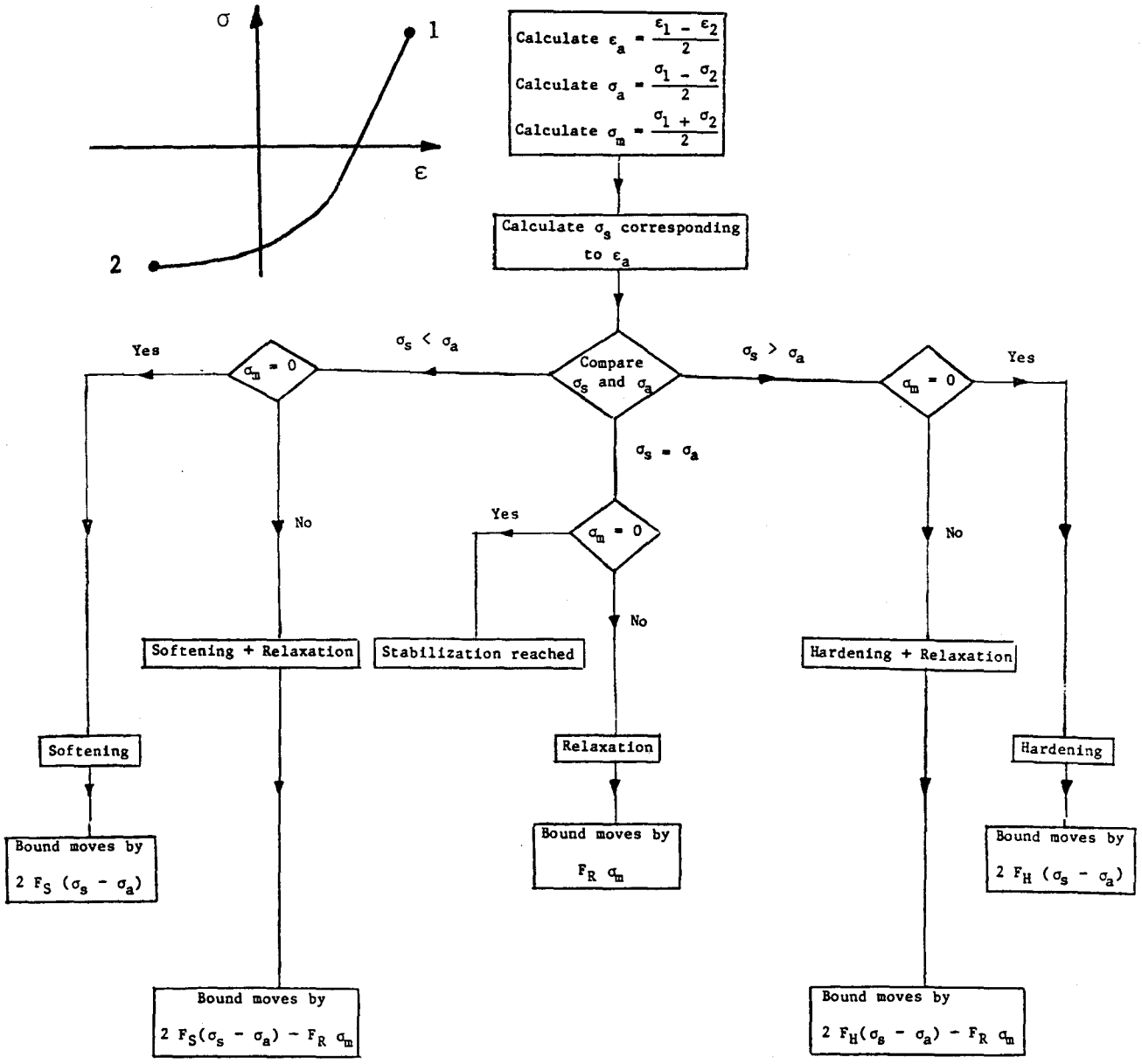

Fig. 4.8 Flowchart of Proposed Cyclic Stress-Strain Model

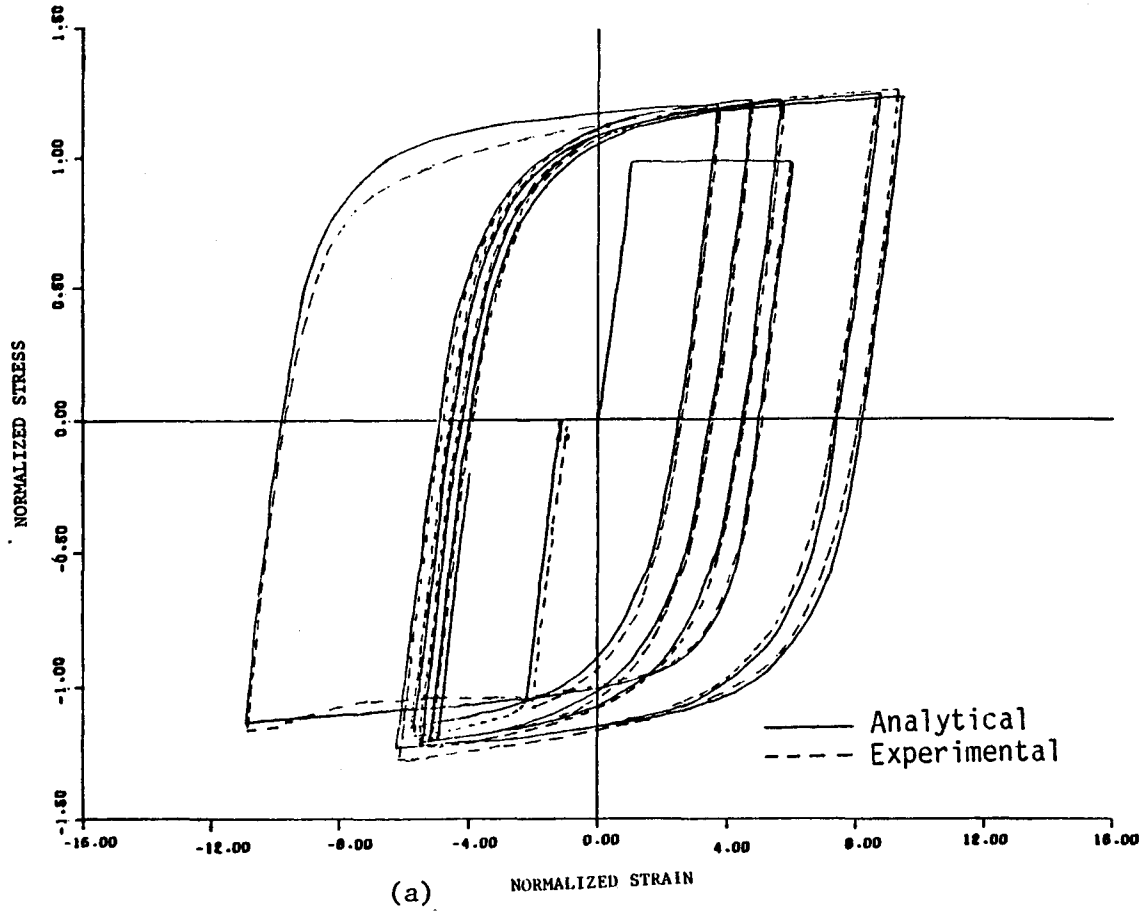

(a)

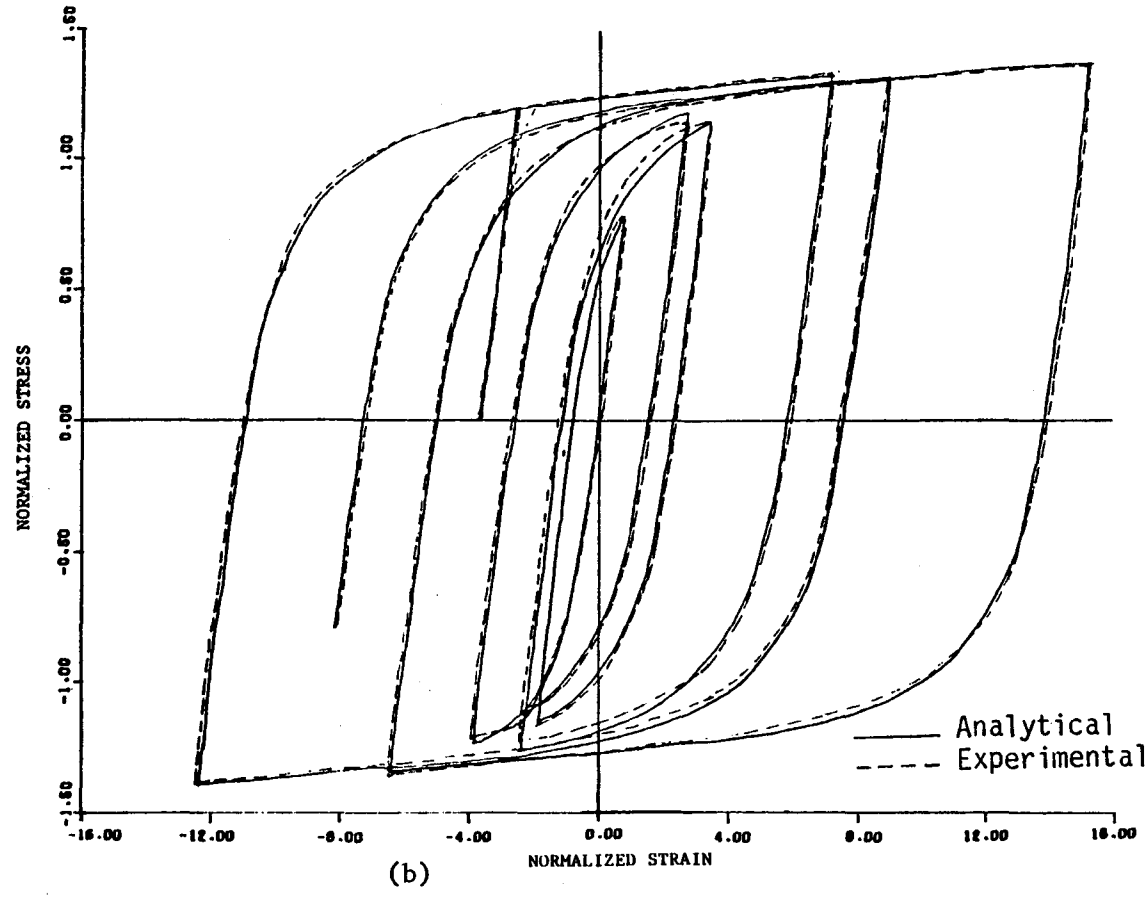

(b)

Fig. 4.9 Comparison of Analytical and Experimental Stress-Strain Histories

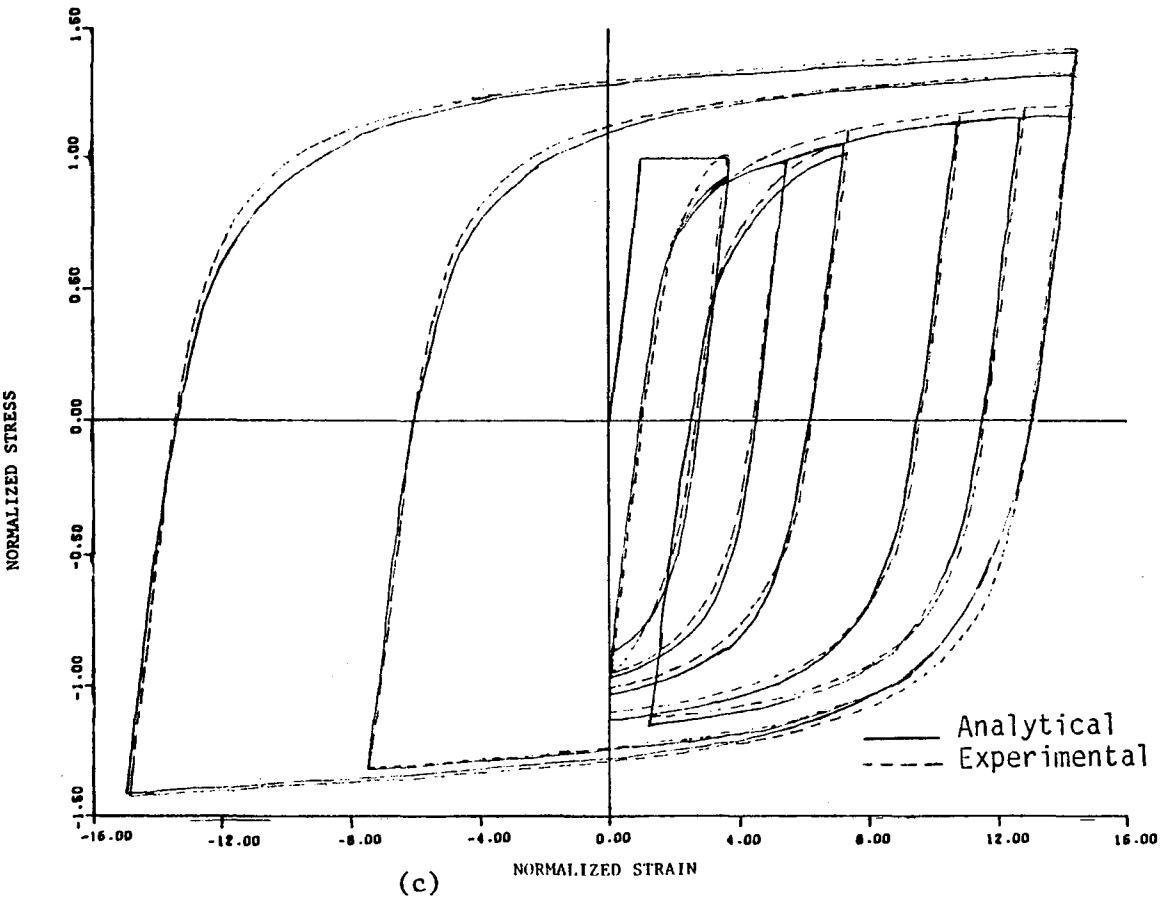

(c)

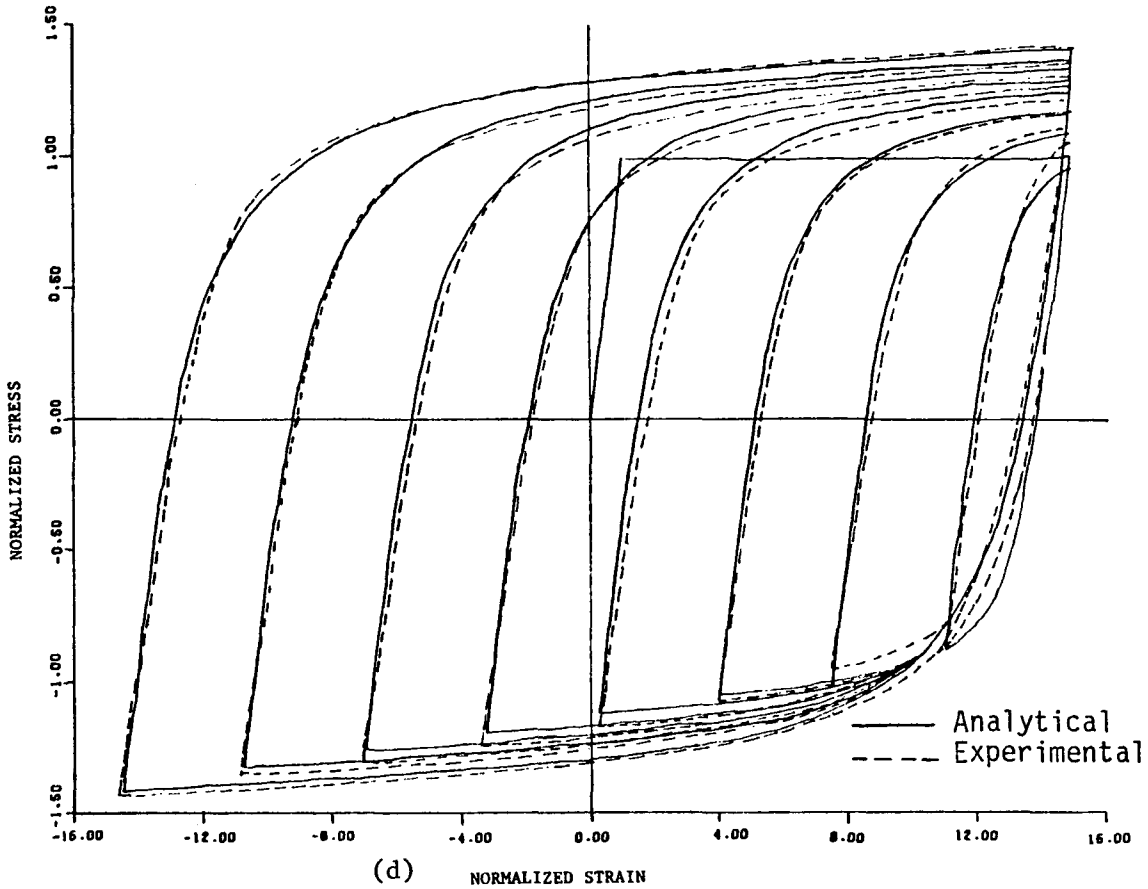

(d)

Fig. 4.9 continued

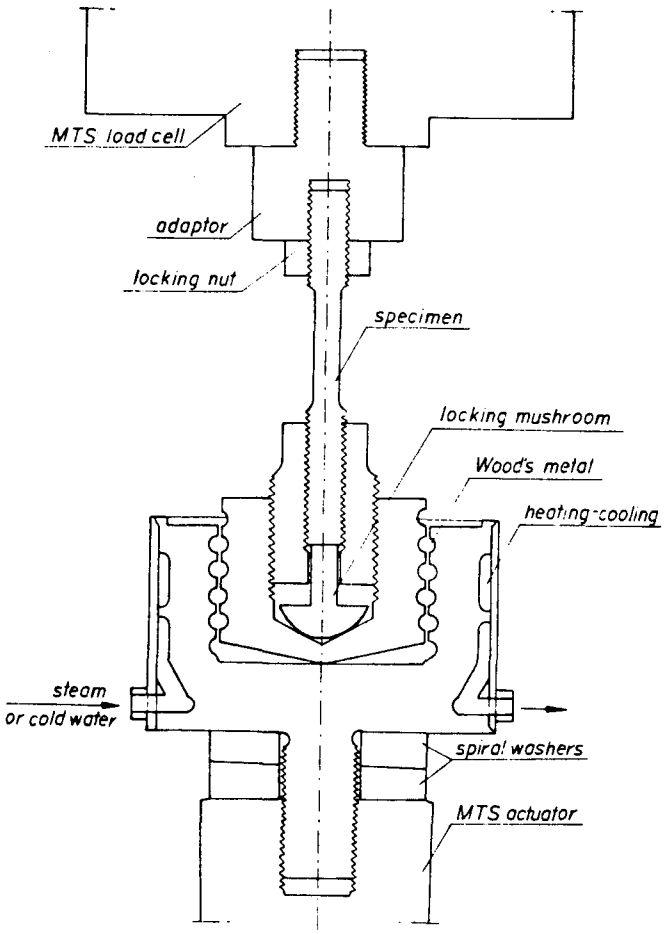

Fig. 4.10 Woods Metal Grip

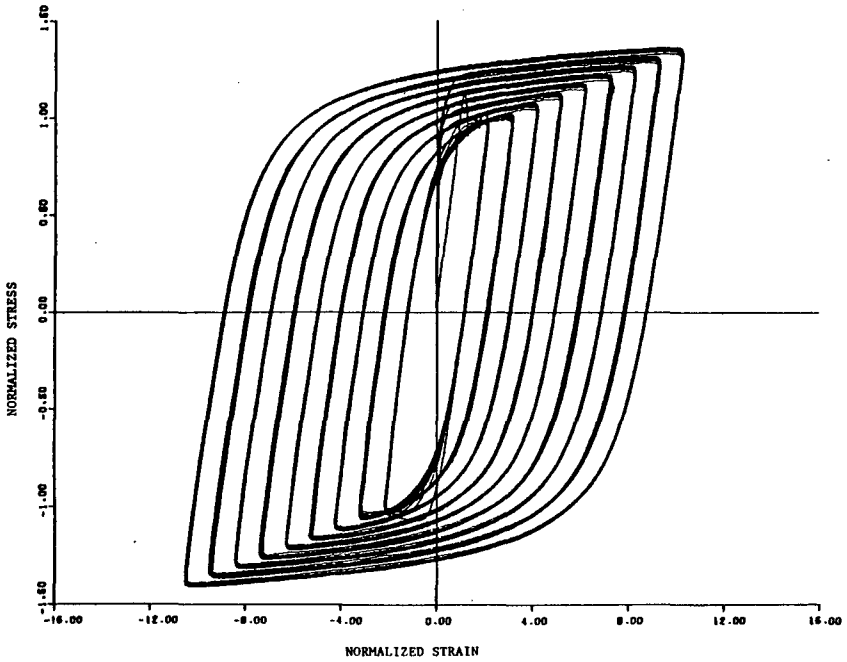

Fig. 4.11 Multiple Step Test

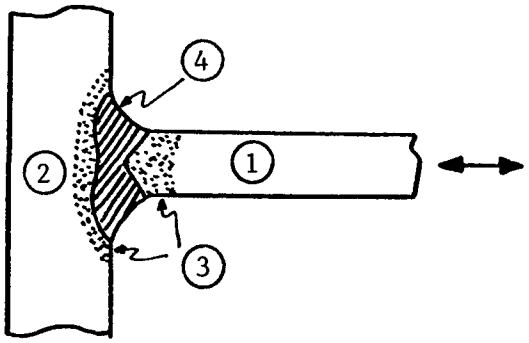

Fig. 4.12 Material Zones in a T-Joint

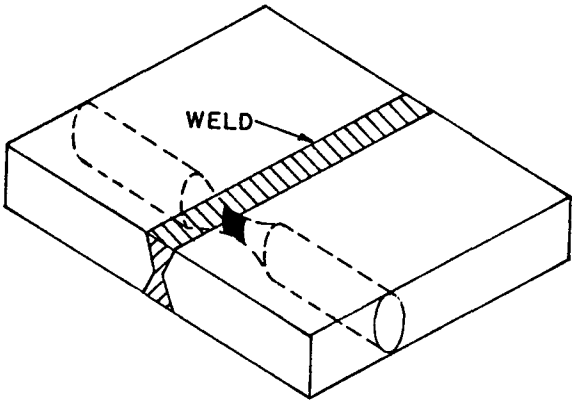

Fig. 4.13 Test Specimen from a Welded Plate, Long. Dir. (Ref. 94)

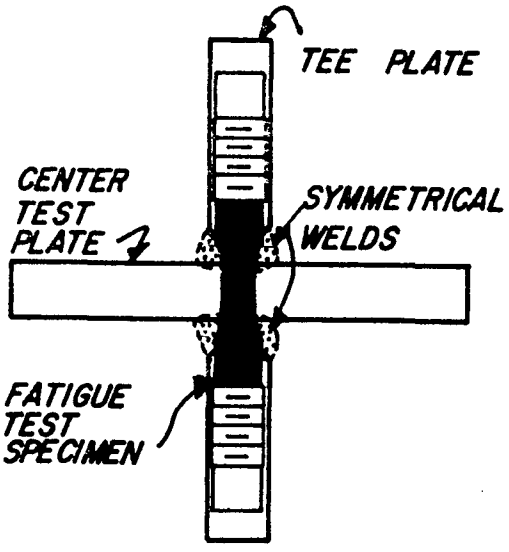

Fig. 4.14 Test Specimen from a Welded Plate, Through Dir. (Ref. 95)

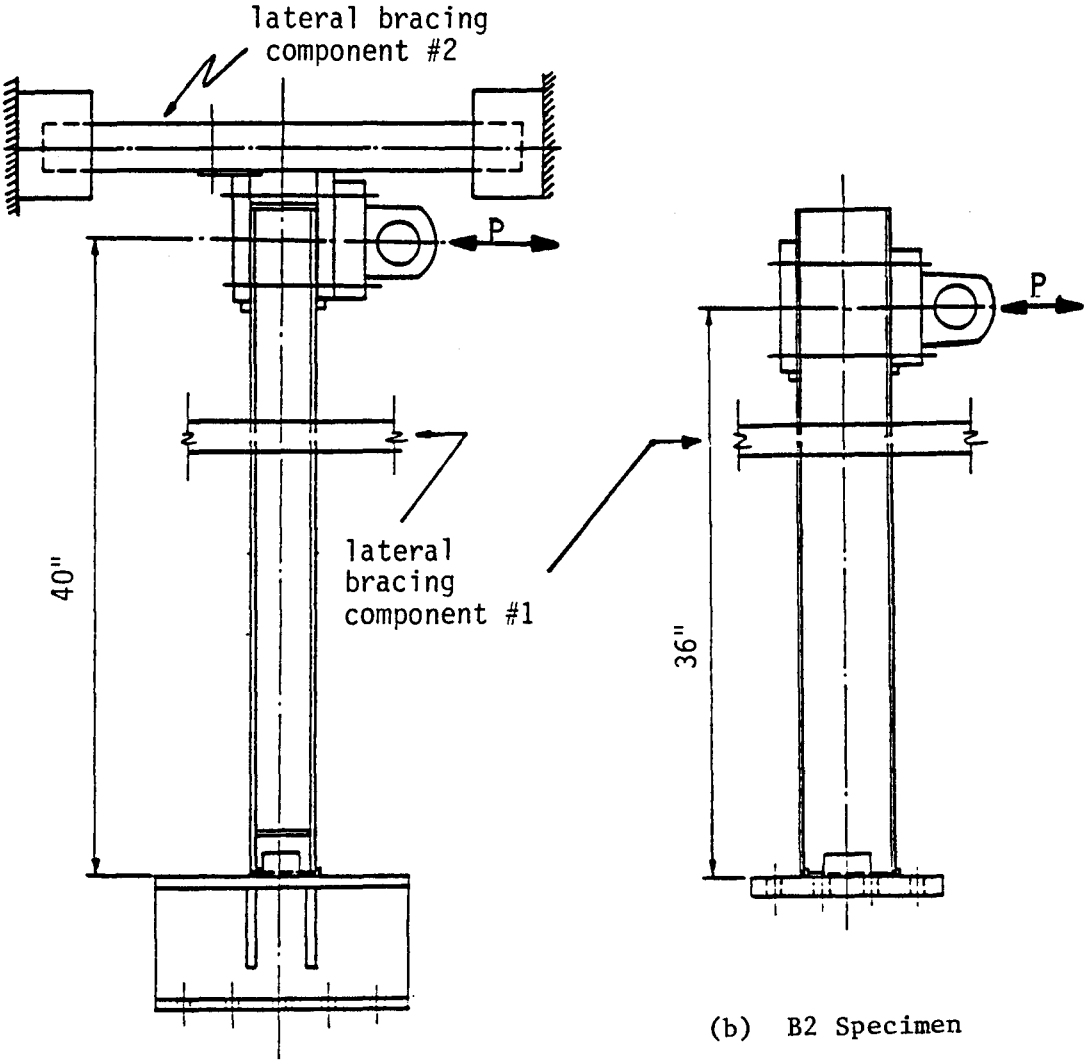

(a) B1 Specimen

(b) B2 Specimen

Fig. 5.1 Test Specimens

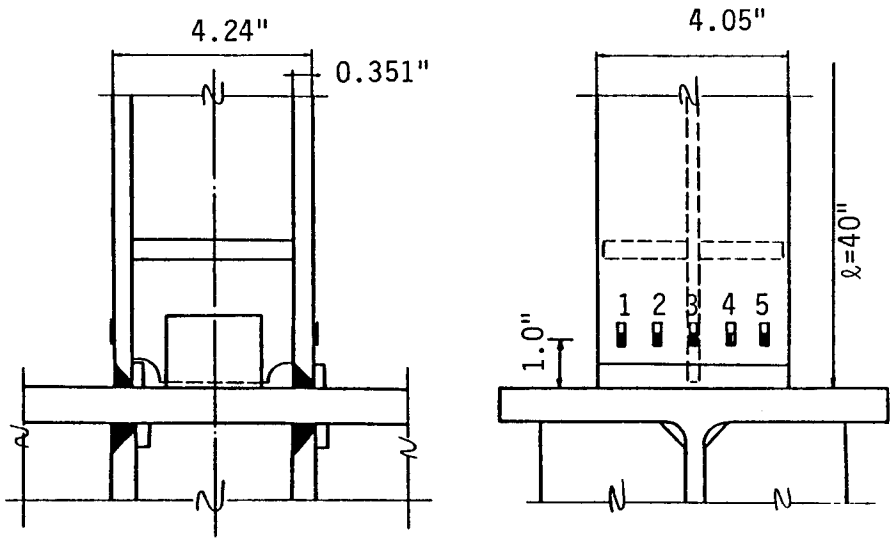

(a) B1 Specimen

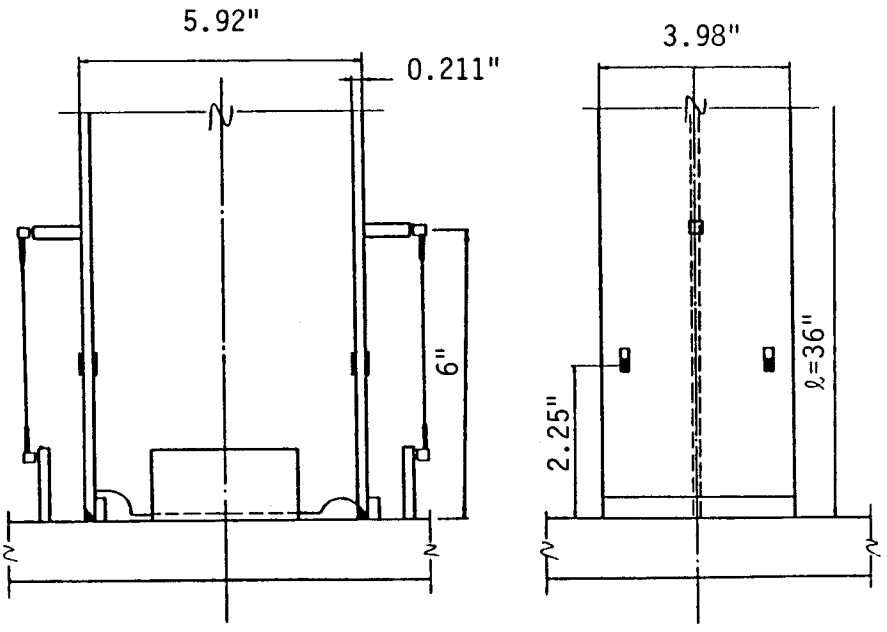

(b) B2 Specimen

Fig. 5.2 Connection Details and Instrumentation

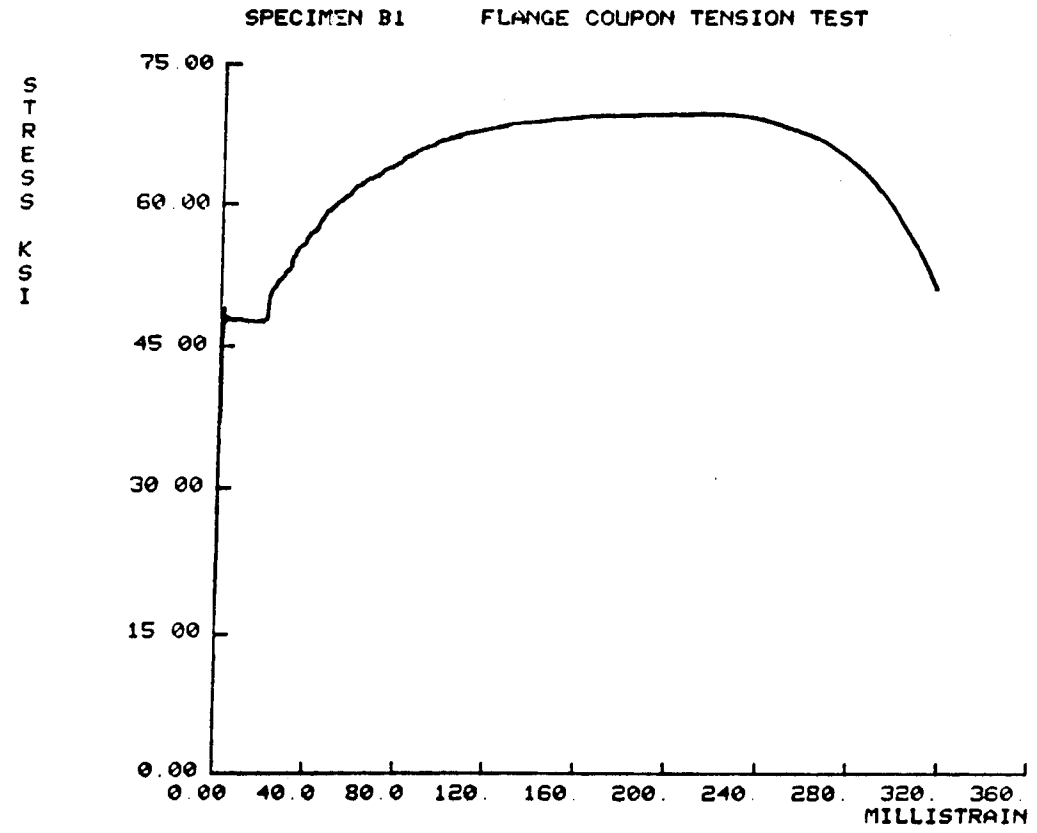

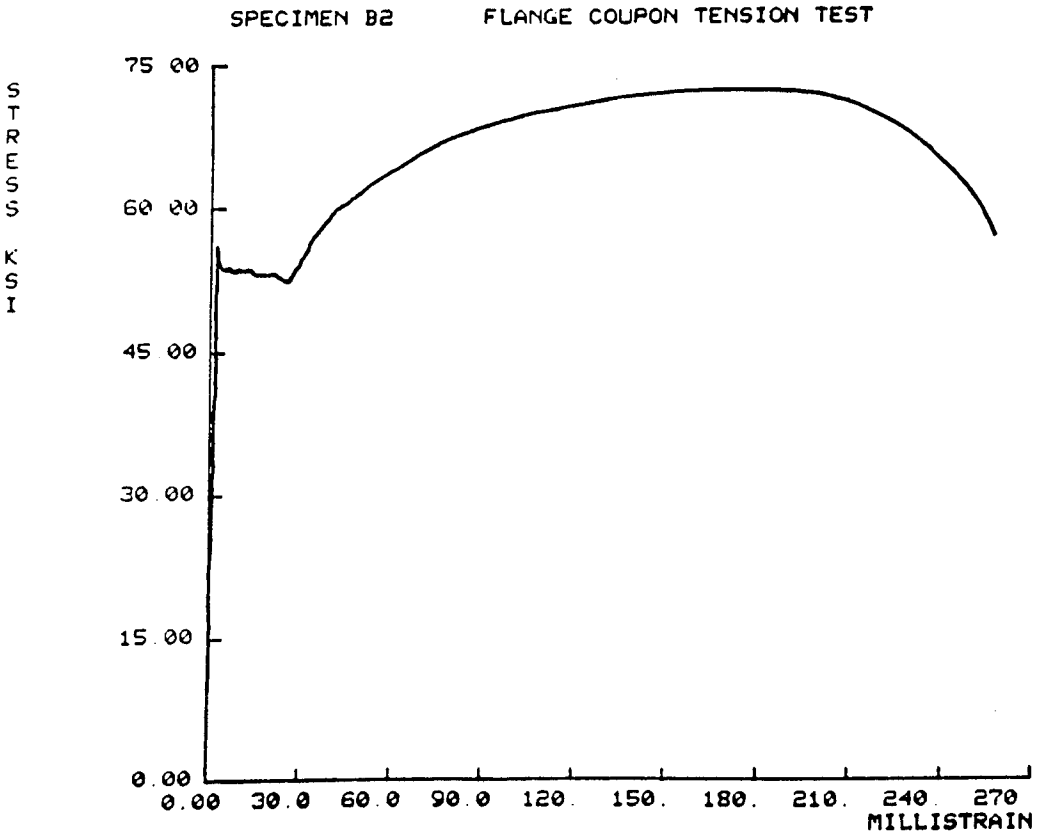

Fig. 5.3 Monotonic Stress-Strain Diagrams of Flange Coupons of Beam Specimens

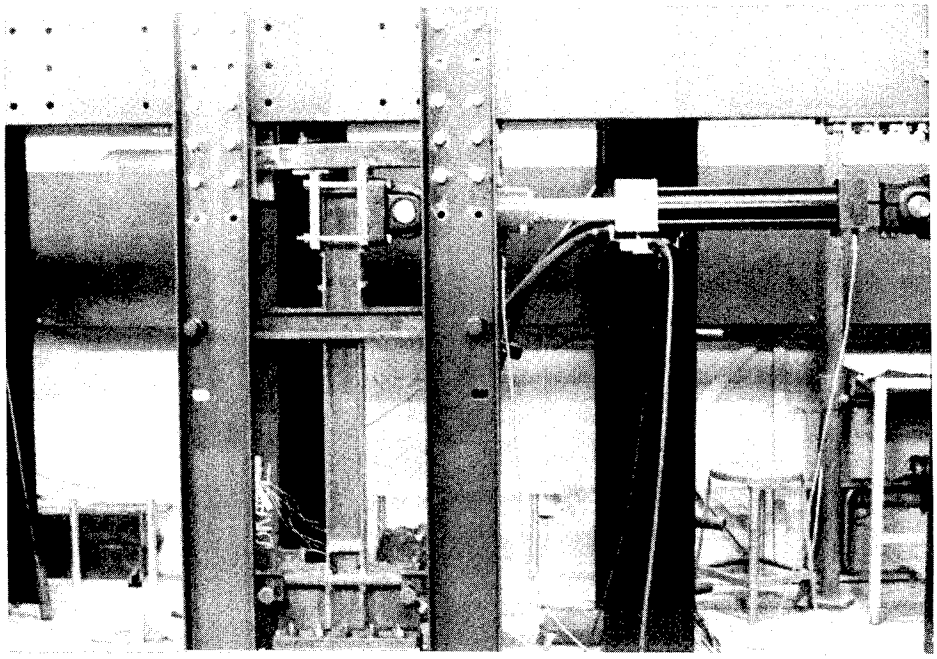

(a) B1 Specimen

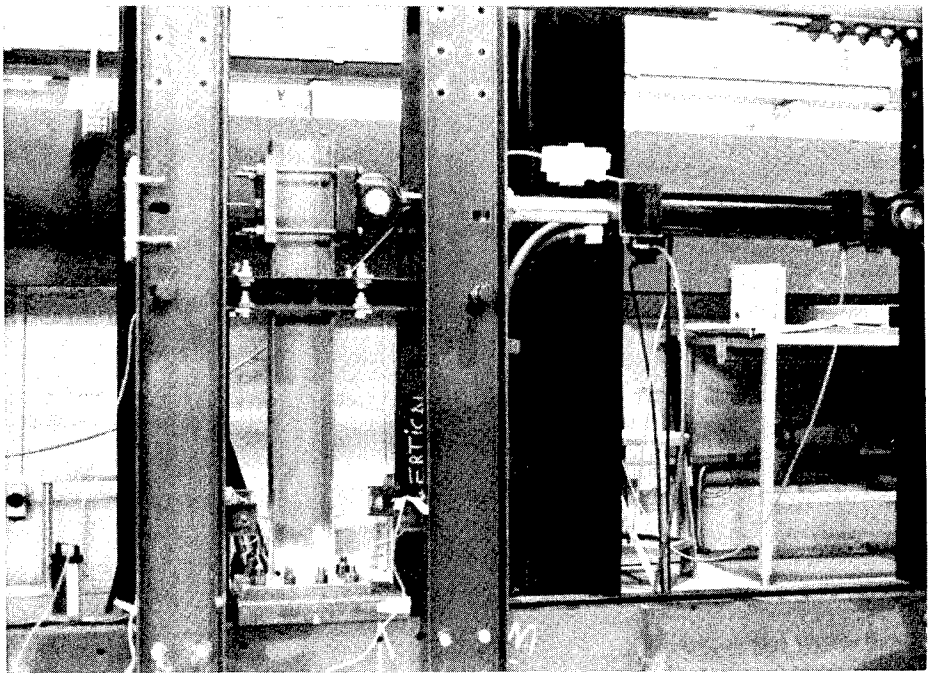

(b) B2 Specimen

Fig. 5.4 Photos of Experimental Set-up

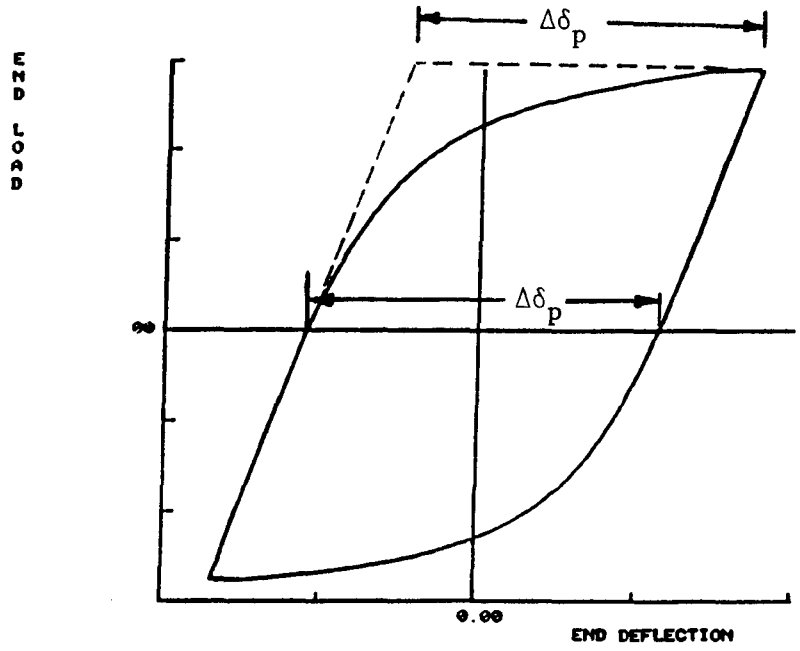

Fig. 5.5 Definition of Plastic Deflection Range $\Delta\delta_p$

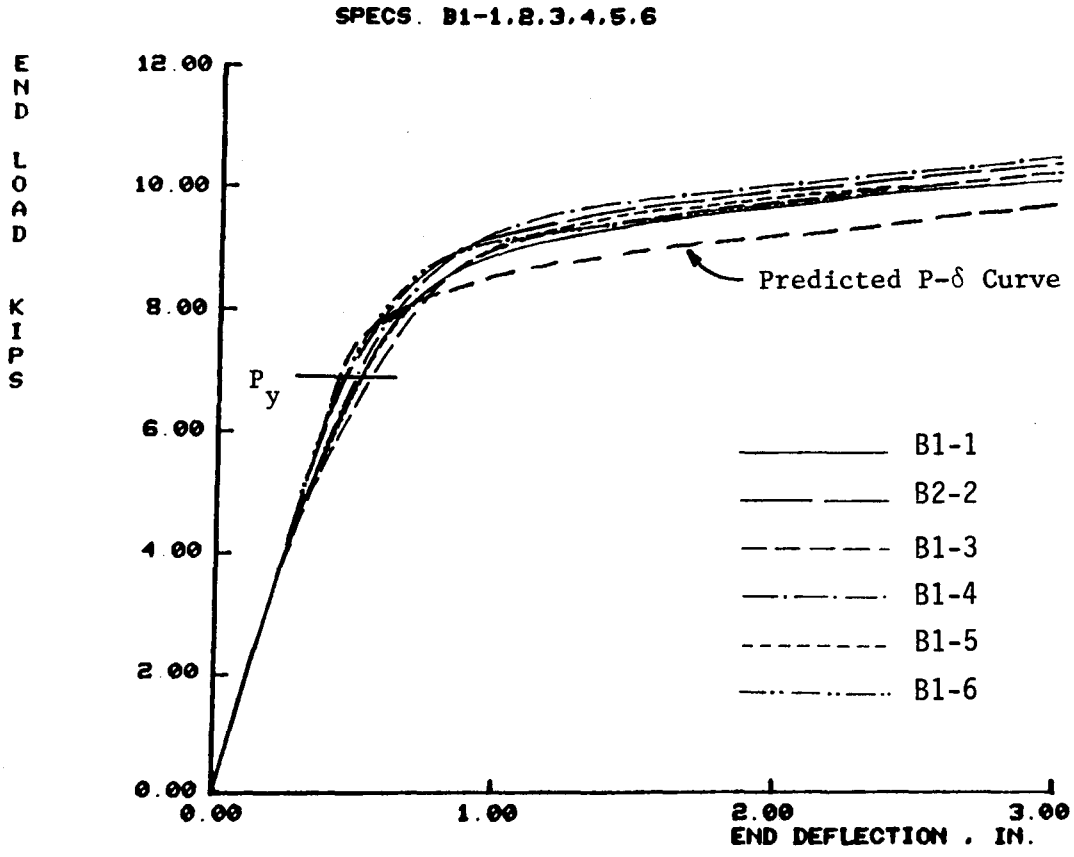

Fig. 5.6 Monotonic Load--Deflection Diagrams, B1 Specimens

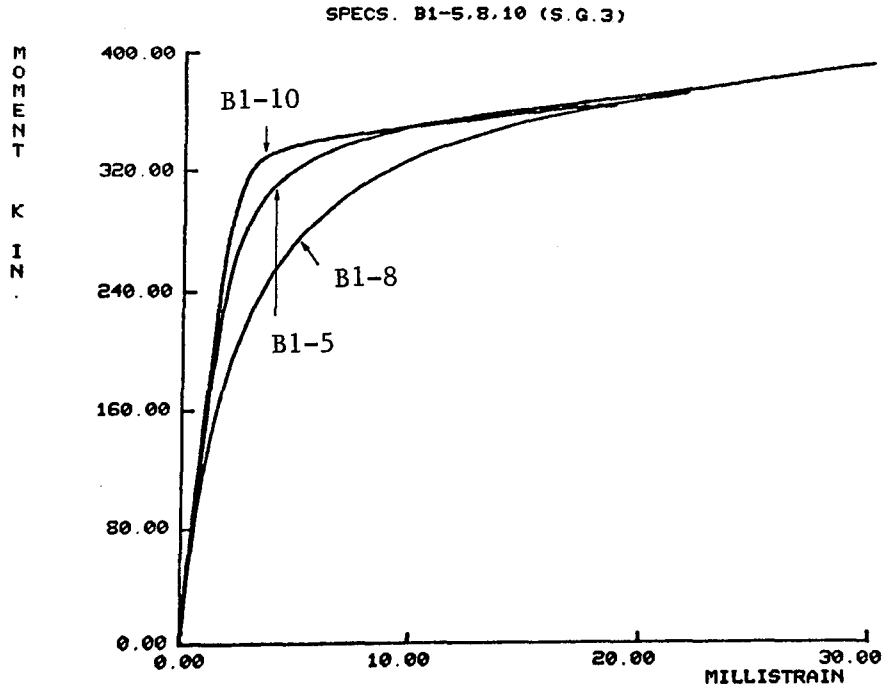

Fig. 5.7 Monotonic Moment--Strain Diagrams of Three B1 Specimens

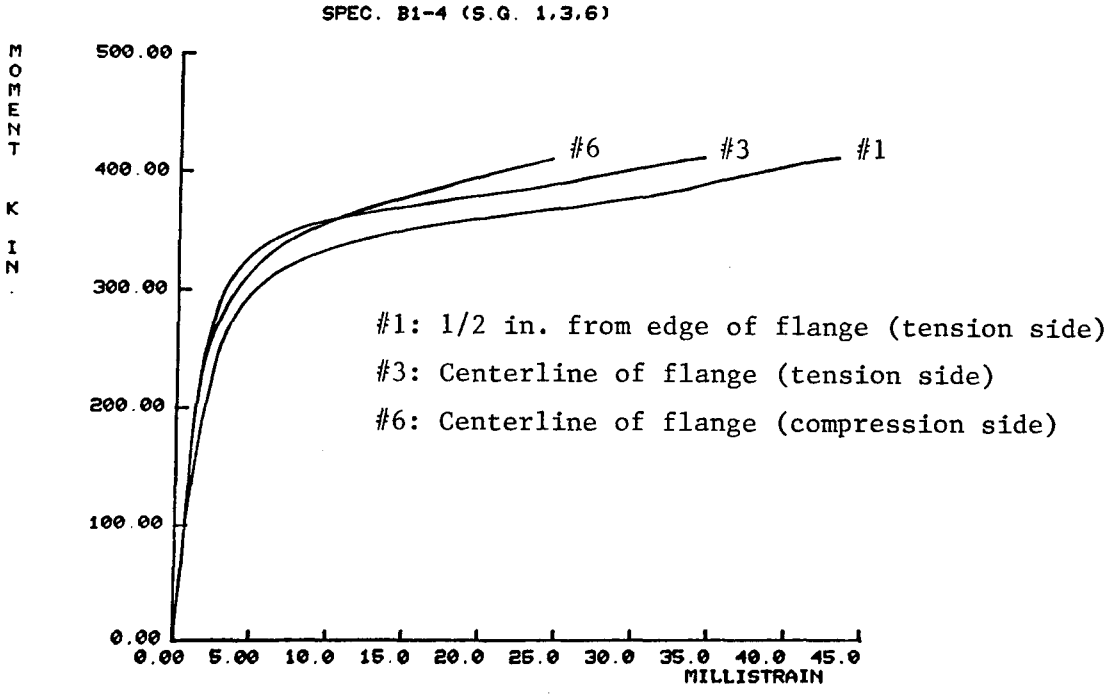

Fig. 5.8 Monotonic Moment--Strain Diagrams from Tension and Compression Flange, Specimen B1-4

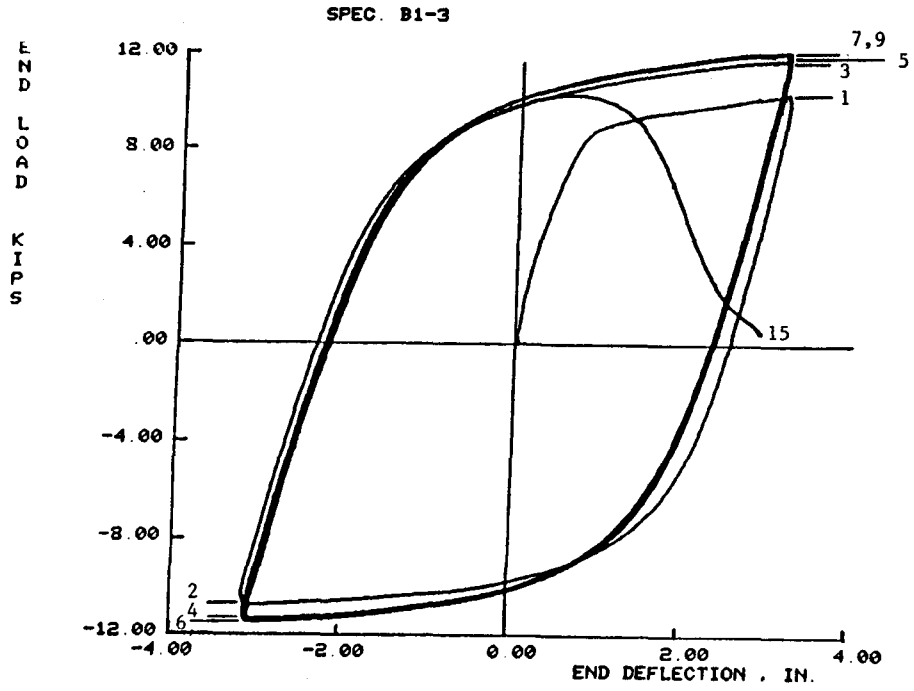

(a)

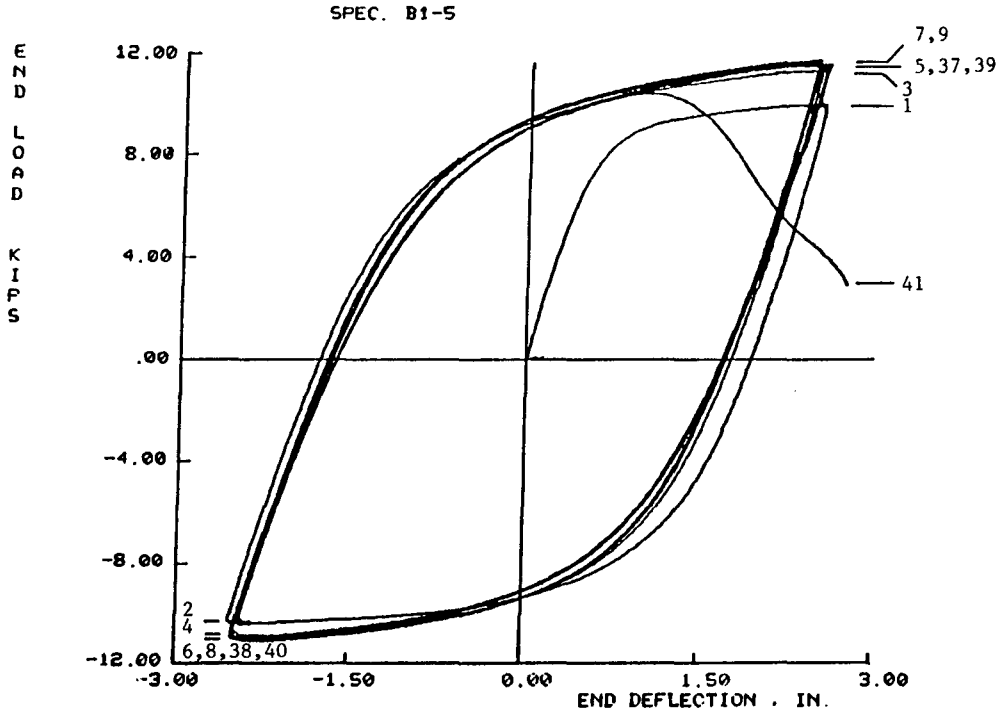

(b)

Fig. 5.9 Cyclic Load--Deflection Diagrams, B1 Specimens

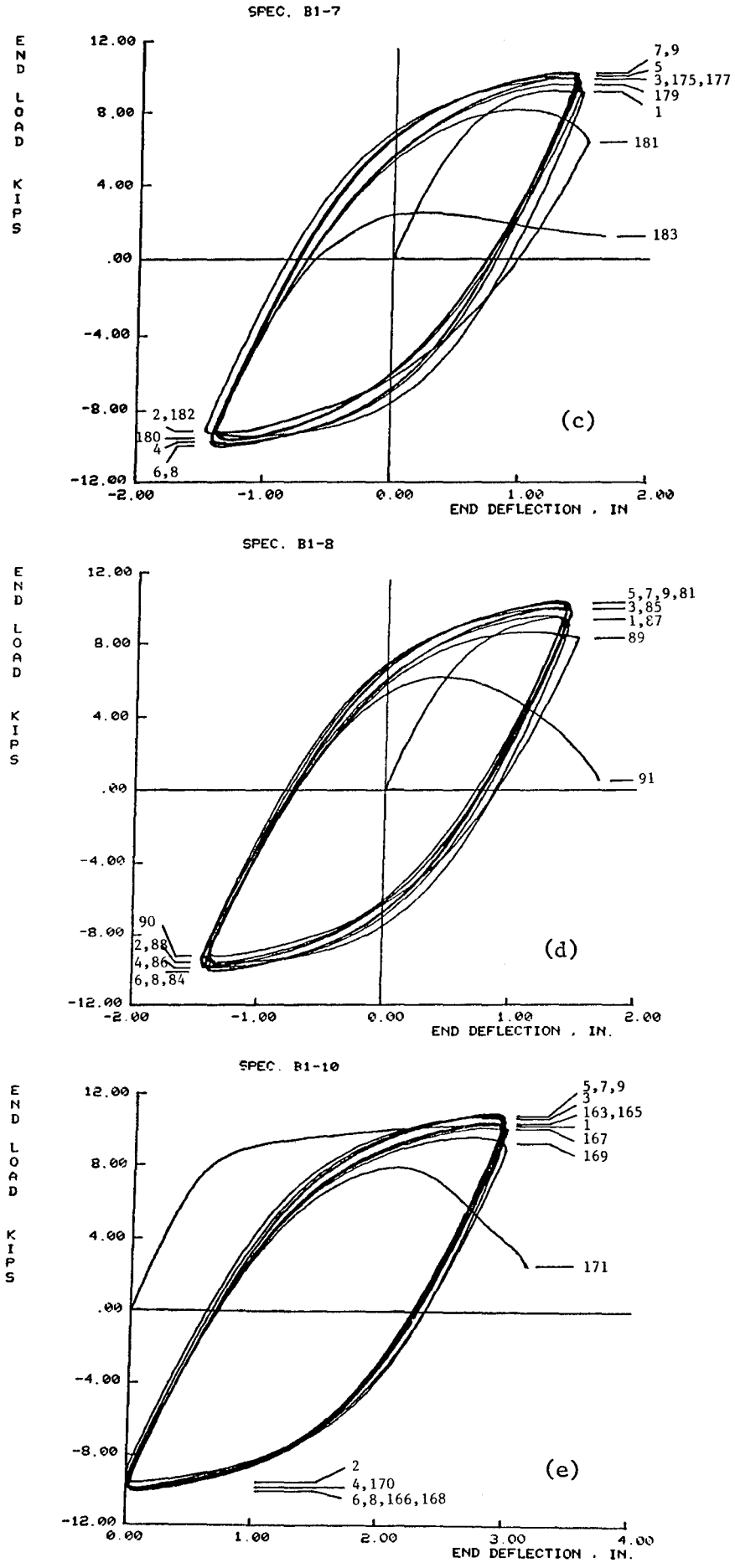

Fig. 5.9 continued

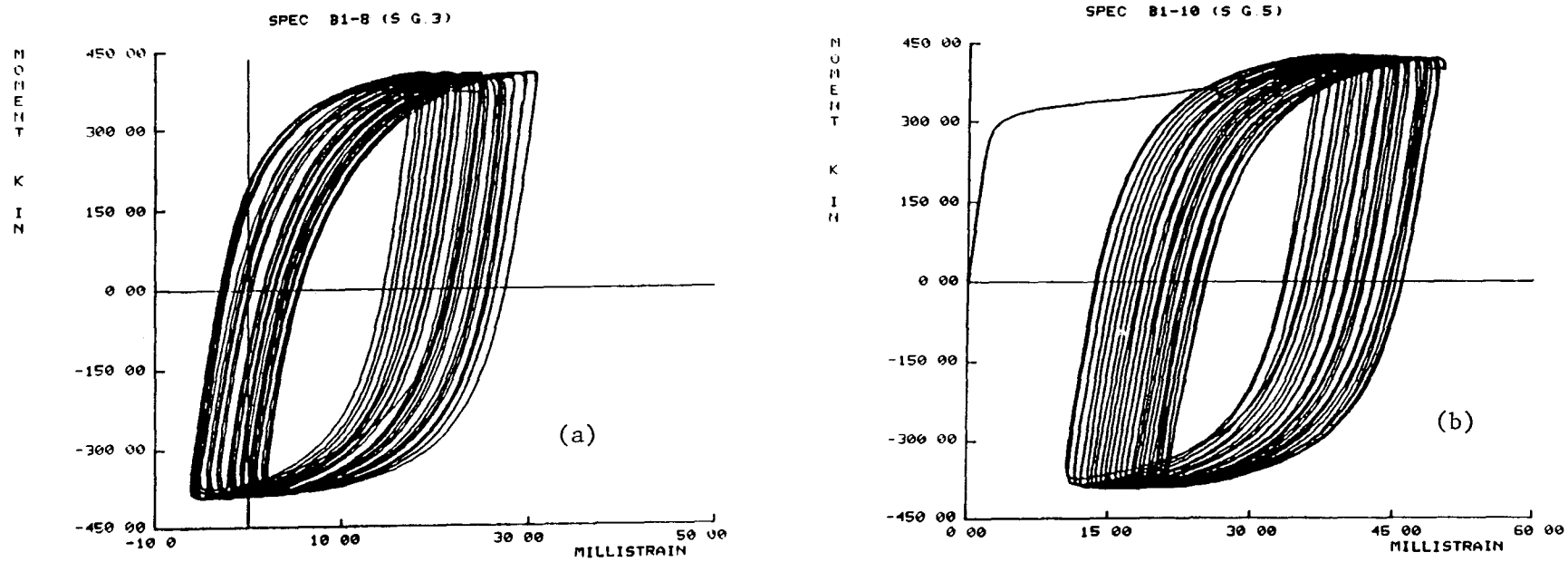

Fig. 5.10 Cyclic Moment--Strain Diagrams, B1 Specimens

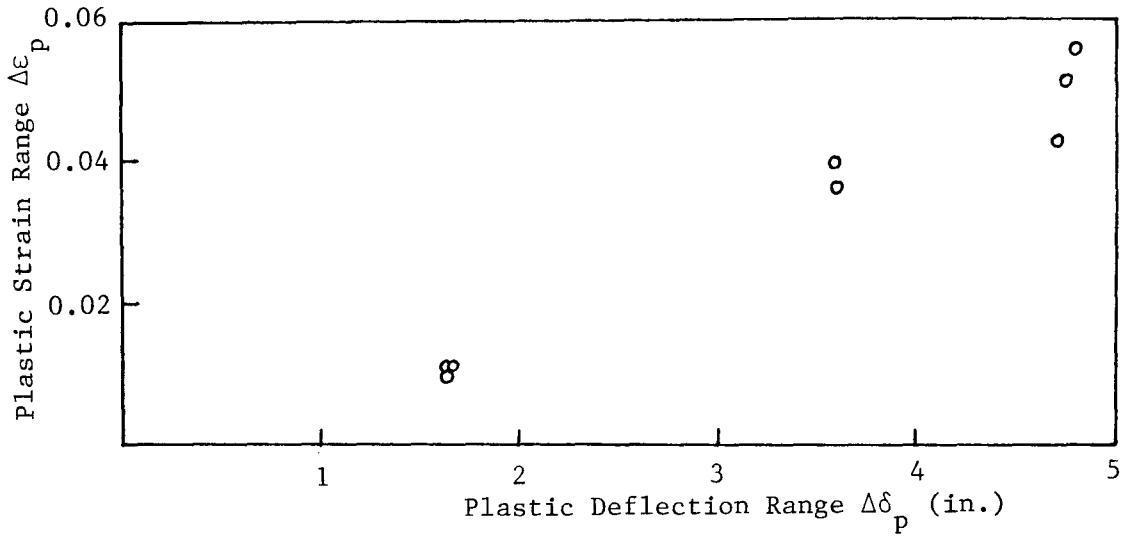

Fig. 5.11 Plastic Deflection Range versus Plastic Strain Range, B1 Specimens

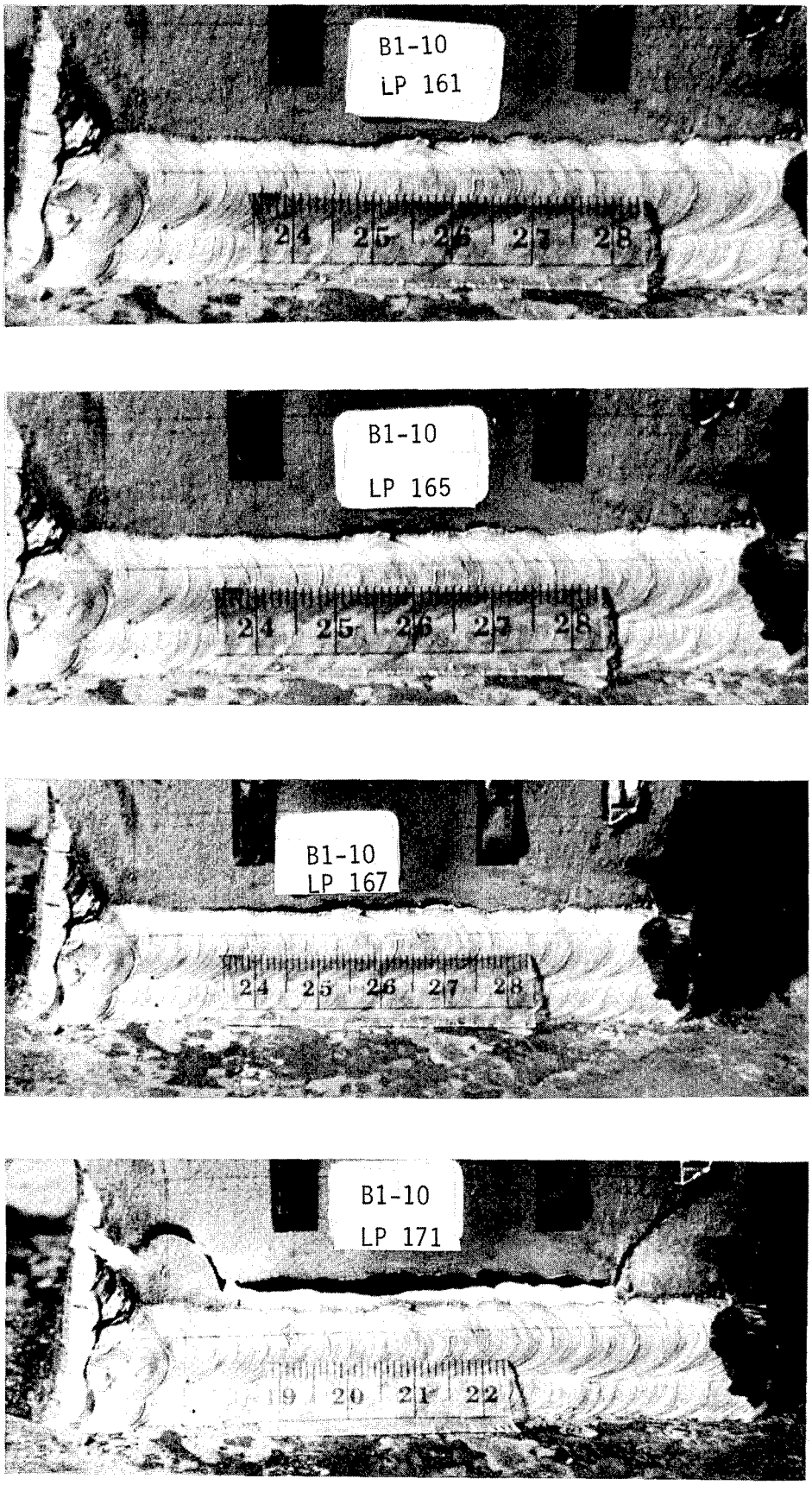

Fig. 5.12 Crack Propagation Through and Across Flange, Specimen B1-10

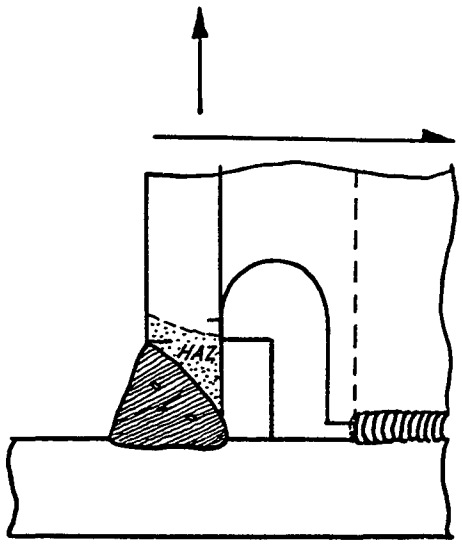

Fig. 5.13 Cracks at Weld Toe and Coping

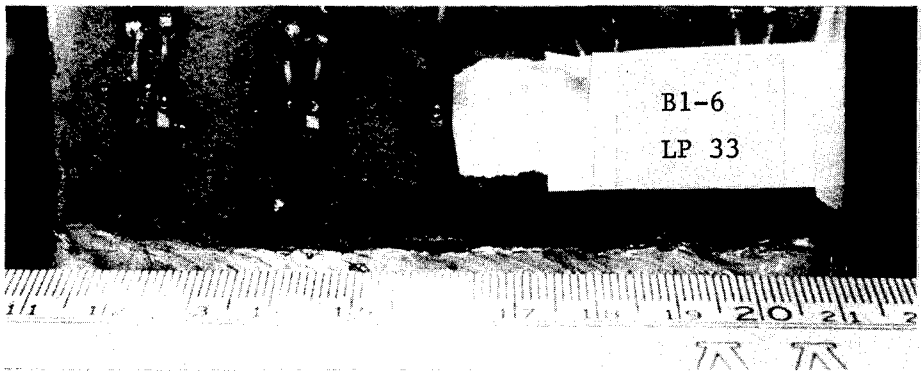

(a)

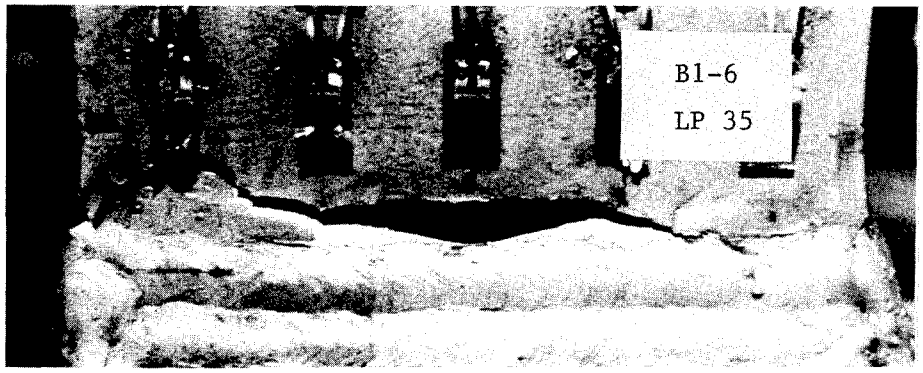

(b)

Fig. 5.14 Crack Growth in Specimen B1-6

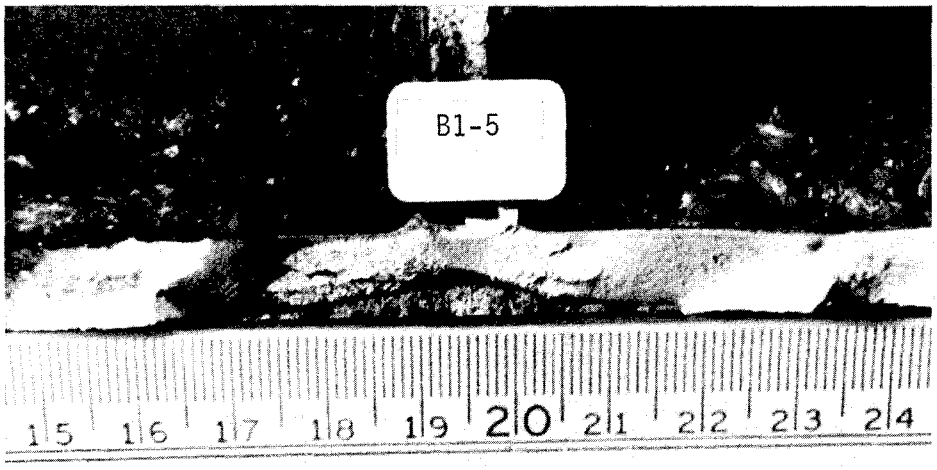

(a)

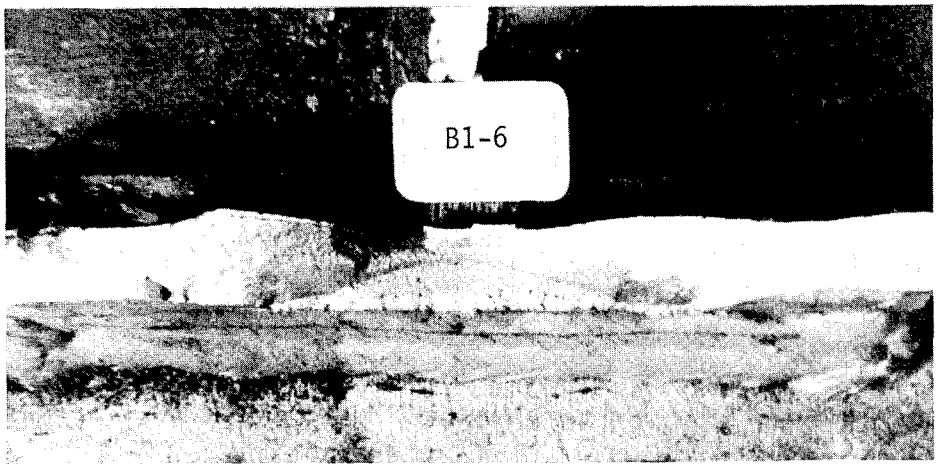

(b)

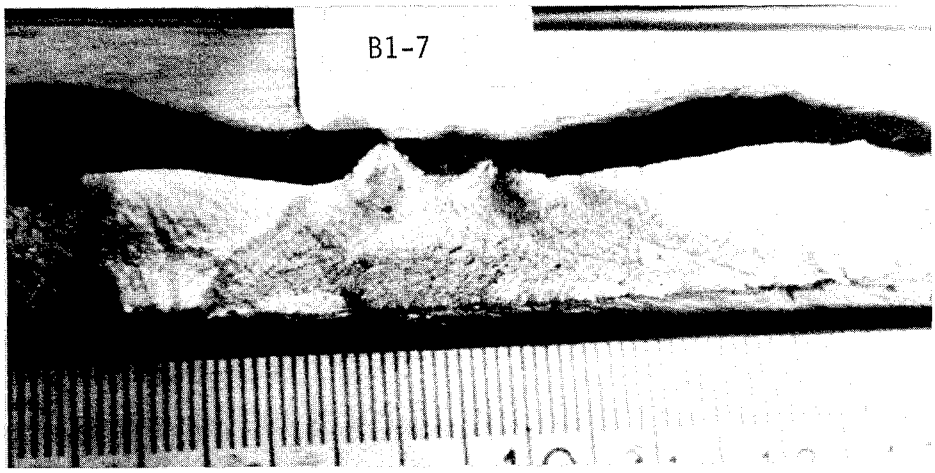

(c)

Fig. 5.15 Regions of Crack Propagation on Fracture Surface

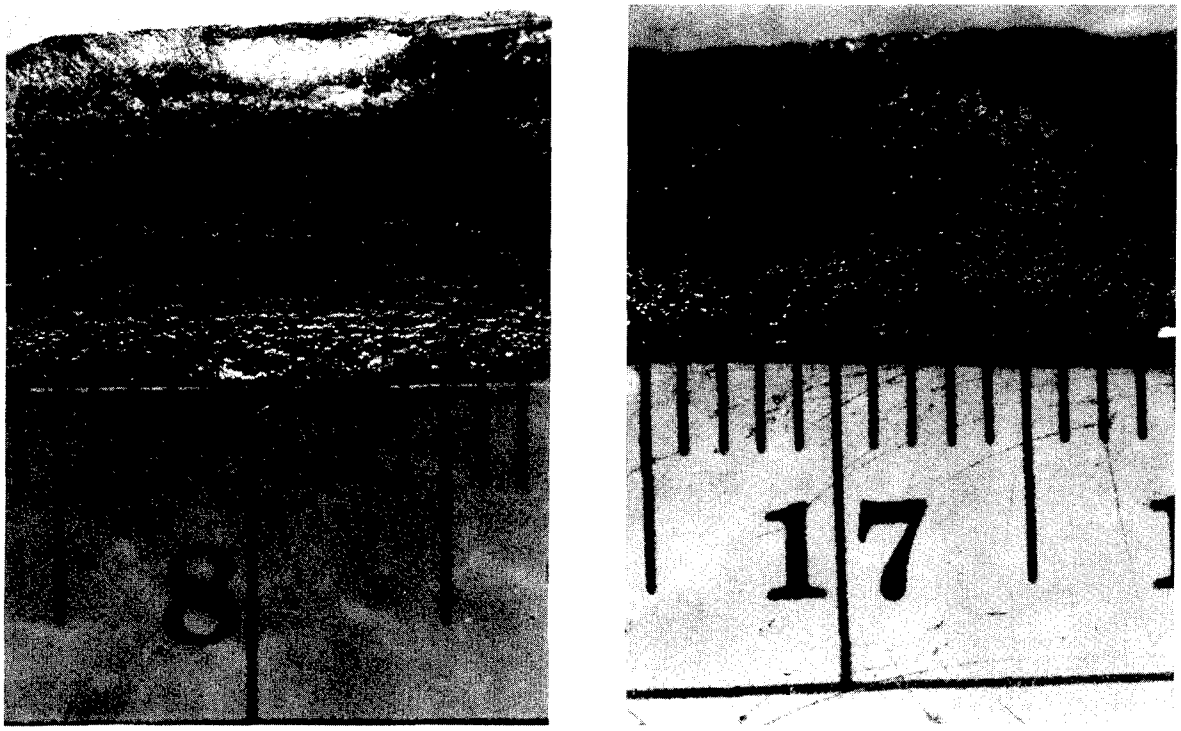

Specimen B1-6 Specimen B1-7

Fig. 5.16 Magnified Photos of Striations on Fracture Surface

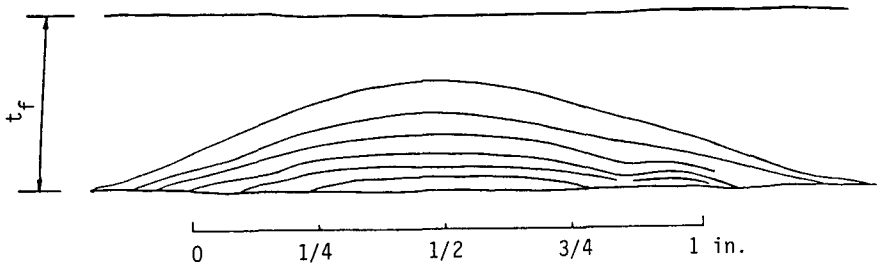

(b) Specimen B1-8

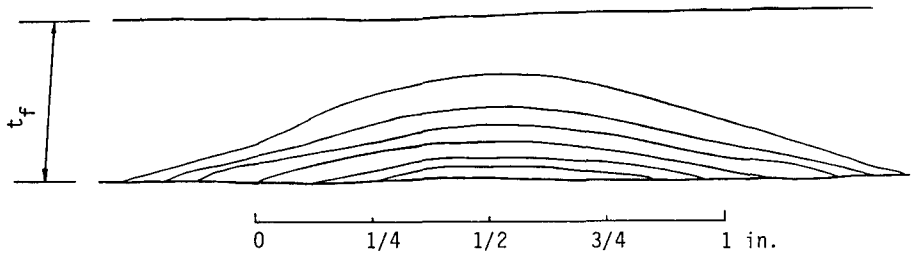

(a) Specimen B1-6

Fig. 5.17 Shapes of Cracks at Diffferent Stages of Growth

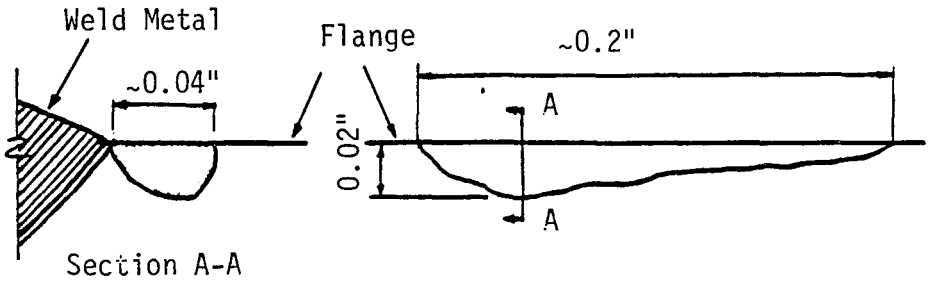

Fig. 5.18 Typical Surface Imperfection at Weld Toe

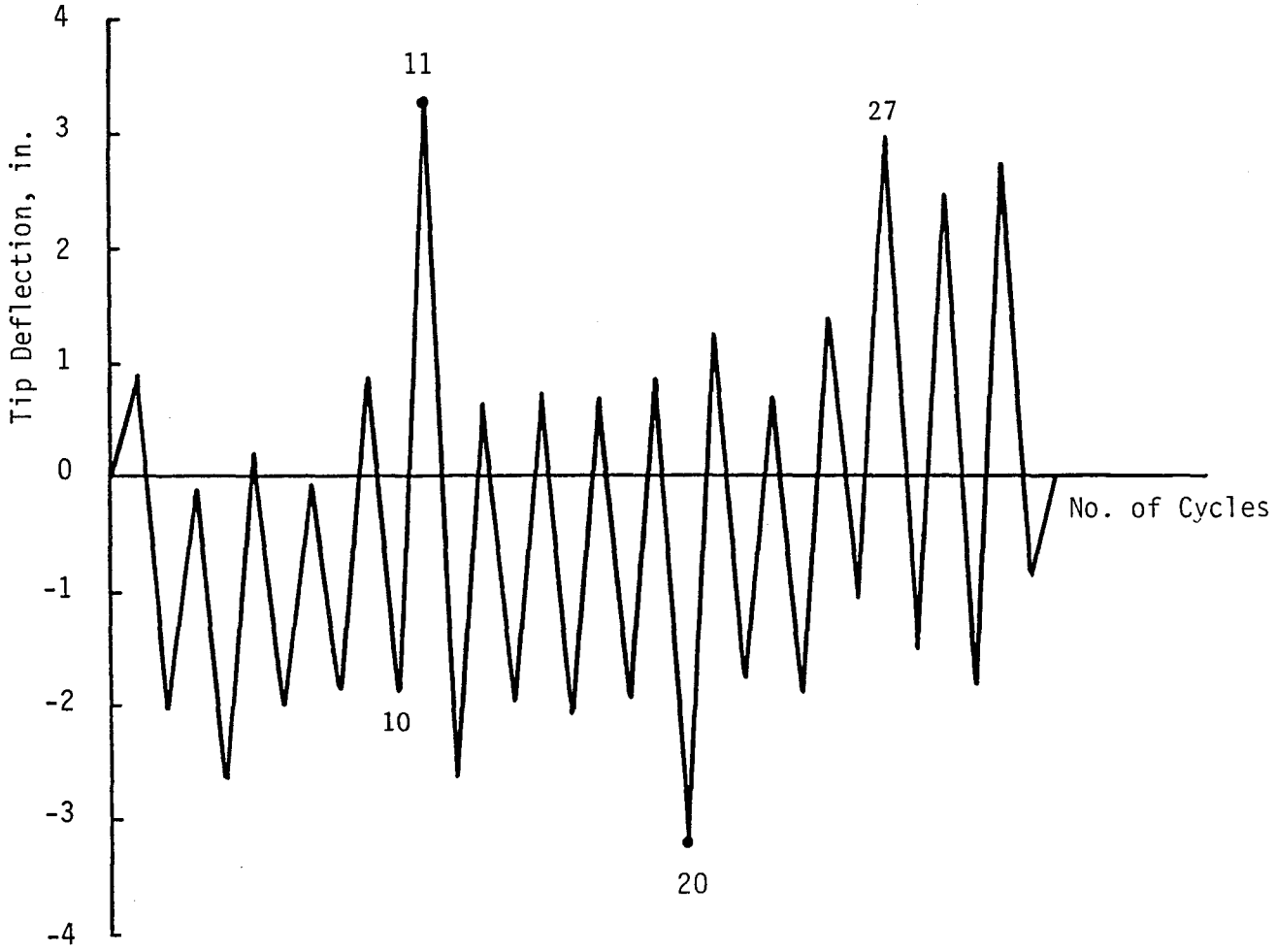

Fig. 5.19 Tip Deflection History for Specimen B1-9

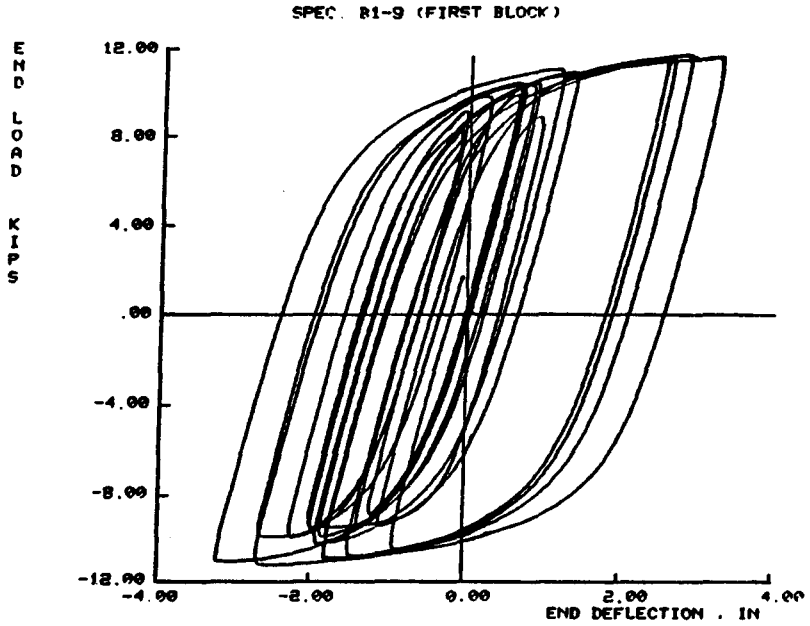

(a)

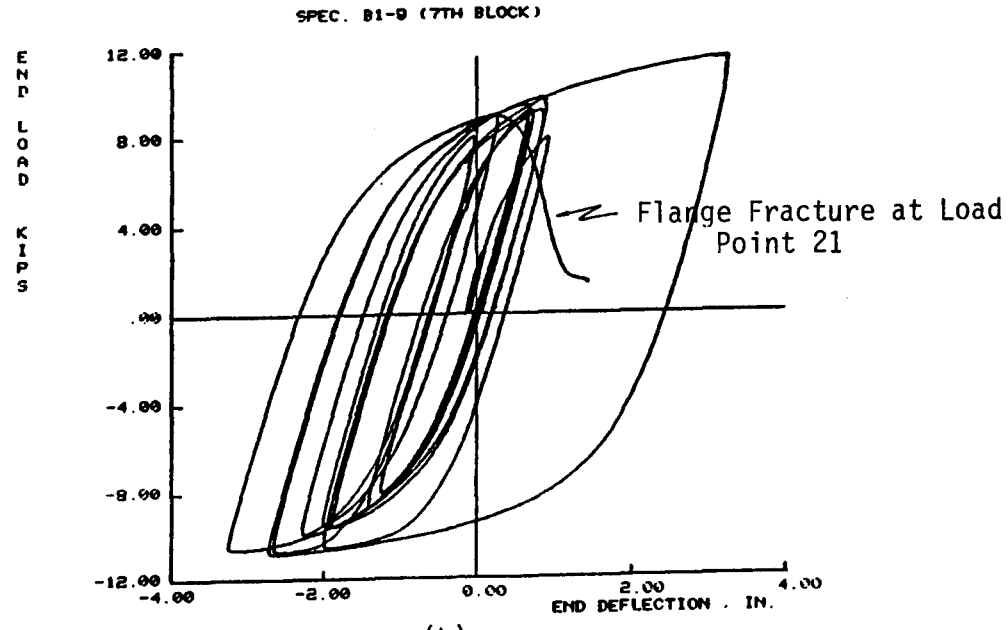

(b)

Fig. 5.20 Cyclic Load--Deflection Diagrams of Specimen B1-9 in First and Last Block of Loading

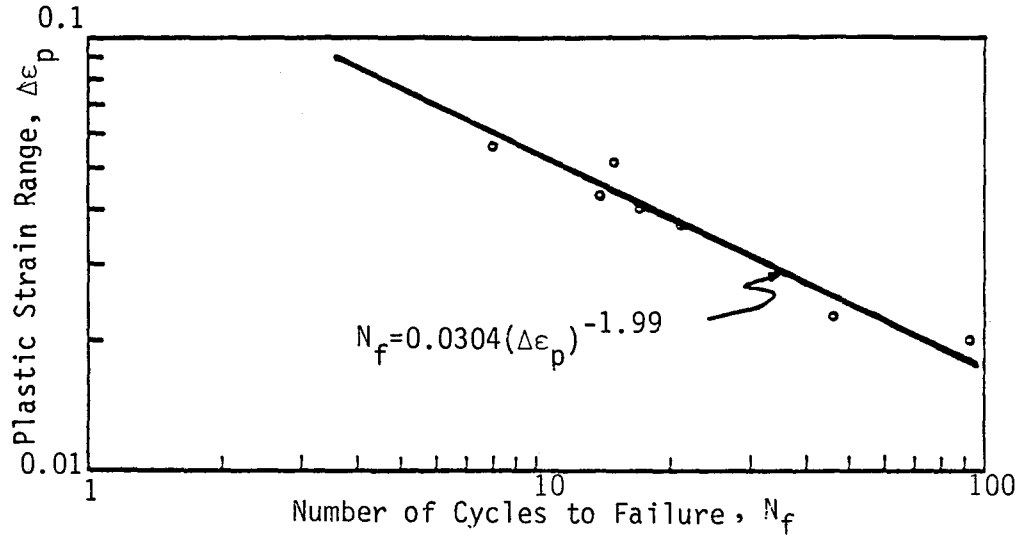

Fig. 5.21 Coffin-Manson Relationship for B1 Specimens Based on Plastic Strain Range Close to Weldment

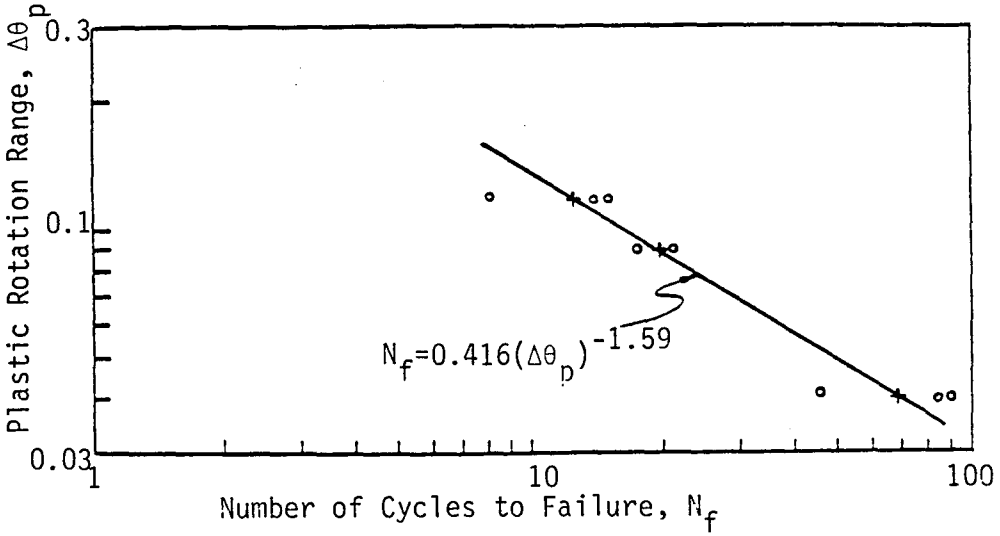

Fig. 5.22 Coffin-Manson Relationship for B1 Specimens Based on Plastic Rotation Range at Support

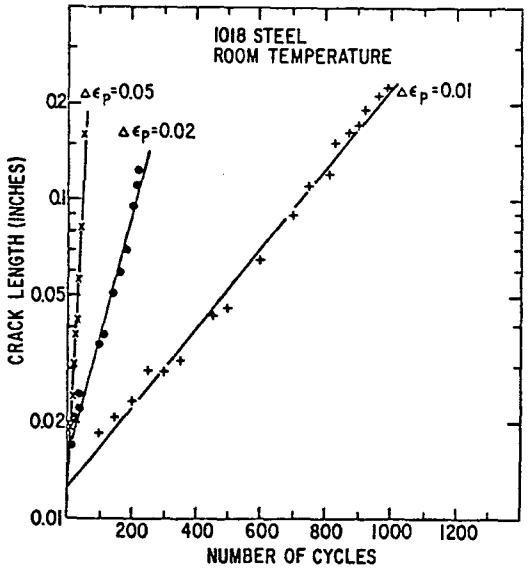

Fig. 5.23 Crack Growth for Constant Plastic Strain Range Tests (Ref. 99)

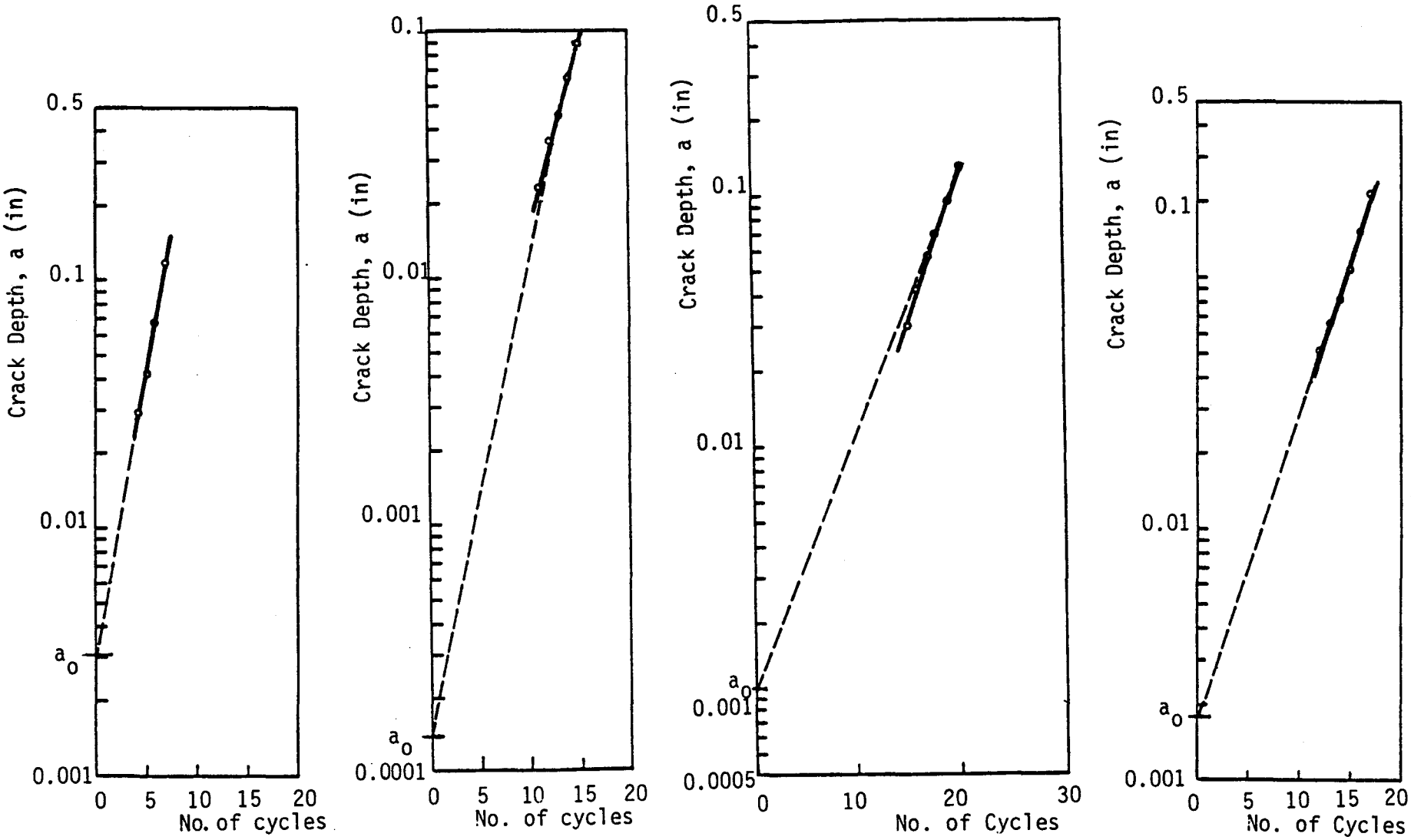

(a) Specimen B1-3 (b) Specimen B1-4 (c) Specimen B1-5 (d) Specimen B1-6

Fig. 5.24 Crack Growth for Constant Amplitude Tests, B1 Specimens

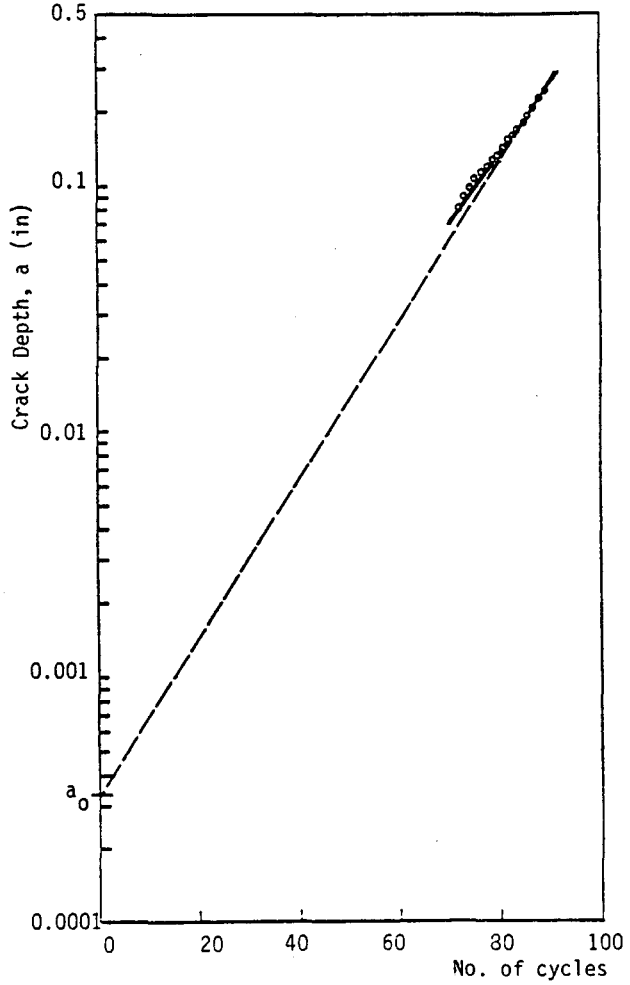

(e) Specimen B1-7

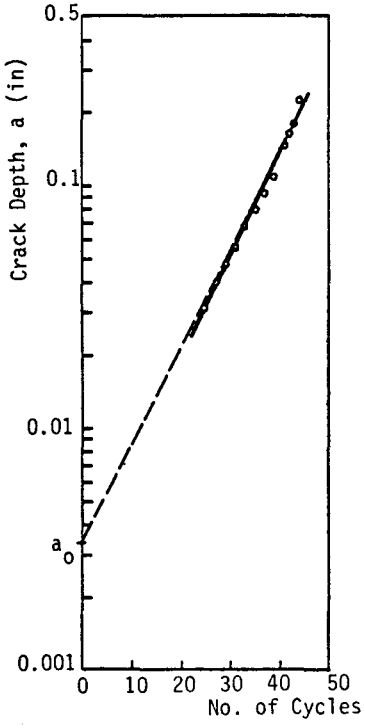

(f) Specimen B1-8

Fig. 5.24 continued

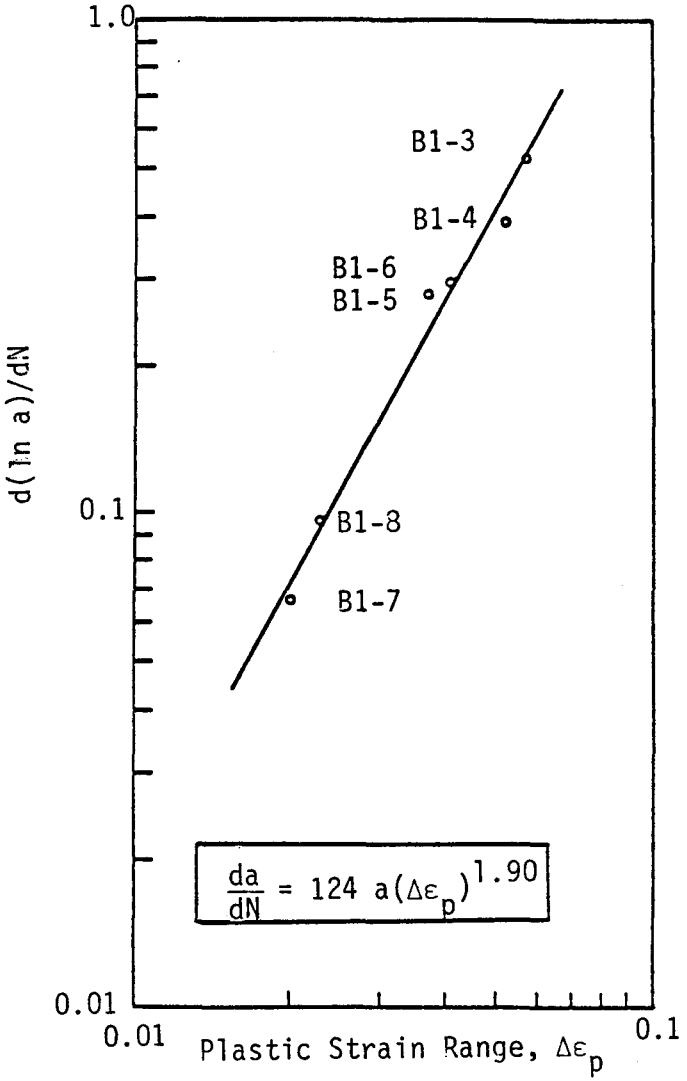

Fig. 5.25 Crack Growth Rate Model for B1 Specimens

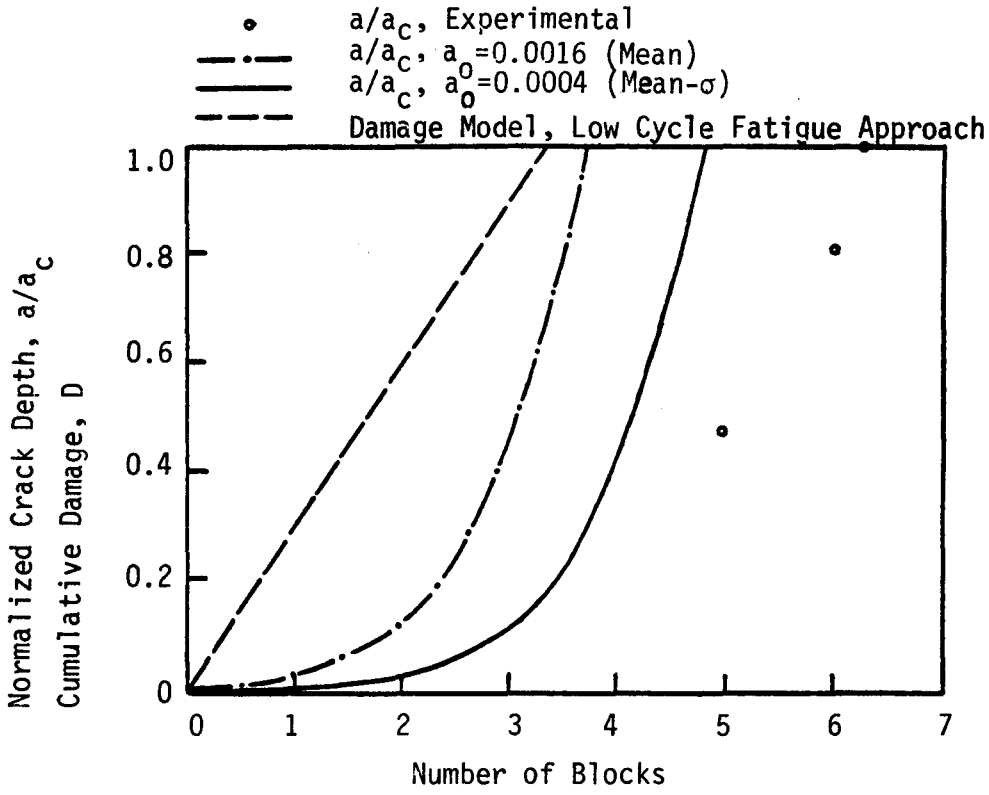

Fig. 5.26 Crack Growth Behavior and Cumulative Damage Prediction for Specimen B1-9

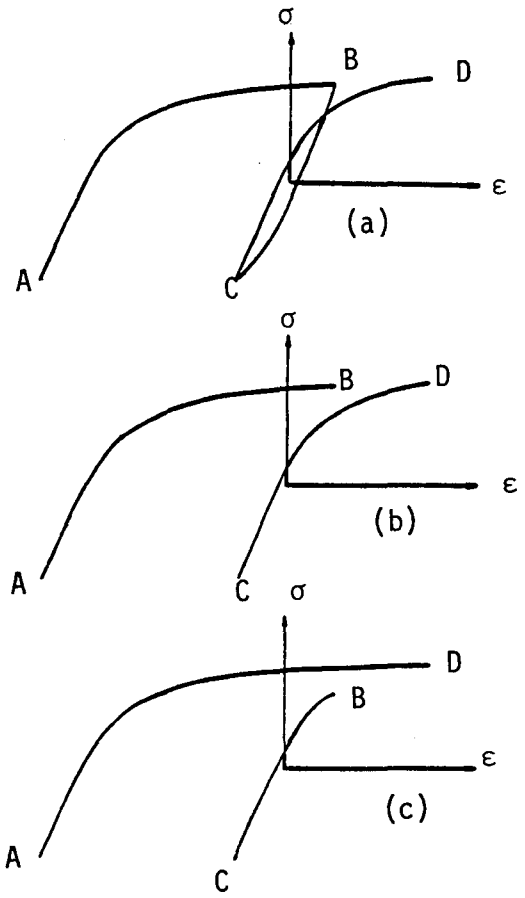

Fig. 5.27 Effect of Cycle Counting on Plastic Strain Ranges

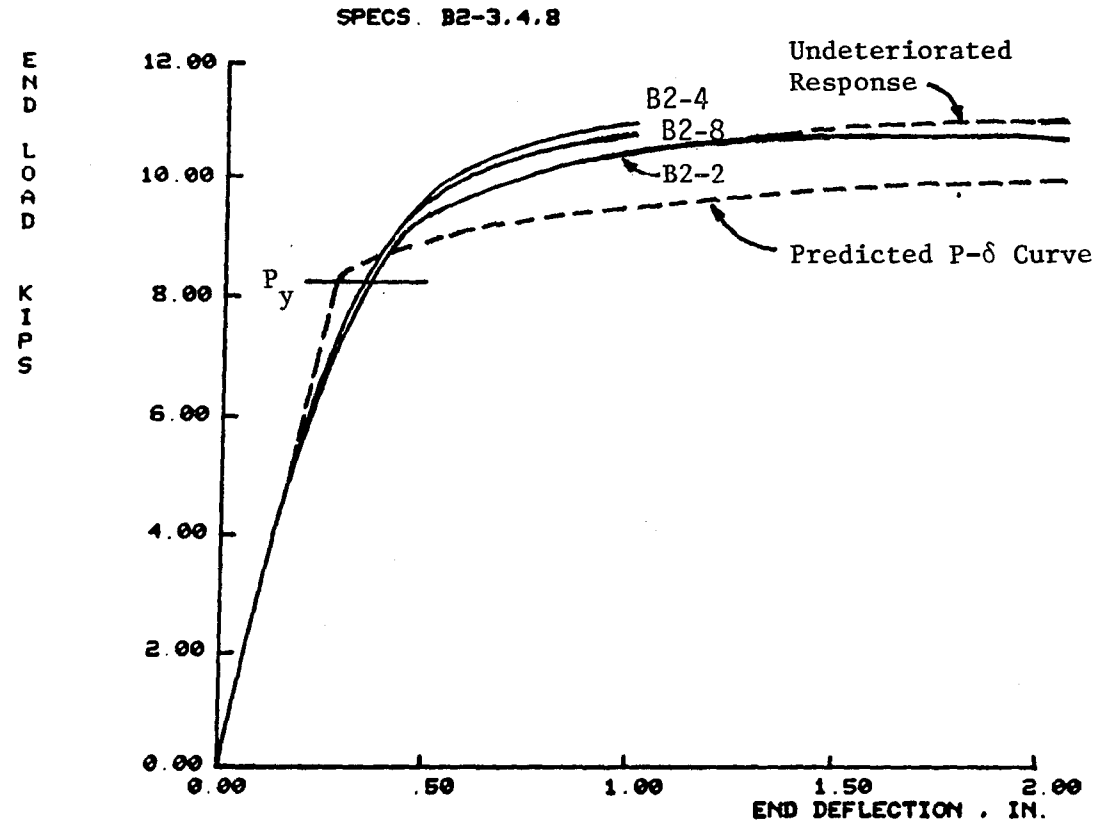

Fig. 5.28 Monotonic Load--Deflection Diagrams, B2 Specimens

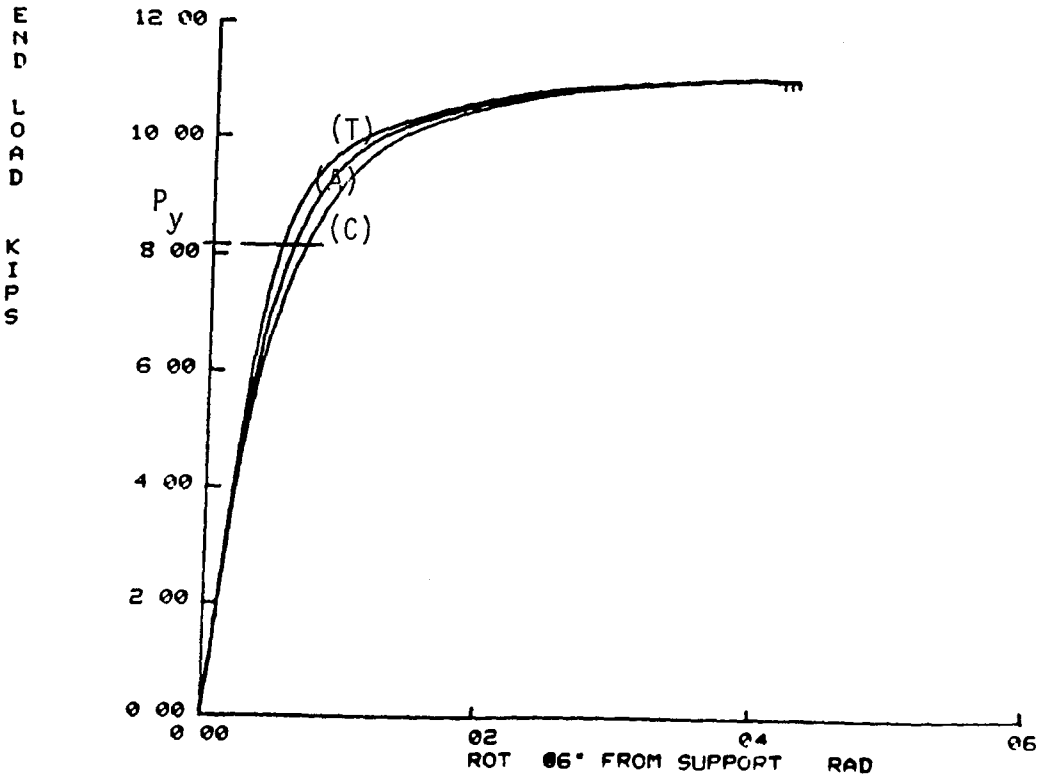

Fig. 5.29 Monotonic Load--Rotation Diagrams Based on Measurements on the Tension Flange (T), Compression Flange (C), and Average Rotation (A)

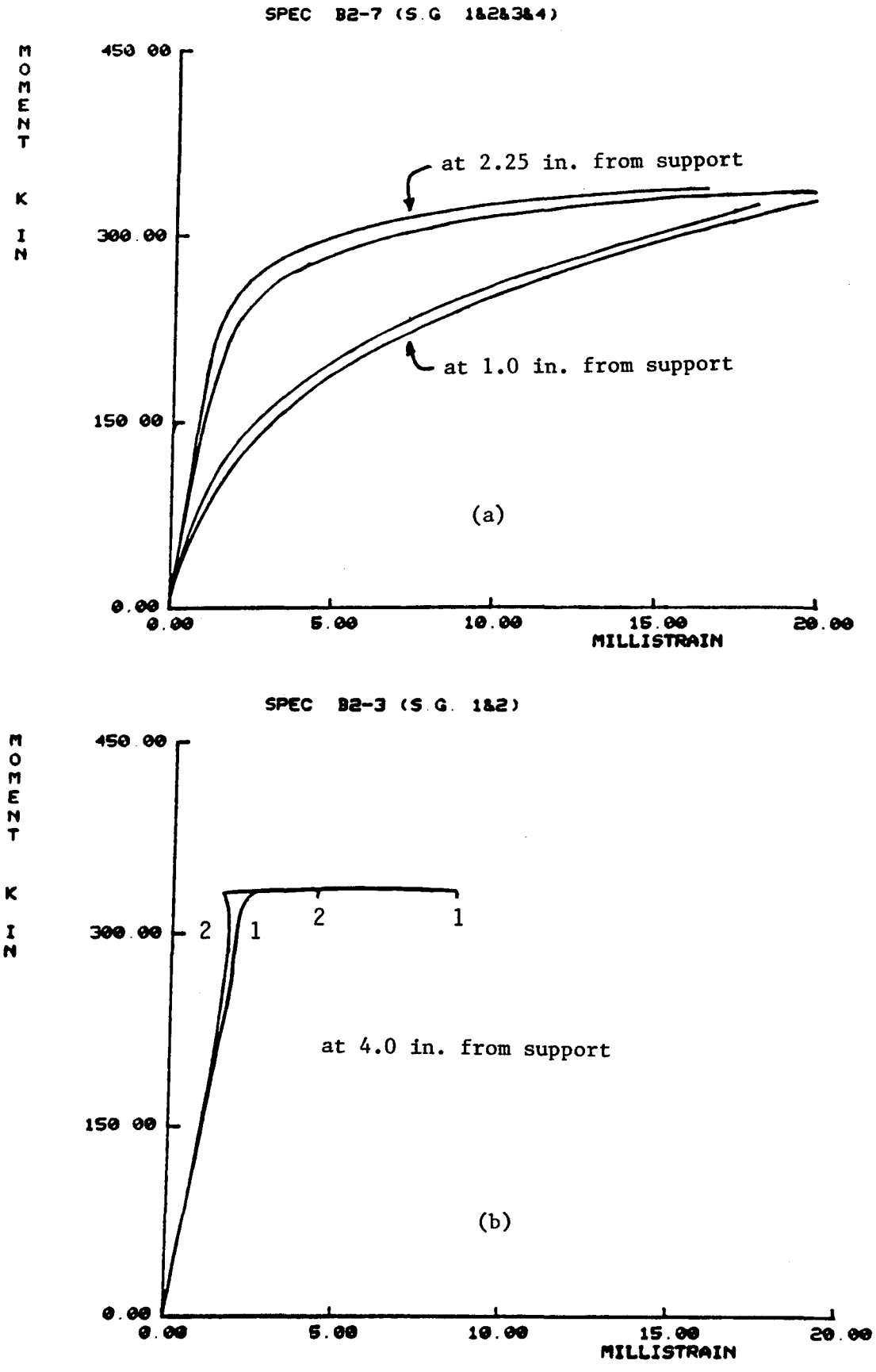

Fig. 5.30 Strain Measurements from Pairs of Strain Gages on the Compression Flange

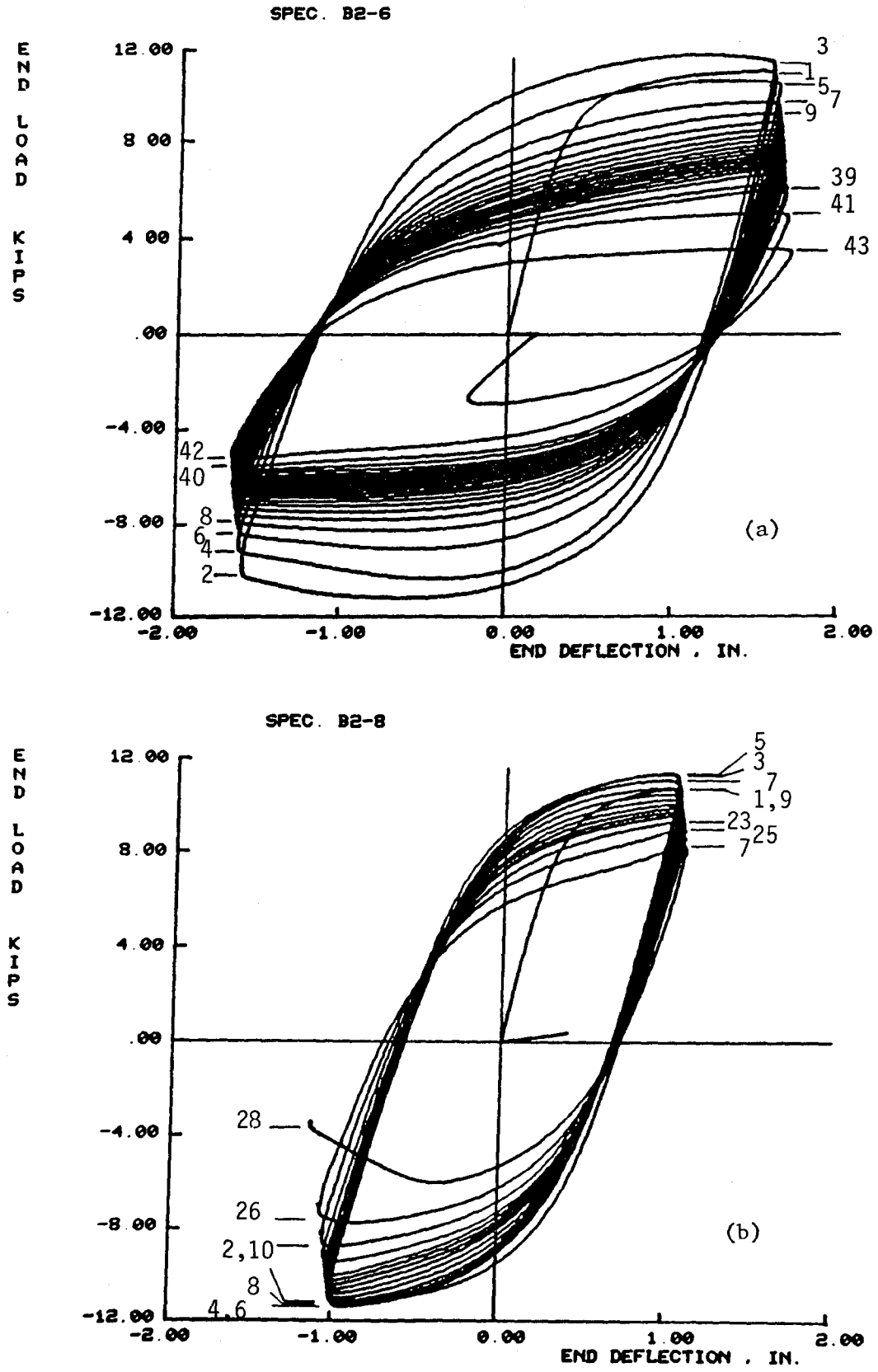

Fig. 5.31 Cyclic Load--Deflection Diagrams, B2 Specimens

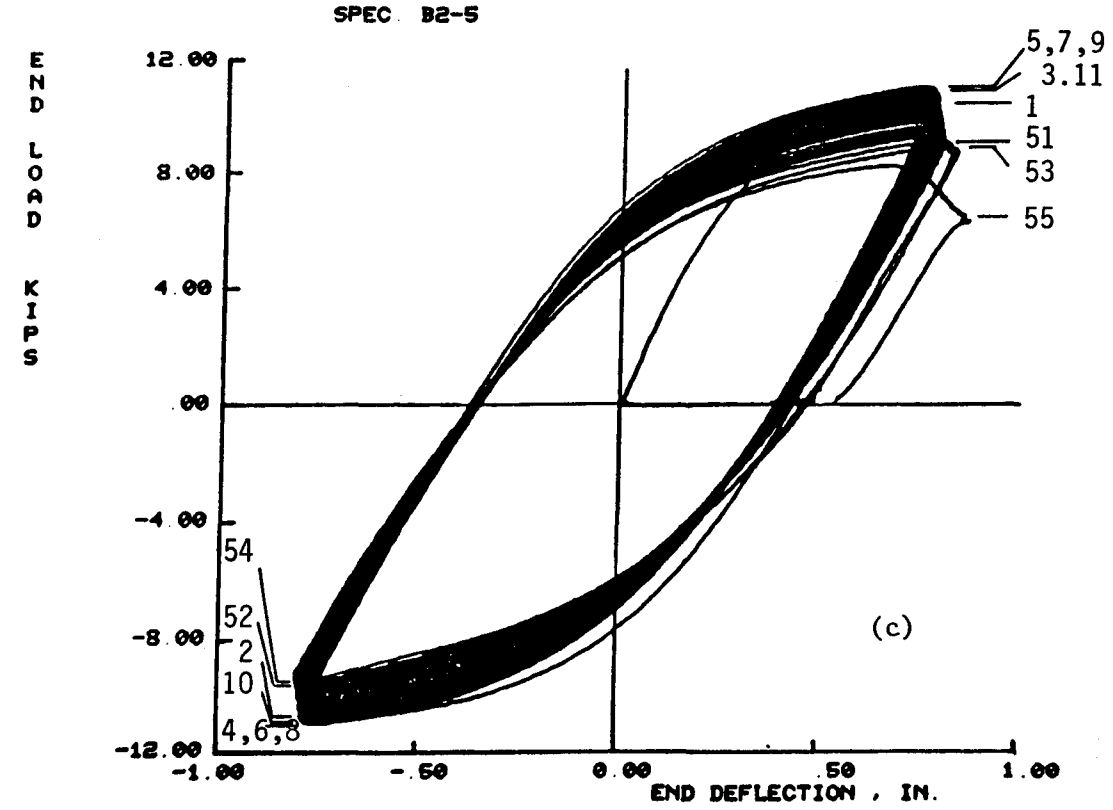

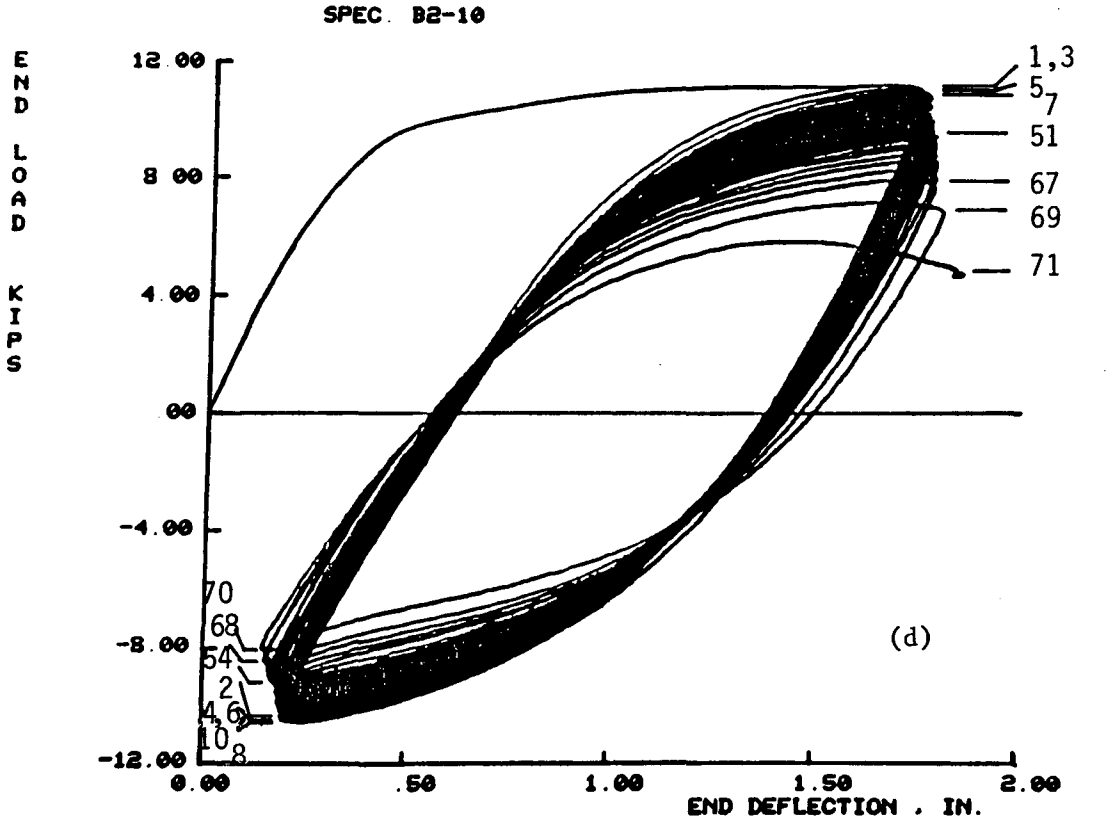

Fig. 5.31 Continued

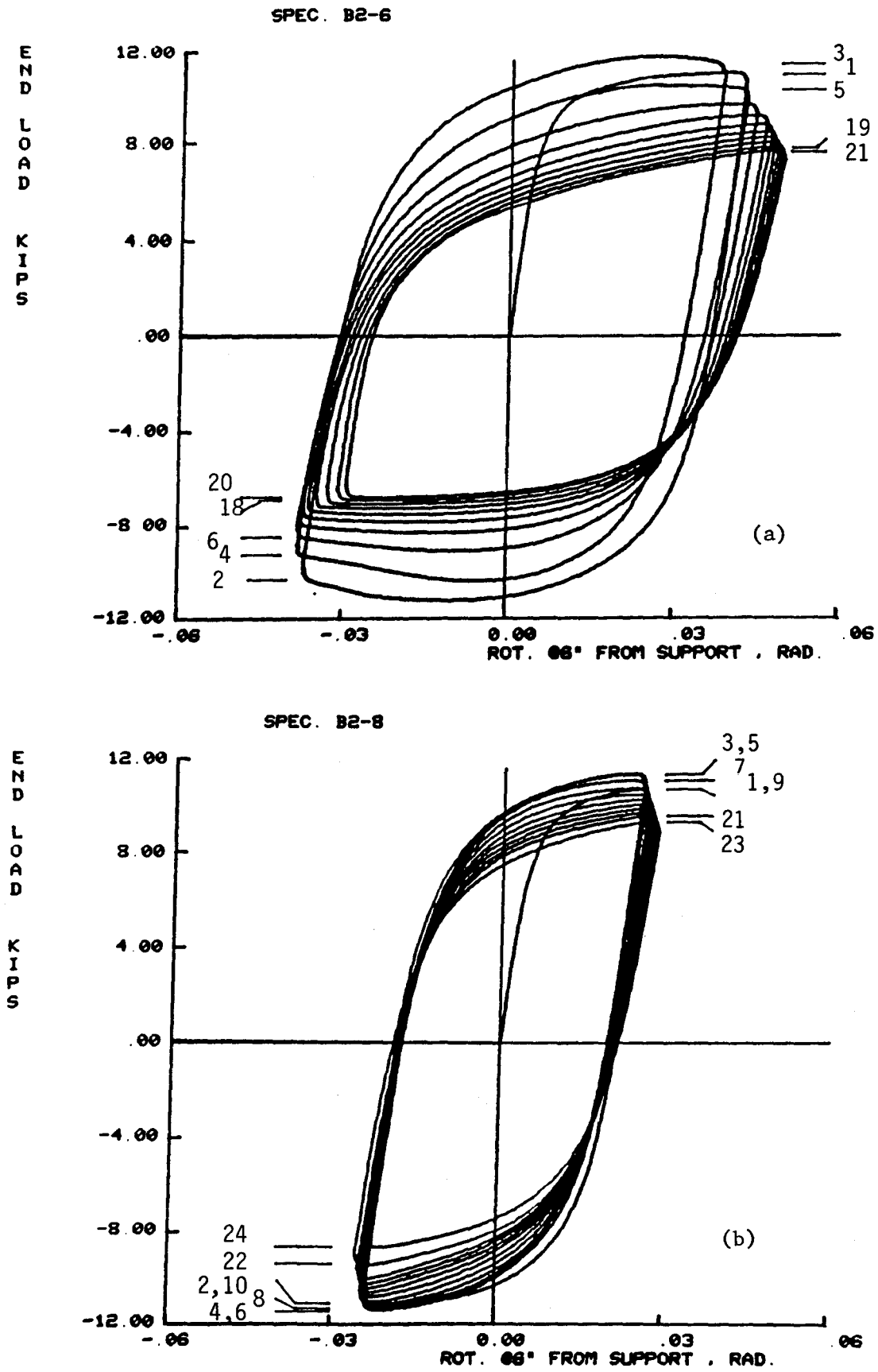

Fig. 5.32 Cyclic Load--Rotation Diagram, B2 Specimens

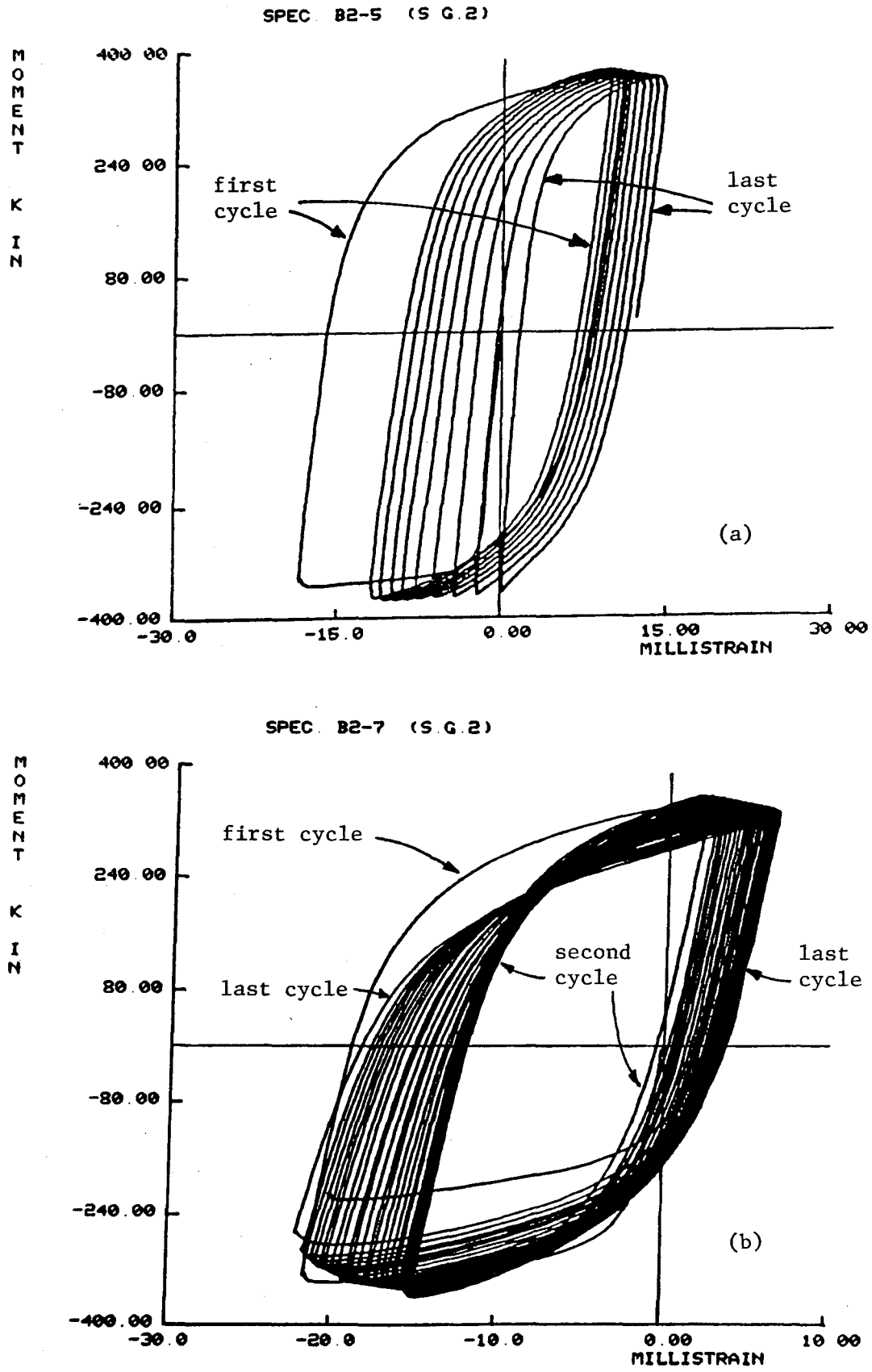

Fig. 5.33 Cyclic Moment--Strain Diagrams, B2 Specimens

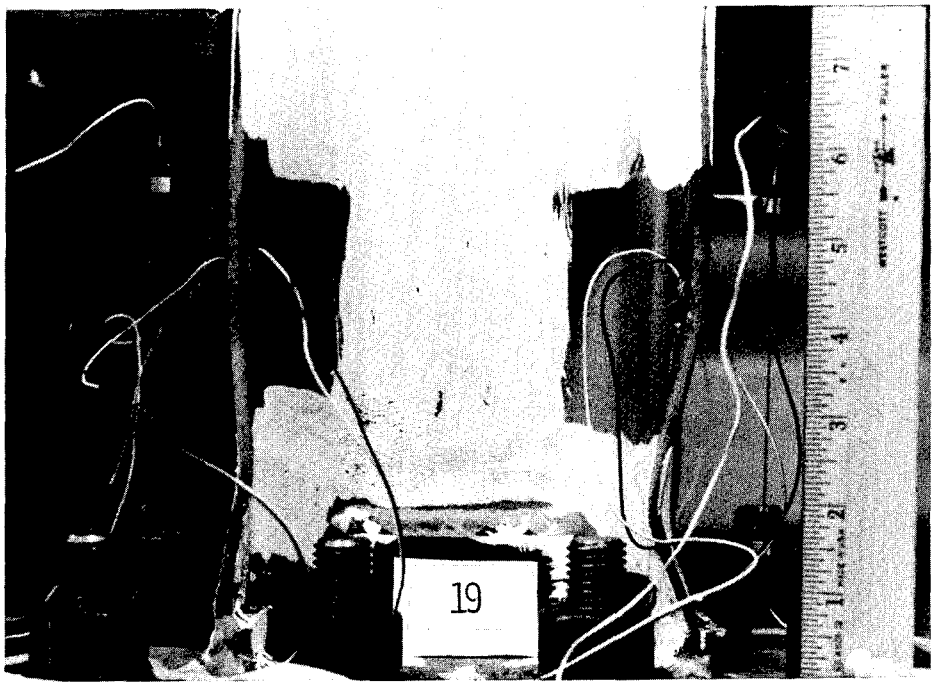

(a) Beam End Deflected to the Right

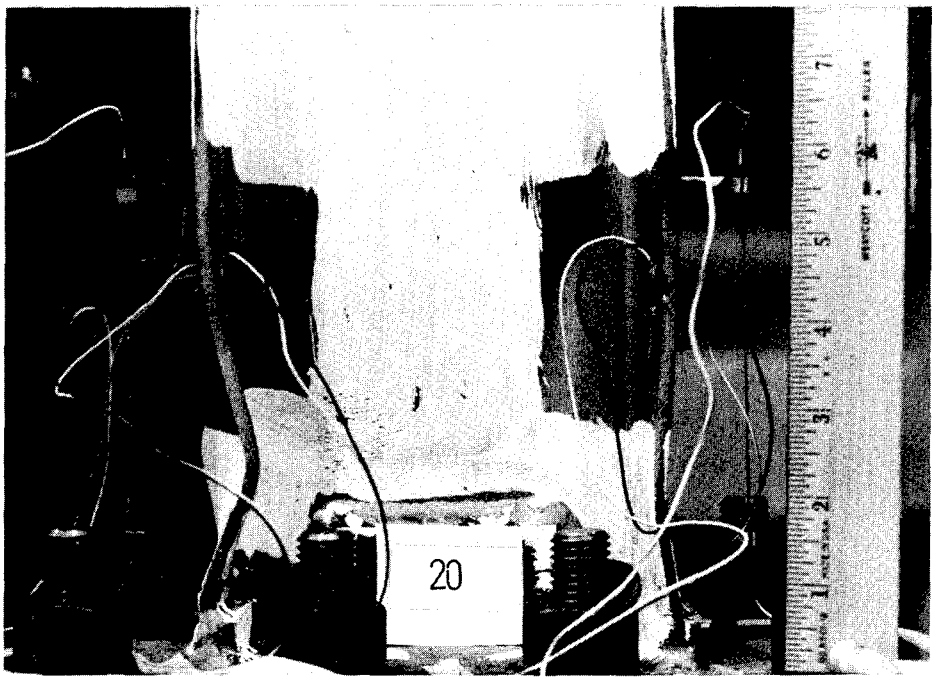

(b) Beam End Deflected to the Left

Fig. 5.34 Photos of Flange Buckles at Two Consecutive Reversal Points

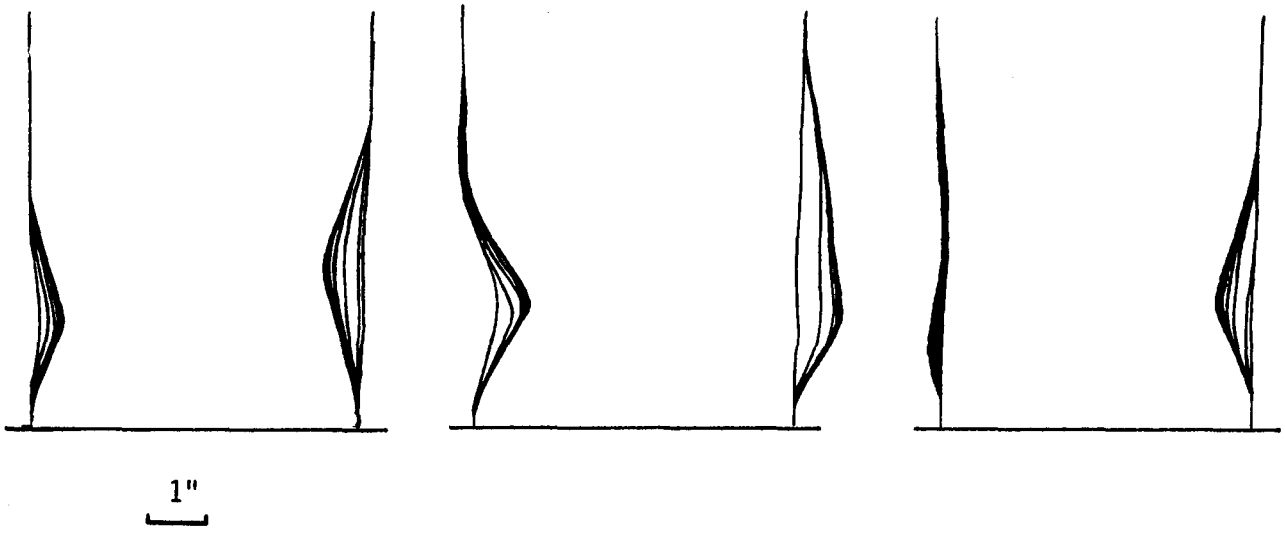

(a) Specimen B2-4 (b) Specimen B2-6 (c) Specimen B2-8

Fig. 5.35 Buckle Shapes at Load Reversal Points (Shown for Every Other Cycle)

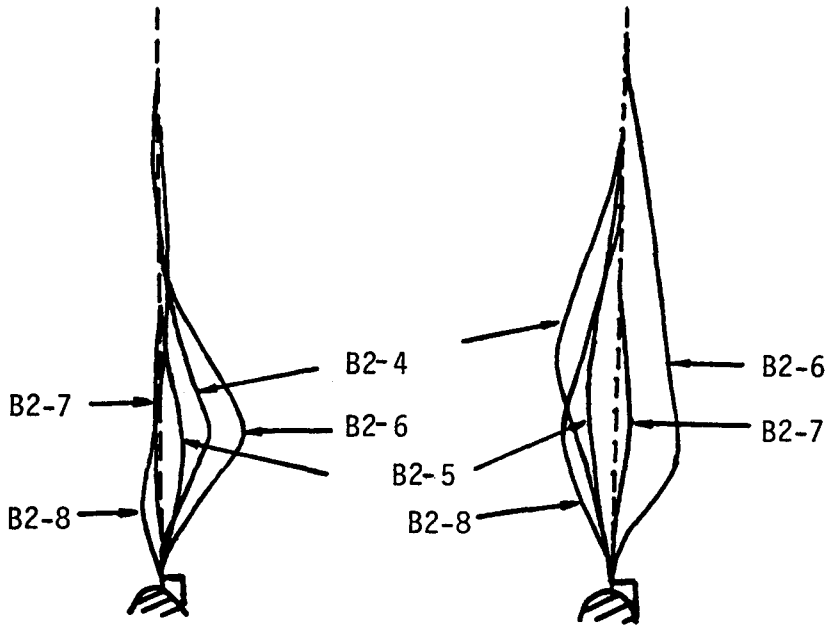

Fig. 5.36 Stable Buckle Shapes

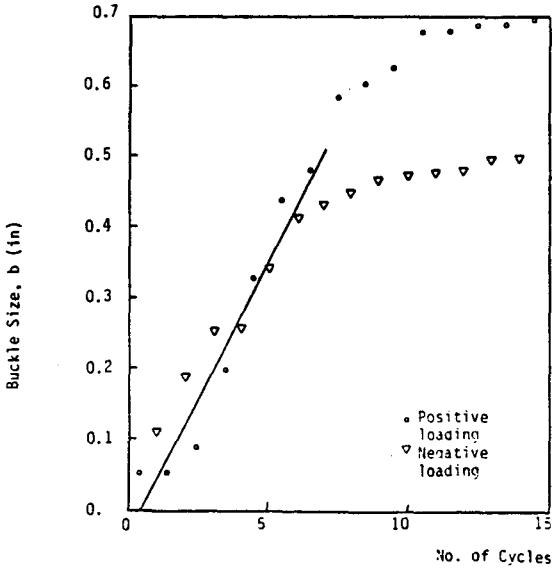

(a) Specimen B2-4

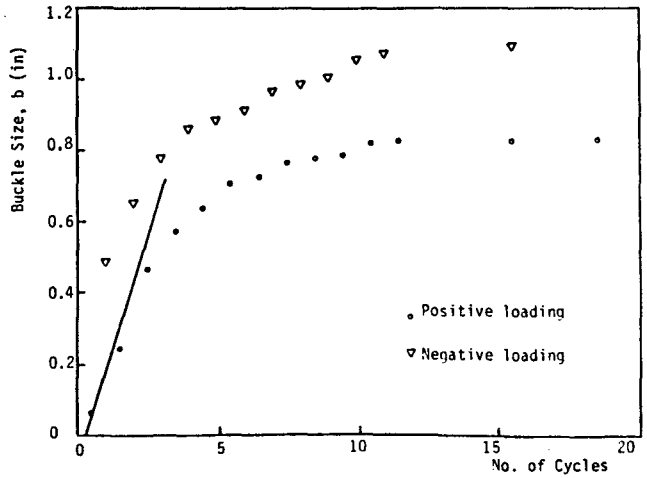

(c) Specimen B2-6

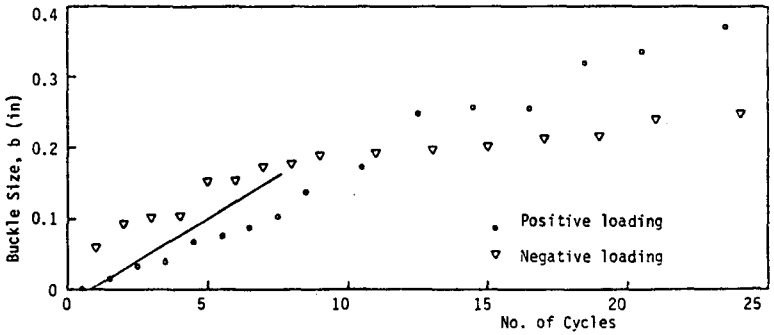

(b) Specimen B2-5

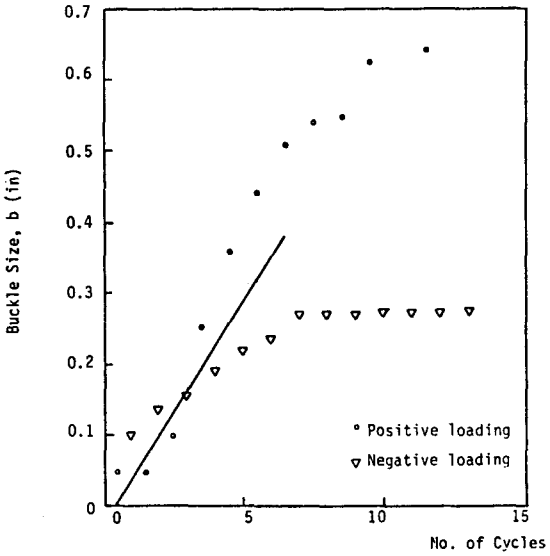

(d) Specimen B2-8

Fig. 5.37 Buckle Sizes versus Number of Cycles

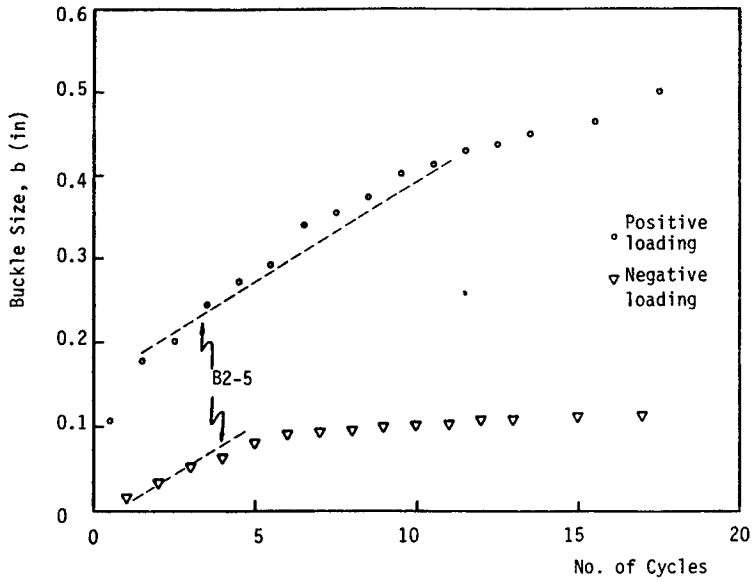

Fig. 5.38 Buckle Sizes for Specimen with Mean Deflection (Specimen B2-10)

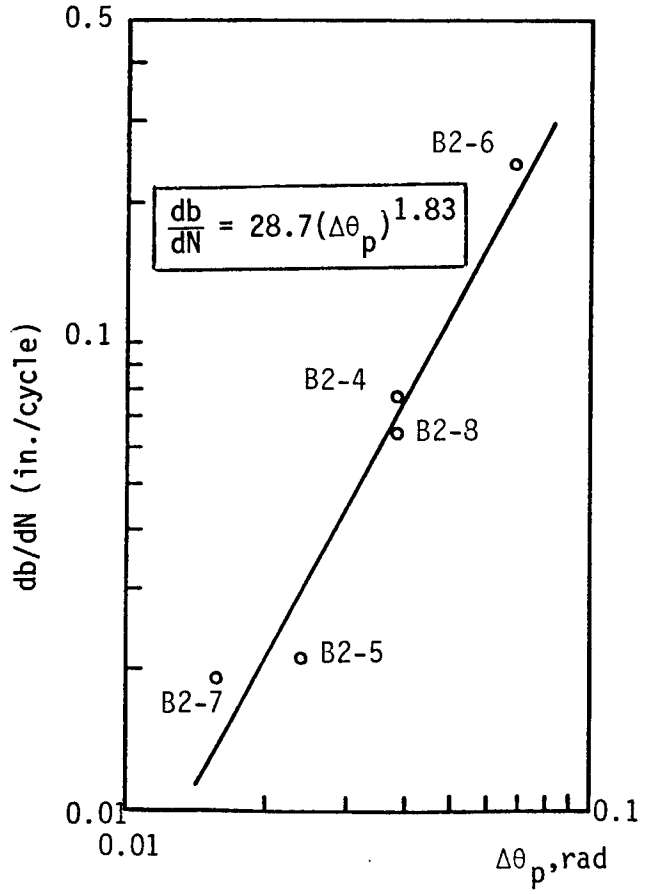

Fig. 5.39 Correlation Between the Rate of Growth in Buckle Size, db/dN, and the Plastic Rotation Range $\Delta\theta_p$

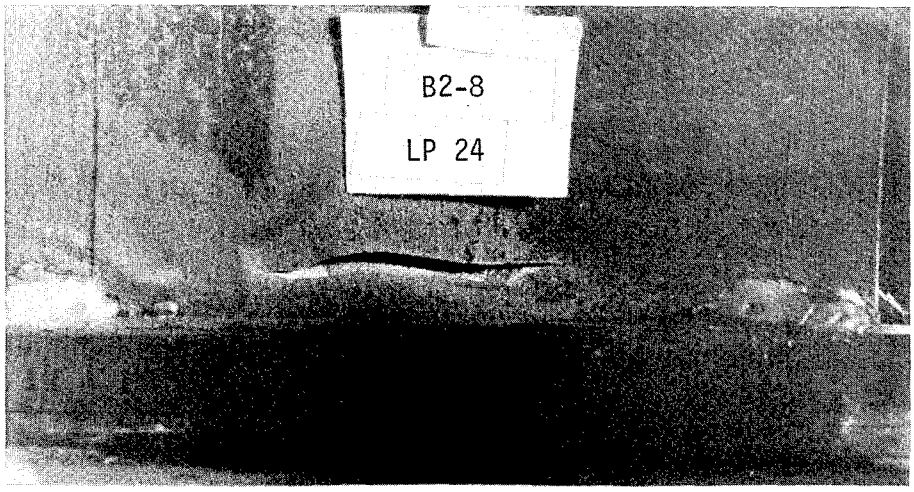

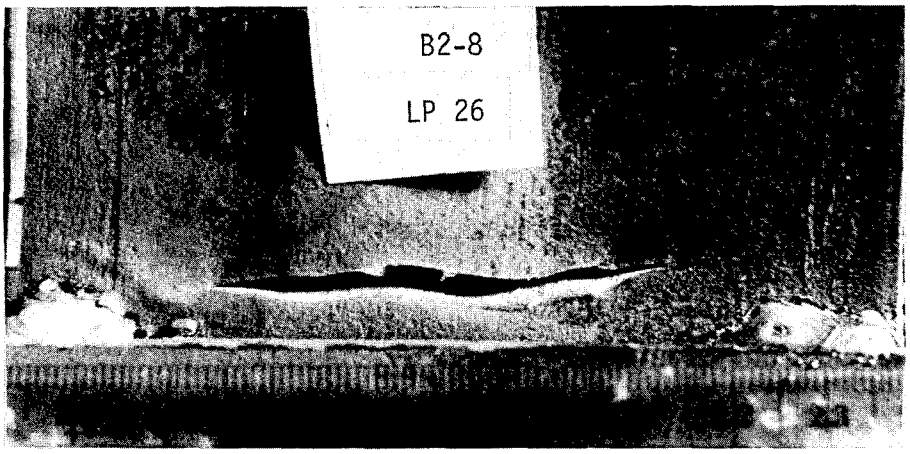

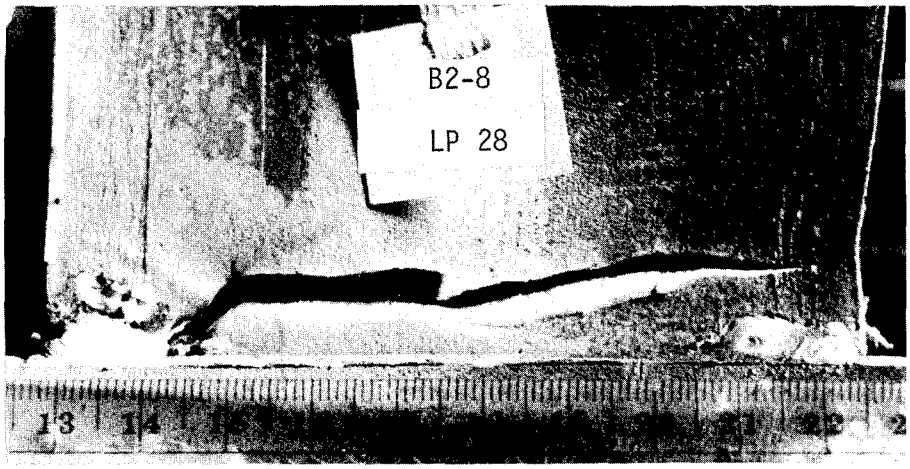

Fig. 5.40 Crack Growth in the Last Three Cycles, Specimen B2-8

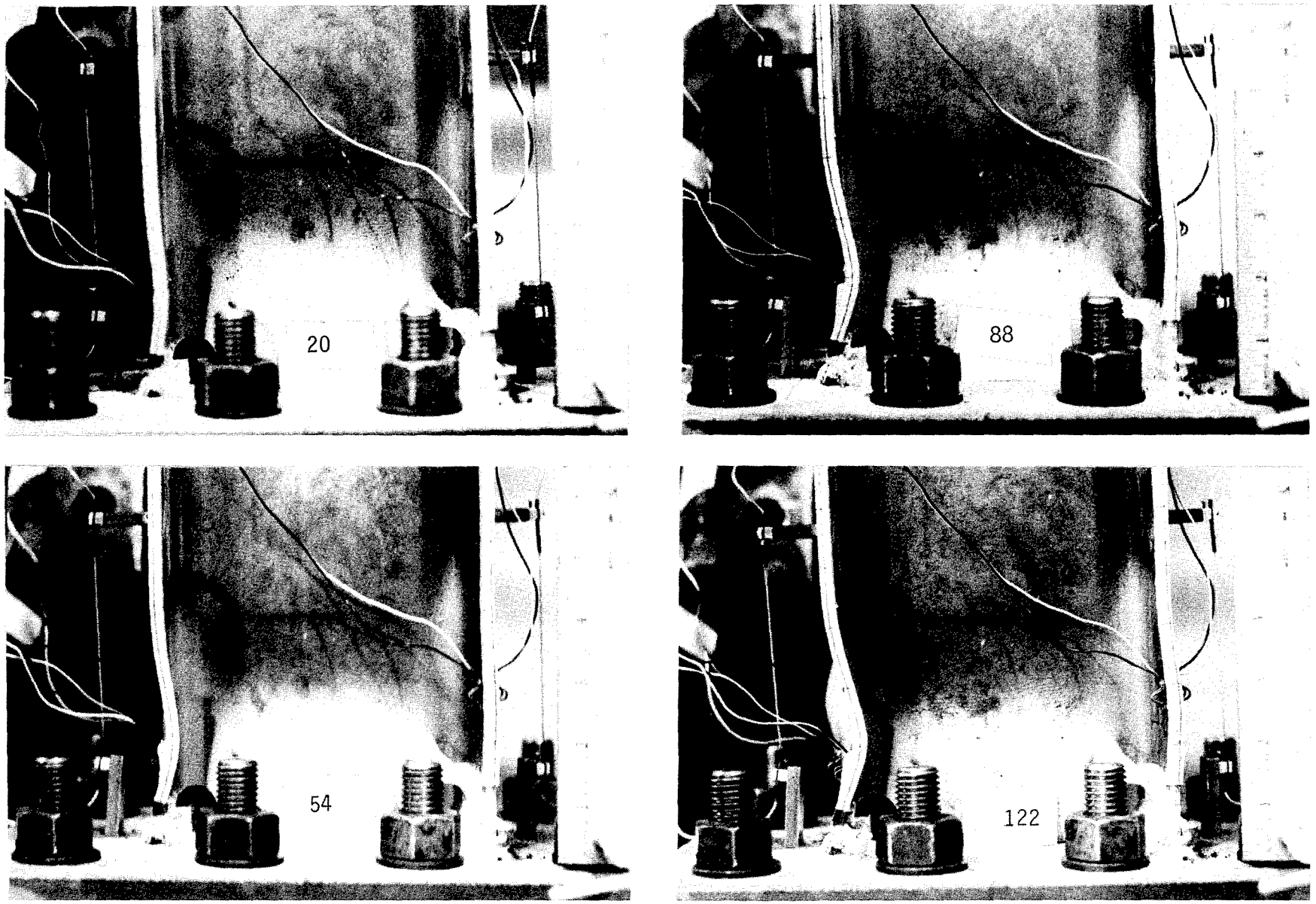

Fig. 5.41 Change in Buckle Shape in Specimen B2-9 during the First Four Blocks of Loading

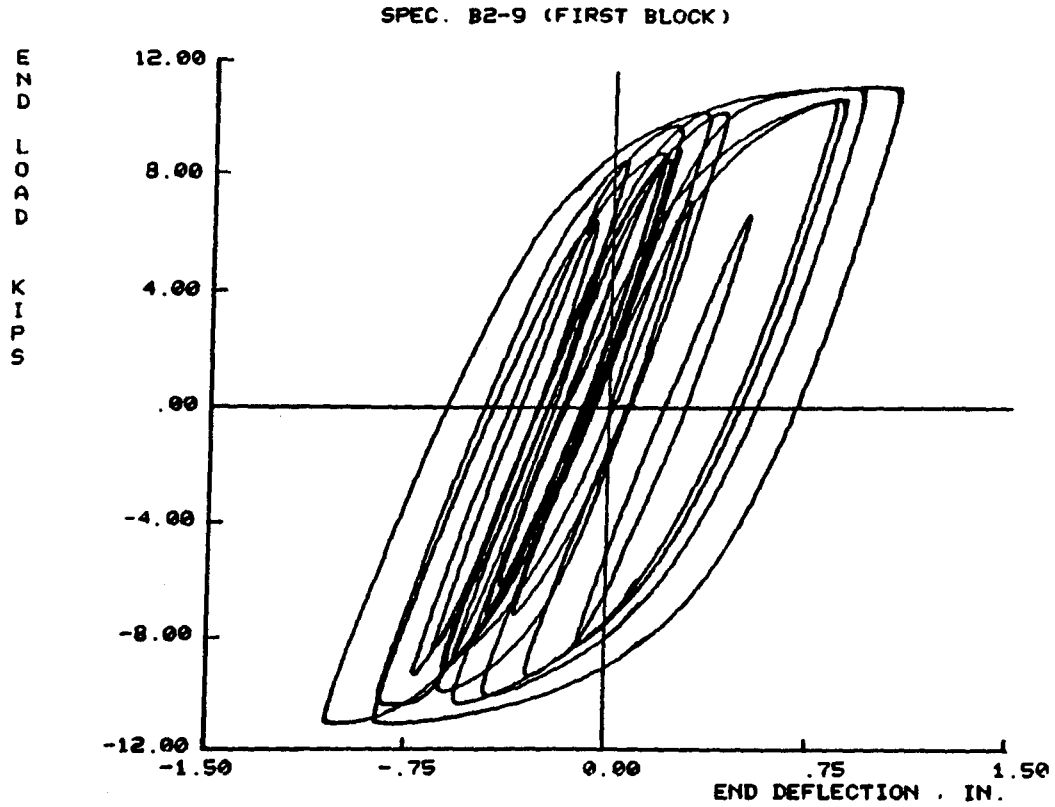

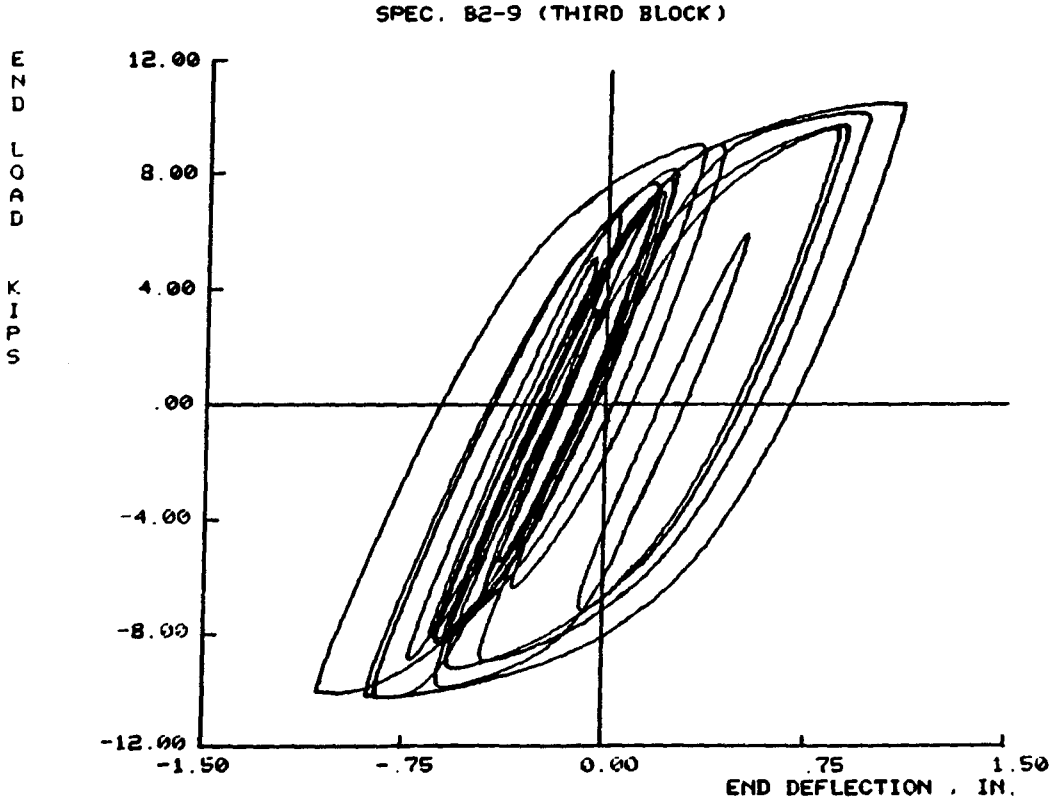

Fig. 5.42 Cyclic Load--Deflection Diagrams of Specimen B2-9 in the First and Third Block of Loading

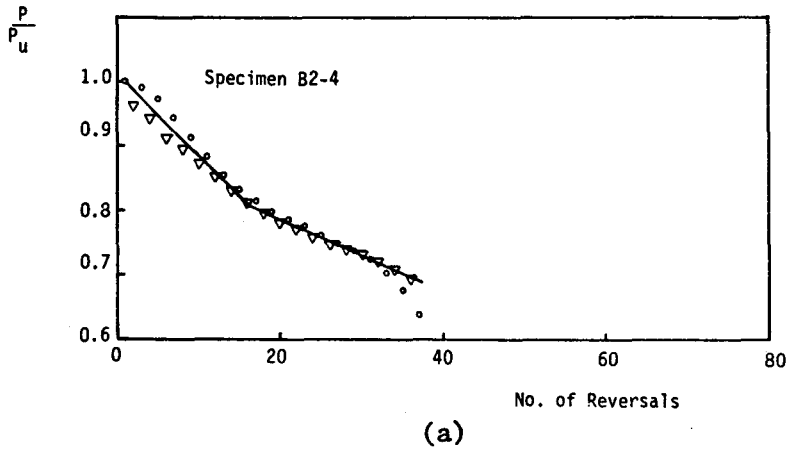

(a)

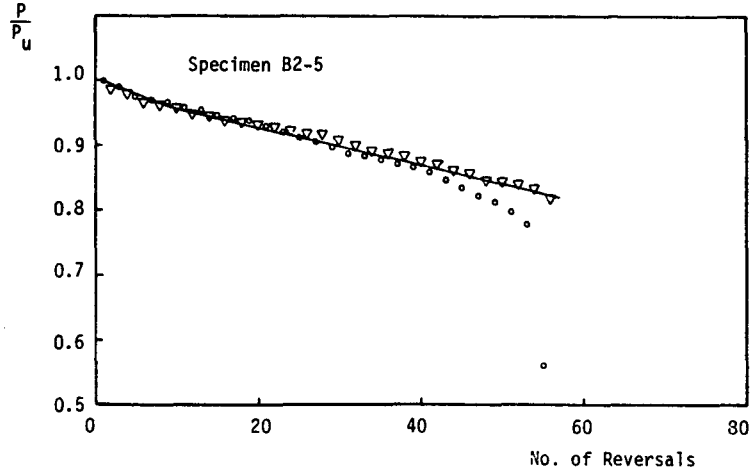

(b)

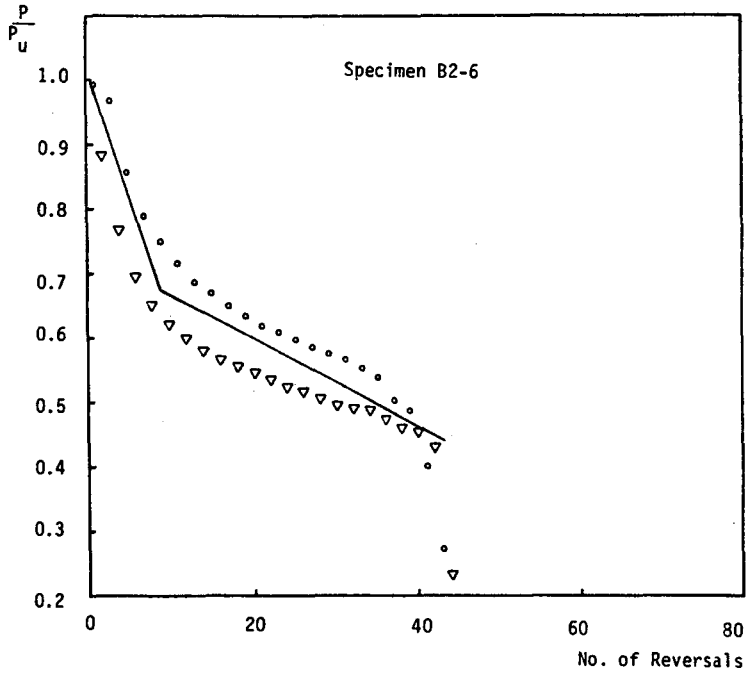

(c)

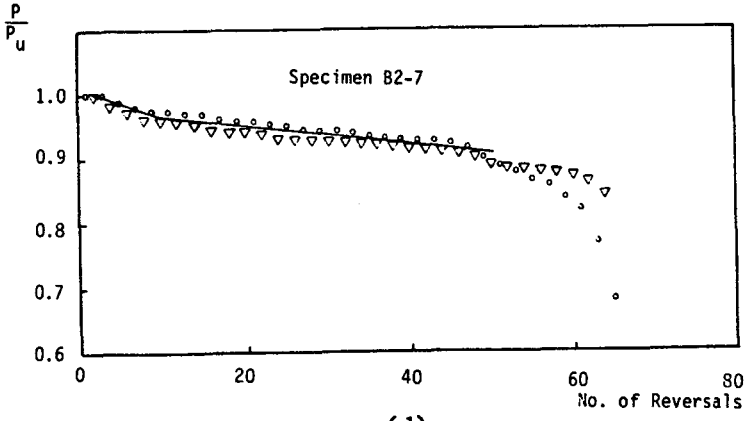

(d)

Fig. 5.43 Strength Deterioration of B2 Specimens

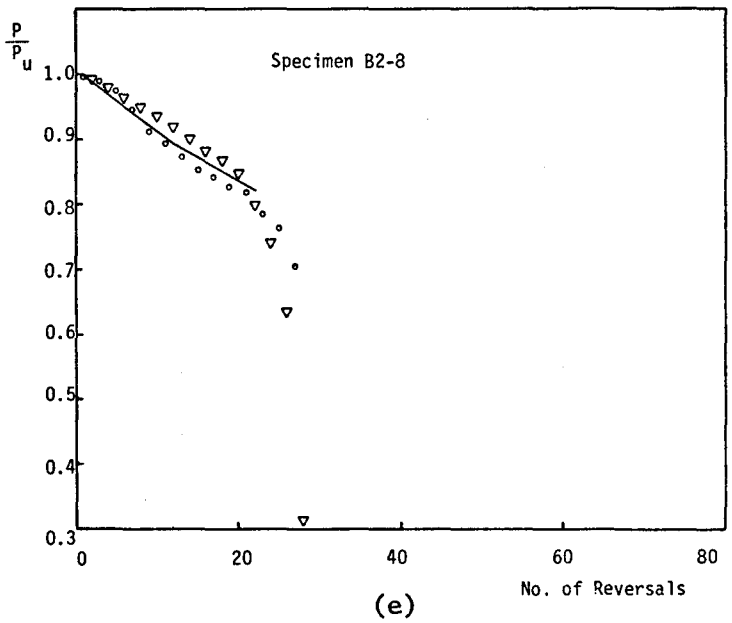

(e)

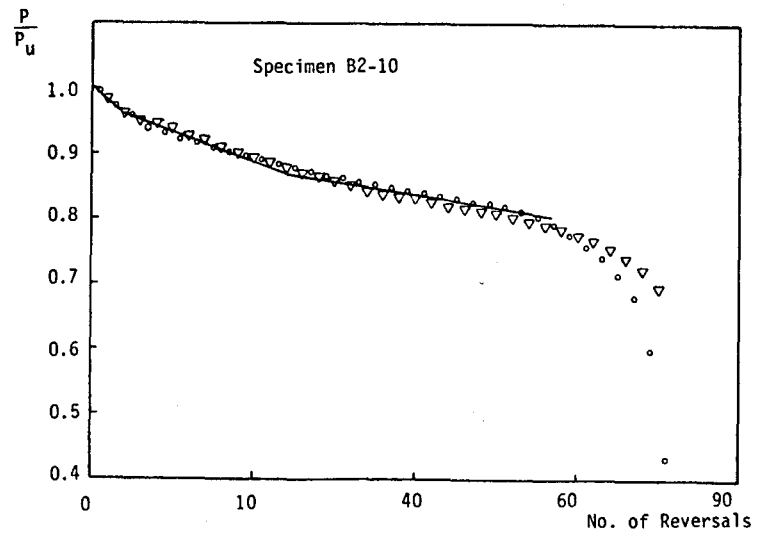

(f)

Fig. 5.43 continued

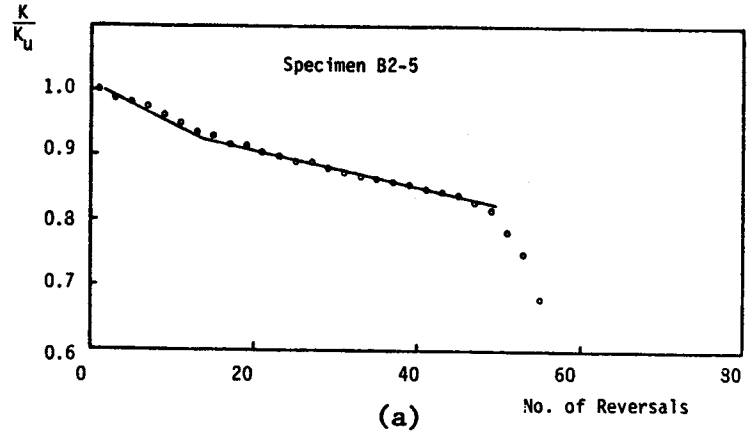

(a)

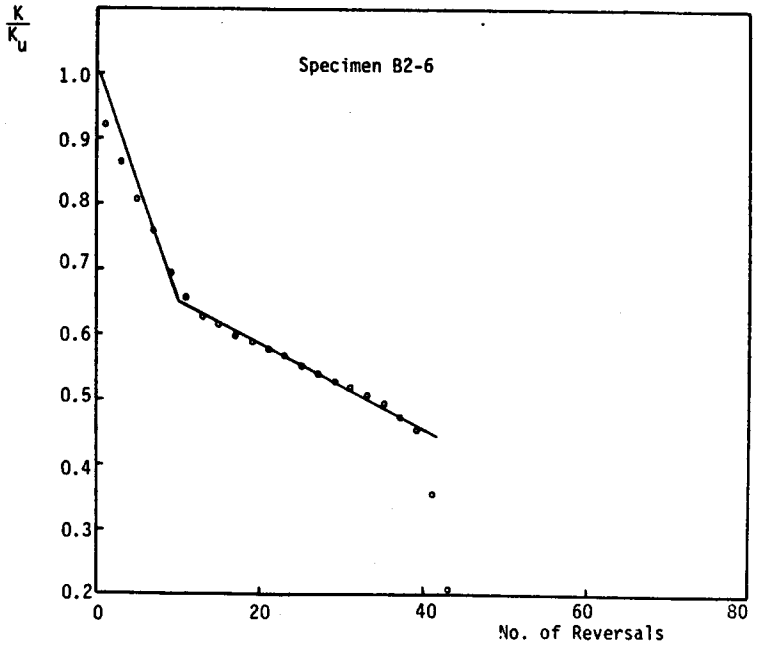

(b)

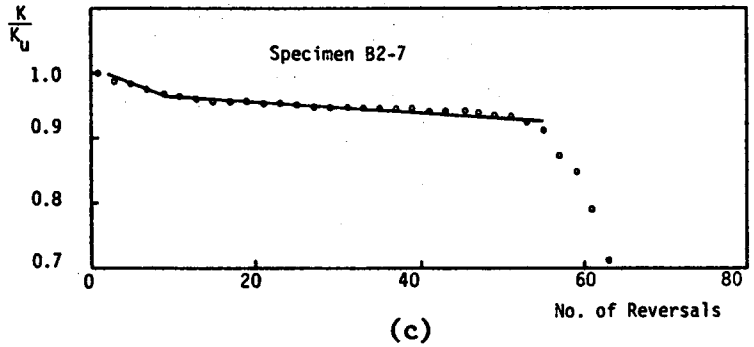

(c)

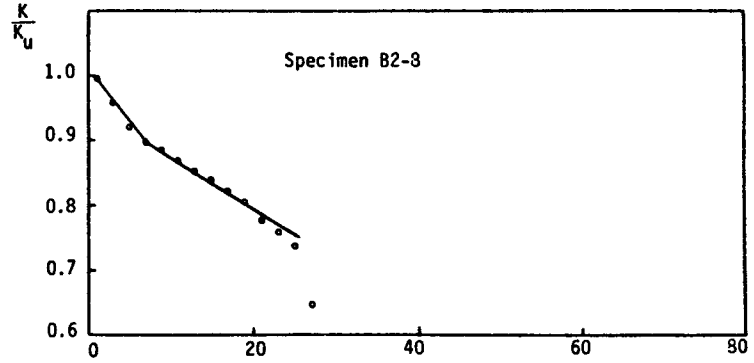

(d)

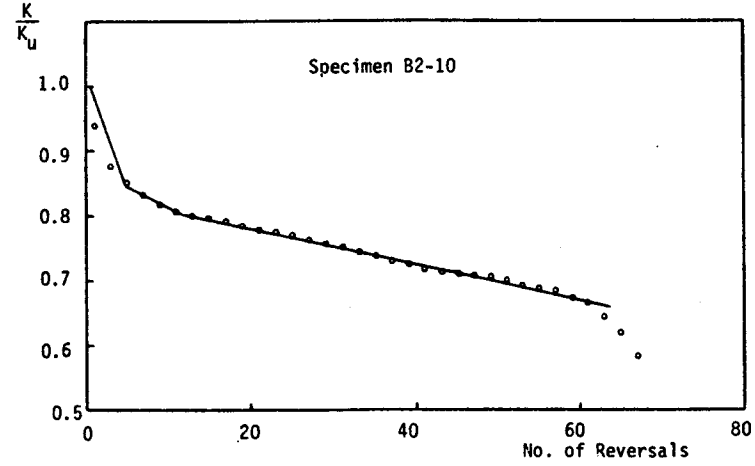

(e)

Fig. 5.44 Stiffness Deterioration of B2 Specimens

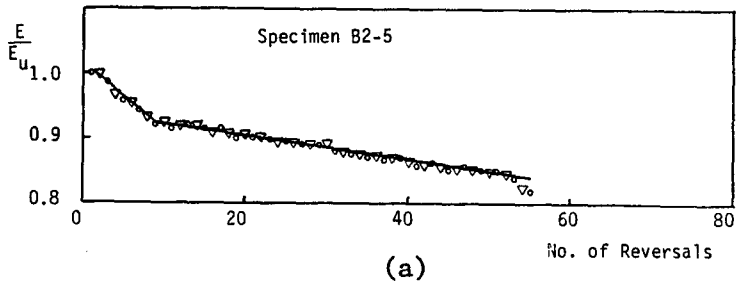

(a)

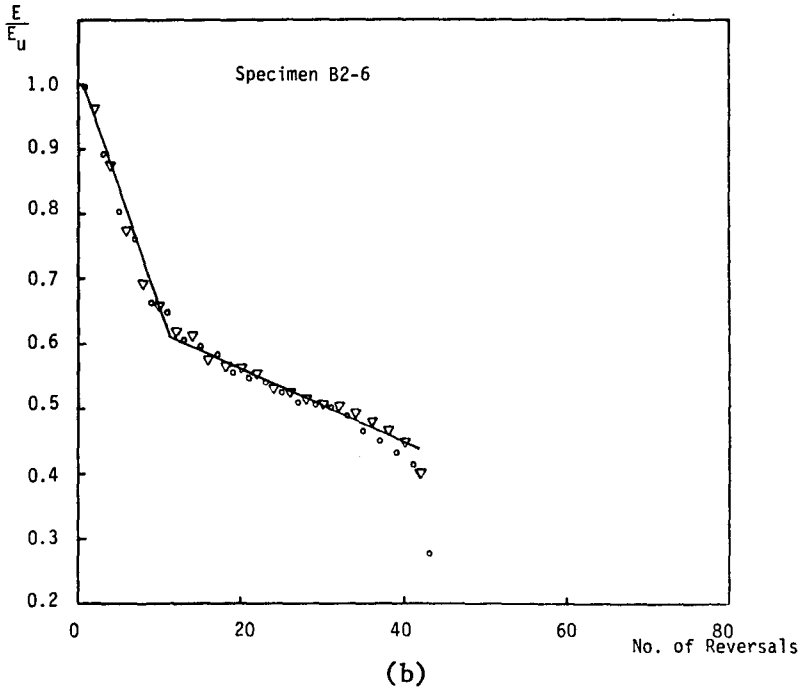

(b)

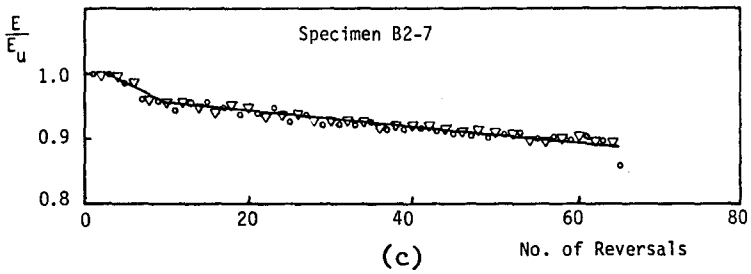

(c)

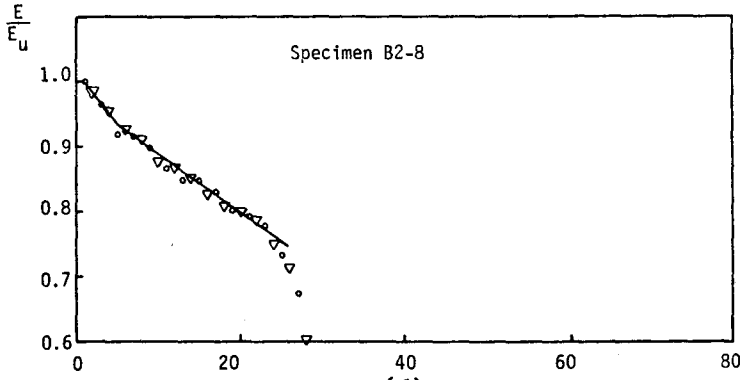

(d)

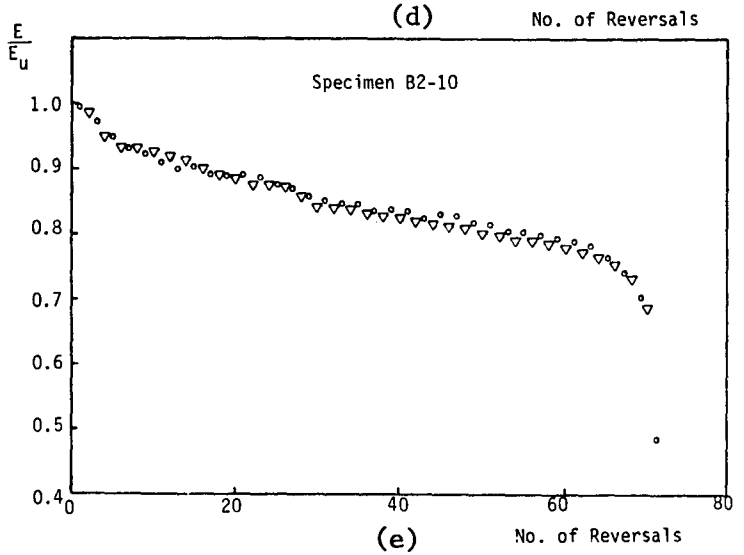

(e)

Fig. 5.45 Hysteresis Energy Deterioration of B2 Specimens

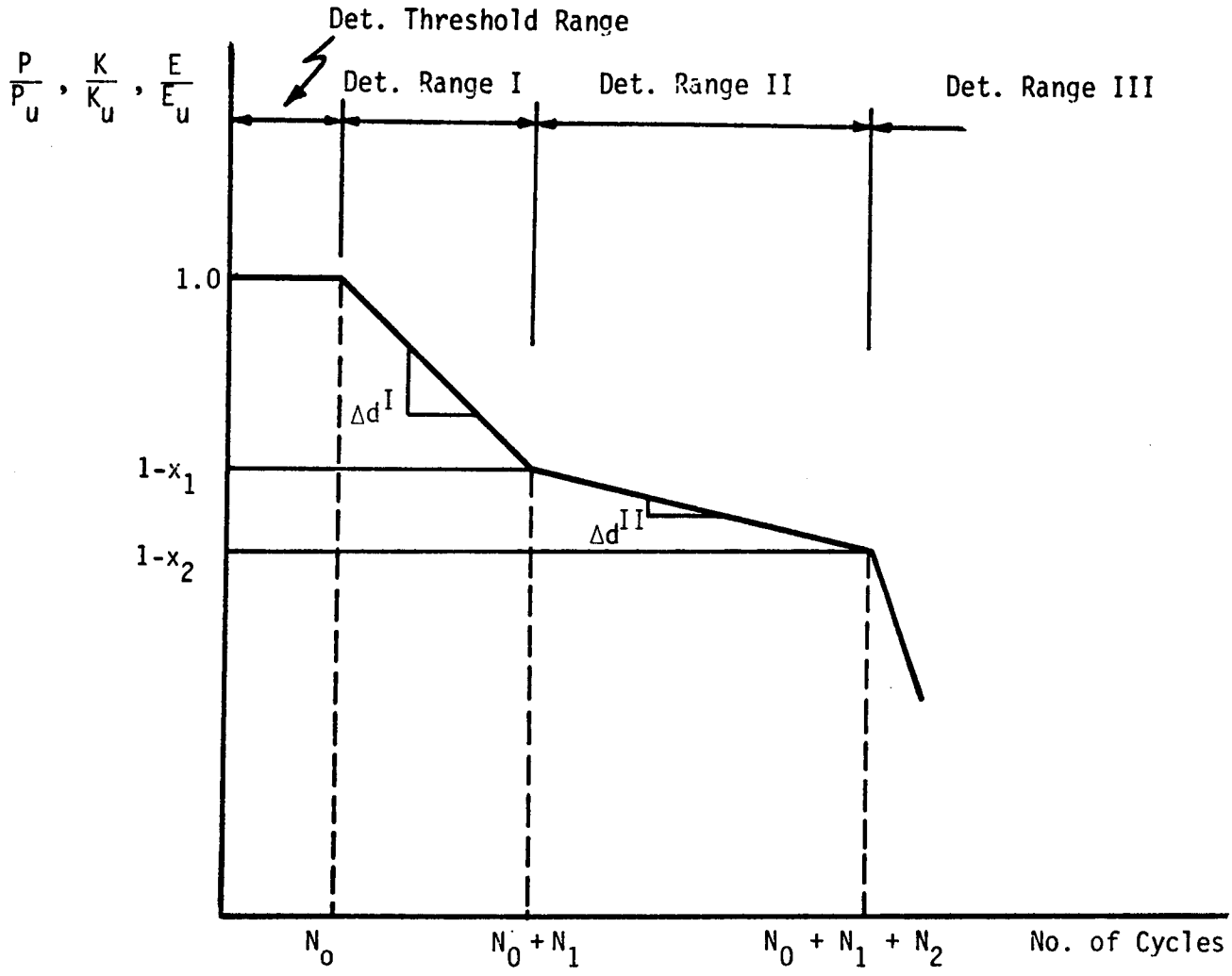

Fig. 5.46 Deterioration Ranges for B2 Specimens

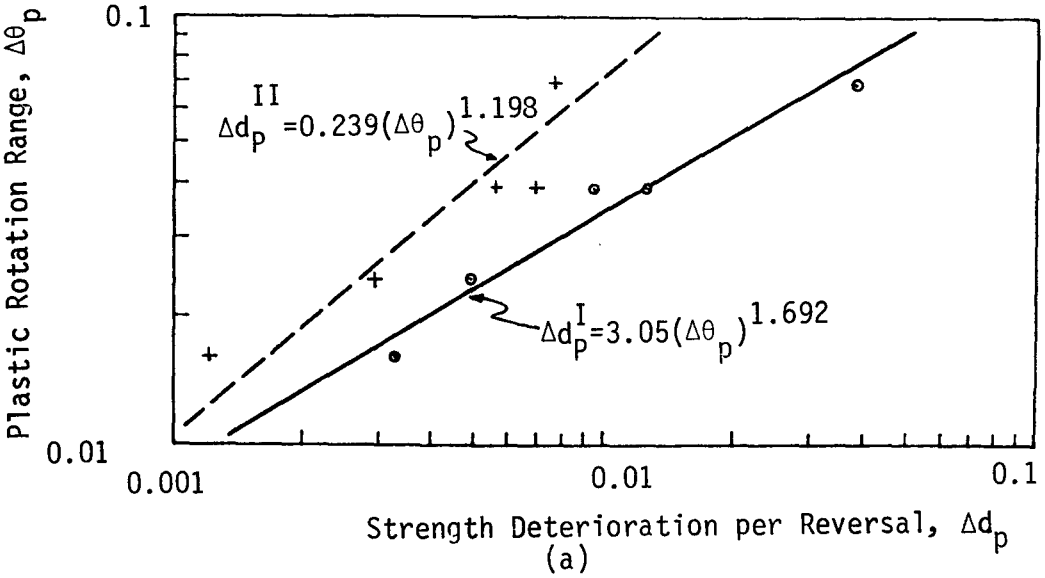

(a)

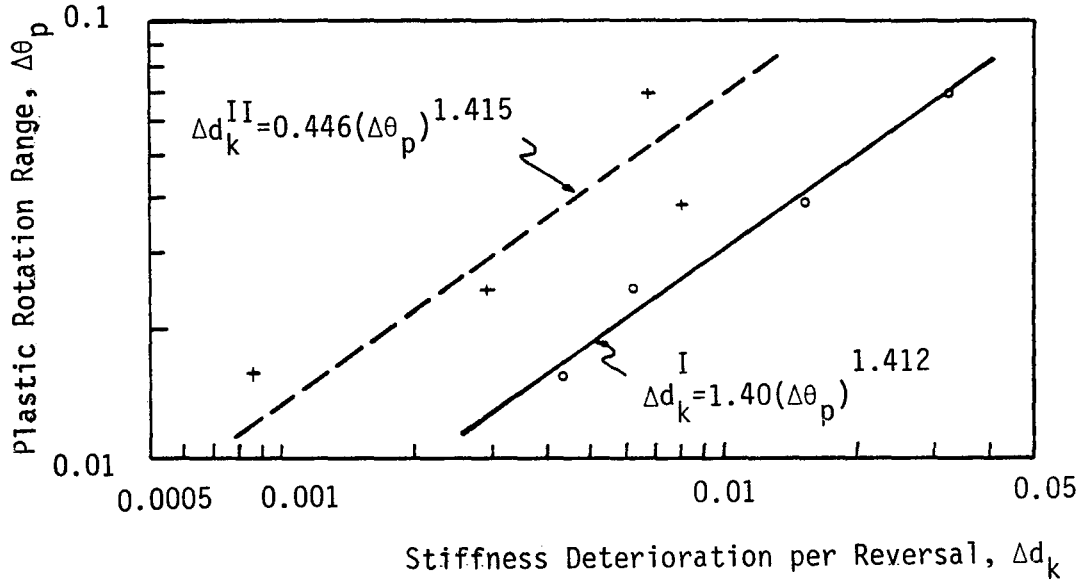

(b)

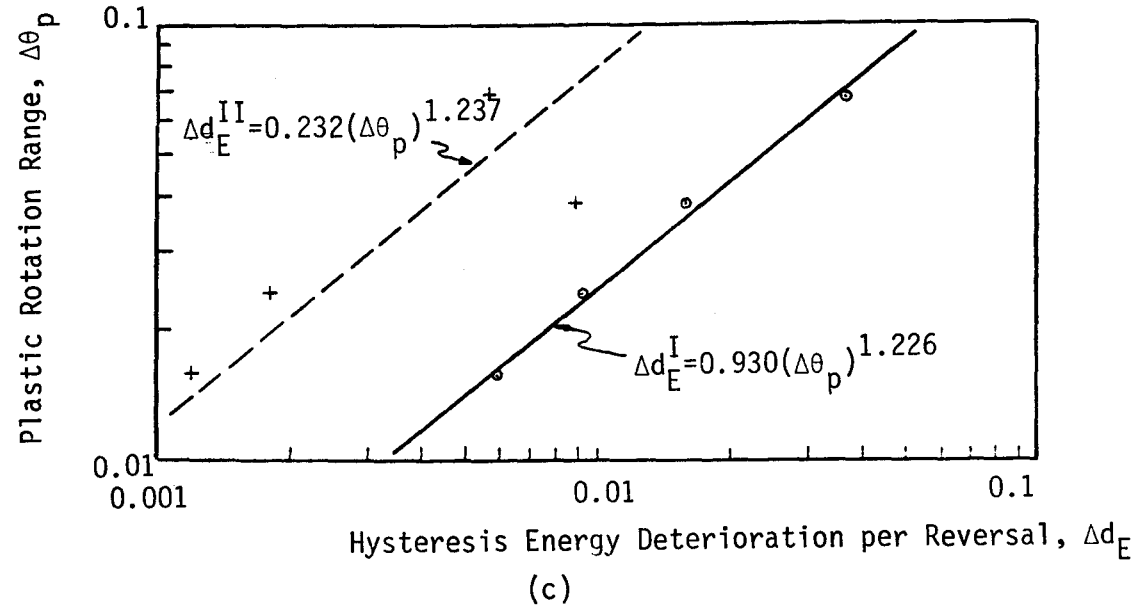

(c)

Fig. 5.47 Deterioration Rate Models

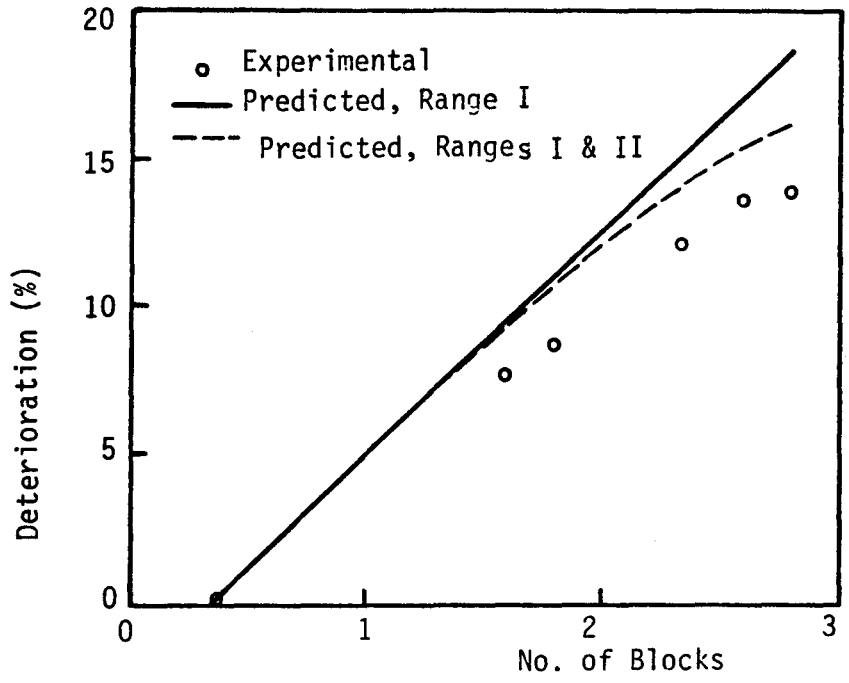

Fig. 5.48 Comparison of Experimental and Predicted Deterioration for Specimen B2-9

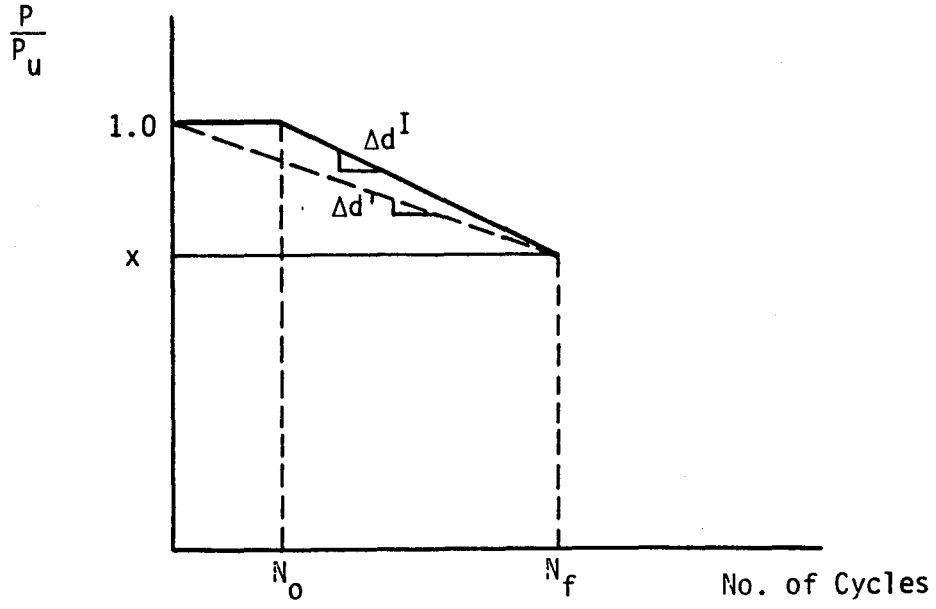

Fig. 5.49 Average Rate of Deterioration, Δd'

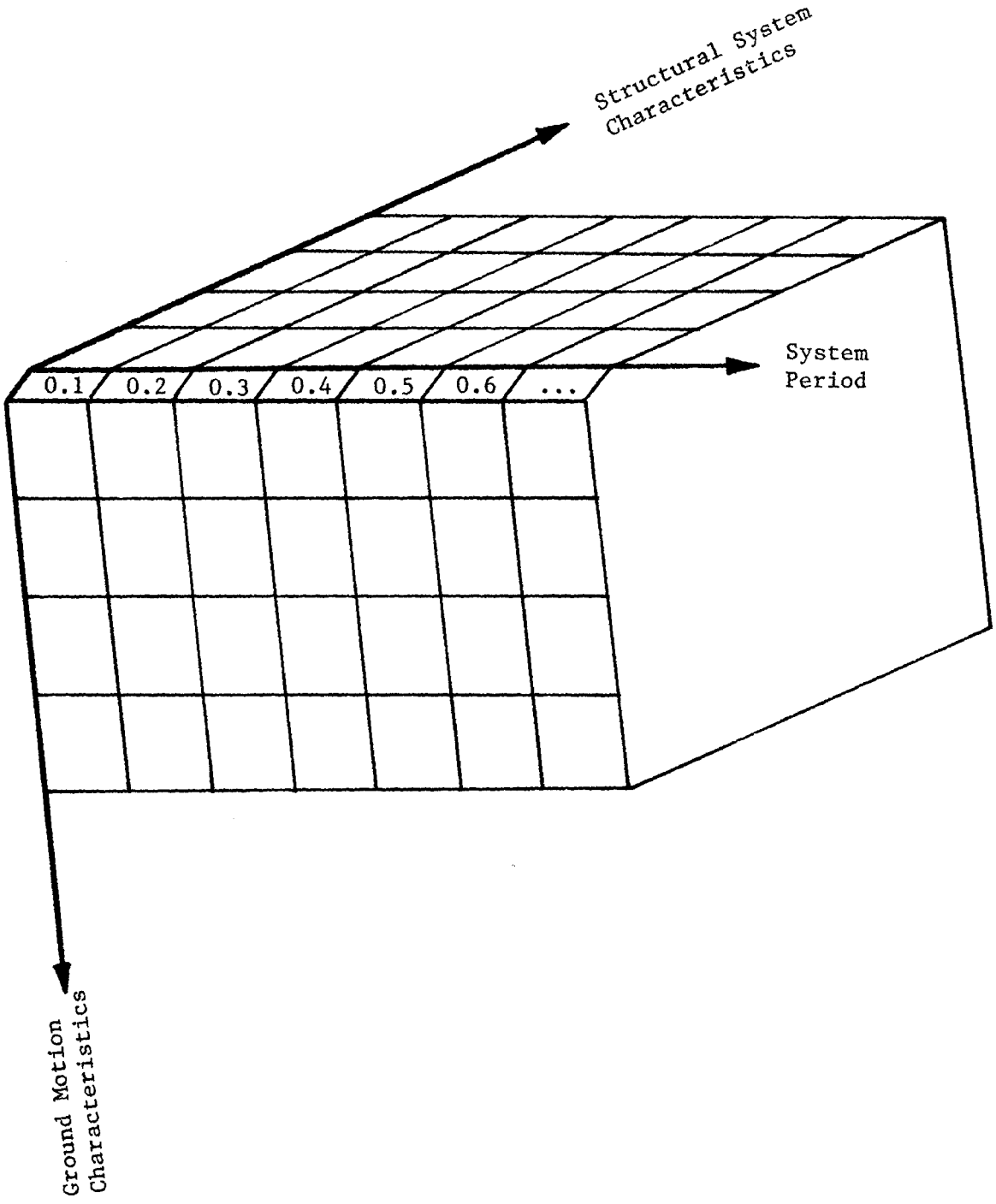

Fig. 6.1 Variables for Comprehensive Parameter Study

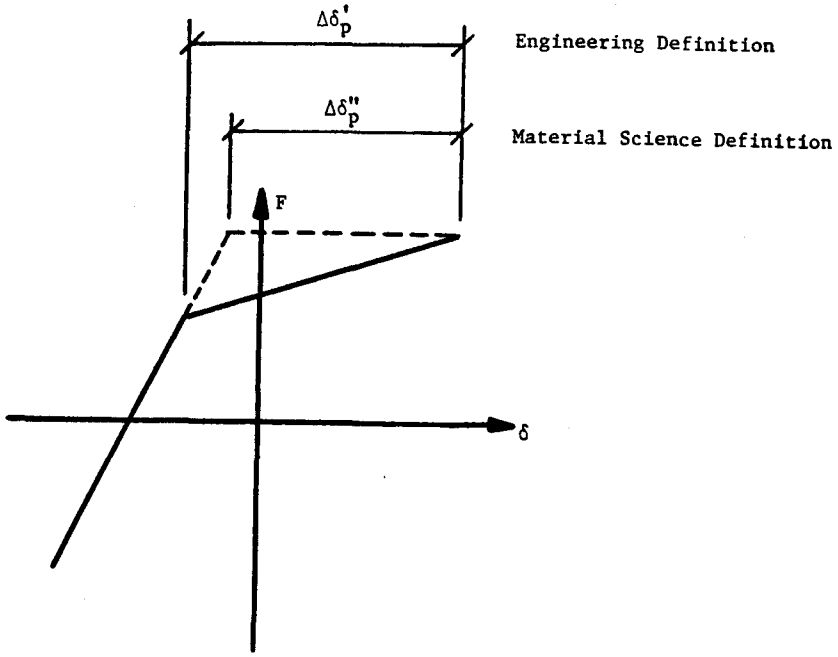

Fig. 6.2 Engineering Definition, $\Delta\delta_p'$, and Material Science Definition, $\Delta\delta_p''$, of Plastic Deformation Range

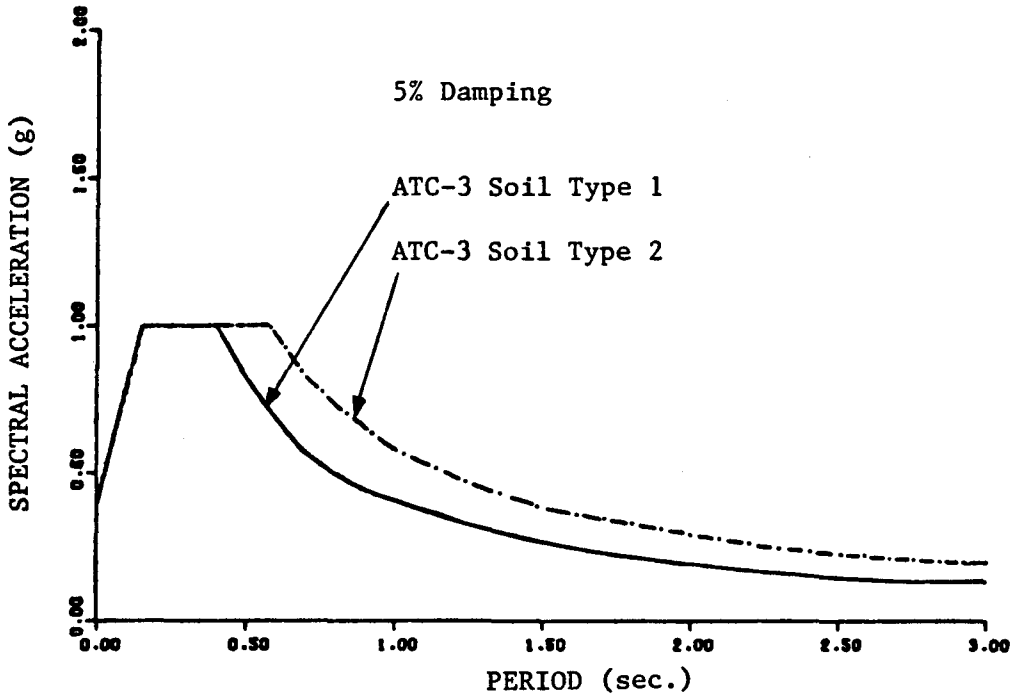

Fig. 6.3 ATC-3 Ground Motion Spectra for Highly Seismic Regions ($A_a = A_v = 0.4$) and Two Types of Soil Profiles

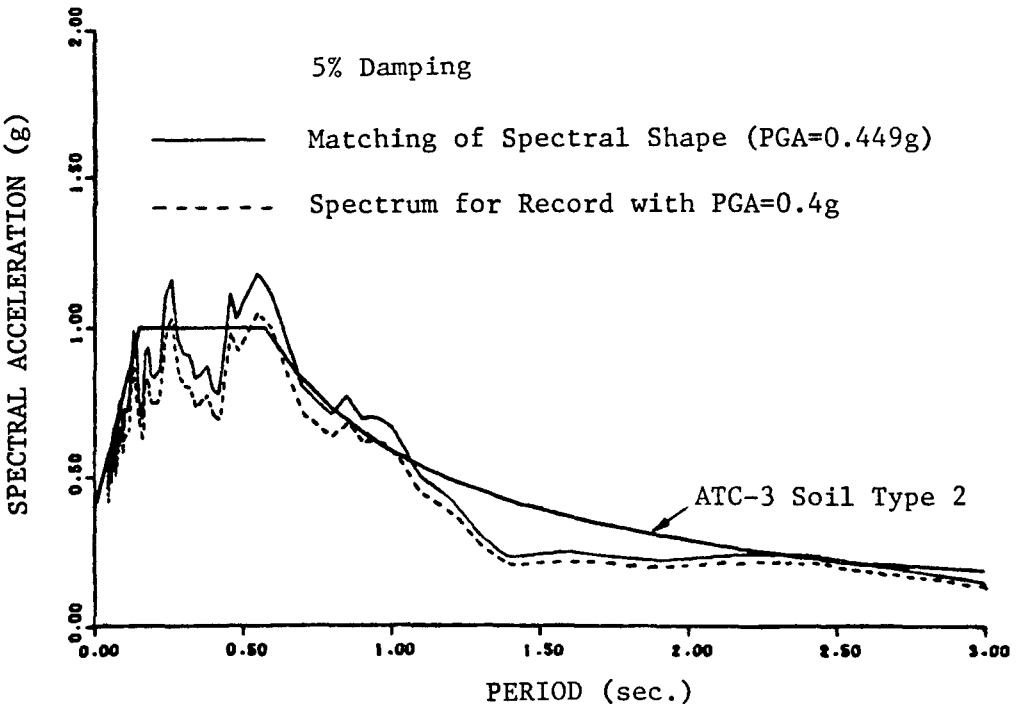

(a) Record A001 Component S00E

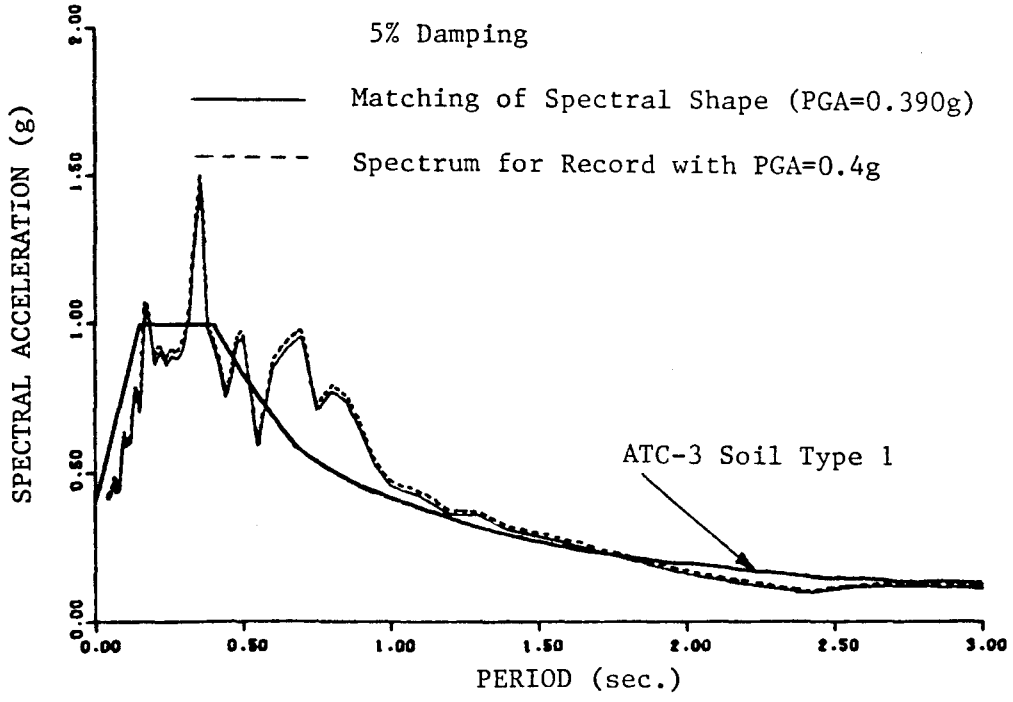

(b) Record A004 Component N21E

Fig. 6.4 Scaled Acceleration Spectra

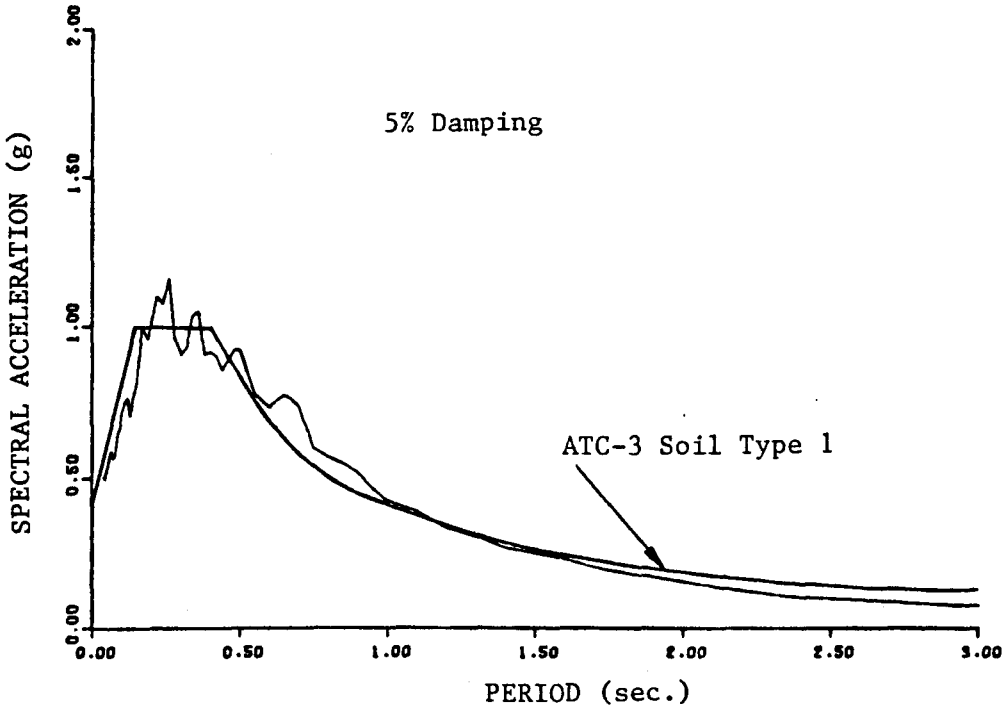

(a) Soil Profile Type 1

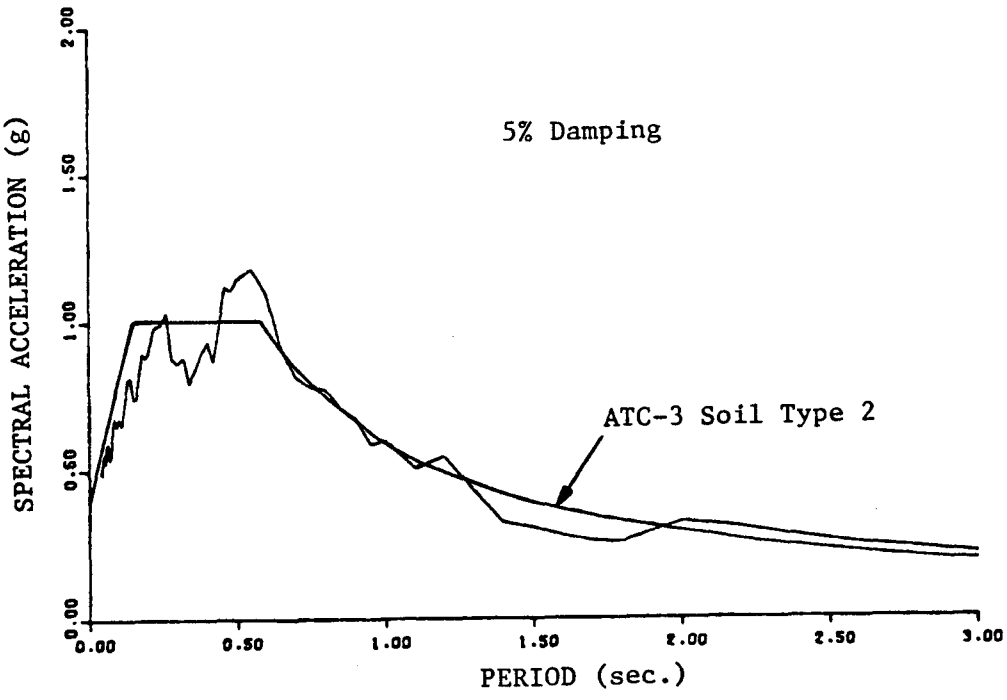

(b) Soil Profile Type 2

Fig. 6.5 Average Acceleration Spectra for Scaled Records

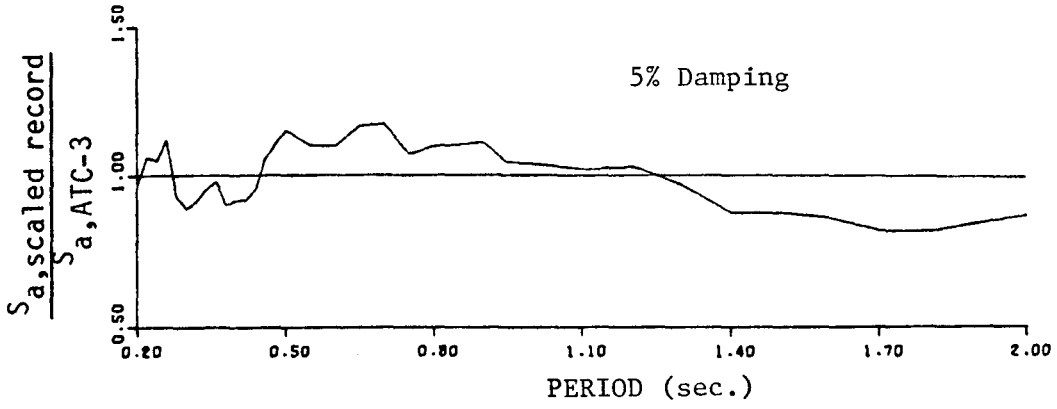

Fig. 6.6 Average Matching of all Six Records to ATC-3 Spectra

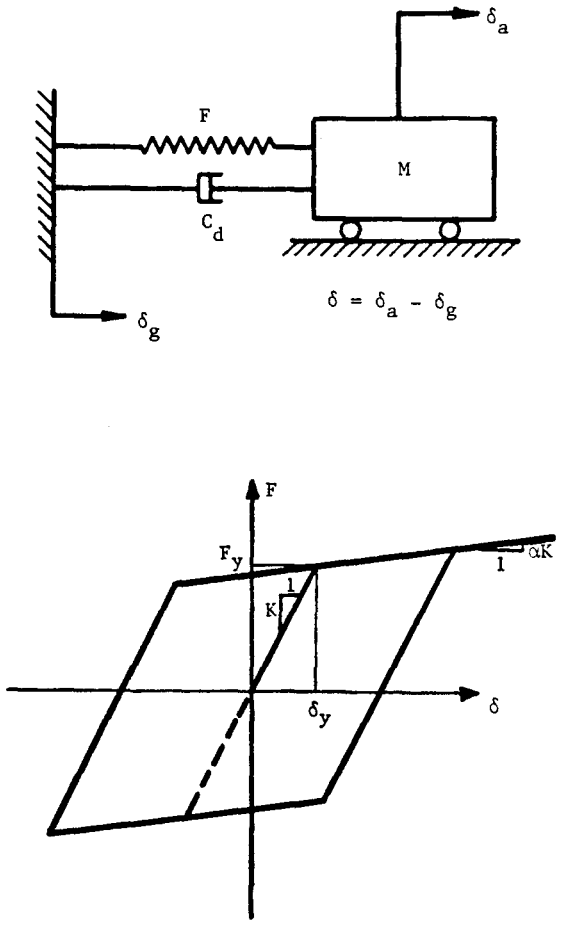

Fig. 6.7 Bilinear Single Degree of Freedom System

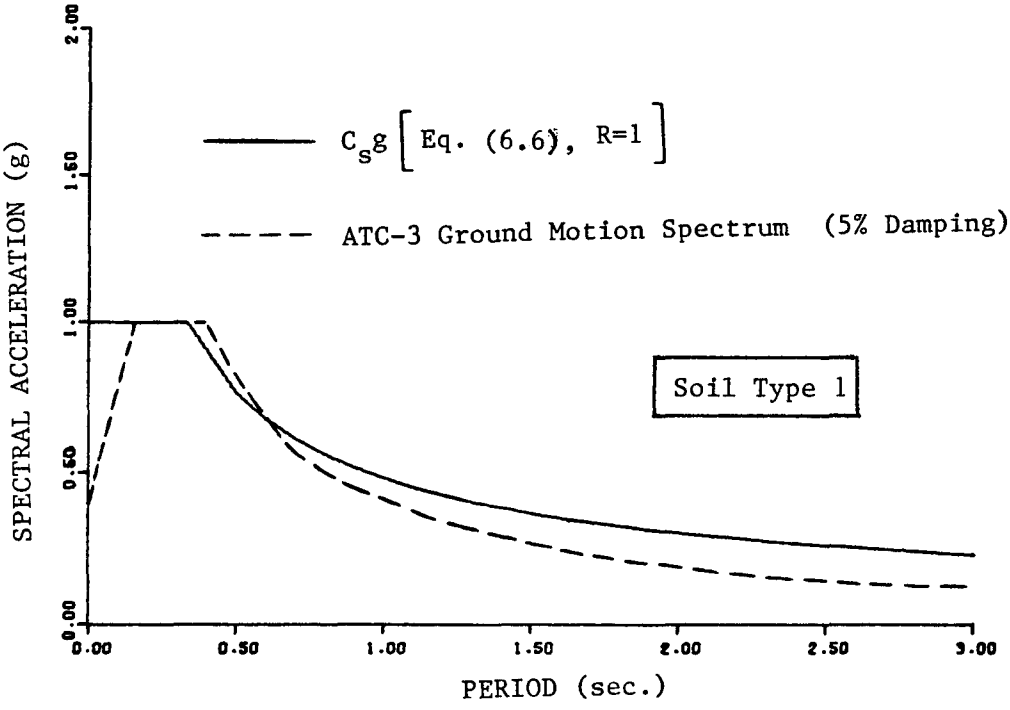

(a)

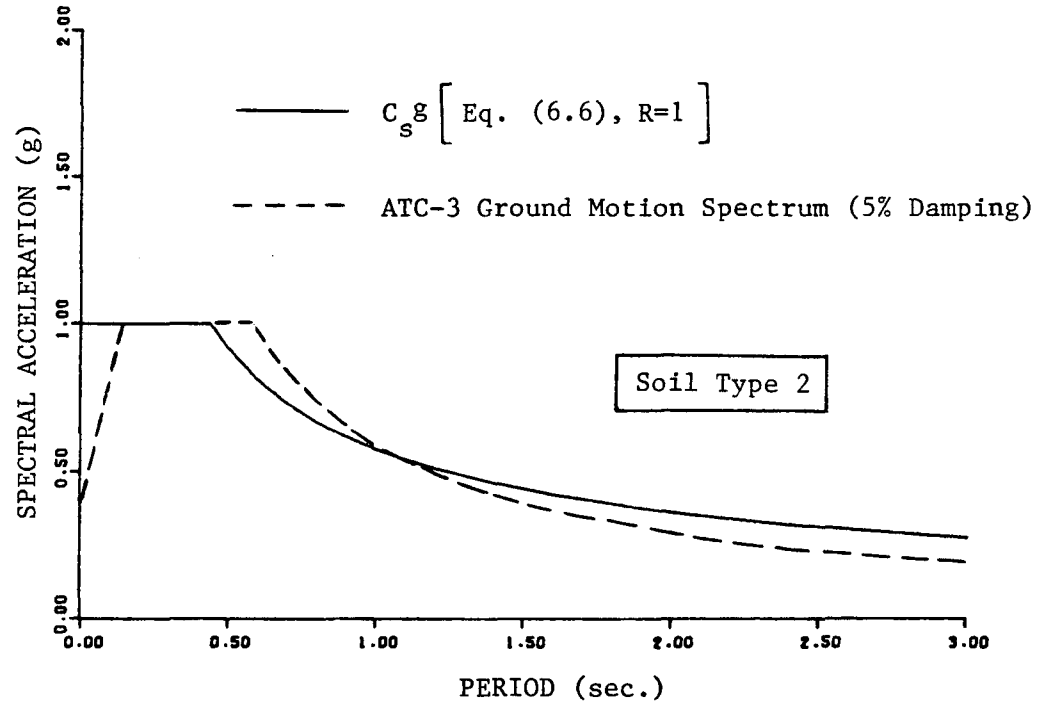

(b)

Fig. 6.8 Comparison between ATC-3 Ground Motion Spectra and Lateral Force Design Spectra

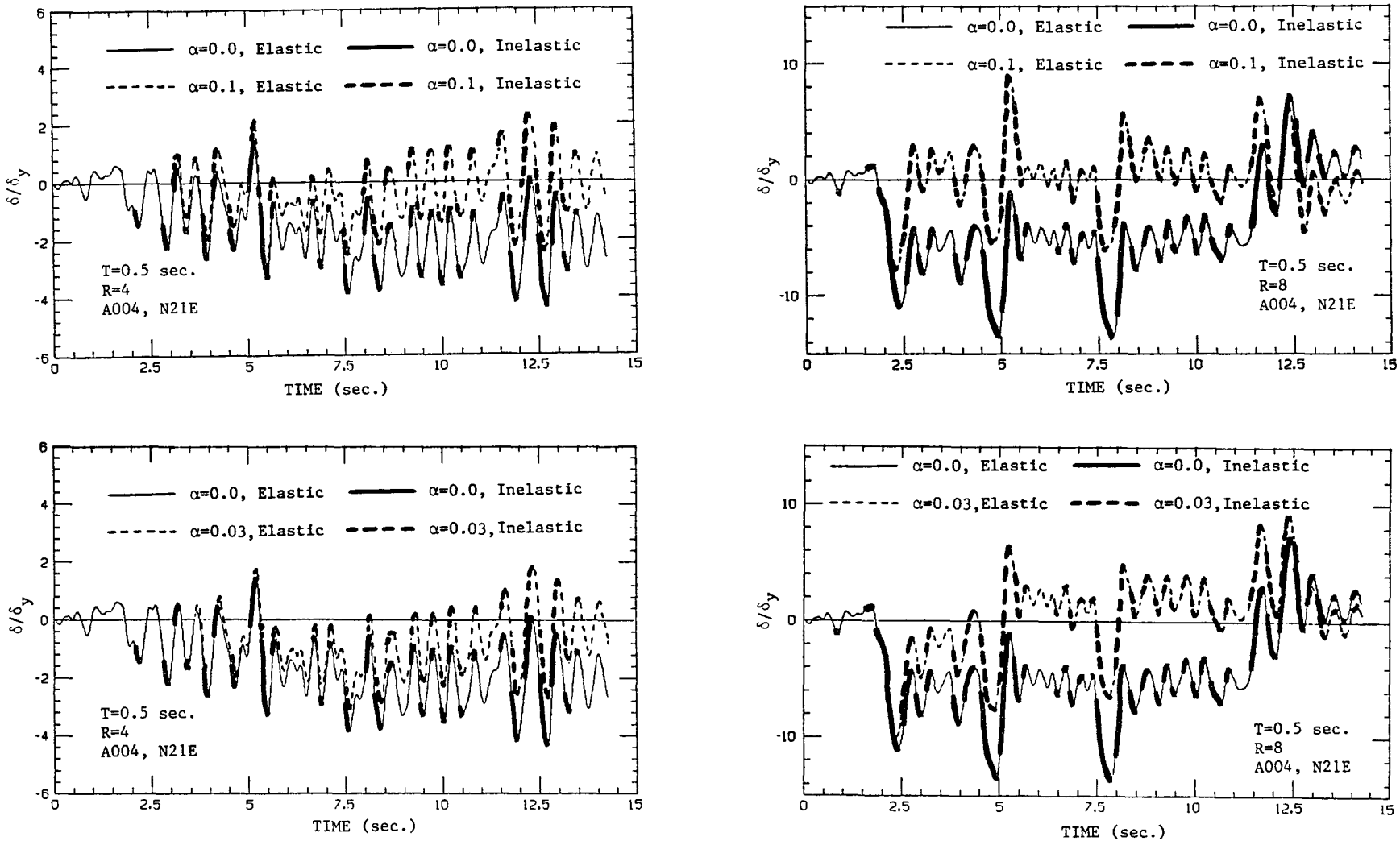

Fig. 6.9 Examples of Normalized Deformation (δ/δy) Histories for Different Systems

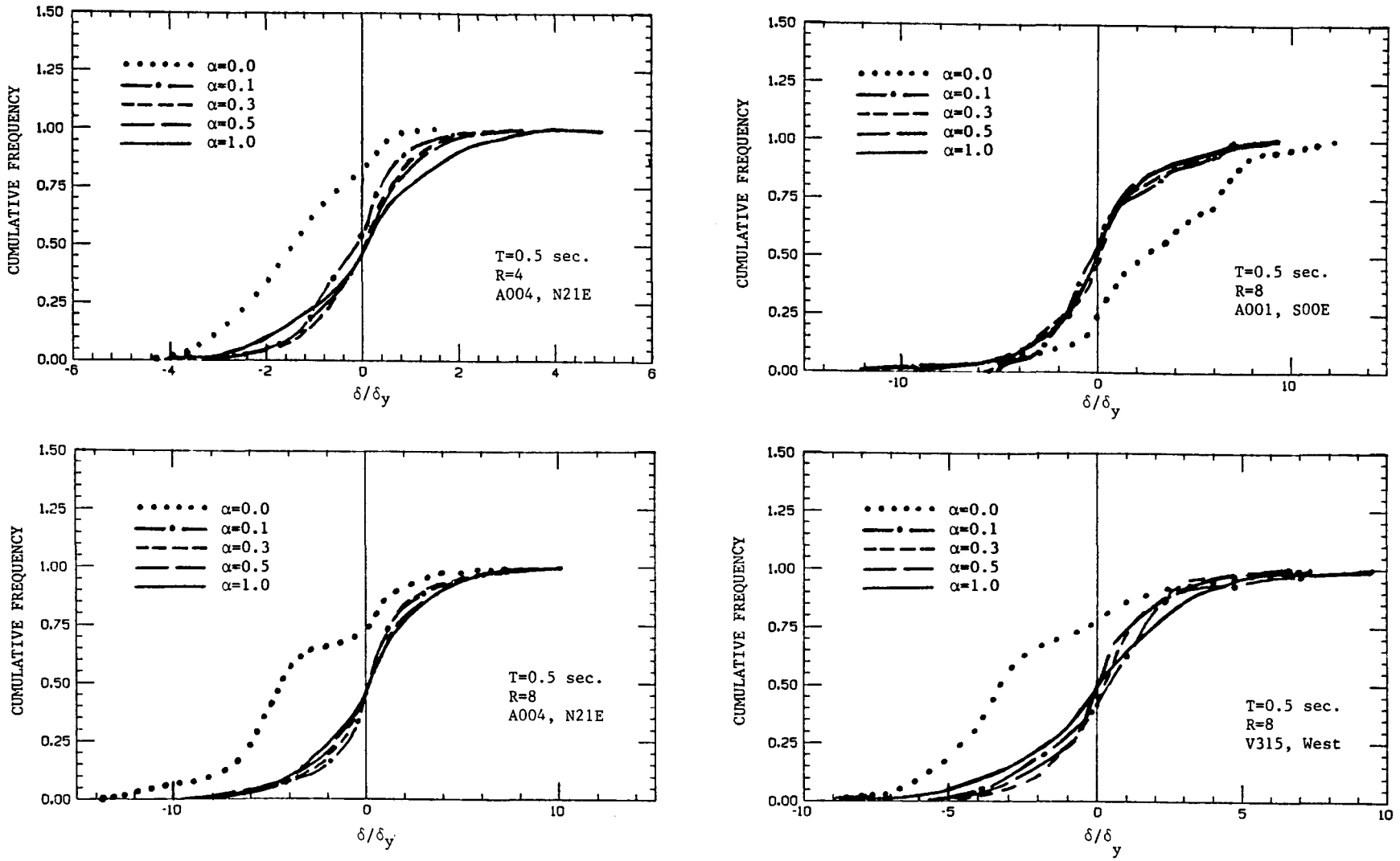

Fig. 6.10 Examples of Cumulative Frequency Polygon of δ/δ_y for Different Systems and Records

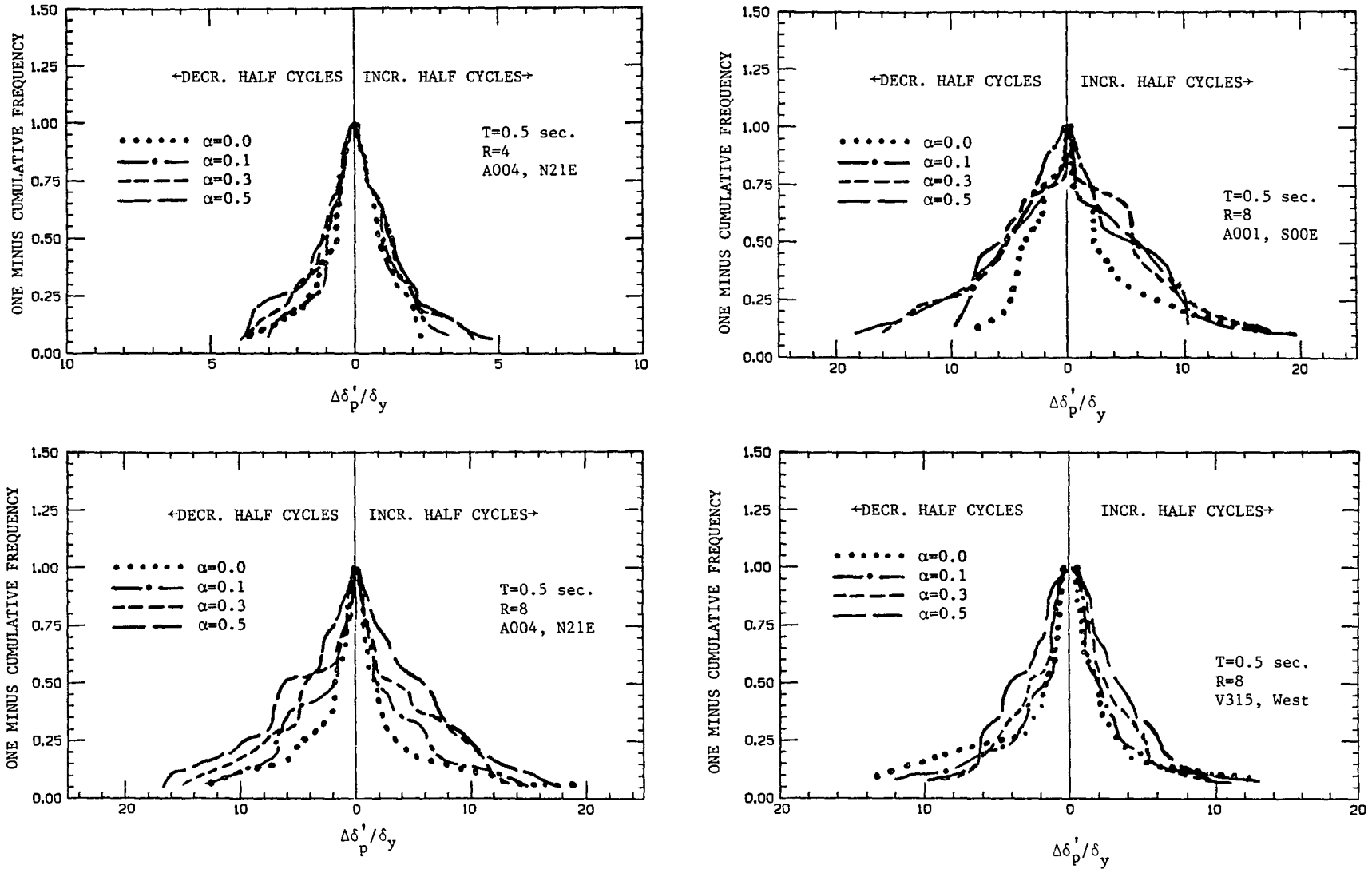

Fig. 6.11 Examples of One Minus Cumulative Frequency Polygon of $\Delta\delta'_p/\delta_y$ for Different Systems and Records

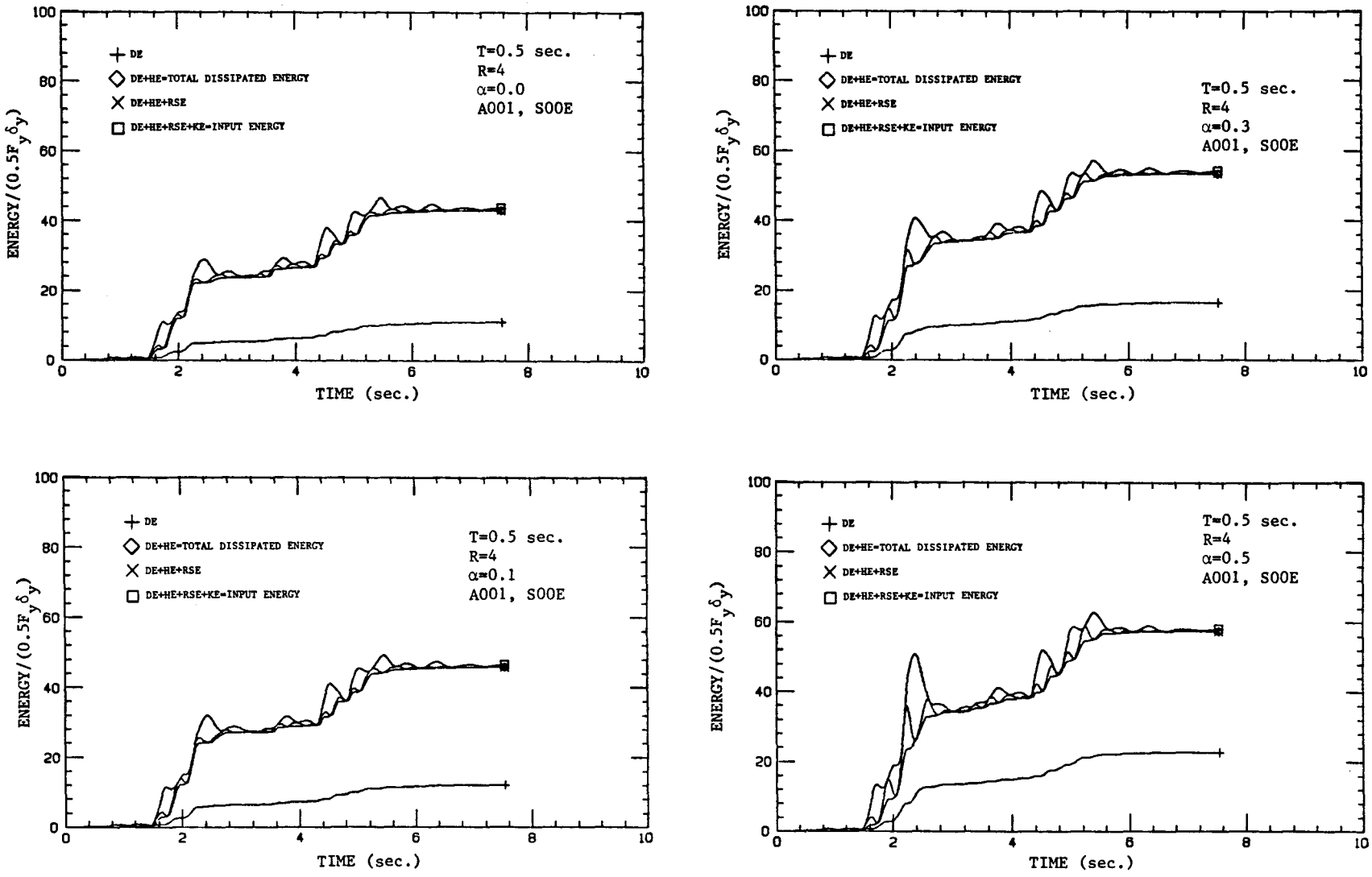

Fig. 6.12 Examples of Time Histories of Normalized Energy Terms for Different Systems

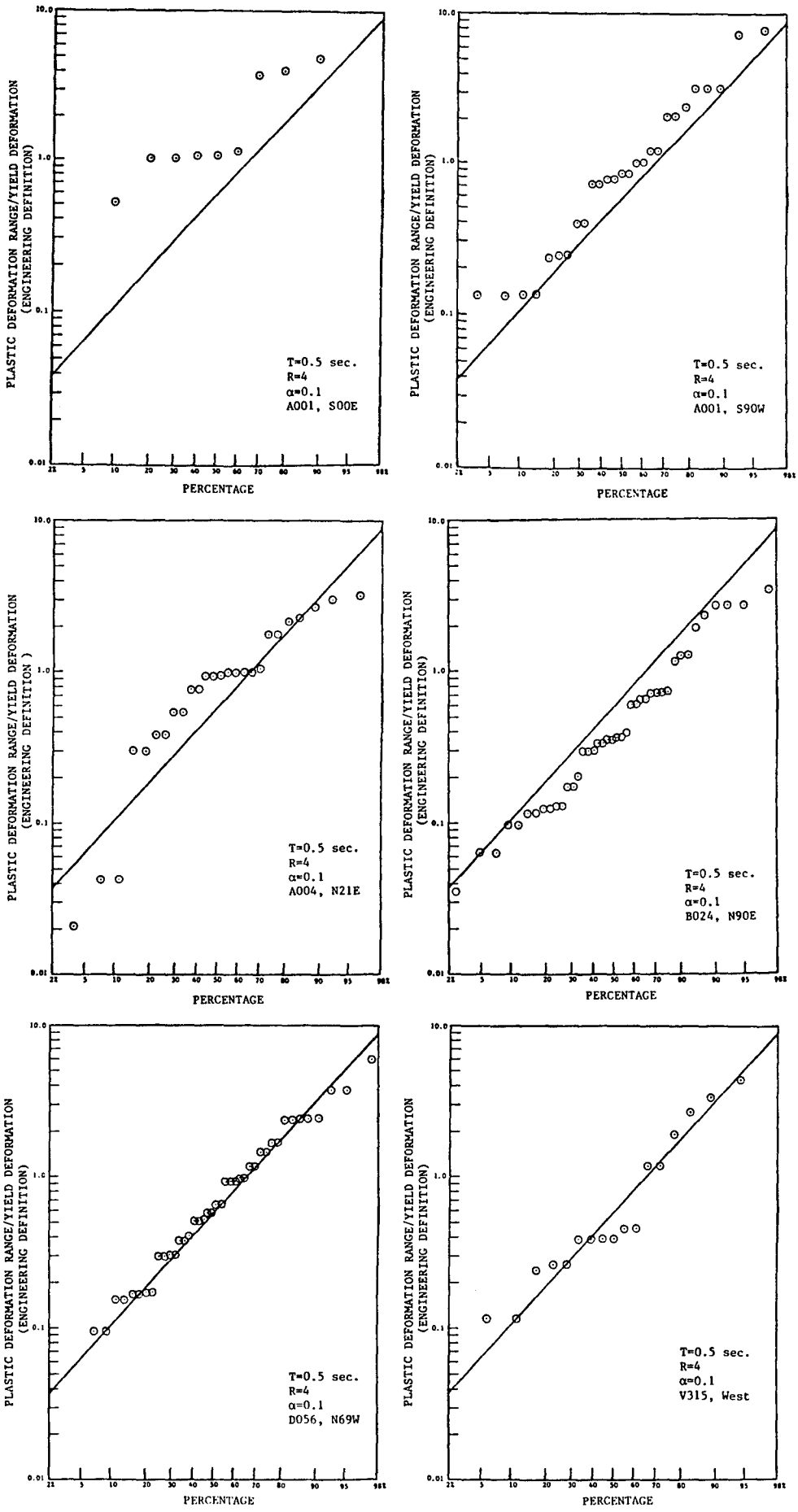

Fig. 6.13 Ordered Data Points of $\Delta\delta_p'/\delta_y$ for a Specific System and Individual Records, Plotted on Lognormal Probability Paper

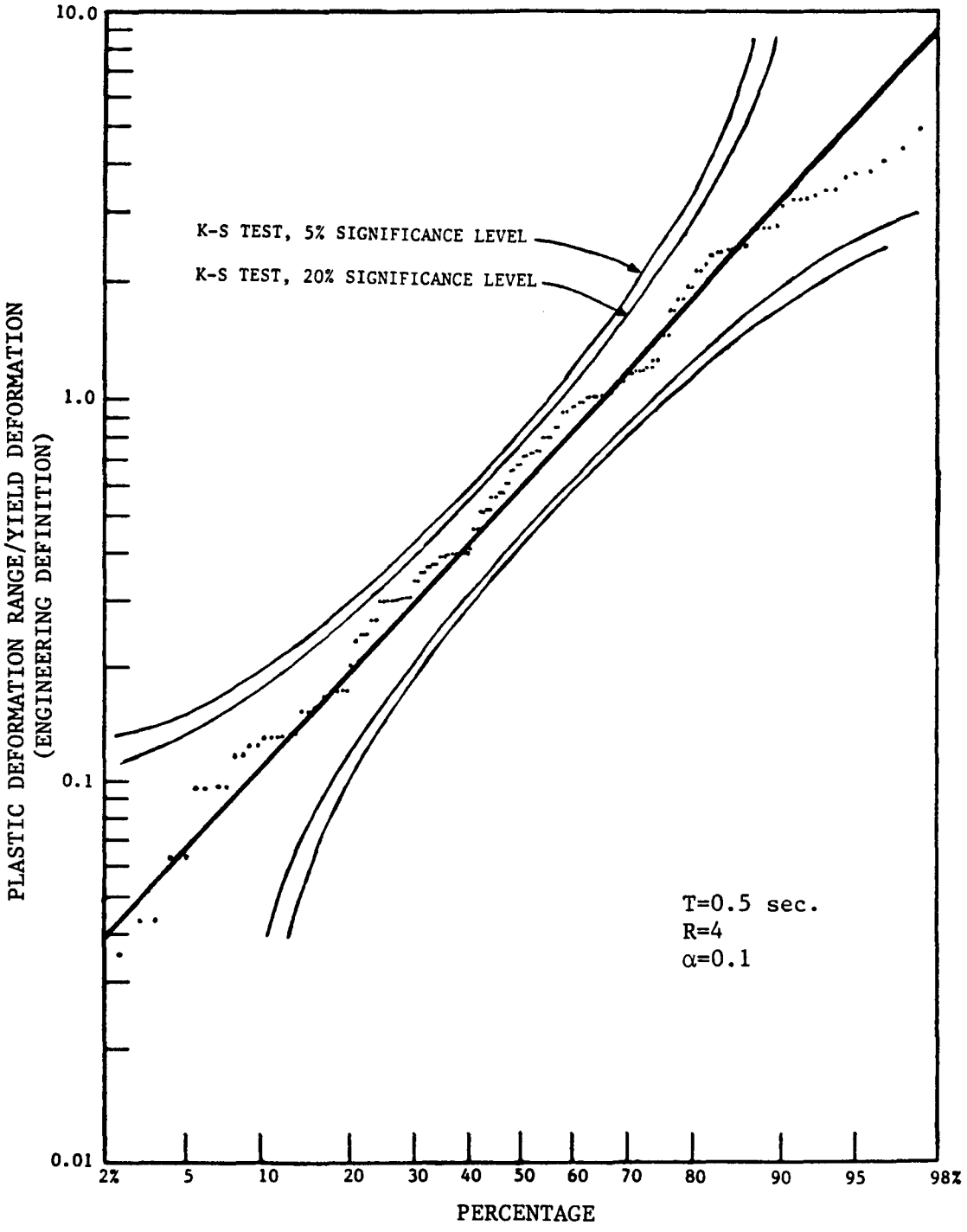

Fig. 6.14 Ordered Combined Data Points and Fitted Lognormal Distribution of $\Delta\delta_p'/\delta_y$ for a Specific System and All Records, Plotted on Lognormal Probability Paper

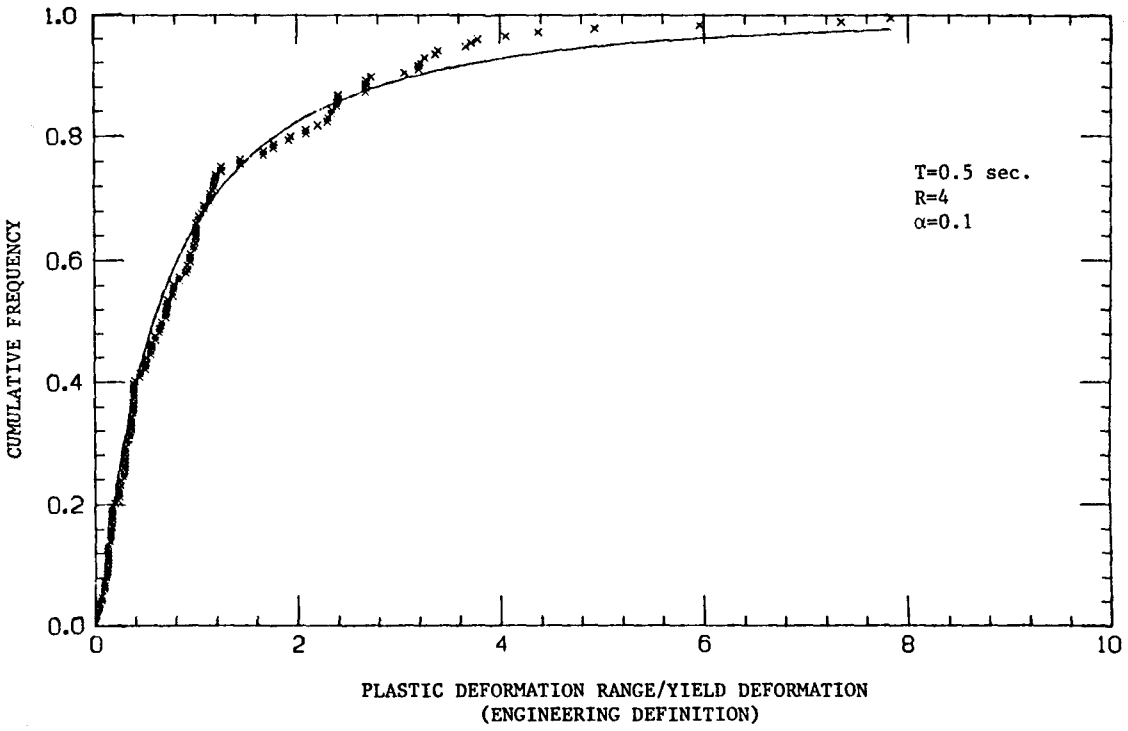

Fig. 6.15 Ordered Combined Data Points and Fitted Lognormal Distribution of $\Delta\delta'_p/\delta_y$ for a Specific System and All Records

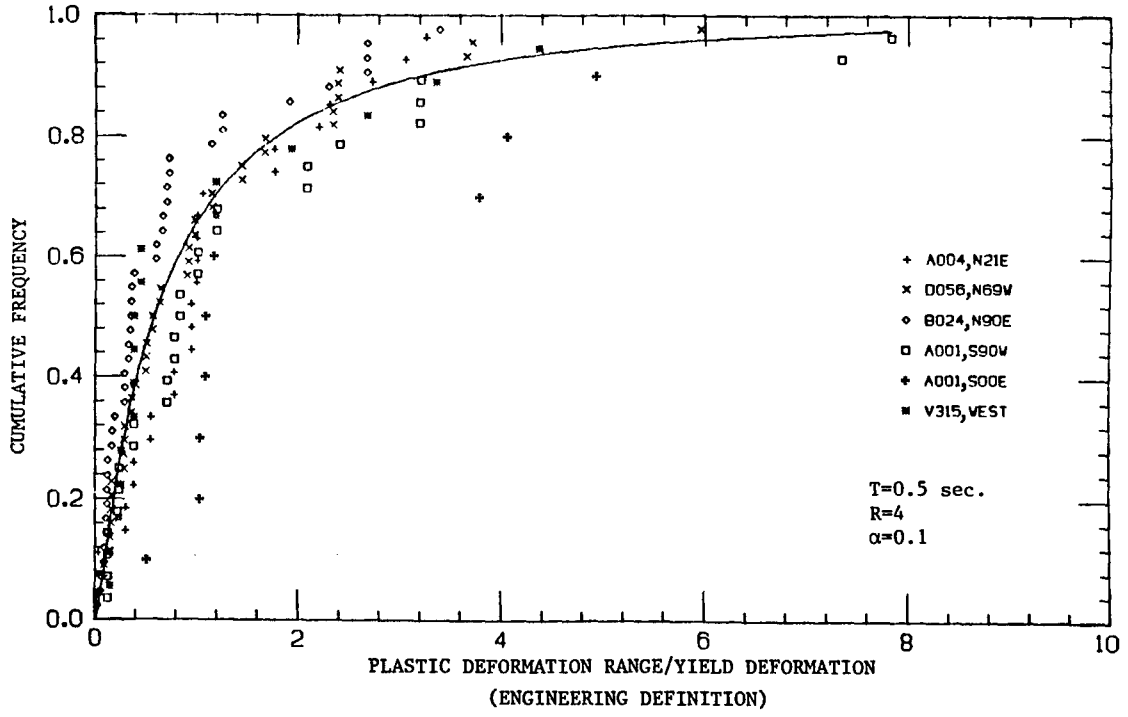

Fig. 6.16 Ordered Data Points of Individual Records and Fitted Lognormal Distribution (All Records) of $\Delta\delta'_p/\delta_y$ for a Specific System

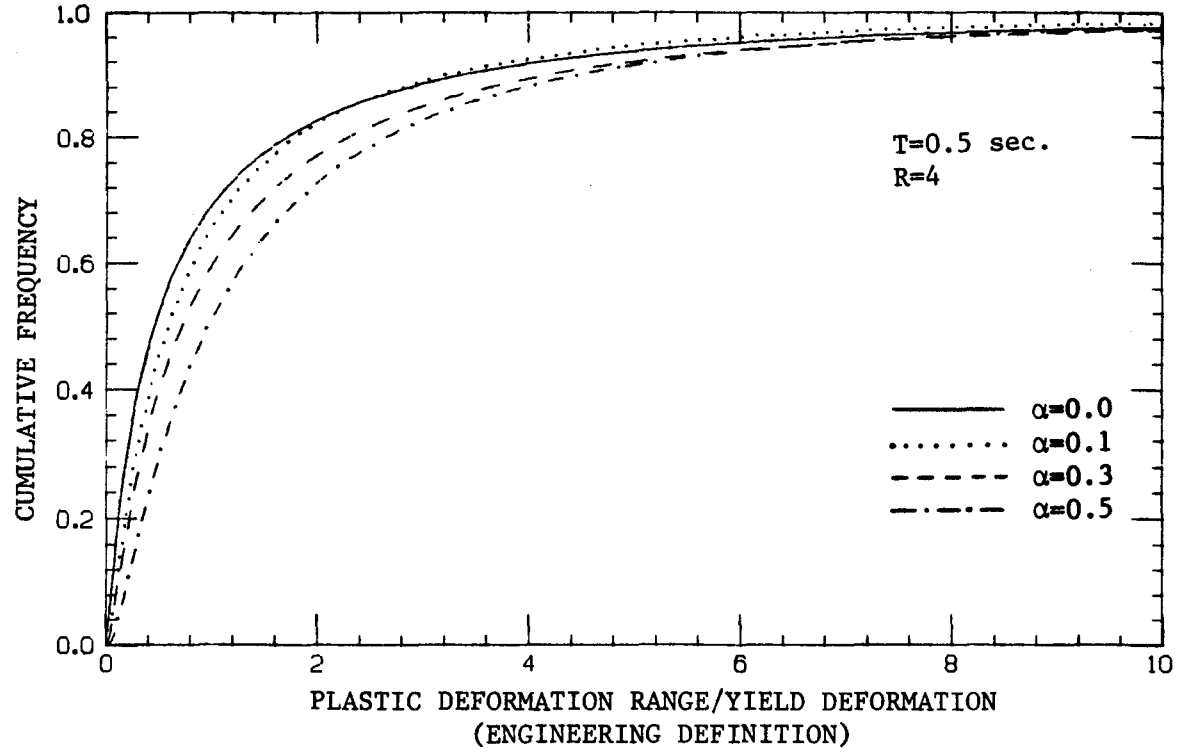

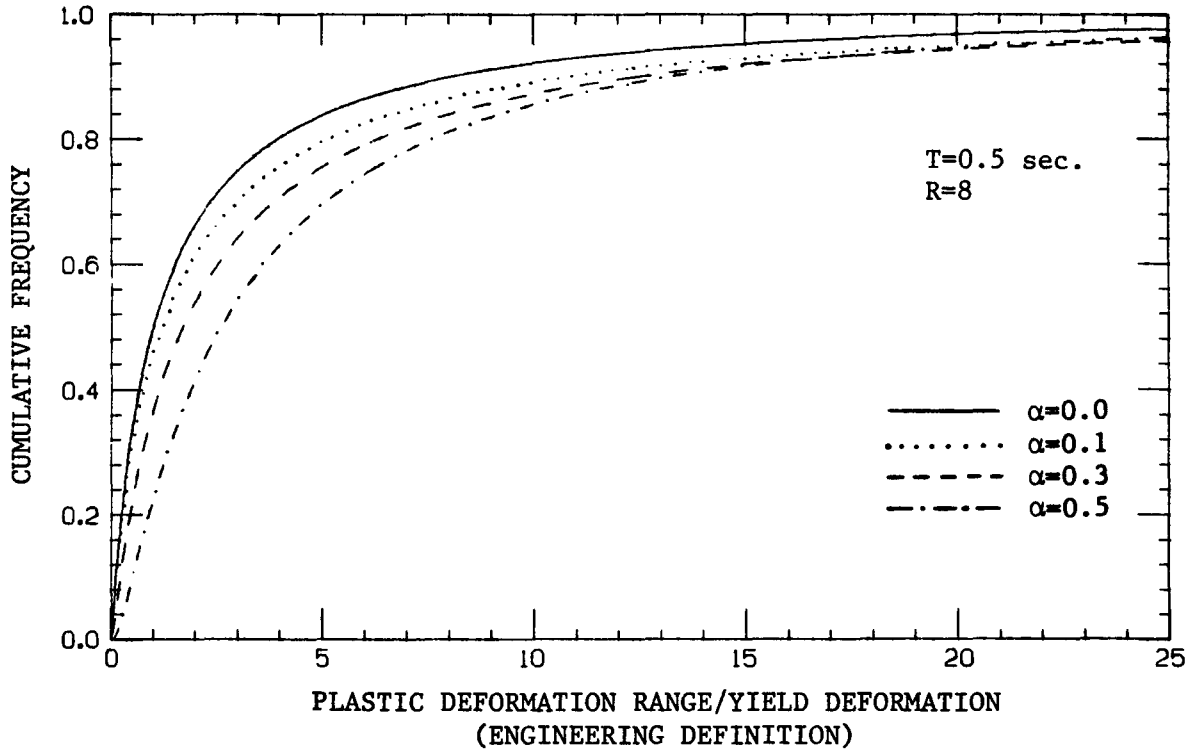

Fig. 6.17 Fitted Lognormal Distribution of $\Delta\delta_p'/\delta_y$ for Systems with Different α Values and R Equal to Four and Eight

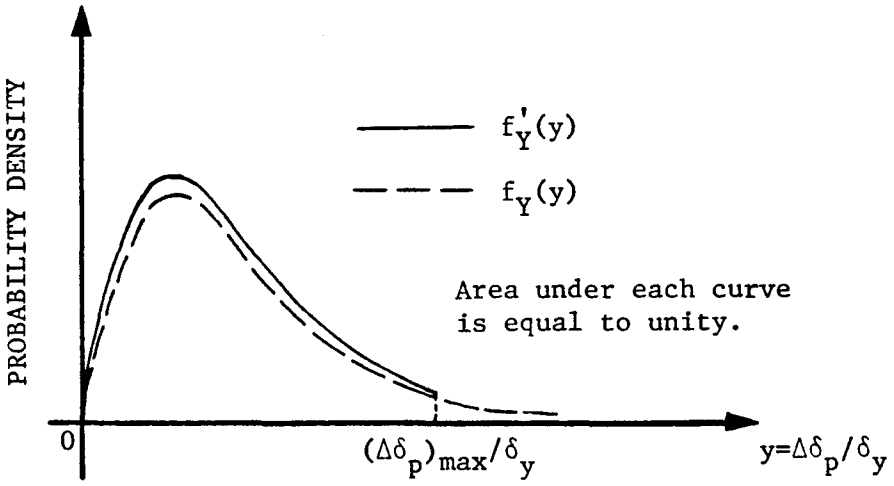

Fig. 6.18 Original $f_Y(y)$ and Truncated $f'_Y(y)$ for Deterministic y_{max}

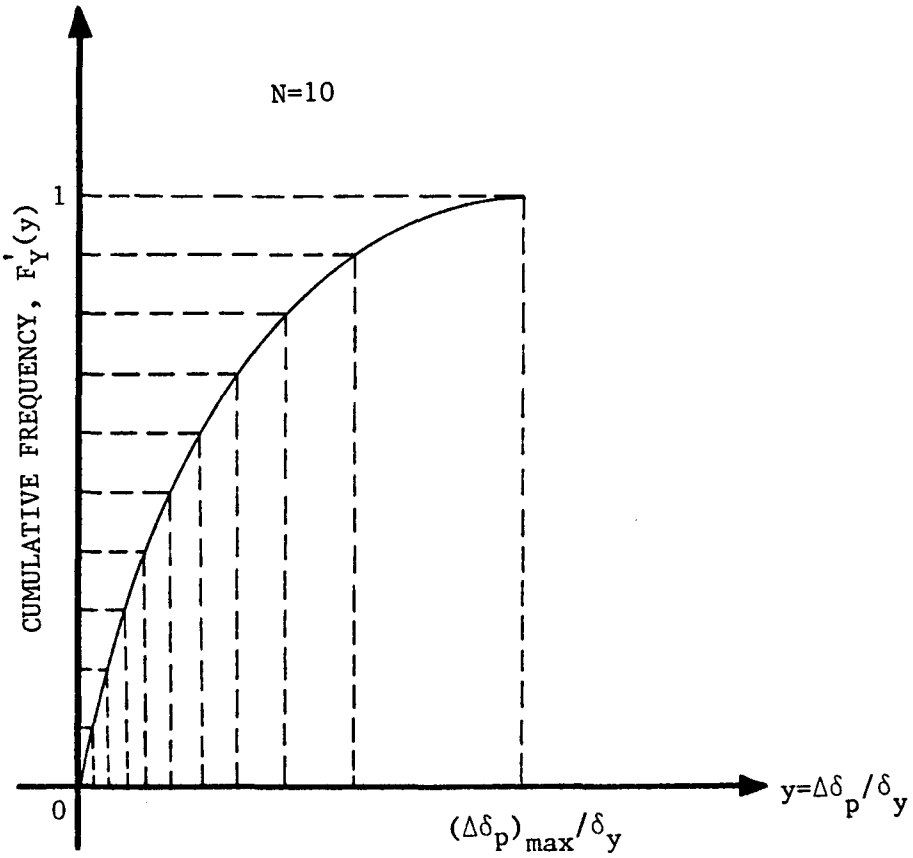

Fig. 6.19 Determination of $\Delta\delta_{pi}/\delta_y$ Values from $F'_Y(y)$

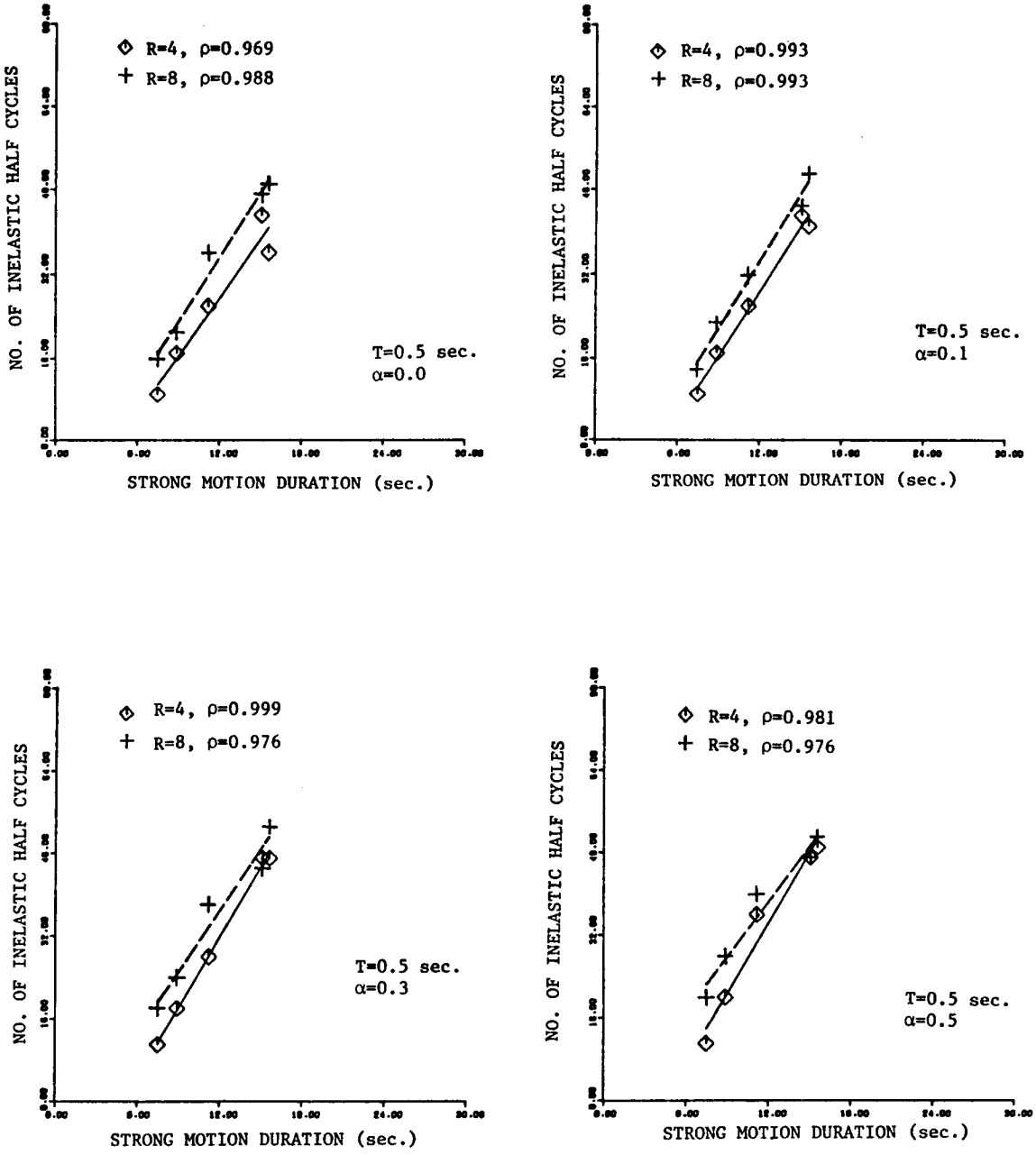

Fig. 6.20 Regression of N' on D_{sm} for Systems with Different α Values

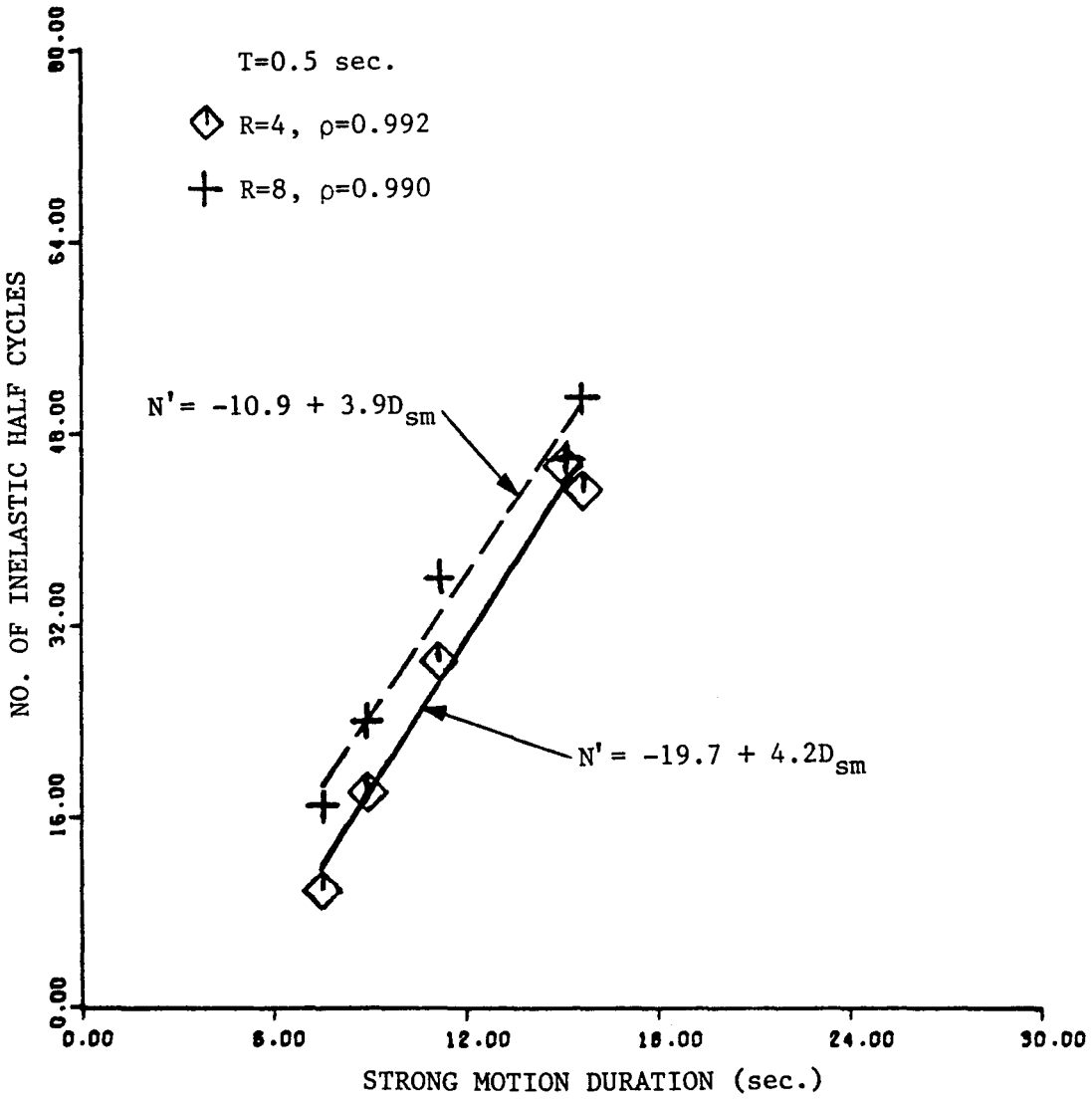

Fig. 6.21 Regression of N' on D_{sm}, Independent of α.

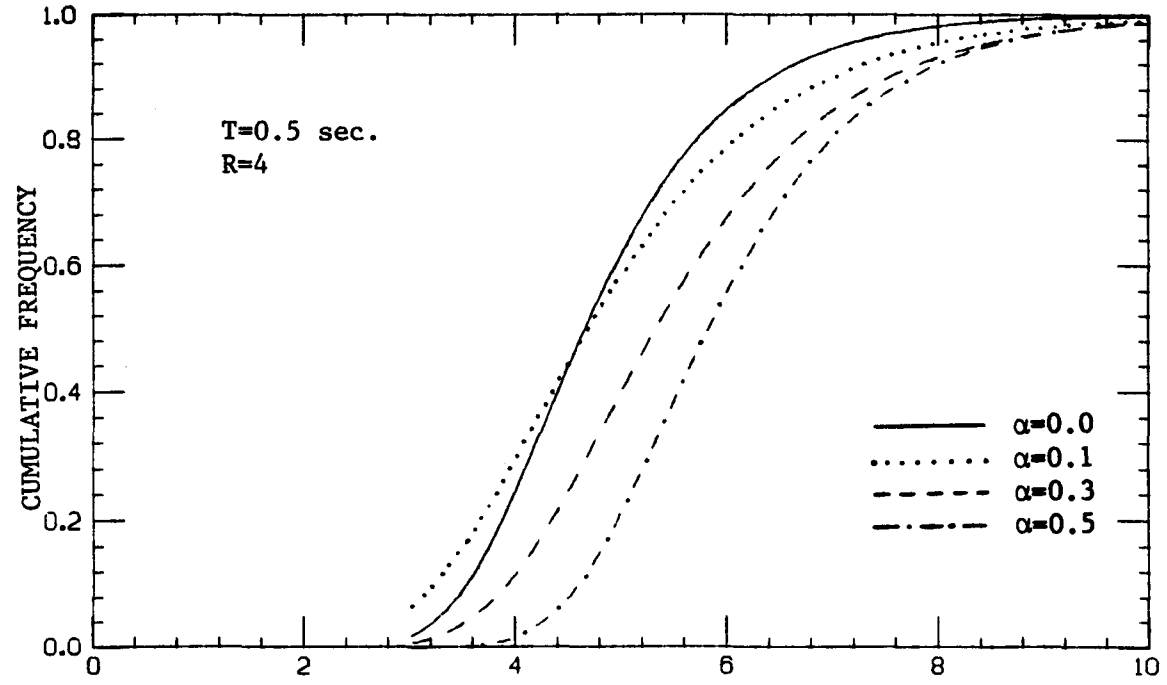

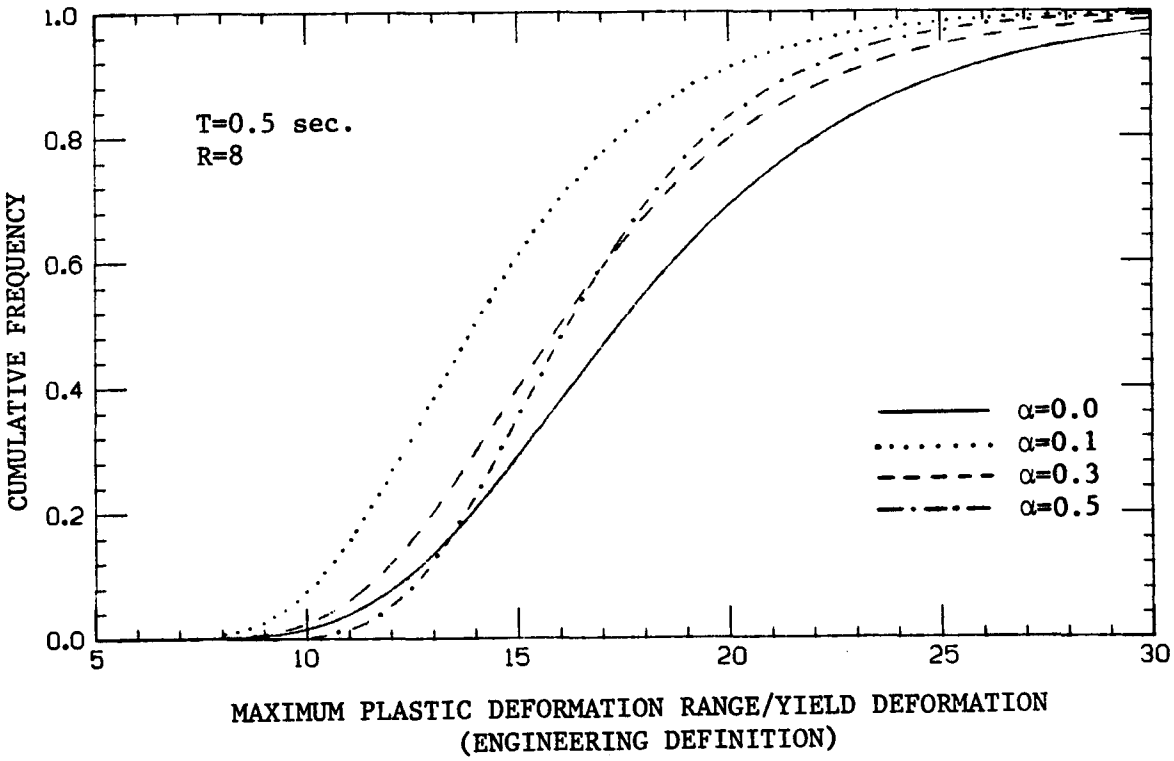

Fig. 6.22 Predicted Type I Extreme-Value Distribution of $(\Delta\delta_p')_{max}/\delta_y$ for Systems with Different α Values and R Equal to Four and Eight

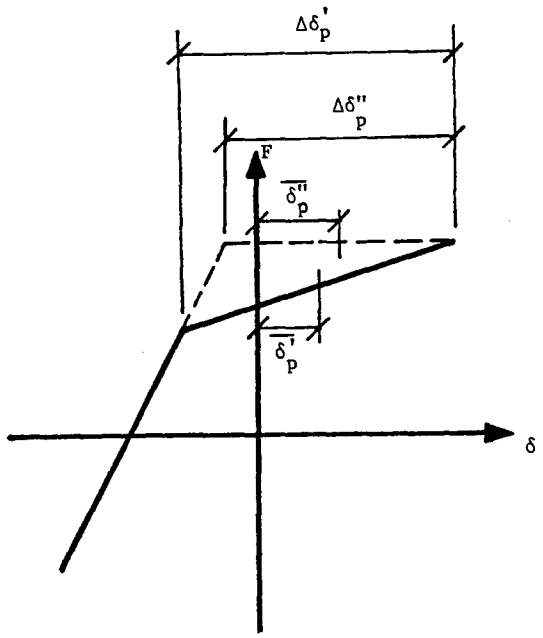

Fig. 6.23 Definition of Parameters Used in the Calculation of $\delta_{p,mean}$

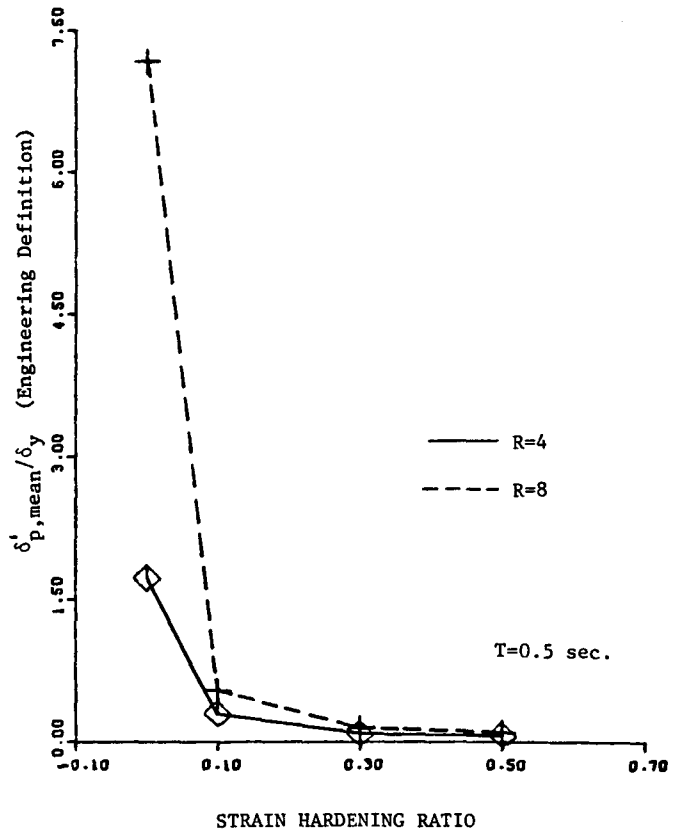

Fig. 6.24 Variation of $\delta'_{p,mean}$ with α for Systems with R equal to Four and Eight

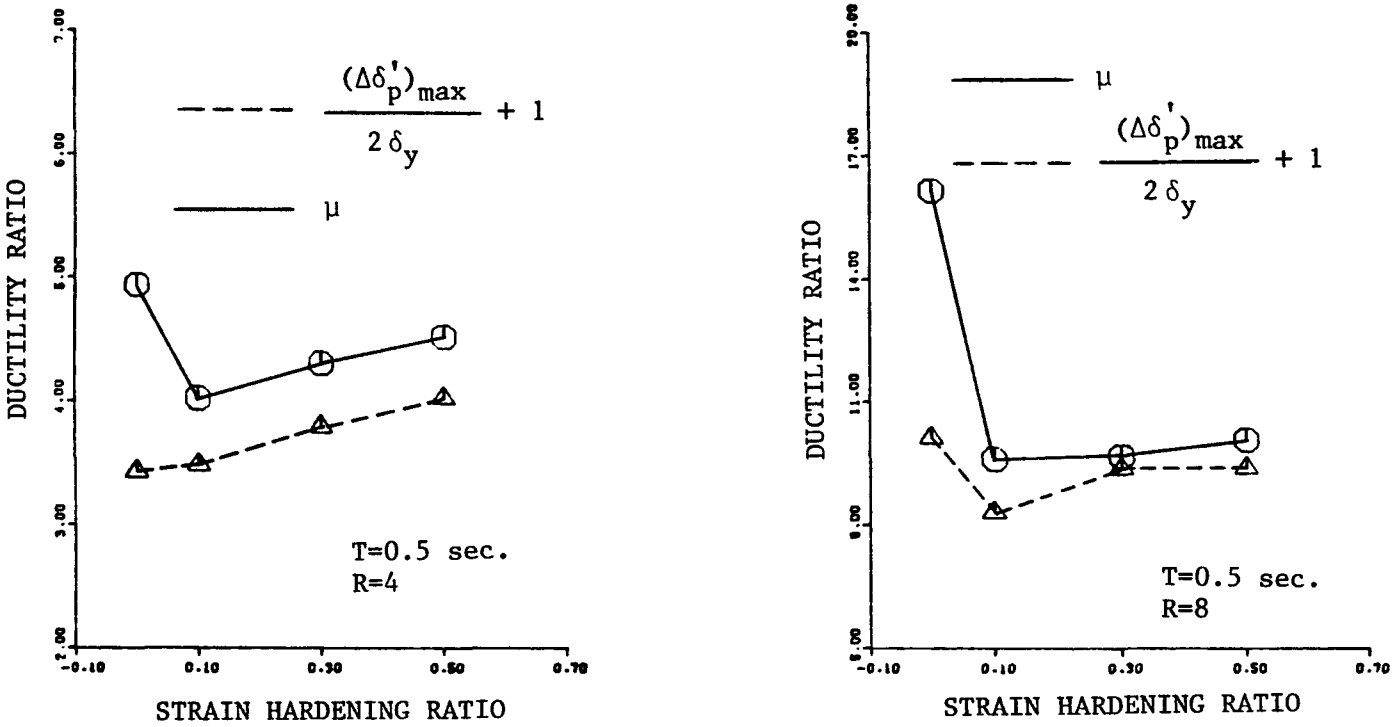

Fig. 6.25 Comparison Between Observed Mean Values of μ and Eq. (6.27) for Different α Values

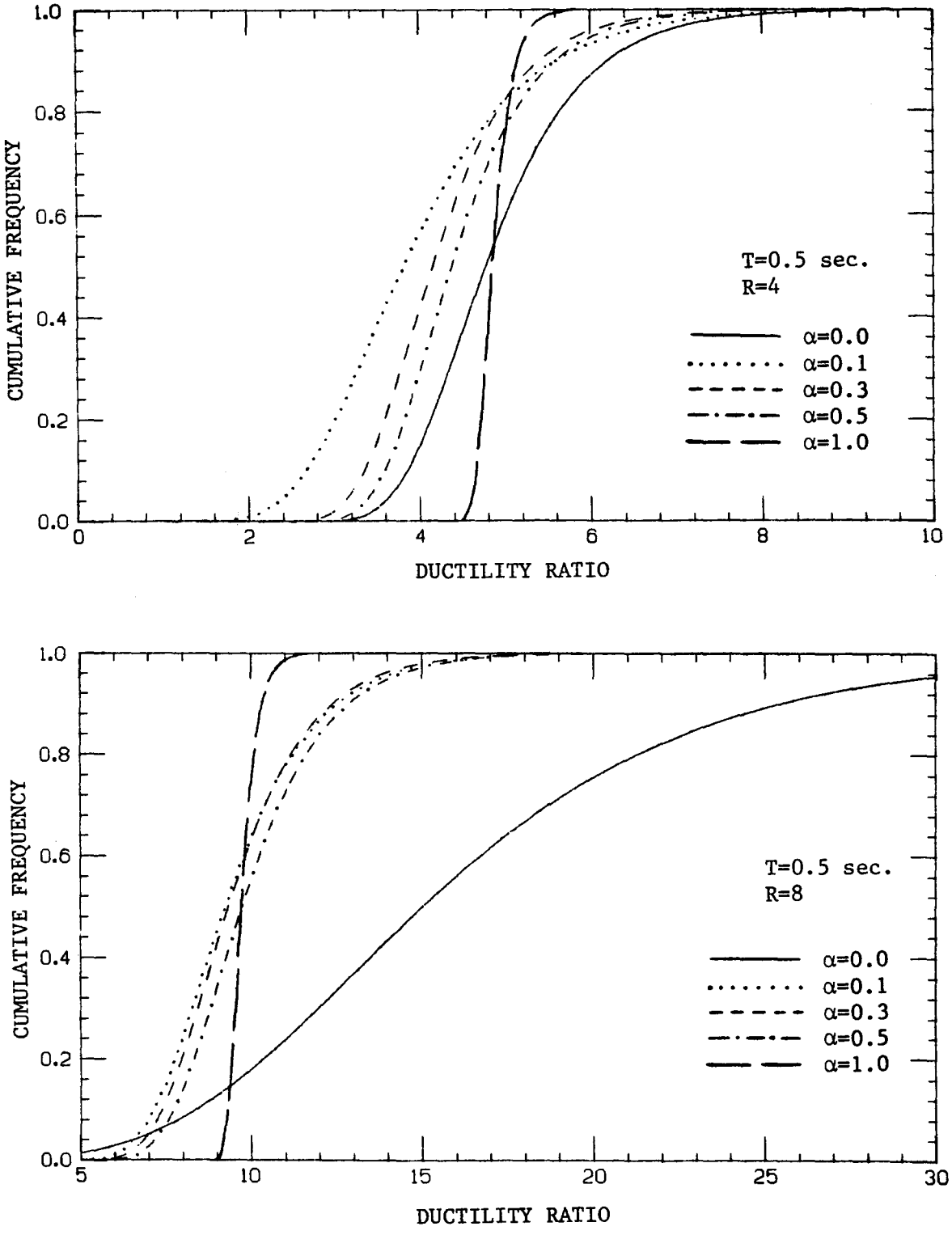

Fig. 6.26 Predicted Type I Extreme-Value Distribution of μ for Systems with Different α Values and R equal to Four and Eight

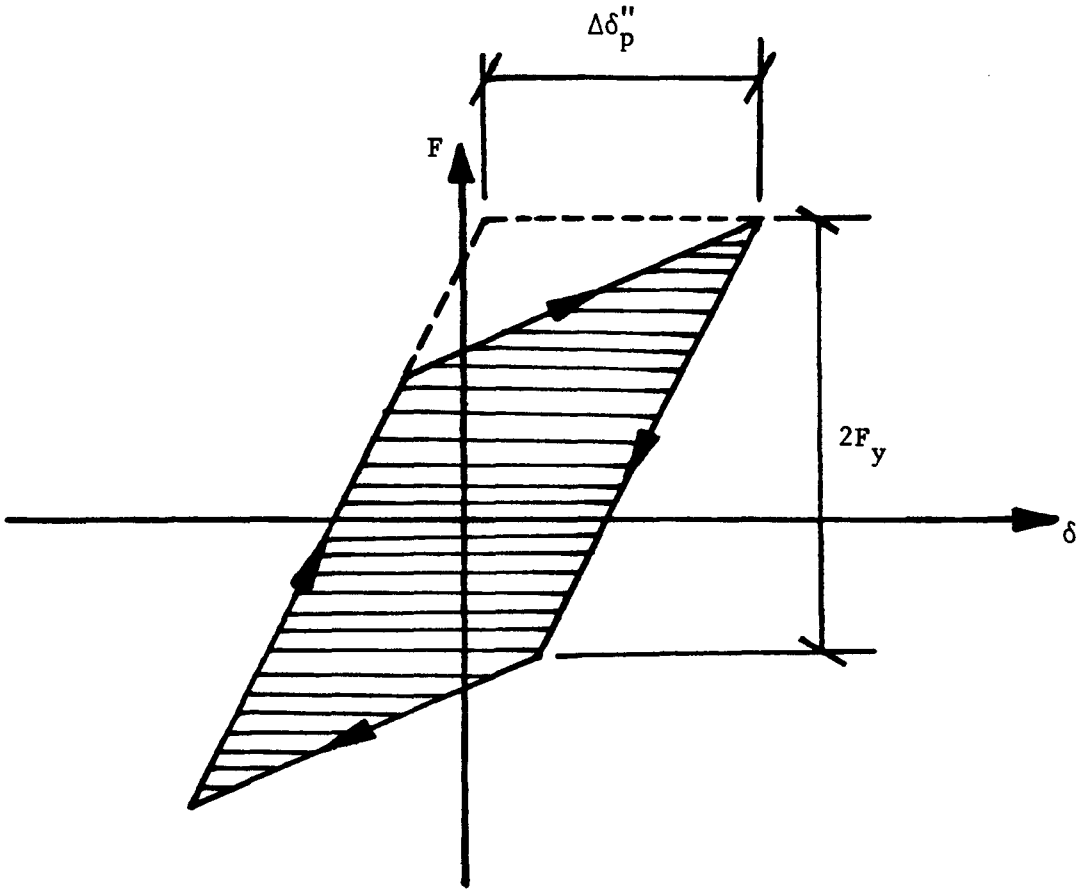

Fig. 6.27 Hysteretic Energy Dissipation per Cycle

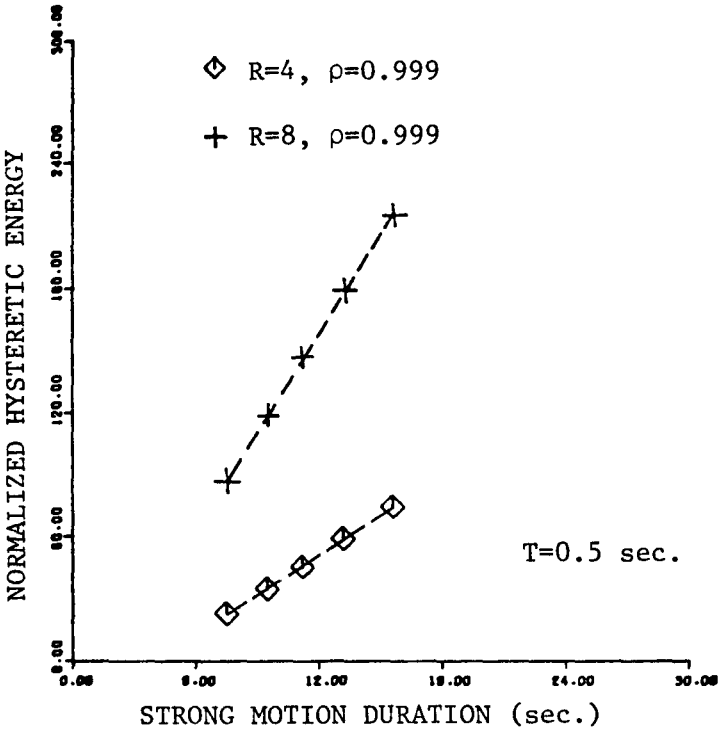

Fig. 6.28 Regression of Predicted $HE_t/0.5F_y\delta_y$ (Average for α = 0.0 to 0.5) on Strong Motion Duration

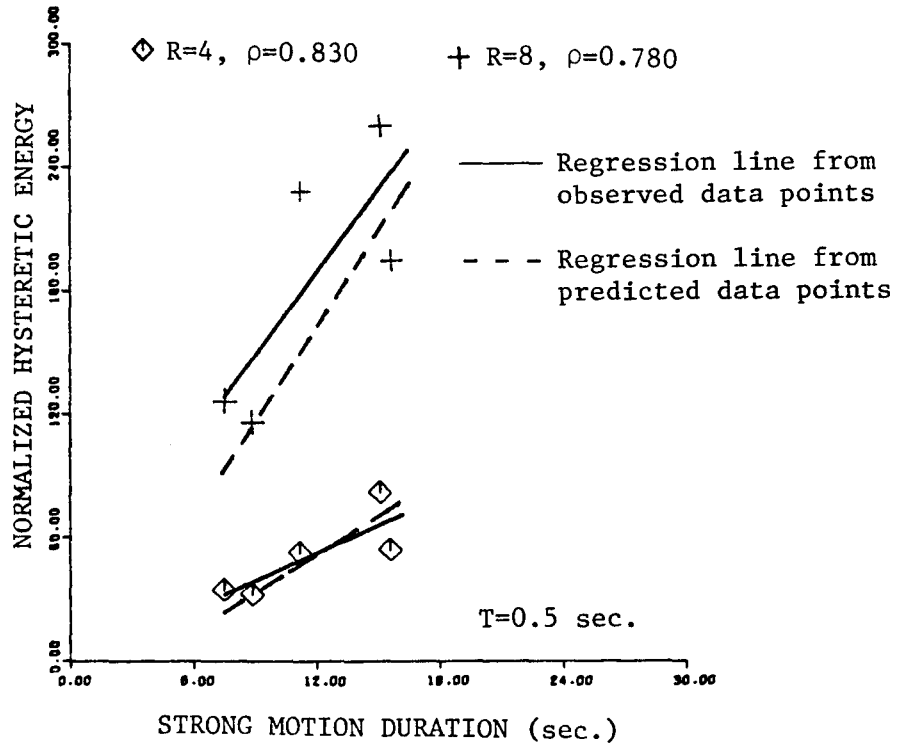

Fig. 6.29 Regression of Observed $HE_t/0.5F_y\delta_y$ (Average for α = 0.0 to 0.5) on Strong Motion Duration

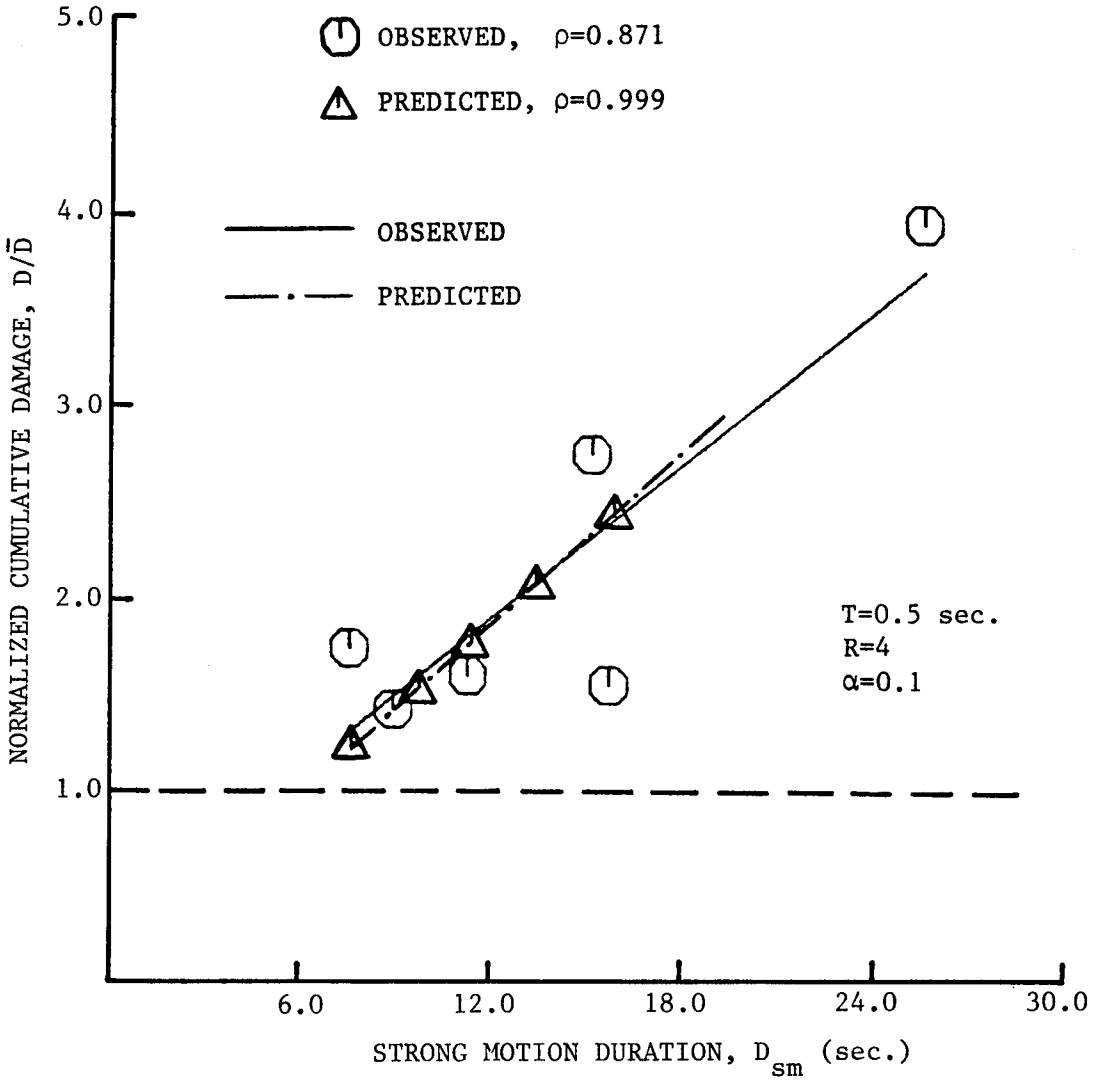

Fig. 6.30 Variation of Observed and Predicted Normalized Cumulative Damage with Strong Motion Duration for a Specific System

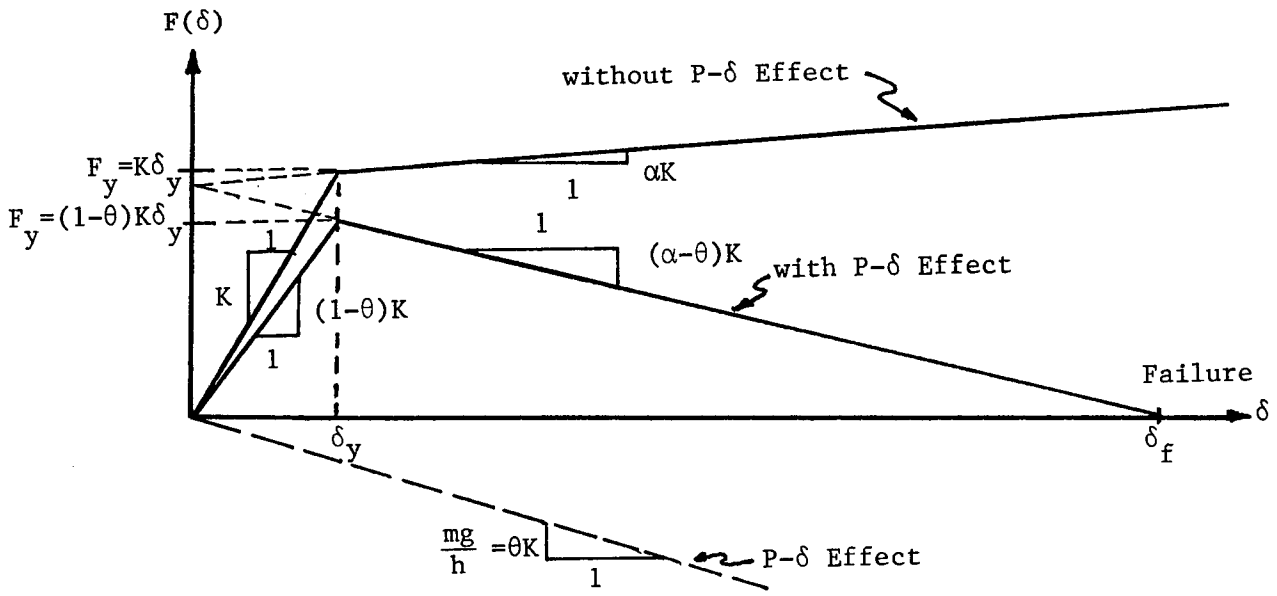

Fig. 6.31 Effect of P-δ on Structural System

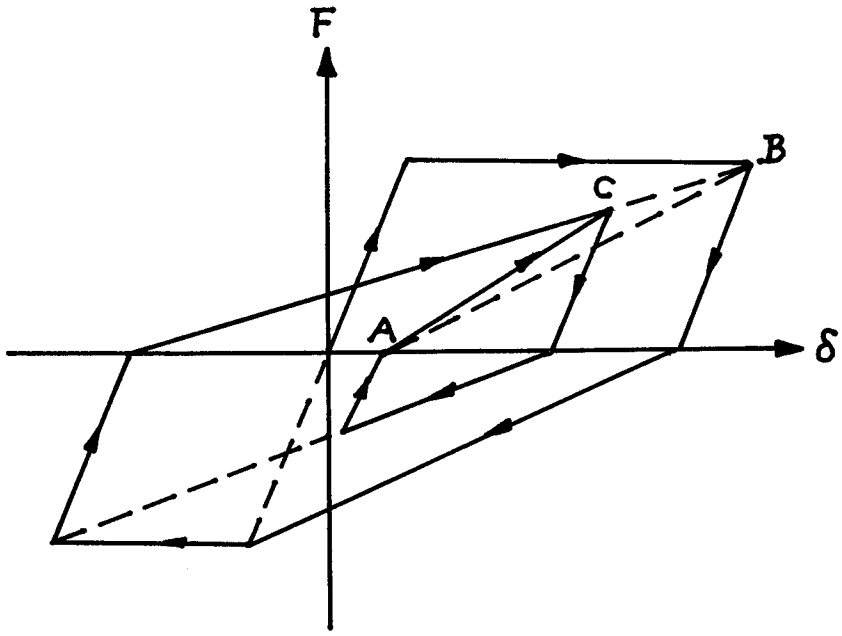

Fig. 6.32 Modified Clough Model

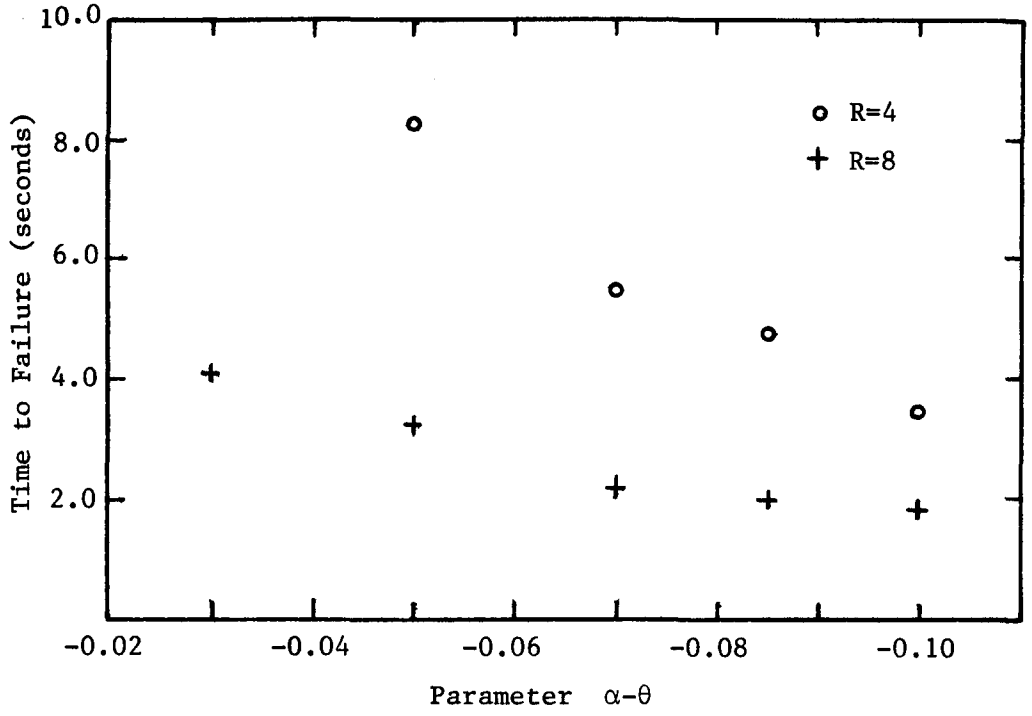

Fig. 6.33 Average Times to Failure for Nondegrading Elastic-Plastic Systems (α = 0.0) with P-δ Effect

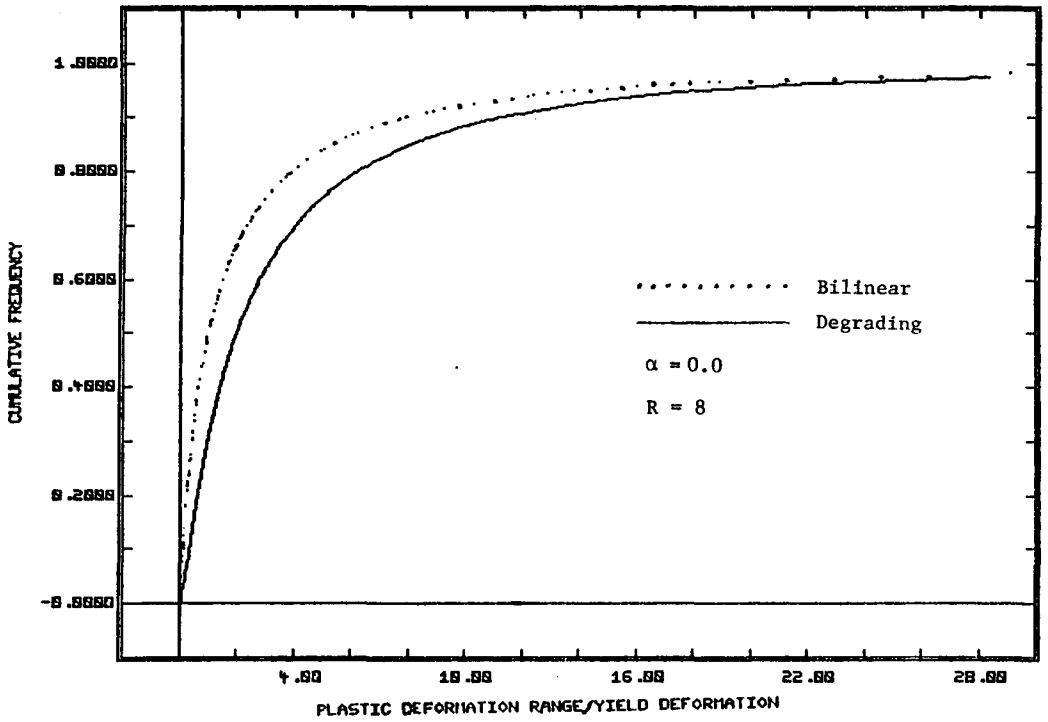

Fig. 6.34 Effect of Stiffness Degradation on the Fitted CDF of $\Delta\delta_p/\delta_y$

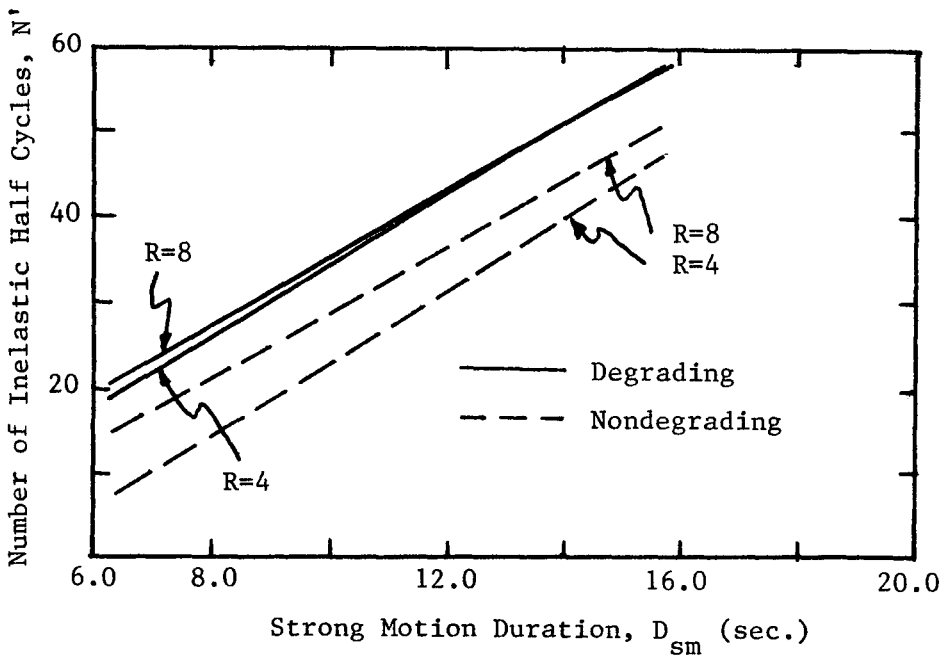

Fig. 6.35 Effect of Stiffness Degradation on the Correlation between the Number of Inelastic Half Cycles and Strong Motion Duration

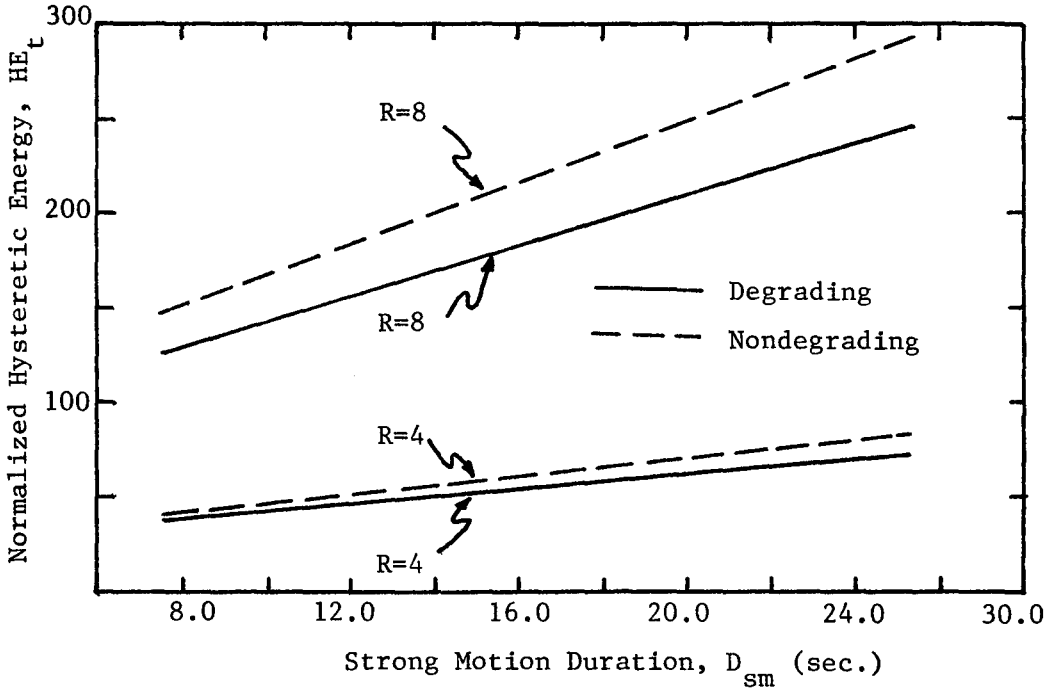

File 6.36 Effect of Stiffness Degradation on the Correlation betwen Normalized Hysteretic Energy and Strong Motion Duration

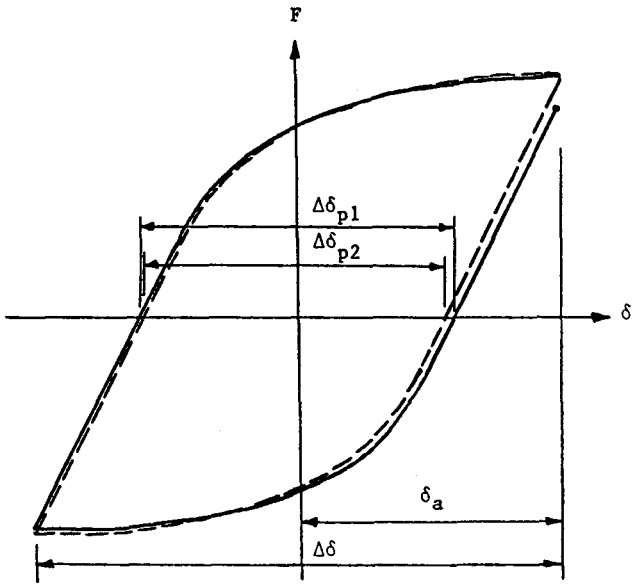

Fig. 7.1 Constant Deflection Amplitude Cycles

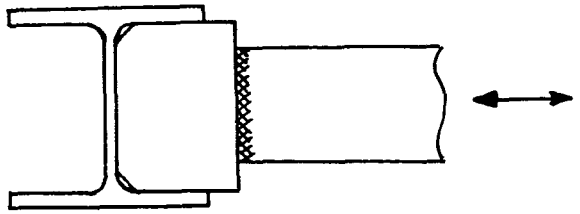

Fig. 7.2 Beam Flange to Column Web Connection

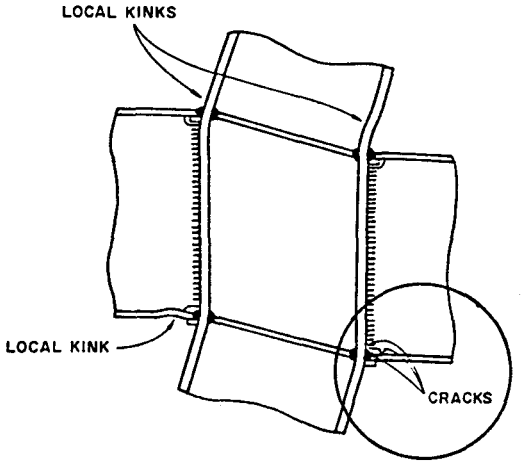

Fig. 7.3 Cracks in Beam Weld due to Distortion of Panel Zone

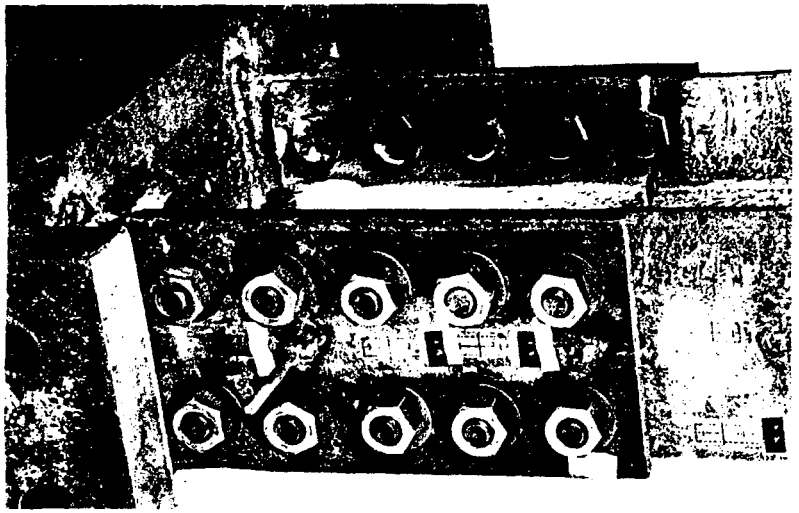

Fig. 7.4 Fracture in Bolted Moment Splice (Ref. 23)

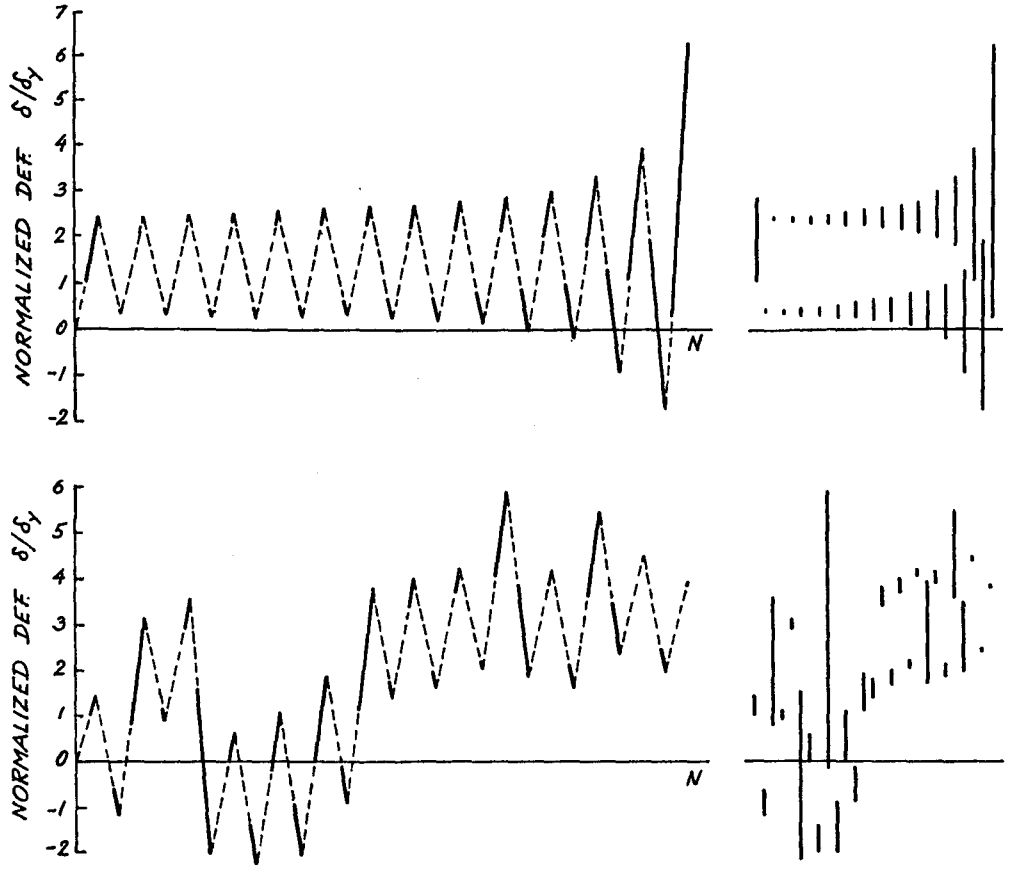

Fig. 7.5 Examples of Representative Loading Histories

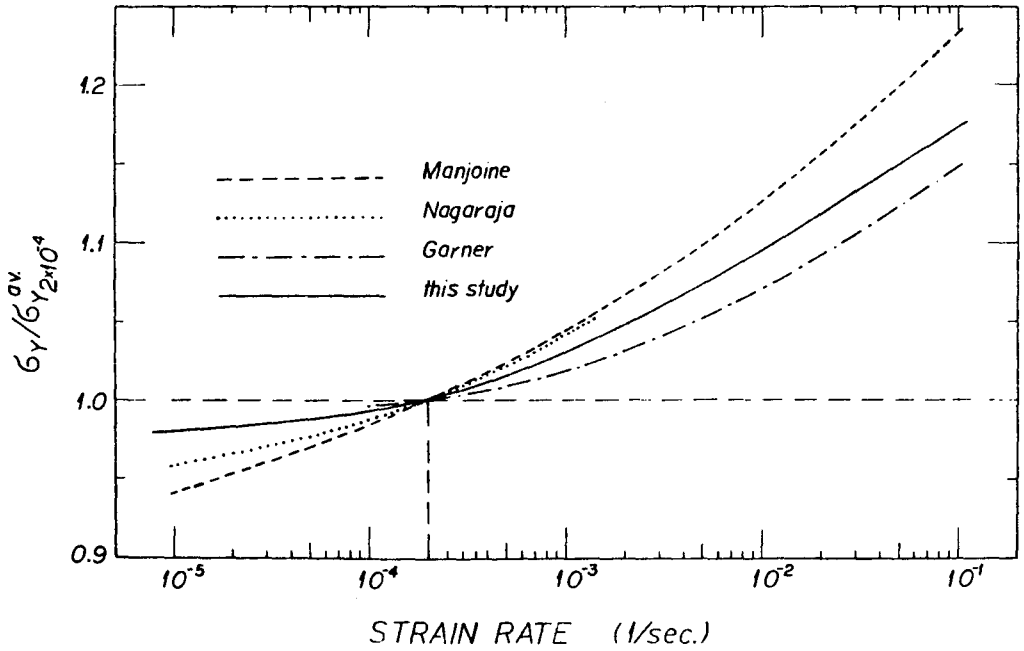

Fig. 7.6 Effect of Strain Rate on Yield Strength of Structural Steel (Ref. 129)